Realtime imaging of force fields at the nanoscale with a 2D nano-mechanical probe

Philip Heringlake

Philip Heringlake. Realtime imaging of force fields at the nanoscale with a 2D nano-mechanical probe. Condensed Matter [cond-mat]. Université Grenoble Alpes [2020-..], 2021. English. NNT : 2021GRALY063 . tel-03579099

Université
Grenoble Alpes

THÈSE

Pour obtenir le grade de

DOCTEUR DE L'UNIVERSITÉ GRENOBLE ALPES

Spécialité : **Physique**

Arrêté ministériel : 25 mai 2016

Présentée par

Philip Heringlake

Thèse dirigée par **Olivier Arcizet**
et codirigée par **Benjamin Pigeau**

préparée au sein du **l'Institut Néel, CNRS**
dans **l'École Doctorale Physique**

Realtime imaging of force fields at the nanoscale with a 2D nano-mechanical probe

Exploration des champs de force à l'échelle nanométrique avec une sonde nano-optomécanique

Thèse soutenue publiquement le **26 octobre 2021,**
devant le jury composé de :

Mme. Elisabeth Charlaix
Professeur des Universités, Université Grenoble Alpes,
Présidente de jury

M. Serge Reynaud
DR émérite, Laboratoire Kastler Brossel, *Examinateur*

M. Adrian Bachtold
Professeur, ICFO Barcelone, *Examinateur*

M. Antoine Heidmann
Directeur de recherche, Laboratoire Kastler Brossel,
Rapporteur

M. Alessandro Siria
Chargé de recherche, Laboratoire de Physique de
l'Ecole Normale Supérieure, *Rapporteur*

Realtime imaging of force fields at the nanoscale with a 2D nano-optomechanical probe

Exploration of electrostatic, proximity and synthetic force fields

P. Heringlake

I dedicate this work to my parents and grandparents who are always supportive even though they never really knew what I was doing.

Diese Doktorarbeit ist meinen Eltern und Großeltern gewidmet auf deren Unterstützung immer Verlass ist, auch wenn ihnen nie klar war was ich eigentlich tue.

Realtime imaging of force fields at the nanoscale with a 2D nano-optomechanical probe
Thesis, Université Grenoble Alpes, Grenoble

This thesis has been realized in *GNU Emacs'* [45] magnificient markdown language *Org Mode* [82] using the fabulous *DOOM Emacs* [68] configuration framework and a strongly modified thesis template [46]. The document has been typeset in LaTeXwith the *Mimosis* style [97]. With few exeptions, figures have been creates using free software, such as *Python* [114], *pgfplots*[25], *Inkscape*[30] or *GIMP* [42].

Preface

When, in 2017, I first visited the group of *Olivier Arcizet* and *Benjamin Pigeau*, I was greeted by an outstanding excitement for science and research that has been conveyed also by my predecessor *Laure Mercier de Lépinay* who handed over to me a setup with which the first scanning nanowire microscopy has been realized recently. At that time I strove to work at the interface between photonics, nanomechanics and quantum effects. In the nanowire based force detection at sensitivities where the interaction of a single spin with the oscillating nanowire can be resolved, I found the ideal project to work on during my PhD. We then applied for the *Grenoble Quantum Engineering* (*GreQuE*) and the Quantum Engineering Grenoble (*QuEnG*) partial scholarships, which were both granted. Originally, this thesis was to deal with repulsive Casimir forces measured with the nanowire and the first mechanical readout of single spin states in nitrogen vacancy centers (NV) in diamonds. However, at that point we did not know about the numerous discoveries we would make and we were ignorant of the many side paths (some with, some without an end) this project would go (of course, this is how science often works). Now, we can say that the finding of this PhD project were much more manifold than what we originally expected, having advanced the field of nanowire force field measurements by a large step.

Author's contribution The inherited force field measurement setup with the 2D detection of the nanowire Brownian motion had already been in place when this project started. At that time, the measurement was purely based on thermal noise analysis, which was a hindrance for fast nanowire force field microscopy since the acquisition of full trajectories/spectra is time-consuming and requires complex post processing. One of the first advancements implemented by the author was therefore the utilization of a dual lock-in measurement technique with frequency tracking using two phase-locked loops (PLLs). In particular, this meant to expand the scanning software by adding a large amount of new functionalities to it. Beside the direct imaging and computation of force field parameters such as the force divergence in realtime, a set of advanced scanning options (e.g. the simultaneous measurement of the voltage parabola, force and gradient simultaneous readout functionalities, etc.) was developed.

A second practical contribution is the implementation of the *FPGA* based digital signal processing unit which allows flexible access to lock-in measurements using inexpensive hardware. The developed dual-channel, four frequency lock-in is now regularly used to measure the readout vector in the experiment in realtime. In addition to this application, the FPGA module is also used for the active feedback, described in Chapter 4.

Even though the development was in cooperation with the electronics department of the institute, particularly with *Julien Minet*, the author was still required to learn the *C*-programming language as well as the basics of *FPGA* programming in *VHDL*.
The developed measurement protocols and the improvements in soft- and hardware are now used in most of the group's experiments (e.g. in [36]).

To explore the proximity forces above nanostructured surfaces, many samples were fabricated, often with the help of the Nanofab team (in particular with *J.F. Motte*, *G. Julie* and *B. Fernandez*), as well as *S. Le Denmat*. The measurements we realized allowed us to acquire certain knowledge on the sample fabrication techniques and their impact on the final surface quality, and in particular on the role of surface electric fields. For the investigations of Casimir forces at the nanoscale, we adapted specialized simulation tools and set up a dedicated machine in the institute's computation cluster to run Casimir force simulations.
After a brief introduction, this thesis is structured into four chapters.

Chapter 1 In the first part, we lay the principles of nanowire force field microscopy out, starting with fundamentals of force measurements with mechanical oscillators to the reconstruction of a full 2D map of the force field based on the tracking of the eigenmode properties of the nanowire. The second part covers the experimental setup with the two-dimensional optical position readout and a detailed description of the advanced fast force microscopy experiment. The described advanced protocols allow to reach a quasi realtime force sensing.

Chapter 2 In the first experimental chapter, we discuss the measurement of the electrostatic force above nanostructured metallic surfaces. The forces are quadratic in the electric field surrounding the nanowire. We first exploit the component of the force field gradients that vary quadratically with a bias voltage applied to the sample, allowing for imaging the force field topology created by the underlying nanostructures. Those measurements are illustrated on different samples presenting positive or negative nanostructurations, responsible for laterally trapping or anti-trapping force fields. We investigate the force contributions arising from contributions linear to the bias voltage created by the existence of residual electrostatic fields which are independent from the bias voltage, such as electrostatic surface patches. Those residual electric fields add up to the electric field produced by the bias voltage and are responsible for two force contributions: one linear, and one independent in the bias voltage. In order to better understand the measured force field, we give a description of the local physics at the nanowire's tip based on the Maxwell stress tensor formalism. We end the chapter with a comparison of the force field gradients determined by the realtime routines and the gradients of the simultaneously measured force field, using a dedicated measurement protocol.

Chapter 3 Having discussed the quadratic and linear contributions in the bias voltage in chapter two, the third chapter takes a look at the residual forces that remain when the tunable contributions of the voltage are properly cancelled, and particularly at the Casimir force. Using again the Maxwell stress tensor formalism, we analyze how the spatial contribution of fluctuating fields causes a measurable force on the nanowire. We then discuss recent predictions of exotic Casimir forces above nanostructures and present numerical simulations of the Casimir force experiences by the nanowire above different geometries. For the discussion of the experimental results, we first present an approximate method to determine the mean workfunction difference between the nanowire and the surface which provides the voltage around which the linear contributions should be cancelled. This evaluation does not compensate for the quadratic contribution in the residual electrostatic fields but, despite those limitations, the values of the residual force field we obtain present a good qualitative agreement both in magnitude and geometric profile with the numerical simulations we conducted. To obtain a more quantitative evaluation, at the end of the chapter we describe a method to compensate the parasitic fields in 3D making use of extra control electrodes, which should allow a better isolation of the Casimir contribution.

Chapter 4 In the fourth part of this thesis we further use the 2D optical readout and the realtime signal processing unit developed on the FPGA module to create a 2D active feedback scheme allowing to generate synthetic 2D force fields, and to test their impact on the nanowire thermal noise: since one can measure the nanowire position in realtime, one can also apply a force in a chosen direction proportional to the motion readout in another chosen direction. Here, we discuss the linear feedback regime in the parallel and transverse cases with and without incorporating an additional delay, meaning that the synthetic force field can be of reactive or of viscous nature. Using the different feedback schemes, we demonstrate that we can gain a complete control over the nanowire eigenmodes, for instance allowing for generating artificial frequency shifts, or implementing a cold damping scheme. By fully exploiting the 2D character of the readout and actuation tools, we also implemented transverse synthetic force fields, and demonstrated that transverse force fields can be used to generate a noise squeezing of the nanowire motion in the 2D position and velocity spaces, as well as to create circularly polarized precessing eigenmodes. These manipulation tools should allow the realization of future force sensing experiments that could be based on the realtime stabilization of the nanowire's mechanical properties through the application of a counter-acting force field in 2D, so that it could operate in intense and weak force field gradients equally well.

"Je n'ai fait celle-ci plus longue que parce que je n'ai pas eu le loisir de la faire plus courte."

- Blaise Pascal, 4. Dezember 1656, *Les Provinciales* [85]

Table of Contents

Force measurements with mechanical oscillators – an introduction

The basic concept of mechanical systems – translating an applied force into mechanical motion or displacement – has been used to measure forces for a long time. In this chapter we lay out a selection of the historical path the field of force measurements took from the first realizations in modern science in the 18th century before the development of microscale force measurements, notably the development of atomic force microscopy (AFM)*. We finish the chapter with a discussion of the recent advancements of more exotic force field microscopy, in particular force field microscopy with nanowires.*

✦

This thesis discusses the measurements of force fields with nanomechanical oscillators. They are possible due to the fact that a force changes the state of a movable mechanical object, which can be read out by various probes. The probably most employed force measurement technique in the history of humankind uses the deflection of a mechanical lever caused by an added mass. Examining the deflection for different masses then permits to have a quantitative comparison between the mass of different objects – the base of any scale, a tool indispensable in the history of trade. While mass measurements are the most common type of force sensing, the precise determination of forces in general is a requirement for (modern) science. For instance, until 2019, the unit of the electric current *Ampère* has been defined via the value of the force exerted between two wires carrying a static current [3].

In this chapter we will take the opportunity to trace the path from previous scientific techniques for force sensing to nanowire force field nanoscopy, the topic of this work.

Early scientific force measurements

The earliest and most prominent dynamic force measurement is *Cavendish*'s experiment to measure the mass of the earth, conducted in 1798 [17]. The difference between a static measurement and a dynamic measurement is that static methods measure a mechanical property, such as the deflection of a lever or the extension of a spring, in a non-motional state, while dynamic measurement detect changes of an oscillating system, such as a change of the oscillation period or the maximum deflection. *Cavendish*'s mechanical system was a torsion oscillator – a stiff rod with two masses at each end, that is attached at its center on a single string. When the rod rotates in the horizontal plane, the torsion of the string creates a restoring force which causes a periodic oscillation. *Cavendish* positioned two large masses in vicinity to the smaller masses, the gravitational force between each mass pair then initiates the movement of the rod. When the movement of the rod came to a rest, the experimenter placed the large masses on the other side of the small masses, which caused a movement in the opposite direction. Each time, the maximal deflection amplitude and the oscillation period from one maximum to the other is measured.

Figure 1a shows the original experimental setup. The response of the rod to the instantaneously applied action from the gravitational force between the masses, is a damped oscillation from one equilibrium point to another. From his measurements *Cavendish* inferred the earth's density and even though it has not been the primary purpose of his work, one can also calculate the gravitational constant G from his results.

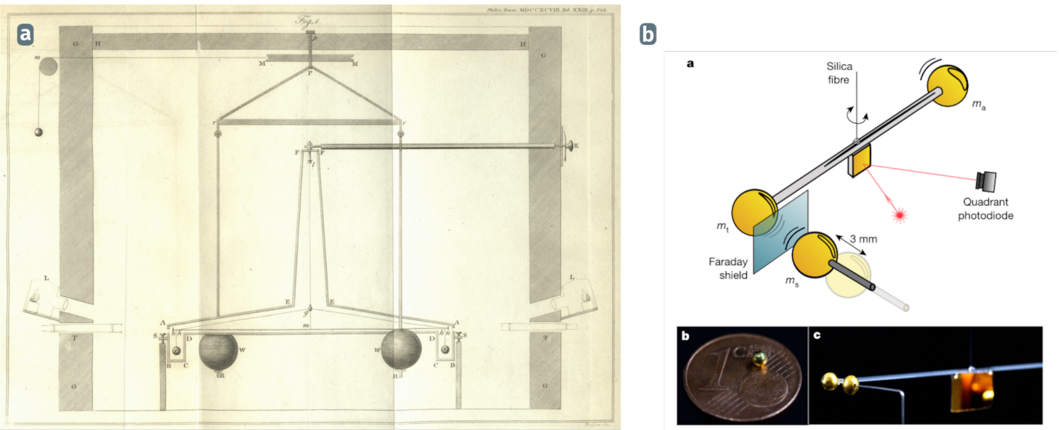

Fig. 1: (**a**) Original drawing of *Cavendish*'s experiment for the determination of the earth's density from [17]. The torsional balance is in the center of the setup, contained in a wooden box to isolate it from the environment. Via two view ports on the side and illumination of two candles, the experimenter could read the displacement of the rod. (**b**) A recent realization of *Cavendish's* setup using a millimetric version of the original setup [115]. While the experiment has shown the gravitational coupling between the two masses, the deducted gravitational constant is subject to a large error.

The original setup needed to be highly sensitive as the force between the two pairs of lead balls with two and six inch diameter, respectively, is only in the range of 170 nN. A scale with this sensitivity would be able to measure the weight difference caused by less then a tenth of a small grain of sand. Additionally, the readout of the rod's position was purely manual and needed to be repeated over several days. Consequently, the experiment was large in order to increase the oscillation period and the displacement amplitude. With modern equipment one can now perform a miniaturized version of the direct measurement of the gravitational interaction between two massed, as done in [115]. Here, the lead spheres are replaced with millimetric gold spheres and only external mass is periodically approached to one end of the rod. The experimental design is illustrated in Figure 1b.

Nanomechanical sensors

The advances of nanotechnology and micro-fabrication in the last decades allows to realize mechanical systems on the nanoscale in a controlled manner. Thus, modern nanomechanical mass sensors operate on an even smaller scale with unprecedented sensitivity due to the small mass of the mechanical systems themselves. A common realization of a nanomechanical resonator has a geometry similar to that of a guitar string that is attached at its two ends and vibrates in the center. Amongst the oscillators with the smallest mass are carbon nanotube (CNT) such as shown in Figure 2a, which in the perfect case consist only of a single layer of carbon atoms that form a cylindric tube. When a part of the CNT is suspended, it can vibrate at an intrinsic frequency. If a particle is adsorbed at the surface of the CNT, its vibrational frequency will change (bottom graph in 2a), and one can infer from this frequency change how many and which kind of molecules have been adsorbed. One future application for this kind of sensors could be virus detection on *Lab on a Chip* devices [53].

Beside CNTs, other popular models are vibrating membranes, which are read out electrically as presented in Figure 2b [62], or disc resonators which are at the same time mechanical resonators and optical cavities through circularly travelling whispering gallery modes as shown in 2c [103].

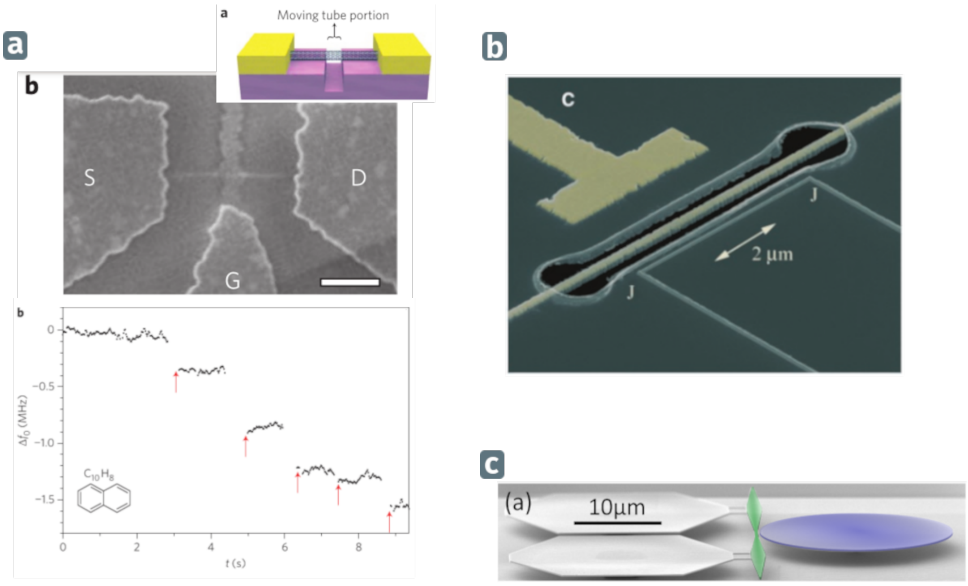

Fig. 2: A carbon nanotube is suspended between two electrodes as shown in the two upper graphics of (**a**). The vibration of the free part of the CNT is read out via the signal measured on the third gate electrode. Chaste et al. used this configuration to detect the adsorption of single naphtalene molecules (bottom graph of (**a**)). A similar setup that uses a suspended silicon nitride (SiN) bridge is shown in (**b**) [62]. The vibration of the metal covered bridge is detected electronically via the capacitive modulation imposed on a single electron transistor, which dynamically changes its conductance. While in this particular study, the resonator has not been used for mass sensing, LaHaye et al. showed unprecedented readout sensitivity close to the quantum limit. Figure (**c**) shows a realization of another popular on-chip geometry, which consists of a circular suspended disk (blue) that hosts a variety of mechanical modes. Additionally, light can propagate circularly in the disk, making it an optical cavity whose parameters are coupled to the mechanical motion of the disk. Via a waveguide (green) it is possible to couple light into the cavity and to detect the transmitted light, which is modulated by the mechanical vibrations of the resonator [103].

Force microscopy

An important application of force sensing is force microscopy which started around thirty to forty years ago and soon achieved atomic resolution. Here, a mechanical oscillator – typically a cantilever or a tuning fork – is scanned over a surface. At its extremity it has an extruded tip that faces the sample and is the point closest to the sample. When this probe is scanned over the sample, the interaction between the tip and the sample surface changes the mechanical properties of the probe. Typically, one reads out the vibration of the probe to detect its resonance frequency, when this changes due to the interaction with the sample surface, the probe-sample distance is adjusted such that the frequency remains constant. This *non-contact* mode of atomic force microscopy (AFM), represents a non-invasive imaging technique with sub-nanometer resolution which is independent of the sample material. The upper graphic of Figure 3a presents a sketch of the zoomed in tip above a sample surface.

Atomic force microscopy

A previous imaging technique, the scanning tunneling microscopy (STM), measured the tunneling current between a static conducting tip and the surface, which depends on the distance between probe and sample. This technique, however, requires a conducting sample surface.
The first realization of an AFM was done in 1986 by Binnig et al. [8]. They combined an AFM cantilever – at this time an aluminum foil with a diamond tip as probe – and a STM, whose purpose was to reliably measure the deflection of the cantilever (compare bottom part of 3a). Via different feedback mechanisms they managed to realize noncontact measurements in which the tip is moved at a static height with respect to the surface. The vibration of modern AFMs are typically read out optically as sketched in Figure 3b. The back of commercial AFM cantilevers, one example of which is shown in 3c, are therefore coated with a metal to enhance their reflectivity.

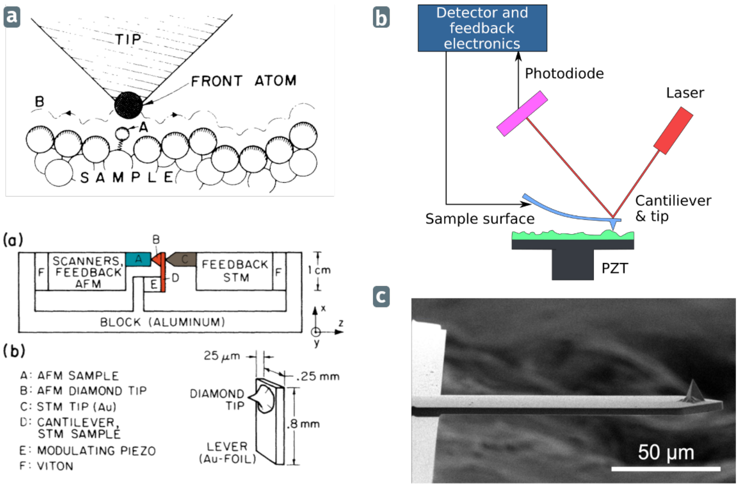

Fig. 3: The basic principle of atomic force microscopy – a small tip scans over a surface and the force between the very tip and the surface atoms deflects the supporting cantilever– is shown in (**a**). In this first realization of AFM, the deflection of the cantilever (central image, orange) due to the sample (blue) has been read out with a scanning tunneling microscopy (brown) [8]. The Al cantilever with a diamond tip is sketched in the bottom right of (**a**). The modern AFM readout method uses the reflection of a laser, which is detected on a quadrant photodiode (**b**) [1]. The image in (**c**) shows a common cantilever from its bottom site, with the tip visible at the right end.

Even a tip that has a single atom at its end, has a tip radius that is comparable to the structure of the surface. AFMs therefore always measure a convolution of the surface structure with the shape of the tip, and it has become a scientific challenge in itself to interpret the effect of the tip's shape.

Scanning probe microscopy (SPM), to which AFM belongs as well, has been an important tool in the last decades, particularly in the fields of nanotechnology where it is used to characterize surfaces or as tool in nanofabrication [57, 69], and biology, where it is used to observe dynamic biologic processes [31, 48]. Additionally, the probe's tip can be functionalized with a biomarker that binds to specific parts of a molecule, allowing advanced biologic imaging and manipulation.

This work benefits from this scientific know-how, gained in the last thirty years, and covers an application of nanowires for force microscopy. While miniaturization of the existing techniques is often difficult, nanowires present one way to reduce the probe's size. Since sensitivity scales with mass and flexibility of the oscillating probe this presents a possibility to achieve even higher force sensitivities in the $\mathrm{aN}/\sqrt{\mathrm{Hz}}$ regime at room temperature. Furthermore, nanowire based force probes provide another access to the detection of force fields due to their mechanical characteristics.

Previous experiments with nanowire force probes

Nanowire force sensors provide an intrinsically high force sensitivity ($\mathrm{aN}/\sqrt{\mathrm{Hz}}$) thanks to their low mass. They can be fabricated in high quality which leads to excellent mechanical properties and their large interaction with a focussed light beam make them ideal for opto-mechanical applications. By tailoring their aspect ratio, one can engineer nanowires for a wide range of applications. A particularity of nanowires compared to AFM cantilevers is that they vibrate in the two dimensional transverse horizontal plane and henceforth are susceptible to the 2D in-planar force field. By measuring their vibrations in two dimensions, it is possible to reconstruct the force field they are submitted to. How this is done will be discussed in the following chapter.

Force field measurements with nanowires

Two force field microscopy experiments which employ nanowires in a similar manner as typical scanning probe experiments have been conducted in 2017 [29, 100] using different measurement techniques. Rossi et al. used an one dimensional interferometric readout of the nanowire vibrations while de Lépinay et al. employed an optical 2D detection. Both experiments achieved the measurement of force fields with gradients as small as a few $\mathrm{fN\,nm^{-1}}$ (see Figure 4).

With AFMs measuring forces in the vertical direction (the direction of the cantilever vibration) and nanowires force fields in the horizontal plane, there is a third mechanical system that can be used to measure force fields along three axes, consisting of a single trapped particle. The position of the levitating particle can be controlled by the trap parameters. A measurement of the particle's Brownian motion in a force field then permits to infer the force field – the same technique as nanowire force field microscopy, with an additional dimension. In particular the group around *Giorgio Gratta* performed experiments using levitating particle force sensors with sensitivities around $10\,\mathrm{aN}/\sqrt{\mathrm{Hz}}$ [9].

Besides scanning probe measurements, our group also successfully employed SiC nanowire force probes to map the optical force experienced by the nanowire in a focussed laser beam [43] (Figure 5a) by spectral analysis of the nanowire's random trajectories. In a more recent work [35], we mapped the optical force in a fibred microcavity (Figure 5b) using the new force sensing protocols that have been developed in the scope of this work

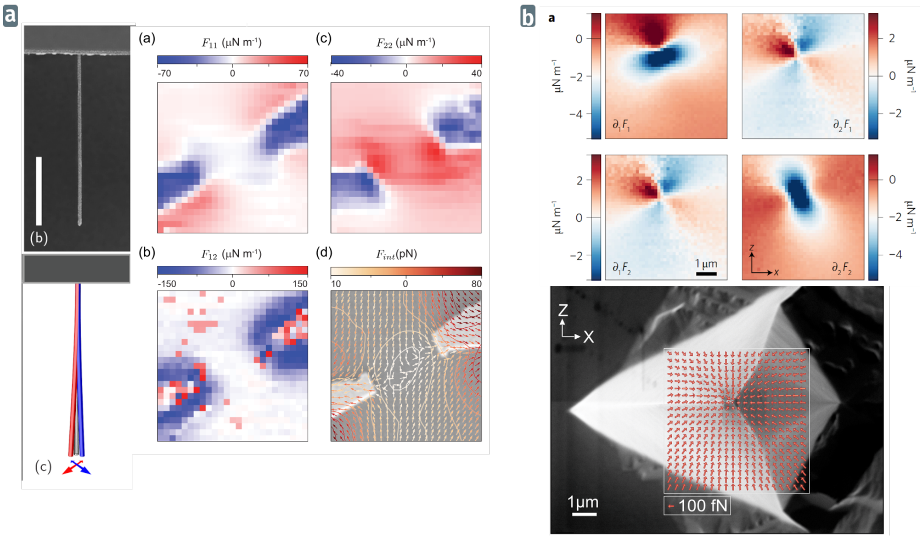

Fig. 4: Two force field microscopy experiments that employed nanowires published in 2017. The experiment by Rossi et al. in (**a**) maps the electrical force field between two concentric structured electrodes [12, 100]. The experiment conducted in the group of the author by his predecessor *Laure Mercier de Lépinay* maps the force field above a single electrode (**b**) (electrostatic force field gradient (*top*) and field (*bottom*)) using a spectral analysis of the nanowire's Brownian motion [28, 29].

Recent experiments

(see Chapter 1). With prospective force sensitivities of $40\,\mathrm{aN}/\sqrt{\mathrm{Hz}}$ at mK Temperature [37], the nanowire force sensing platform is also well suited for nano-optomechanical experiments [36] or coupled spin-mechanical systems (Figure 5c)[87].

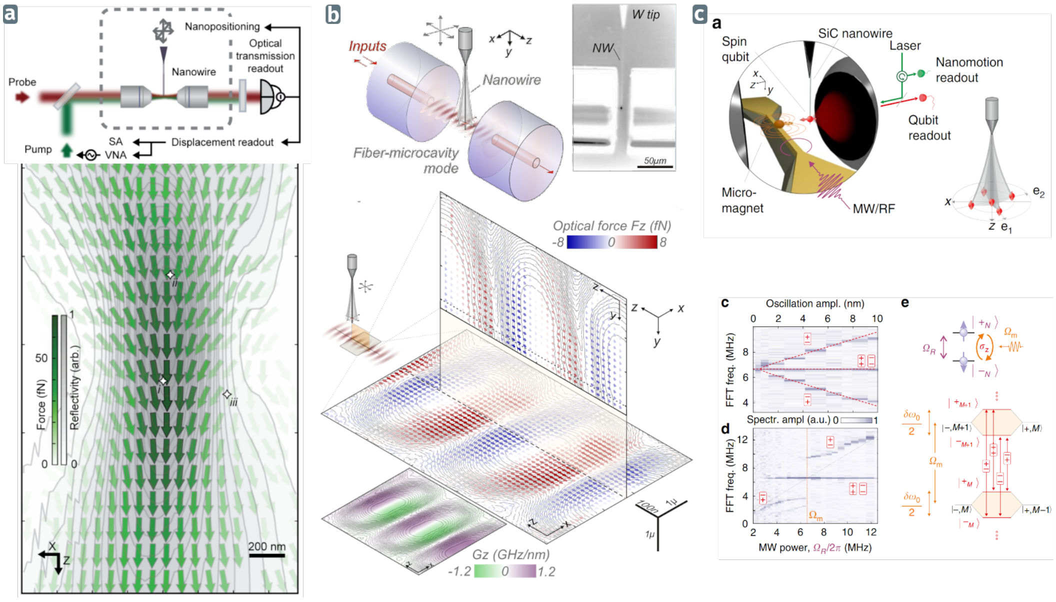

Fig. 5: Force field measurement experiments performed with SiC nanowires: (**a**) Mapping of the force field of a focussed laser beam from [43], (**b**) Intra-cavity optical force field [36], (**c**) Realization of a phononic Mollow-Triplet using the coupling between mechanical oscillator and a nitrogen vacancy (NV) center in diamond [87].

How exactly one can exploit the mechanical properties of a nanowire to measure force fields is subject of the next chapter. It lays out the physical foundations behind nanowire based force microscopy and detailedly explains the 2d detection setup that permits to read out the nanowires motion. Furthermore, we present an improved detection protocol based on a fast resonant readout, which surpasses the precedent tools used in our group and opens the way to realtime imaging of 2D force fields using nanowires.

1 Fast scanning nanowire probe experiment

Nanowire force sensors can achieve a high sensitivity in force, due to their intrinsic small mass and good mechanical properties such as good quality factors, large linearity or efficient optical readout, and first realizations of force microscopy experiments with nanowires [29, 100] have proven the suitability of this technique for the mapping of force fields. Compared to standard AFM, the nanowire oscillates equivalently along its 2 transverse directions and thus nanowire based force microscopy is a 2D force sensing technique that requires a similar but distinct signal processing than in standard AFM: two projective measurements need to be processed in order to access the measured 2D force field. Additionally, experimental prototypes have to overcome some practical challenges such as the readout of the freely suspended nanowire, which has a sub-wavelength sized diameter.

In the first part of this chapter, we present the theoretical foundations for 2D nanowire force field microscopy and discuss the necessary mathematical concepts that are used in the proceedings of this work. This part finishes with the formulation of the relation between the measured perturbations of the mechanical properties of the nanowire in a force field and the spatial structure of the surrounding force field. We then continue with a detailed description of the experimental setup, covering the 2D optical position readout developed [29] and focussing on the new, response based detection techniques developed in the scope of this work. These improvements set the cornerstone of the experiments conducted in this work and beyond its scope [36].

◆

◆

1.1 Nanowires as force sensing probes

This section lays out the fundamentals of the motion of a singly clamped nanowire, first regarding a 1D model and later the full 2D movement of the realistic nanowire. The reconstruction of the force field in 2D, based on this description, is the core of nanowire force field microscopy and is discussed subsequently in this section.

1.1.1 The deformation of a suspended nanowire

The vibrations of a nanowire clamped at one side without mechanical constraints at the other side can be described by the mechanics of a stiff beam. The exact deformation of a thin beam with fixed position at one end is given by the Euler-Bernouilli equation that connects the amplitude of deflection $r(y)$ with the position y along the axis of the beam

Euler-Bernouilli equation for a thin beam

$$\rho A \frac{\partial^2 \delta r}{\partial t^2}(y,t) + EI \frac{\partial^4 \delta r}{\partial y^4}(y,t) = 0, \tag{1.1}$$

where we introduce the volume density ρ, the cross section area A, the materials Young's modulus E, and I the second moment of inertia. The stationary state of Equation 1.1 can be solved exactly [28, 104] resulting in a series of spatial mode profiles. For the n^{th} mode the solution writes

$$\delta r_n(y) = A_n \cos(k_n y) + B_n \cosh(k_n y) + C_n \sin(k_n y) + D_n \sinh(k_n y), \tag{1.2}$$

where

$$k_n = \left(\frac{\Omega_n^2 \rho A}{EI}\right)^{1/4}. \tag{1.3}$$

In order to obtain the concrete solution for a special case we need to take into account the boundary conditions. For the fixed end ($y = 0$) these are

$$\delta r_n(0) = 0 \text{ and } \frac{\partial \delta r_n}{\partial y}(0) = 0, \tag{1.4}$$

meaning that the nanowire's displacement is zero and the nanowire itself is straight at its anchor point. For the free end, we have the condition of zero torque whose derivative is zero as well [22]:

$$\frac{\partial^2 \delta r_n}{\partial y^2}(L) = 0 \text{ and } \frac{\partial^3 \delta r_n}{\partial y^3}(L) = 0. \tag{1.5}$$

Applying these boundary conditions to (1.2) one obtains the relation for the coefficients: $A_n = -B_n,\ C_n = -D_n$. And thus we obtain the simplified expression:

$$\cos(k_n L) \cosh(k_n L) = -1. \tag{1.6}$$

This equation yields the possible values for the coefficient k_n that also defines the mechanical frequency of the modes. The relation between the frequency of the first four modes of a circular nanowire are given in Table 1.1. The spatial profile of the first flexural modes for a singly clamped nanowire are illustrated in Figure 1.1.

Vibrational eigenmodes of a nanowire oscillator

Tab. 1.1: Frequencies of the first four eigenmodes of a singly, symetrically clamped nanowire in multiples of the first eigenmode frequency.

n	1	2	3	4
Ω_n/Ω_1	1	6.267	17.548	34.393

An oscillating cylindrical nanowire beam has two motional degrees of freedom so that each eigenmode family n has two degenerated modes. Asymmetric boundary conditions or imperfections in the real nanowire usually lift this degeneracy, such that both spatial modes are frequency separated. The measured deflection amplitude at position y on the nanowire then is a vectorial quantity given by the sum of the individual mode profiles:

$$\delta \mathbf{r}_y(t, y) = \sum_n a_n(t) \mathbf{u}_n(y) \tag{1.7}$$

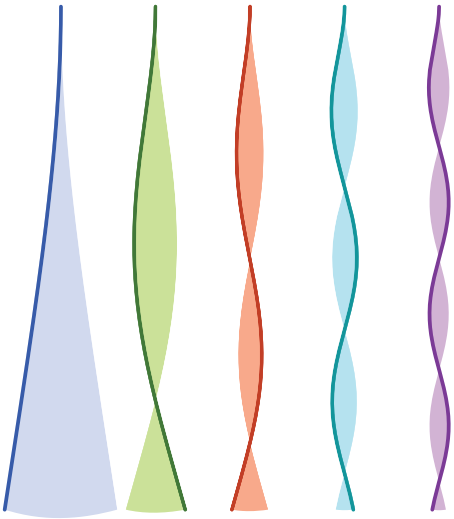

Fig. 1.1: First five flexural modes of a nanowire with mechanical constraints at one end.

where $a_n(t)$ is the oscillation time profile per mode and $\mathbf{u}_n(y)$ the position dependent modal basis vector. The equation of motion for each individual mode describes the time profile for its oscillation:

Equation of motion for the n^{th} mode

$$\ddot{a}_n(t) = -\Omega^2_{\mathrm{m},n} a_n(t) - \Gamma_{\mathrm{m},n}\dot{a}_n(t) + \frac{1}{M_n}\big(F_{th,n}(t)\langle \mathbf{f}_{\mathrm{ext}}(r,t), \mathbf{u}_n(r)\rangle\big), \tag{1.8}$$

where the index m of $\Omega_{\mathrm{m},n}$ denotes the mechanical frequency for mode n with the mechanical damping coefficient $\Gamma_{\mathrm{m},n}$ and the dynamical mass per mode $M_n = \rho \int \mathrm{d}^3\mathbf{r}\ \mathbf{u}_n^2(y)$. We also introduced a statistical Langevin force F_{th} driving a thermal Brownian movement of the nanowire. The fluctuation-dissipation theorem determines the spectral density of the thermal force per mode [89]:

Spectral density of the Brownian motion of mode n

$$S_{F_{\mathrm{th},n}}[\Omega] = \hbar\left|\mathfrak{I}\left(\frac{1}{\chi_n[\Omega]}\right)\right|\coth\left(\frac{\hbar\Omega}{2k_BT}\right), \tag{1.9}$$

with the mechanical susceptibility χ. Additionally to this statistical force, the term $\langle \mathbf{f}_{\mathrm{ext}}(r,t), \mathbf{u}_n(r)\rangle$ in (1.8) introduces an external force via its volume density $\mathbf{f}_{\mathrm{ext}}$. The force acting on the nanowire is given by the overlap integral between force density and each mode profile, defined via the scalar product:

$$\langle \mathbf{a}, \mathbf{b}\rangle \equiv \int_0^L \frac{\mathrm{d}r}{L}\mathbf{a}(r)\mathbf{b}(r). \tag{1.10}$$

The force acting on the nanowire is thus that of a reduced force field at the free end of the nanowire as illustrated in Figure 1.2. By probing the force at different positions and heights, one can thus realize a cartography of the reduced force.

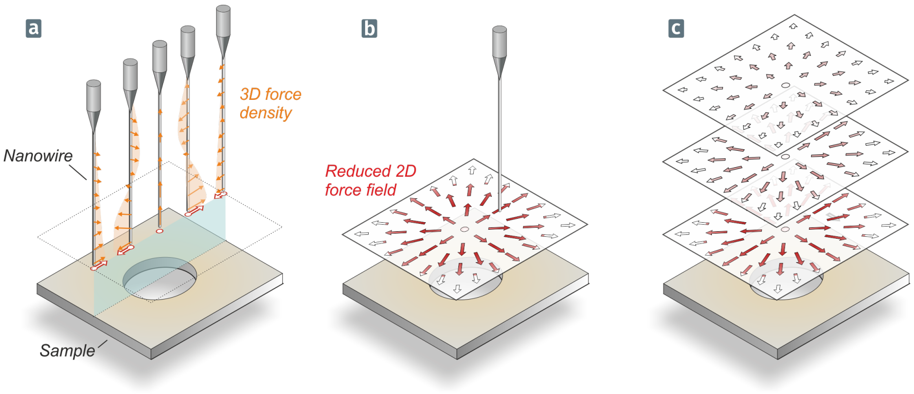

Fig. 1.2: (**a**) The force is acting on the nanowire over its full length with different volumic profiles depending on its position. The integrated force can be regarded as a reduced force at the end of the nanowire and a force map can be obtained by plotting the force field in a plane (**b**) and at different heights (**c**).

Because of the typically long nanowires ($\approx 100\,\mu\mathrm{m}$), many forces can be regarded as local. An example is the optical force of a narrowly focused laser beam that is used in this work to exert a modulated force on the oscillator. With a waist diameter of about one micrometer, the region where $f_{\mathrm{ext}} \neq 0$ is small compared to the characteristic length of the mode profiles (distance between node and antinode) so we can approximate that $\mathbf{f}_{\mathrm{ext}}(r) = \delta(r - r_0)\,\mathbf{F}_{\mathrm{ext}}$. The overlap between force and mode profile then simplifies to

$$\langle \mathbf{f}_{\mathrm{ext}}(r,t), \mathbf{u}_n(r) \rangle = \mathbf{F}_{\mathrm{ext}} \mathbf{u}_n(r_0). \tag{1.11}$$

This leads to an external force that acts more efficiently on the oscillator if it is applied at positions r_0 where the mode's oscillation amplitude is maximal. We can use this observation to define an effective mass $M_{\mathrm{eff},n}$:

Effective mass definition

$$M_{\mathrm{eff},n} = \frac{M_n}{\mathbf{u}_n^2(r_0)} = \frac{\rho \int \mathrm{d}^3\mathbf{r}\ \mathbf{u}_n^2(y)}{\mathbf{u}_n^2(r_0)}. \tag{1.12}$$

Experimentally, the optical force is applied a few micrometers away from the end ($y = L$) of the nanowire at the same position as the readout so that $r_0 \approx L$. In this case, the ratios of effective mass to dynamical mass for the first four modes are provided by Table 1.2.

Tab. 1.2: The ratio between effective and dynamical mass of the first four vibrational mode families for a force acting close to the end of the nanowire.

n	1	2	3	4
$M_{\mathrm{eff},n}/M_n$	0.2500	0.2500	0.2433	0.9646

The fact that the effective mass of the first two mode families is identic close to the nanowire's end makes it easy to compare the results measured with either mode family. For one specific mode we can then write the equation of motion

Equation of motion for a driven mode

$$\delta\ddot{\mathbf{r}}(t) = -\Omega_{\mathrm{m}}^2\delta\mathbf{r}(t) - \Gamma\delta\dot{\mathbf{r}}(t) + \frac{\delta F_{\mathrm{th}}(t) + \mathbf{F}_{\mathrm{ext}}(t)}{M_{\mathrm{eff}}}, \tag{1.13}$$

with an effective Langevin force $\delta F_{th} = F_{th}/u_n(r_0)$. The first term of (1.13) describes the intrinsic restoring force of the mechanical system with Ω_{m} as the frequency of the oscillation. The second term where Γ is the damping rate modelling the dissipation of the mode, dominated by acoustic emission at large pressure, and by internal dissipation at low pressures. The third term presents a time dependent external drive $\delta F(t)$ acting on the resonator's extremity [107].

In the following paragraphs, we discuss the coupling of the nanowire to an external bath, inherent to the existence of a dissipation channel and will then look at the effects of external force fields on the nanowire in Equation 1.13.

1.1.1.1 Mechanical susceptibility of a harmonic oscillator

The interactions of the mechanical oscillator with its environment are modelled by a linear viscous damping term and a stochastic random force $\delta F_{th}(t)$. In the case of an acoustic damping, the dissipation results from the collision of the nanowire with molecules in the surrounding medium. The random movement of the surrounding thermal bath's molecules and their collisions with the oscillator create a stochastic random force $\delta F_{th}(t)$, called *Langevin* force, which drives the nanowire motion and is responsible for its Brownian motion. The transposition of the equation of motion (1.13) in Fourier space gives:

$$\delta r[\Omega] = \frac{1}{M_{\mathrm{eff}}}\frac{1}{(\Omega_{\mathrm{m}}^2 - \Omega^2 - i\Gamma\Omega)}\delta F_{\mathrm{th}}[\Omega] \equiv \chi[\Omega]\delta F_{\mathrm{th}}[\Omega]], \tag{1.14}$$

where Ω_{m} is the eigenfrequency of the mechanical mode and i is the imaginary unit $i = \sqrt{-1}$. Here, we also introduce the frequency dependent mechanical susceptibility χ that relates force and mechanical displacement.

The Langevin force $\delta F_{\mathrm{th}}[\Omega]$ is by nature a white Gaussian noise with a constant power spectrum. The spectrum of a stochastic process is related to the autocorrelation function via the Wiener-Khintchin theorem [116]:

$$S_{\delta F_{\mathrm{th}}}[\Omega] = \mathcal{F}\langle F_{\mathrm{th}}(t)F_{\mathrm{th}}(t+\tau)\rangle. \tag{1.15}$$

Fourier transform

Where $\mathcal{F}$ represents the Fourier transform with the convention $\mathcal{F}f(t) = \int_{\mathbb{R}} f(t)e^{-i\Omega t}dt$. The brackets $\langle\ldots\rangle$ signify the averaging on all configurations taken by the reservoir, which in the ergodic case is equivalent to a time average. In the case of white gaussian noise, the auto-correlation function is equal to a delta function with a constant prefactor $2M_{\text{eff}}\Gamma k_B T$ determined by applying the fluctuation-dissipation theorem introduced in (1.9) with the susceptibility χ of equation Equation 1.14 [13, 60, 89]:

$$\langle \delta F_{\text{th}}(t)\delta F_{\text{th}}(t+\tau)\rangle = 2M_{\text{eff}}\Gamma k_B T\delta(\tau). \tag{1.16}$$

Fluctuation-dissipation theorem

Applying the Wiener-Khintchin theorem to Equation 1.14 yields the spectral density of the mechanical displacement $S_{\delta r}$

$$\begin{aligned} S_{\delta r}[\Omega] &= \mathscr{F}\langle \delta r(t)\delta r(t+\tau)\rangle \\ &= (2\pi)^{-1}\langle \delta r(\Omega)\delta r(\Omega')\rangle\delta(\Omega+\Omega') \\ &= |\chi[\Omega]|^2 S_{\delta F_{\text{th}}}. \end{aligned} \tag{1.17}$$

To express $S_{\delta r}$ in terms of $S_{\delta F_{\text{th}}}$ we used the fact that the displacement $\delta r(t)$ are purely random and not correlated in time.

With $S_{\delta F_{\text{th}}} = 2M_{\text{eff}}\Gamma k_B T = \textit{const}$, the shape of the noise spectral density $S_{\delta r}$ is determined by the susceptibility χ. Figure 1.3 illustrates the amplitude and the argument of the susceptibility χ which follows the form of a complex Lorentzian with a phase change from 0 to π at its central frequency Ω. A metric that describes the narrowness of such a resonance is the quality factor Q that is the ratio between resonance frequency Ω_m and linewidth Γ

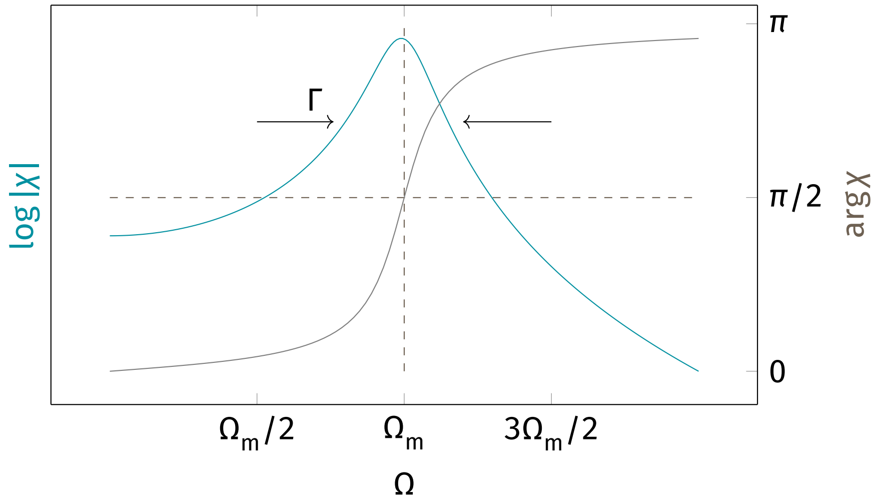

Fig. 1.3: Amplitude and argument of the complex susceptibility χ.

$$Q = \frac{\Omega_m}{\Gamma}. \tag{1.18}$$

Q factor

1.1.1.2 Coherent excitation and the dynamic sensitivity limit

Additionally to the thermal Langevin force that causes the Brownian motion of the oscillator, an additional exciting force $\delta F_{\mathrm{pump}}(\Omega)$ can be used to drive the oscillator. The displacement spectrum of mechanical motion is then

$$\delta r[\Omega] = \chi[\Omega]\big(\delta F_{\mathrm{th}} + \delta F_{\mathrm{pump}}[\Omega]\big). \tag{1.19}$$

Here, we used that there is not temporal correlation in the Langevin force and that the driving force can be written as a sum of monochromatic terms. The observed displacement $\delta r[\Omega]$ is the response to the thermal Langevin force and the monochromatic excitation. The linear response in (1.19) implies that the displacement amplitude directly scales with the amplitude of the driving force. It is therefore possible to increase the measured signal δr without affecting the physics of the oscillator. This presents a practical advantage to purely noise based measurements since a higher amplitude is easier detectable. Additionally, homodyne measurements at the frequency of excitation can be used to measure the resonant response of the oscillator and thus its susceptibility. Response measurements at multiple frequencies, either in parallel or as consecutive measurements in a sweep, present a powerful tool to probe the oscillators susceptibility and its dressing due to an external force field.

To get the power spectral density which is the typically measured signal on a spectrum analyzer, we need to integrate $S_{\delta r}$ over the resolution bandwidth (RBW) around the measurement frequency Ω'

$$PSD_{\delta r}(\Omega') = \int\limits_{\Omega'-RBW}^{\Omega'+RBW} d\Omega |\chi(\Omega)|^2 \left|\delta F_{\mathrm{th}} + \delta F_{\mathrm{pump}}(\Omega)\right|^2. \tag{1.20}$$

For a monochromatic drive $\delta F_{\mathrm{pump}}[\Omega] = \delta F \delta\big(\Omega_{\mathrm{pump}} - \Omega\big)$ and when the resolution bandwidth is sufficiently small compared the oscillator damping rate, the measured power at the driving frequency is

Displacemnt Power spectral density

$$PSD_{\delta r}\big(\Omega_{\mathrm{pump}}\big) = \left|\chi\big(\Omega_{\mathrm{pump}}\big)\right|^2 \big(S_{\delta F_{\mathrm{th}}}\, RBW + \delta\, F^2_{\mathrm{pump}}\big). \tag{1.21}$$

In order to detect a driving force δF_{pump} in the measured power spectrum, we require a signal to background ratio (SNB) larger than one. This implies that the second summand in Equation 1.21 is equal or larger than the integrated noise contribution. We thus obtain as frequency independent sensitivity limit

Force sensitivity limit

$$\delta F_{\mathrm{min}} = \sqrt{2 M_{\mathrm{eff}} \Gamma k_B T \cdot RBW}, \tag{1.22}$$

which represents a fundamental limit for dynamic lock-in based detection. The force field microscopy measurements in this work are usually performed with a higher modulation force δF in order to enhance the SNB and operate with higher detection speed (larger RBW of the frequency tracking PLL). The dynamic limit can be improved by cooling of the mechanical system passively, meaning by reducing the temperature of the oscillator and its environment cryogenically.

1.1.1.3 Static force gradient sensing

A static but anisotropic one dimensional force field $F_{\mathrm{ext}}(x)$ can be linearized around the equilibrium position of the resonator x_0 as

$$F_{\mathrm{ext}}(r_0 + \delta r) = F_{\mathrm{ext}}(r_0) + \left.\frac{\partial F_{\mathrm{ext}}}{\partial r}\right|_{r_0} \delta r \tag{1.23}$$

The static force $F_{\mathrm{ext}}(r_0)$ modifies the working point of the system, thereby potentially bringing the oscillator to a new operating point, where the force gradient is now evaluated (compare box 1.a). Except this modification, the static force does not contribute to the fast dynamics of the oscillator. The motion of the oscillator $\delta r(t)$ in the force field, being due to its Brownian motion or to an external drive, will create an effective force modulation δF_{ext} that is proportional to the force field gradient as illustrated in Figure 1.4.

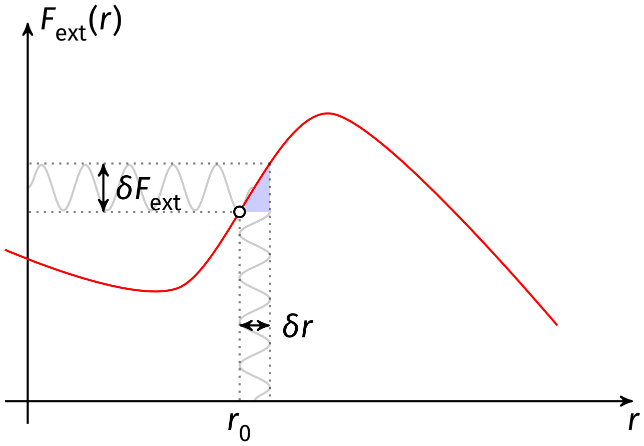

Fig. 1.4: Schematic representation of the force field linearization around the rest point of the oscillator r_0. The static force $F_{\mathrm{ext}}(r_0)$ has no effect on the oscillator's dynamics whereas the modulated δF_{ext} leads to a dressing of the resonators eigenmodes.

With this additional force that, similarly to the restoring force, depends on the oscillator position we can write the equation of motion (1.13) as

$$\delta\ddot{r}(t) = -\Omega_{\mathrm{m}}^2 \delta r(t) - \Gamma \delta\dot{r}(t) + \frac{\delta F_{\mathrm{th}}(t)}{M_{\mathrm{eff}}} + g\delta r, \tag{1.24}$$

Force field gradient g

where we introduced $g = \left.\frac{\partial_r F_{\mathrm{ext}}(r)}{M_{\mathrm{eff}}}\right|_{r_0}$ as measure for the force gradient in units of s^{-2}. The susceptibility of the resonator thus gets an additional term g:

$$\chi^{-1} = \left(\Omega_{\mathrm{m}}^2 - \Omega^2 - i\Gamma\Omega + g\right) \tag{1.25}$$

$$= \left(\Omega_{\parallel}{}^2 - \Omega^2 - i\Gamma\Omega\right). \tag{1.26}$$

Note that in Equation 1.26 we combined the cold frequency of the mechanical mode Ω_{m} and the dressing term from the force gradient's contribution g to the frequency $\Omega_{\parallel} = \sqrt{\Omega_{\mathrm{m}}^2 + g}$ that is the resonant frequency of the new dressed mode. To approximate the sensitivity of the oscillator to the external force gradient, we can estimate the force gradient at which the relative frequency shift becomes larger than the mechanical linewidth:

$$\Gamma \leq \left|\Omega_{\parallel} - \Omega_{\mathrm{m}}\right| = \left|\sqrt{\Omega_{\mathrm{m}}^2 + g} - \Omega_{\mathrm{m}}\right|. \tag{1.27}$$

This inequality becomes at first order:

$$\begin{aligned} \Gamma &\leq \frac{1}{2}\Omega_{\mathrm{m}}^{-1} g \\ \Rightarrow g &\geq 2\Gamma\Omega_{\mathrm{m}}, \end{aligned} \tag{1.28}$$

or

Force gradient sensitivity limit

$$\partial_x F_{x,\mathrm{ext}} > 2\frac{M_{\mathrm{eff}}\Omega_{\mathrm{m}}^2}{Q} = 2\frac{k_{\mathrm{m}}}{Q}, \tag{1.29}$$

where we have introduced the stiffness of the oscillator $\mathrm{k_m}$. The experimental realization allows us to detect frequency shifts far smaller than the mechanical linewidth, so that such a measurement is ultimately limited by the oscillator's frequency noise.

Panel 1.a: Static Force Offset

In a static force field, the nanowire is displaced by the perpendicular force. The displacement can be calculated with

$$\Delta r = \frac{F_{\mathrm{const}}}{k_{\mathrm{m}}} = \frac{F_{\mathrm{const}}}{M_{\mathrm{eff}}\Omega_{\mathrm{m}}^2}. \tag{1.30}$$

While this displacement does not change the oscillator's dynamics, we obtain a new working point $r_1 = r_0 + \Delta r$ (Figure 1.5 **a**). In the case that the force is unrelated to the force field created by the sample, as for the case of a constant optical force that is constant over a large area compared to the test force field, one can neglect this static shift. If, however, the static shift is created by strong local forces in the test force field, then the intended working point does not correspond to the real working point during a measurement.

Figure 1.5 **b** plots the expected displacement for a realistic parameter range. With possible displacements over 100 nm, we need to consider the static shift for very sensitive nanowires and for geometries where large local forces can be expected.

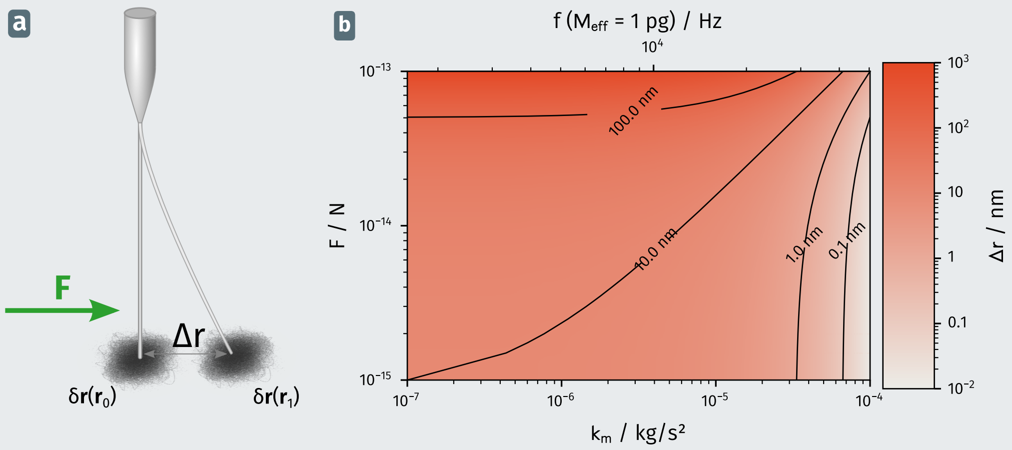

Fig. 1.5: A constant force F displaces the nanowire by δr, changing the working point from $\mathbf{r}_0$ to $\mathbf{r}_1$ (**a**). The displacement $\delta r = F/k_m$ depends on the force and stiffness k_m of the nanowire. (**b**) presents the expected static displacement for a realistic range of forces and stiffness coefficients.

1.1.1.4 2D nanowire system

The ideal nanowire is an axially symmetric beam with a fixed mechanical boundary at one end. The two dimensional displacement $\delta\mathbf{r}(y)$ at a position y along its length takes place in the transverse perpendicular (x, z) plane. The resulting two degrees of freedom allow two perpendicular eigenmodes of the resonator that are degenerated in the ideal case, meaning that they are indistinguishable in frequency: $\Omega_1 = \Omega_2$. For a real nanowire this degeneracy is typically lifted by 1%, under the influence of structural defects in the nanowire's crystallinity or the mechanical clamping that induces an asymmetry. The susceptibility matrix of such a 2D oscillator in the base of its two independent eigenmodes can be written as

$$\chi^{-1} = \frac{1}{M_{\text{eff}}} \begin{pmatrix} \Omega_1^2 - \Omega^2 - i\Gamma_1\Omega & 0 \\ 0 & \Omega_2^2 - \Omega^2 - i\Gamma_2\Omega \end{pmatrix}, \tag{1.31}$$

Nanowire susceptibility matrix

where the indices 1, 2 denote the first and second mode of the oscillator in order of increasing eigenfrequency $\Omega_{1,2}$, with the convention of an orthonormal eigenvector basis (e_1, e_2). The left graphics in Figure 1.6 depicts the perpendicular polarizations of a suspended nanowire. The indicated eigenvectors $\mathbf{e}_1, \mathbf{e}_2$ of the susceptibility correspond to the eigenfrequencies Ω_1, Ω_2.

The dynamics of the two dimensional system is analogue to the one dimensional oscillator and we can calculate the displacement of the nanowire with:

$$\delta\mathbf{r}[\Omega] = \chi[\Omega]\,\delta\mathbf{F}_{th}. \tag{1.32}$$

Due to the lack of transverse, diagonal terms in the susceptibility matrix in Equation 1.31, the dynamics of each eigenmode are completely independent from one another. The presence of an external force field can create such transverse coupling terms in the susceptibility matrix.

In the following, we discuss how external force fields change the eigenmodes of the nanowire and how χ can be expressed in the basis of the new eigenmodes. We further discuss how the force field gradients can be deduced from measurements of the dressed eigenproperties of the nanowire.

1.1.2 A nanowire in a force field

As in Section 1.1.1.3, a static inhomogeneous force field can again be linearized around the nanowire's rest position

$$\mathbf{F}_{\mathrm{ext}}(\mathbf{r}_0 + \delta\mathbf{r}) = \mathbf{F}_{\mathrm{ext}}(\mathbf{r}_0) + \nabla\mathbf{F}_{\mathrm{ext}}|_{\mathbf{r}_0}\delta\mathbf{r}, \tag{1.33}$$

where $\nabla\mathbf{F}_{\mathrm{ext}}$ is the gradient matrix of the force field that can be written as

Force field gradient matrix

$$\nabla\mathbf{F} = \begin{pmatrix} \frac{\partial F_{x_1}}{\partial x_1} & \frac{\partial F_{x_1}}{\partial x_2} \\ \frac{\partial F_{x_2}}{\partial x_1} & \frac{\partial F_{x_2}}{\partial x_2} \end{pmatrix} = M_{\mathrm{eff}}\begin{pmatrix} g_{11} & g_{21} \\ g_{12} & g_{22} \end{pmatrix}. \tag{1.34}$$

Here, we rewrote the partial derivatives as components $g_{ij} = 1/M_{\mathrm{eff}}\partial_i F_j$ of the gradient matrix. In the influence of an external force field, the equation of motion in two dimensions then reads in the basis of the cold eigenmodes $(\mathbf{e}_1, \mathbf{e}_2)$:

2D equation of motion for a nanowire in a force field

$$\delta\ddot{\mathbf{r}}(t) = -\begin{pmatrix} \Omega_1^2 & 0 \\ 0 & \Omega_2^2 \end{pmatrix}\delta\mathbf{r} - \begin{pmatrix} \Gamma_1 & 0 \\ 0 & \Gamma_2 \end{pmatrix}\delta\dot{\mathbf{r}} + \frac{\delta F_{\mathrm{th}}}{M_{\mathrm{eff}}} + \begin{pmatrix} g_{11} & g_{21} \\ g_{12} & g_{22} \end{pmatrix}\delta\mathbf{r}. \tag{1.35}$$

1.1.2.1 Dressed eigenmodes

In analogy to the one dimensional oscillator (Section 1.1.1.1), we obtain the susceptibility matrix by using a Fourier transform of the equation of motion (1.35) and obtain, again in the basis of the cold eigenmodes:

$$\begin{aligned}\delta F_{\mathrm{th}} &= \chi^{-1}[\Omega]\delta\mathbf{r}[\Omega]\\ &= \frac{1}{M_{\mathrm{eff}}}\begin{pmatrix}\Omega_1^2-\Omega^2-i\Gamma_1\Omega-g_{11} & -g_{21}\\ -g_{12} & \Omega_2^2-\Omega^2-i\Gamma_2\Omega-g_{22}\end{pmatrix}\delta\mathbf{r}[\Omega].\end{aligned} \tag{1.36}$$

Performing the matrix inversion to calculate $\chi[\Omega]$, we get

Dressed susceptibility matrix

$$\begin{aligned}\chi[\Omega] &= \frac{1}{\det\chi^{-1}[\Omega]}\begin{pmatrix}\Omega_2^2-\Omega^2-i\Gamma_2\Omega-g_{22} & g_{21}\\ g_{12} & \Omega_1^2-\Omega^2-i\Gamma_1\Omega-g_{11}\end{pmatrix}\\ &= \begin{pmatrix}\chi_{11}[\Omega] & \chi_{12}[\Omega]\\ \chi_{21}[\Omega] & \chi_{22}[\Omega]\end{pmatrix},\end{aligned} \tag{1.37}$$

where the determinant of inverse susceptibility is

$$\frac{\det\chi^{-1}[\Omega]}{M_{\mathrm{eff}}} = \left(\Omega_1^2-\Omega^2-i\Gamma_1\Omega-g_{11}\right)\left(\Omega_2^2-\Omega^2-i\Gamma_2\Omega-g_{22}\right)-g_{12}g_{21} \tag{1.38}$$

The diagonal elements of the force gradient matrix g_{11}, g_{22} cause the eigenfrequencies of the two resonances to shift spectrally, and we can define the variable for this pseudo eigenfrequency

$$\Omega_{\parallel 1}^{\ 2} = \Omega_1^2 - g_{11};\ \Omega_{\parallel 2}^{\ 2} = \Omega_2^2 - g_{22} \tag{1.39}$$

The off diagonal terms in Equation 1.36 couple both eigenvectors, and thus cause a mode rotation. The new eigenmodes and the eigenfrequencies are the eigenvalues of $\chi[\Omega = 0]$. Thanks to the symmetry[1] of the eigenvalue problem, we solve $\det\left(\chi^{-1}[\Omega=0]-1\lambda_\pm\right)=0$ which yields the eigenvalues $\lambda_\pm \equiv M_{\mathrm{eff}}\Omega_\pm^2$ with

$$\Omega_\pm^2 \equiv \frac{\Omega_{\parallel 1}^{\ 2}+\Omega_{\parallel 2}^{\ 2}}{2} \pm \sqrt{\frac{\left(\Omega_{\parallel 2}^{\ 2}-\Omega_{\parallel 1}^{\ 2}\right)^2}{4}+g_{12}g_{21}} \tag{1.40}$$

as new squared eigenfrequencies of the two dimensional oscillator.

We now solve the eigenvector equation $\chi^{-1}(\Omega = 0)\mathbf{v} = \lambda\mathbf{v}$ which writes

$$\begin{vmatrix}\left(\Omega_{\parallel 1}^{\ 2}-\Omega_\pm^2\right)v_1-g_{21}v_2 & =0\\ -g_{12}v_1+\left(\Omega_{\parallel 2}^{\ 2}-\Omega_\pm^2\right)v_2 & =0\end{vmatrix}. \tag{1.41}$$

---

[1] The eigenvectors of $\chi^{-1}[\Omega = 0]$ are also eigenvectors of χ, it is thus easier to calculate the eigenvalue and eigenvectors for $\chi^{-1}[\Omega = 0]$.

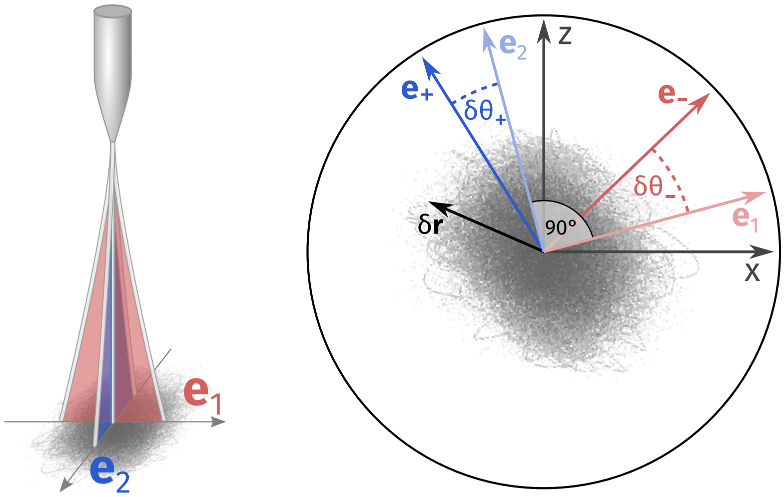

Fig. 1.6: Sketch of the two polarizations of the nanowire modes. The direction of the eigenmodes are labeled $\mathrm{e}_1, \mathrm{e}_2$. A time trace of the nanowire's Brownian noise trajectory is plotted to indicate the movement of the nanowire. The right graphic illustrates the two perpendicular cold eigenmodes $\mathbf{e}_{1,2}$ and the dressed eigenmode orientations $\mathbf{e}_{+,-}$. The rotation angles $\delta\theta_{+,-}$ are indicated with respect to the corresponding cold modes.

Using Ω_+ in the first and Ω_- in the second equation we obtain the normalized eigenvectors:

Dressed eigenvectors

$$\begin{aligned} \Rightarrow \mathbf{e}_- &= \frac{1}{\sqrt{g_{12}^2 + \left(\Omega_{\parallel 2}^{2} - \Omega_-^2\right)^2}} \begin{pmatrix} \Omega_{\parallel 2}^{2} - \Omega_-^2 \\ g_{12} \end{pmatrix} \\ \Rightarrow \mathbf{e}_+ &= \frac{1}{\sqrt{g_{21}^2 + \left(\Omega_+^2 - \Omega_{\parallel 1}^{2}\right)^2}} \begin{pmatrix} -g_{21} \\ \Omega_+^2 - \Omega_{\parallel 1}^{2} \end{pmatrix}, \end{aligned} \tag{1.42}$$

where both eigenvectors converge towards the uncoupled eigenvectors if no force field is present.

We can introduce for each eigenvector the angle of the mode orientation with respect to the x-axis $\theta_- = \theta_1 + \delta\theta_- =$ and $\theta_+ = \theta_2 + \delta\theta_+$ and write the normalized eigenvectors in terms of $\delta\theta_{-,+}$:

$$\mathbf{e}_- = \begin{pmatrix} \cos\delta\theta_- \\ \sin\delta\theta_- \end{pmatrix}, \mathbf{e}_+ = \begin{pmatrix} -\sin\delta\theta_+ \\ \cos\delta\theta_+ \end{pmatrix}, \tag{1.43}$$

in the $(\mathbf{e}_1, \mathbf{e}_2)$ basis. The change of the orientation angles then calculates:

Mode orientation

$$\tan\delta\theta_- = \frac{g_{12}}{\Omega_{\parallel 2}^{2} - \Omega_-^2} \quad \text{and} \quad \tan\delta\theta_+ = \frac{g_{21}}{\Omega_+^2 - \Omega_{\parallel 1}^{2}}. \tag{1.44}$$

1.1.2.2 Calculation of the force field gradients

For the calculation of the force field gradients, we define the following identities:

$$\begin{aligned} \Omega_+^2 + \Omega_-^2 &= \Omega_{\parallel 1}^{\ 2} + \Omega_{\parallel 2}^{\ 2} \\ \Delta_2\Omega_\parallel &\equiv \Omega_{\parallel 2}^{\ 2} - \Omega_{\parallel 1}^{\ 2} \\ \mu &\equiv \tan\delta\theta_- \tan\delta\theta_+ \\ \Omega_+^2 - \Omega_-^2 &= \sqrt{\Delta_2\Omega_\parallel^{\ 2} + 4g_{12}g_{21}}, \end{aligned} \tag{1.45}$$

where we used the result for the dressed eigenfrequencies (1.40) in the last identity.

Using the first two expressions we note that

$$\Omega_+^2 - \Omega_{\parallel 1}^{\ 2} = \Omega_{\parallel 2}^{\ 2} - \Omega_-^2 = \frac{1}{2}\left(\Delta_2\Omega_\parallel + \Omega_+^2 - \Omega_-^2\right) = K. \tag{1.46}$$

Combining this identity with (1.44), one has

$$g_{12}g_{21} = \tan\theta_- \tan\theta_+ \, K^2, \tag{1.47}$$

and can thus rewrite the fourth expression of (1.45) as

$$\begin{aligned} \left(\Omega_+^2 - \Omega_-^2\right)^2 &= \Delta_2\Omega_\parallel^{\ 2} + 4g_{12}g_{21} \\ &= \Delta\Omega_\parallel^{\ 4} + \mu\left(\Delta_2\Omega_\parallel + \Omega_+^2 - \Omega_-^2\right)^2. \end{aligned} \tag{1.48}$$

This quadratic equation can be solved for $\Delta_2\Omega_\parallel$ by

$$\Delta_2\Omega_\parallel = \left(\Omega_+^2 - \Omega_-^2\right)\frac{-\mu \pm 1}{1+\mu} \tag{1.49}$$

The "−" solution implies that the $g_{12}g_{21}$ has to be zero in all situations which is a non-realistic over constraint of the solution and therefore discarded. The remaining solution then is:

$$\Omega_{\parallel 2}^{\ 2} - \Omega_{\parallel 1}^{\ 2} = \left(\Omega_+^2 - \Omega_-^2\right)\frac{1-\mu}{1+\mu}. \tag{1.50}$$

By replacing $\Omega_{\parallel 2}^{\ 2}$ in the first identity of (1.45) with the obtained result we can write an expression for g_{11} and analogously for g_{22}:

Force field gradients as function of the eigenmode properties

$$g_{11} = \Omega_1^2 - \frac{1}{1+\mu}\left(\Omega_-^2 + \mu\Omega_+^2\right) \tag{1.51}$$

$$g_{22} = \Omega_2^2 - \frac{1}{1+\mu}\left(\Omega_+^2 + \mu\Omega_-^2\right) \tag{1.52}$$

It is then possible to obtain the expressions for g_{12}, g_{21} from equations (1.44) where g_{11}, g_{22} are replaced by the above result:

$$g_{12} = \frac{\tan \delta\theta_-}{1+\mu}\left(\Omega_+^2 - \Omega_-^2\right) \tag{1.53}$$

$$g_{21} = \frac{\tan \delta\theta_+}{1+\mu}\left(\Omega_+^2 - \Omega_-^2\right) \tag{1.54}$$

These four expressions for the force gradient terms depend only on directly measurable quantities (the frequency shifts and the eigenmode rotations) that can be obtained experimentally by a Fourier analysis of the nanowire's trajectory in the two dimensional oscillation plane. This requires a two dimensional detection protocol that is in the focus of Section 1.3.

1.1.2.3 Force field signatures

Depending on the shape and orientation of the force field with respect to the nanowire eigenmodes, it dresses them differently. As we have seen in the above equations, the force field components g_{ij} depend on the eigenfrequency shifts and on the rotation of the eigenmode basis. Here, we will investigate how those nanowire mechanical properties are affected by a set of fundamental force field gradients which form a basis of the linear 2D force field gradients.

Force divergence – simultaneous eigenfrequency shift The sum of the squared eigenfrequencies can be expressed as

$$-\left(\Omega_-^2 + \Omega_+^2 - (\Omega_1^2 + \Omega_2^2)\right) = g_{11} + g_{22} = \frac{1}{M_{\mathrm{eff}}} \operatorname{div} \mathbf{F}. \tag{1.55}$$

In case of a pure divergent force field ($g_{11} = g_{22}$), at first order in the force gradients, the eigenfrequencies shift as a block. A shift of the two frequencies together is thus a direct measure for the divergence of the force field. The sum of the dressed frequencies squared is sensitive towards force gradients along both eigenmodes. We note that since the determination of the mechanical eigenfrequencies is in principle only weakly affected by experimental bias, they present a very practical role in an imaging scanning mode. A purely divergent local force field is illustrated in the first plot of Figure 1.7.

Aligned hyperbolic force field – eigenfrequency splitting The frequency splitting of the dressed eigenmodes (Equation 1.40) is given by

$$\Omega_+^2 - \Omega_-^2 = \sqrt{\left(\Omega_2^2 - \Omega_1^2 - (g_{22} - g_{11})\right)^2 + 4 g_{12} g_{21}} \tag{1.56}$$

which for small off diagonal terms can be approximated in first order as

$$\Omega_+^2 - \Omega_-^2 = \Omega_2^2 - \Omega_1^2 - (g_{22} - g_{11}). \tag{1.57}$$

Rotated hyperbolic force field – eigenvectors basis rotation The transverse terms g_{12}, g_{21} of the force gradient matrix create a coupling of the modes since for a movement in one direction they create a force along the other. The new, rotated basis of this coupled mode is a linear combination of the cold eigenmode basis. We can calculate the difference between the mode angles (following the definition in (1.43)) with

$$\theta_1 - \theta_2 = \arctan \frac{g_{12}}{\Omega_{\parallel 2}^{\,2} - \Omega_-^2} - \arctan \frac{\Omega_{\parallel 2}^{\,2} - \Omega_-^2}{-g_{21}}. \tag{1.58}$$

In the case of small force gradients with $\frac{g_{ij}}{\Omega_{1,2}} \to 0$, we can approximate the mode orientations by the approximations:

$$\Omega_{\parallel 1,2} \to \Omega_{1,2} \text{ and } \sqrt{\left(\Omega_{\parallel 2}^{\,2} - \Omega_{\parallel 1}^{\,2}\right)^2 - g_{12}g_{21}} \to \left(\Omega_{\parallel 2}^{\,2} - \Omega_{\parallel 1}^{\,2}\right),$$

so that:

$$\theta_- \approx \arctan \frac{g_{12}}{\Omega_2^2 - \Omega_1^2}, \; \theta_+ \approx \frac{\pi}{2} + \arctan \frac{g_{21}}{\Omega_2^2 - \Omega_1^2}. \tag{1.59}$$

For $g_{12} = g_{21}$, the rotational of the force field is zero $\nabla \times \mathbf{F} = 0$ and the arguments of the arcus tangens in (1.58) become the mutual inverse. Applying the identity $\arctan x - \arctan y = \arctan \frac{x-y}{1-xy}$ gives that the angle difference is the limit of the arcus tanges at $\frac{\pi}{2}$ so the modes turn as block, resting perpendicular to each other. This is the standard case for conservative force fields such as electrostatic fields.

A rotation as block due to a shearing force field is illustrated in the third column of Figure 1.7.

General eigenmode rotation In a force field with nonzero rotational $\nabla \times \mathbf{F} \neq 0$, the diagonal components of the force gradient tensor g_{12}, g_{21} are not equal and the mode orientation of both modes can vary independently. The angle difference between both modes can then be calculated via

$$\cos(\theta_1 - \theta_2) = \mathbf{e}_- \cdot \mathbf{e}_+ = \frac{(g_{12} - g_{21})\left(\Omega_{\parallel 2}^{\,2} - \Omega_-^2\right)}{\sqrt{\left(g_{21}^2 + \left(\Omega_{\parallel 2}^{\,2} - \Omega_-^2\right)^2\right)\left(g_{12}^2 + \left(\Omega_+^2 - \Omega_{\parallel 1}^{\,2}\right)^2\right)}} \tag{1.60}$$

where we used the results from Equation 1.42 and the identity:

$$\Omega_+^2 - \Omega_{\parallel 1}^2 = \Omega_{\parallel 2}^2 - \Omega_-^2. \tag{1.61}$$

Under the same assumptions as for Equation 1.59 we can approximate in first order

$$\cos(\theta_1 - \theta_2) \approx \frac{g_{12} - g_{21}}{\Omega_2^2 - \Omega_1^2}. \tag{1.62}$$

The rotation asymmetry $g_{12} - g_{21}$ is thus directly connected to mode shearing and can be measured by detection of the mode's rotation. It is important to highlight that the shearing angle in (1.62) as well as the total rotation in (1.59) are larger the smaller the intrinsic mode splitting $\Omega_2^2 - \Omega_1^2$ is, which implies higher sensitivity for resonators with small splitting.

Table 1.3 summarizes the four base signatures. The corresponding spatial shapes of the local force field and their effect on eigenmode spectrum and mode orientation is presented schematically in Figure 1.7

Tab. 1.3: Force field properties and the corresponding expressions.

Signature	Expression	Effect on resonator
Divergent	$g_{11} = g_{22}$	Block frequency shift
Hyperbolic aligned	$g_{11} = -g_{22}$	Squared eigenfrequency splitting
Hyperbolic rotated	$g_{12} = g_{21}$	Block eigenmode rotation $\theta_1 - \theta_2 = \frac{\pi}{2}$
Rotation	$g_{12} \neq g_{21}$	Eigenmode orthogonality breaking

1.1.2.4 The noise spectrum of a dressed nanowire

A single, measurement channel provides a scalar information, which corresponds to a projective measurement of the displacement of the nanowire extremity $\delta\mathbf{r}$ along a measurement vector $\mathbf{e}_\mu = (\cos\mu, \sin\mu)$ (written in the $\mathbf{e}_1, \mathbf{e}_2$ basis, μ being the angle between $\mathbf{e}_1$ and $\mathbf{e}_\mu$). In the Fourier domain, we have:

$$\begin{aligned}
\delta r_\mu[\Omega] &\equiv \mathbf{e}_\mu \cdot \delta\mathbf{r}[\Omega] \\
&= \mathbf{e}_\mu \cdot \boldsymbol{\chi}[\Omega] \cdot \left(\delta\mathbf{F}_{\text{th}} + \delta\mathbf{F}_{\text{pump}}\right) \\
&= (\cos\mu\chi_{11}[\Omega] + \sin\mu\chi_{21}[\Omega])\delta F_1 + (\cos\mu\chi_{12}[\Omega] + \sin\mu\chi_{22}[\Omega])\delta F_2.
\end{aligned} \tag{1.63}$$

$\delta F_{1,2}$ are the forces' components projected in the direction of the first and second undressed eigenmode respectively.

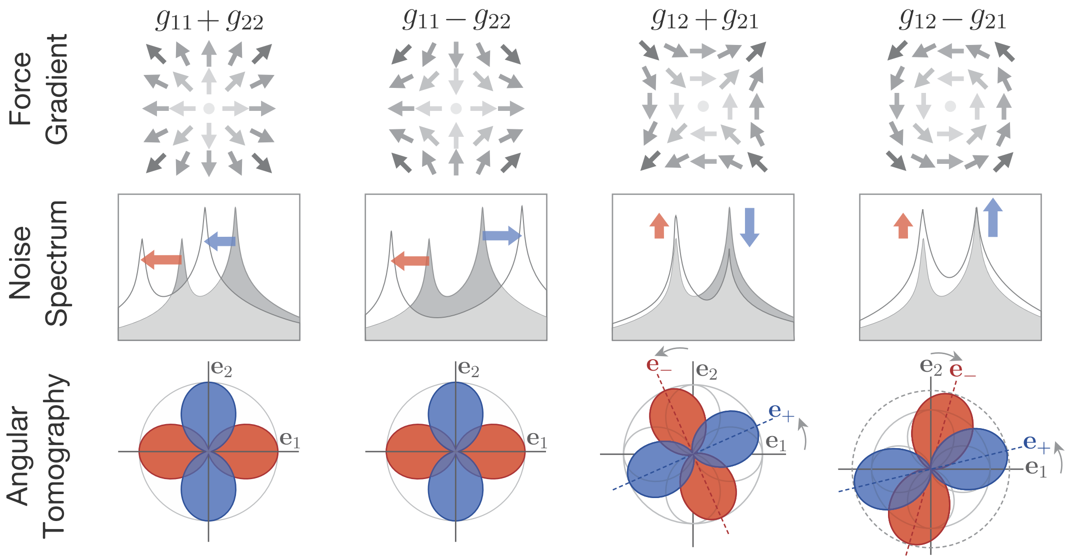

Fig. 1.7: Characteristical force field signatures which form a basis of any force field configuration. The second row shows the spectral change caused by each local force field as would be measured under a 45° projection angle between both modes, while the panels in the third row display the spatial tomography of the eigenmodes illustrating mode rotation and amplitude change.

For a purely stochastic Langevin force as in the case of thermal Brownian motion, the force terms are simply the two Langevin force vectors, which are uncorrelated and we can calculate the noise spectrum $S_{\delta r_\mu}$ for a projection onto the measurement vector μ:

$$\begin{aligned} 2\pi\delta(\Omega+\Omega')S_{\delta r_\mu}[\Omega] &= \left\langle \delta r_\mu(\Omega)\delta r_\mu(\Omega') \right\rangle \\ &= \left|\cos\mu\chi_{11}[\Omega]+\sin\mu\chi_{21}[\Omega]\right|^2\langle\delta F_1\delta F_1\rangle + \\ &\quad \left|\cos\mu\chi_{12}[\Omega]+\sin\mu\chi_{22}[\Omega]\right|^2\langle\delta F_2\delta F_2\rangle \end{aligned} \tag{1.64}$$

Here, we use that the thermal fluctuations $\delta F_{1,2}$ that drive the mechanical modes are uncorrelated and hence $\langle\delta F_1\delta F_2\rangle = 0$. When the damping matrix is isotrope, the spectral density for each of these forces is identical to the spectral density of the Langevin force in Section 1.1.1.1 with $S_{F_{th}} = 2M_{\text{eff}}\Gamma k_B T$. Plugging the matrix elements of $\boldsymbol{\chi}$ in Equation 1.64, we obtain the projected thermal noise spectrum as

Vibrational noise spectrum projected on an arbitrary measurement angle

$$S_{\delta r_\mu}[\Omega] = \frac{S_{F_{th}}}{\left|\det\boldsymbol{\chi}^{-1}[\Omega]\right|^2}\begin{pmatrix} \cos^2\mu\Big(\big(\Omega_{\parallel 2}^2-\Omega^2\big)^2+\Omega^2\Gamma^2+g_{21}^2\Big) \\ +\sin^2\mu\Big(\big(\Omega_{\parallel 1}^2-\Omega^2\big)^2+\Omega^2\Gamma^2+g_{12}^2\Big) \\ +2\cos\mu\sin\mu\Big(g_{12}\big(\Omega_{\parallel 2}^2-\Omega^2\big)+g_{21}\big(\Omega_{\parallel 1}^2-\Omega^2\big)\Big) \end{pmatrix} \tag{1.65}$$

with the same $\boldsymbol{\chi}^{-1}[\Omega]$ as given in Equation 1.38.

In the next section we discuss the effect of a resonant external force on the oscillator's mechanics and how the oscillator's response can be used to obtain the dressed mechanical properties and thus to infer the force field gradients.

1.1.3 The nanowire's driven response

Classical AFM techniques include a homodyne lock-in based detection that allows a fast low-noise measurement. The oscillation of the cantilever probe is driven at resonance and the measured signal from the vibration detection is demodulated at the drive frequency.

Applying this idea to the two dimensional nanowire oscillator, the driving force from Equation 1.35 can be expressed as the sum of the frequency independent Langevin force δF_{th} and the resonant driving force $\delta\mathbf{F}_{\mathrm{pump}}[\Omega]$ as described in Section 1.1.1.2. As shown, the physics of the oscillator in a static force field is not affected as long as the applied force has a constant amplitude. This section takes a look on the driven trajectory in two dimensions and discusses effects arising when the force does not represent an instantaneous drive but contains a delayed part as well.

1.1.3.1 Driven response of a 2D oscillator

After having investigated the nanowire's thermal noise structure in 2D in Section 1.1.1.2, we now turn to its response to an external driving force. We will see that such a coherent drive, which generates coherent trajectories in the stationary regime, can also be used to determine the mechanical properties of the nanowire, and can thus serve to measure external force field gradients.
We consider the situation where a modulated driving force is resonantly exciting the nanowire at discrete frequencies Ω_i (here $i = 1, 2$):

$$\mathbf{F}_{\mathrm{pump}}(t) = F_0\mathbf{e}_F + |\delta F|\mathbf{e}_F \cdot (\cos(\Omega_1 t + \phi) + \cos(\Omega_2 t + \phi)). \tag{1.66}$$

When driven at resonance, the nanowire's trajectory describes a narrow ellipse as illustrated in Figure 1.8a for excitation at the eigenmode frequency $\Omega = \Omega_{1,2}$. In order to drive both eigenmodes by the same unidirectional force with a comparable efficiency, the eigenmodes should be oriented in a 45° angle to the driving force. The modulation strength $|\mathbf{F}_{\mathrm{pump}}[\Omega]|$ can in principle also be adjusted for each tone, but this will complexify the subsequent analysis. An external force field can rotate the nanowire's eigenmodes (compare Section 1.1.2.3), leading to perpendicular alignment of one eigenmode and the driving force. This perpendicular mode can thus not be addressed by the driving force.

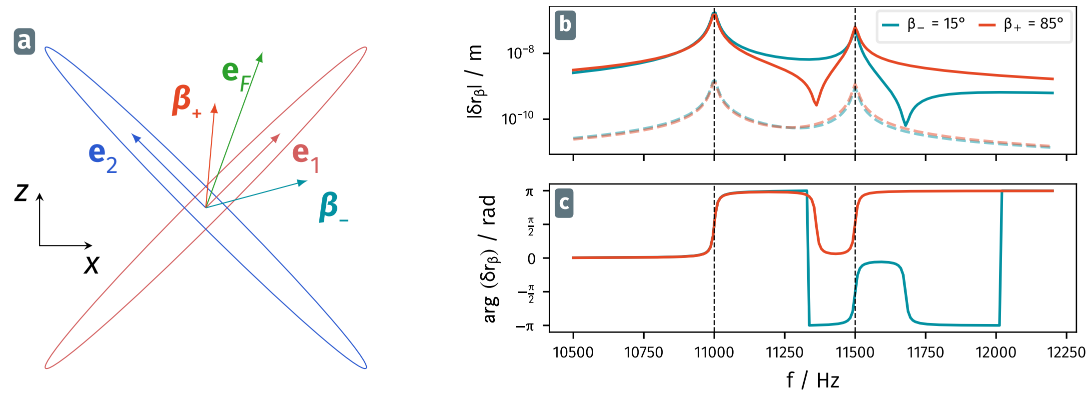

Fig. 1.8: (**a**) Schematic trajectories followed by the nanowire extremity when driven at resonance of both eigenmodes. The eigenmodes are perpendicular to each other and are driven by a force in a 70° angle. The $\boldsymbol{\beta}_{-,+}$ vectors indicate two independent measurement directions. (**b,c**) Expected response of a theoretical nanowire driven by a coherent force in the sketched constellation of (**a**) when sweeping the modulation frequency across the two fundamental resonances. The two curves correspond to a projection of $\delta\mathbf{r}$ on the measurement angles β_- = 15°and β_+ = 85°. The lighter dashed lines present the thermal noise spectrum calculated for the same nanowire at room temperature. The amplitude (**b**) and phase (**c**) of the projected displacement are shown, as measured by a 2-channel network analyzer. Thus, the phase of the projected displacement can be compared to the phase of the modulated force. When using an optical drive, this permits to infer if the optical force follows the intensity modulation instantaneously or not.

By sweeping the frequency Ω of the driving force $\mathbf{F}_{\text{pump}}$, and measuring the projection of the trajectory at each frequency onto a measurement angle $\beta_{-,+}$, one obtains the response curves in amplitude (Figure 1.8b) and phase (1.8c). At the modes' resonance frequencies, the phase increases by π. The coherent excitation of both adjacent modes at the same time leads to characteristic dips depending on the measurement direction where the minimum value of the response falls below the value obtained far of from resonance. The theoretical amplitude of the displacement δr_β only depends on the driving strength and can largely exceed the Brownian noise spectrum that is shown as dashed lined in Figure 1.8b.

Having measured such a response curve at two different measurement angles β, one can deduce the force vector $\mathbf{F}_{\text{pump}}$ and the force field gradient matrix g_{ij} via a fit to Equation 1.63. Here, force and gradients form a set of eight unknowns (F_{pump} can be complex) and the minimal measurement therefore comprises a measurement of amplitude and phase of the response at two frequencies Ω on each measurement vector $\beta_{-,+}$. This holds as far as the damping coefficient is not changed by external effects as discussed later in this work.

A useful configuration for such a measurement is the detection of the phase and amplitude at resonance, since the signal is strongest and an optimal SNR can be obtained. The stable phase change at resonance and the typical high Q-factor of the nanowires also permits to lock the driving force on each resonance with high precision using two independent phase-locked-loops (*PLL*) .

1.1.3.2 Driven trajectories in the position space

Having introduced the nanowire trajectories at resonance in Figure 1.8a and the vectorial displacement measurement, we can now describe the form of a trajectory in the real space of a suspended nanowire, driven at a single frequency, by:

$$\delta r(t) = \Re\Big[\big(|\delta r_x[\Omega]| e^{i\phi_x[\Omega]}\mathbf{e}_x + |\delta r_z[\Omega]| e^{i\phi_z[\Omega]}\mathbf{e}_z\big) e^{-i\Omega t}\Big], \tag{1.67}$$

where the amplitude and phase terms are evaluated at the driving frequency as well. In this expression, we make use of the complex projected displacements quantities $\delta r_{x,z}$, measured along the x and z axis, following the same description as for δr_μ given above. We also introduced the notation $\phi_{x,z} = \arg(\delta r_{x,z})$. With varying time t, this parametric 2D function describes an ellipse. The ellipse at the frequency Ω has the long axis $\delta r_{\max}$, short axis $\delta r_{\min}$ and an inclination angle Ψ of the long axis with respect to the x-axis given by the expressions:

$$\begin{aligned}
\delta r_{\max} &= \frac{|\delta r_x|^2 + |\delta r_x|^2}{2} + \frac{1}{2}\sqrt{\left(|\delta r_x|^2 - |\delta r_x|^2\right)^2 + |\delta r_x \delta r_z|^2 \cos(\phi_z - \phi_x)} \\
\delta r_{\min} &= \frac{|\delta r_x|^2 + |\delta r_x|^2}{2} - \frac{1}{2}\sqrt{\left(|\delta r_x|^2 - |\delta r_x|^2\right)^2 + |\delta r_x \delta r_z|^2 \cos(\phi_z - \phi_x)} \\
\psi &= \frac{\pi}{2} + \frac{1}{2}\tan^{-1}\frac{2\delta r_x \delta r_z \cos(\phi_z - \phi_x)}{\left(|\delta r_x|^2 - |\delta r_x|^2\right)}.
\end{aligned} \tag{1.68}$$

Figure 1.9a provides an example of an elliptical trajectory obtained at a single driving frequency with the parameters from (1.68). The set of trajectories obtained for a subset of frequencies around the two eigenfrequencies of a driven nanowire oscillator are plotted in Figure 1.9b. The driving force is indicated as green arrow. Since it is an asymmetric excitation, the first mode is driven slightly more than the second.

1.1.3.3 Delayed driving force

Experimentally, different techniques are suitable to generate the excitation force $\mathbf{F}_{\text{pump}}$. In particular, optical, electrostatic and mechanical interaction processes are prominent techniques as they are easy to employ and permit good control of $\mathbf{F}_{\text{pump}}$. In the response measurements, the phase of the projected displacement is measured with respect to the phase of the force modulation signal. The interaction processes are not always instantaneous, meaning that there is a delay between the moment where we turn on the force and its application on the nanowire. Such a delay in the application of the force is re-

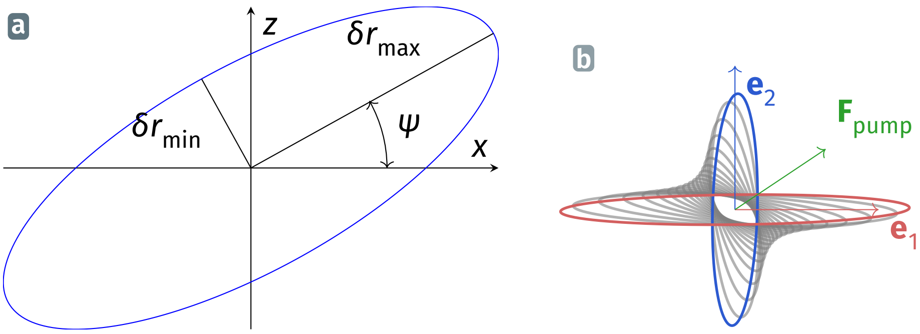

Fig. 1.9: Illustration of the trajectory followed by a resonantly driven nanowire. Under a monochromatic excitation, the nanowire follows an elliptical trace (**a**). If we scan the driving tone across both fundamental modes, one can plot a set of elliptical traces, one for each driving frequency (**b**). The colored trajectories are those obtained when exciting the nanowire at the eigenmode frequencies. The driving force is represented by the green arrow. The trajectories are plotted in the basis of the nanowire's perpendicular eigenmodes. If the eigenmodes are far apart, the resonant trajectories will tend towards single lines, but when their splitting is comparable to their mechanical linewidth, one can obtain larger ellipses, supposing that the driving force vector is not aligned with one eigenmode.

sponsible for an additional $e^{i\Omega\tau}$ term in the force's Fourier component, and will thus be responsible for the apparition of an imaginary contribution in $\mathbf{F}_{\text{pump}}[\Omega]$.

A prominent example for a delayed force is the photo-thermal force where the delay originates from the time the system needs to adapt to a new temperature distribution which is caused by a change in the absorbed optical power. When one modulates the optical power at the mechanical resonance frequencies, the temperature profile does not have time to reach its steady state profile and one thus faces a temperature increase in quadrature with the intensity modulation. Such a temperature increase can then modulate the nanowire's optical cross-section via the temperature dependence of the refractive index (the thermal expansion contribution is approximately ten times smaller), which will cause a delayed optical force, without changing its orientation. Another photo-thermal mechanism involves a bilayer mechanism, acting as a delayed optical force, which is not necessarily oriented along the same orientation as the optical flux, since it comes from a geometric asymmetry in the nanowire material. The photo-thermal effect where a radiation source is locally heating the nanowire that adapts to the new heat distribution is depicted in Figure 1.10a.

Another effect, one that can lead to delayed electrostatic forces, is caused by the RC circuit that forms when the nanowire is close to an electrode (Figure 1.10b). The delay of the applied electrostatic force depends on the system capacitance and the circuit resistivity. This RC-effect is in general rather weak.

Furthermore, when using a piezo actuation, an effective delay can appear due to the system's internal resonances. The frequency response of the piezoelectric effect is dominated by geometry and material dependent resonances (represented by the curve on the piezos in Figure 1.10c) that can cause a delayed response of the mechanical actuation.

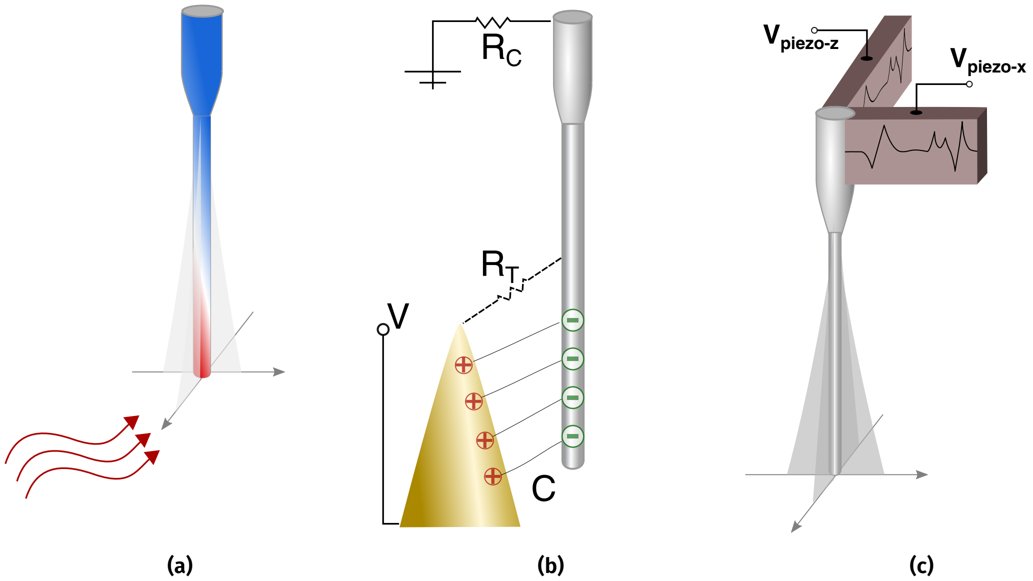

Fig. 1.10: Schematic presentation of the delayed photothermal force (**a**), an electrostatic delayed force due to capacitive effects (**b**) and a mechanical actuation with non constant response of the piezo actuation system (**c**).

A delayed driving force means that the phase at resonance is not equal to $\frac{\pi}{2}$ as the imaginary part of $\delta\mathbf{r} = \chi\delta\mathbf{F}$ now originates not only from the susceptibility but also from the exciting force. In principle those delays can vary with the frequency, and furthermore they can be different along both transverse orientations (in case of a piezo drive for example). It is always possible to calibrate those delays, but the analysis of the response measurement is much more simplified in absence of delays.

Forces that are typically instantaneous thanks to their short characteristic timescale τ_F, are the optical pressure force exerted by an intensity-modulated laser beam and the electrostatic force caused by an inhomogeneous electric field (the dielectric nanowire is attracted towards regions of high field). These forces establish much faster than the mechanical vibration of the oscillator $\tau_F \ll 1/\Omega_\mathrm{m} \approx 10\,\mu\mathrm{s}$.

Depending on the amplitude and delay of the driving force the oscillator can become instable. One example for such an instability is self-oscillation caused by a force with effective negative damping.

1.2 The SiC Nanowire force sensor

The nanomechanical oscillators predominantly used in the group are silicon carbide (SiC) nanowires. Silicon carbide is a compound semiconductor with a bandgap at 385, 405 and 505 nm for the most common crystal structures $4H$, $6H$ and $3C$ respectively. Since SiC is lightweight with a density of $\rho = 3210\,\mathrm{kg\,m^{-3}}$ and has a large stiffness with a Young's modulus of $\mathrm{E} > 400\,\mathrm{GPa}$ [51, 86, 118], SiC based nanomechanical systems have an intrinsically low effective mass that allows achieving good force sensitivity without operating at too small frequencies where there is lot of technical noise. They are therefore well suited for MEMS/NEMS applications [21]. The large refractive index of $n_{\mathrm{SiC}} = 2.6$ in the visible [84] leads to the presence of multiple internal optical resonances for visible wavelengths in the employed nanowires which have diameters between 100 nm to 600 nm. These resonances are described by *Mie theory* [28, 74] which, together with the optical band-gap at short wavelength, allows strong scattering of light even with diameters shorter than the optical wavelength. SiC nanowires are therefore easily detectable through optical microscopes. The large thermal conductivity $\kappa_{\mathrm{th}} = 360\,\mathrm{W\,m^{-1}\,K^{-1}}$ of silicon carbide additionally protects the nanowires from melting at high injected optical power so they can be employed in focussed laser beams of several tens of mW at ambient pressure and up to a few mW under vacuum. The optical microscope image in Figure 1.11 illustrates the scattering of a selection of nanowires with different diameters. The homogeneity of the colours is a sign of quasi uniform radius over the full nanowire length. SiC nanowires were subject of detailed studies for what concerns their use as field emission sources [86, 117] and their electrical properties under large electric fields are well studied.

With diameters of 100 nm to 300 nm and length of 50 µm to 500 µm the utilized nanowires in our group reach effective masses (M_{eff}) in the pg range with observed quality factors of $Q = 1000 - 10000$. The typically achieved force sensitivity after 1.22 is in the range of $\mathrm{aN/Hz^{1/2}}$.

The sensitivity limit for force gradient measurements (Equation 1.28) – valid for noise based and resonant measurements – lies in the range of some $\mathrm{aN\,nm^{-1}}$ to $\mathrm{pN\,nm^{-1}}$ for the first mechanical mode family that is typically located between 5 kHz to 50 kHz,

1.2.1 Selection of a single nanowire

A first criterion for the nanowire selection is the desired force sensitivity as this is the quantity that determines which forces will be measurable. In general it is not appropriate to operate with a too sensitive nanowire (long and thin) if the force field under investigation will over-dress its mechanical properties because it will generate large eigenmode

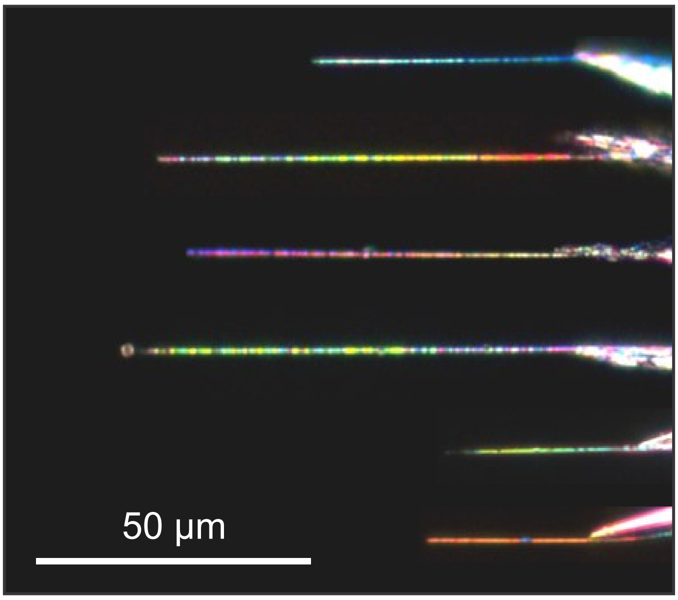

Fig. 1.11: Optical microscope image of multiple SiC nanowires. Different colores are caused by the different thicknesses of the nanowires. Abrupt transitions from one color to another indicate a presence of two crystalline phases along the nanowire. The displayed nanowires are from a different batch than those used in this work which have a much higher homogeneity and better crystallinity.

rotations that cause experimental difficulties[2]. Following the rule for the force gradient sensitivity (1.28), optimal sensitivities are achieved when using nanowires with mechanical resonances Ω_m at low frequency and a high quality factor. Also the force gradient sensitivity scales linearly with the inverse of the effective mass of the nanowire. These critreria translate into nanowires with a small cross section and sufficient length to have both, low mass and small Ω_m. For a good quality factor, choosing a nanowire of highest uniformity and guaranteeing a good mechanical connection to its mount are important criteria that optimize the mechanical damping Γ. Additionally, a uniform nanowire without many geometrical and crystalline defects is less likely to present an optical variability along its length so that the optical measurement process is less sensitive to small vertical drifts with respect to the measurement laser.

The spatial resolution attainable in an experiment is a second criterion for nanowire selection. While the force gradient sensitivity increases with lower resonance frequency Ω_m, the spatial resolution of the measurement depends on the oscillation amplitude of the nanowire tip that is immersed in the external force field. In order to keep this oscillation amplitude in a reasonable range of 10 nm to 100 nm, very long nanowires with a larger cross section are omitted for force field sensing experiments.

---

[2] This concerns for instance the lock stability of the PLLs or the blindness to one of the resonances on a measurement channel if its modal direction is perpendicular.

A third, more practical criterion is the measurability. Since nanowire based force field sensing is a form of scanning probe microscopy, like most imaging techniques it relies on stability and speed. In the resonant measurement performed in this work, stability and speed can be increased by operating at higher mechanical frequencies what permits working with larger mechanical damping rates. This criterion excludes the use of nanowires with the highest sensitivity that generally oscillate at very low frequency (few kHz). Good compromises are therefore thin nanowires measuring about 100 nm to 200 nm in diameter with a mechanical frequency between 10 kHz to 50 kHz. These nanowires still provide sensitivities in the range of tens of atto-newton while remaining friendly to work with. A useful chart that provides the relation between all the mechanical properties is presented in figure Figure 1.12.

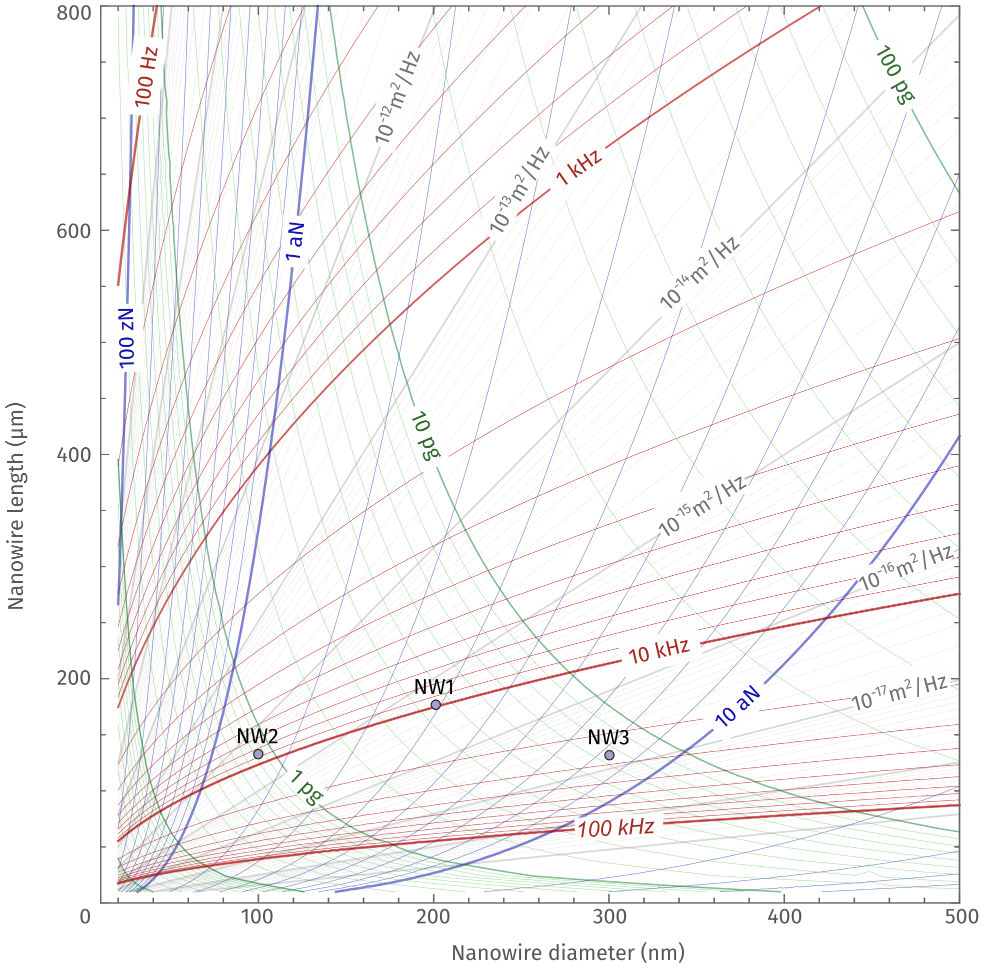

Fig. 1.12: The abacus illustrates the mechanical nanowire properties – freqency, noise level and force sensitivity – at room temperature, in dependence on the nanowire geometry. The three nanowires with whom the results in this thesis were obtained are illustrated as dots. Knowing the length of a nanowire and its frequency, one can deduce its force sensitivity using this representation.

We identify suitable nanowires by optical microscopy where we exploit the scattering properties of nanowires which varies with the diameter of the nanowires. Mie theory that describes light scattering on nanoscopic objects can be solved analytically for cylindrical objects and it is therefore possible to calculate the expected reflection spectrum for a nanowire of a certain thickness, inserted in a given optical waist. For typical diameters ranging between 100 nm to 400 nm the nanowires can host multiple resonant optical modes as shown in the plot of the scattering cross section in Figure 1.13. The scattering from Mie modes is anisotropic and each mode has a characteristic angular dependence that determines its strength in the reflection channel. The blue and red lines in Figure 1.13 show the effective scattering cross section for two different collection angles of 60° and 90°.

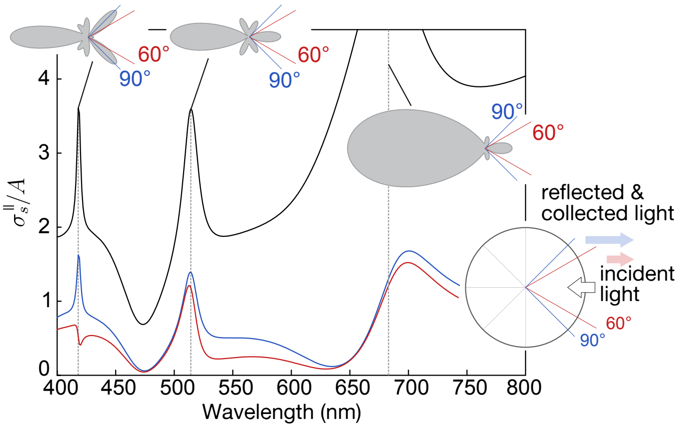

Fig. 1.13: Scattering cross section of a 300 nm thick nanowire as function of the wavelength (black line) and the reflection cross section for solid angles 60° and 90° (red and blue curve). Each Mie resonance has a characteristic scattering as illustrated by the insets.

Based on the theoretical reflection scattering cross section we can plot the perceived colour for nanowires of different thicknesses (Figure 1.14). By comparing the colour of the reflected light in parallel and perpendicular polarizations with respect to the nanowire axis, with the colour in the chart, we obtain a good estimation of the nanowire's thickness. This characterization relies on the knowledge of the transmission properties of the microscope optics and on the RGB spectra of both the CCD camera employed and the computer screen on which the image is displayed. The representation in Figure 1.14 takes into account the numerical aperture (*NA*) of the used 50x objective.

1.2.2 Mounting and installing the nanowire

The nanowires used in the group are mass-produced industrial grade nanowires that come in powder form. We identify nanowire candidates that stick out of the powder ensemble by optical microscopy. With the help of a micro-manipulation stage, we attach a single nanowire to a sharply pointed tungsten wire with a base diameter of 400 µm using electron microscopy conductive carbon glue as adhesion agent. The tungsten wire

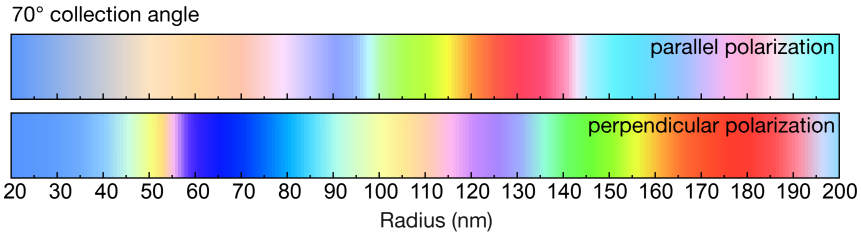

Fig. 1.14: Perceived color for nanowires with radii between 20 and 200 nm in parallel and perpendicular polarization calculated for the 50× microscope objective used for sample preparation ($NA = 0.5$).

tips have been fabricated by electrochemical wet etching in KOH optimized to produce small tip angles using a technique similar to methods employed elsewhere [49, 56, 61]. Figure 1.15 lays out the concept of the fabrication process.

In case of a perfectly attached nanowire, the tip angle is equal to the angle of the nanowire that should be as straight as possible to avoid an inclination with respect to the sample in the experimental setup. Sub-Figure 1.16a shows a microscope image of the tungsten wire (left) attached to a nanowire (centre, light blue) that sticks out of the nanowire powder (right).

The thus obtained nanowires often carry other wires or dirt with them that are loosely attached by electrostatic and Van der Waals forces. These contaminations can be removed by immersion in a water droplet (1.16b). The glued nanowire is then further characterized by optical reflection as described above (1.16c) and scanning electron microscopy (1.16d). Spectral analysis of the electrical current of the secondary electron detector of the scanning electron microscope also provides a first measurement of the mechanical resonant frequency. However, we found that the SEM imaging was responsible for a significant degradation of the surfaces exposed to the beam, so we realize these electronic measurements only at the end of a measurement sequence[3]. The nanowire diameter are efficiently estimated using the color method and the frequency abacus.

For handling and mounting the nanowire, we insert the tungsten carrier in a titanium support that can be screw-mounted in the experimental setup. Here we also set the correct height of the nanowire with respect to the bottom of the mount (19 mm).

The tungsten wire is kept in place by mechanical clamping and a small amount of superglue or a conductive silver based glue. Before being employed in the setup, the nanowire is thermally annealed under vacuum in an induction oven at ~700°C for ~10 min. The curing process serves to harden the carbon glue and thus to improve the mechanical connection between nanowire and tungsten tip. A good mechanical connection is a precondition for high mechanical Q factors (up to 10 000 at room temperature) and thus

---

[3] Not all nanowires survive up to this moment.

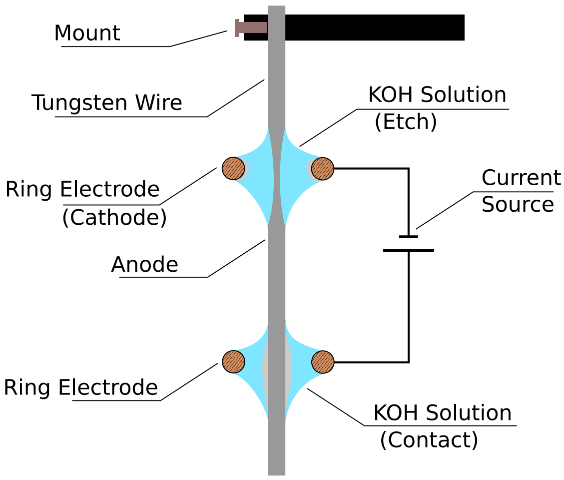

Fig. 1.15: Sketch of the setup for the fabrication of the pointed tungsten tips. The 400 µm thick tungsten wire is mechanically attached to a mount and fed consecutively through two metallic rings with a few mm diameter that are connected with the poles of a current source that operates around 100 mA to 300 mA. Droplets of a KOH solution (concentration 2 mol L^{-1}), posed on the rings, establish the electric connection between electrodes and wire. The relative size of the wire is largely exagerated in order to illustrate the etching progress. During the electrochemical etching process W^+ ions dissolve in the KOH solution around the Cathode replacing K^+ ions that attach to the metallic ring. This leads to a gradial thinning of the wire, most pronounced at height of the ring cathode. The second ring electrode serves to establish an electrical contact, When the whole diameter has been etched away, the lower part of the tungsten wire falls down, opening the electrical circuit and stopping the etch process. It can be collected in a water filled beaker (not shown). Both ends can be used to attach nanowires to, however, the upper part is usually of higher quality as it has the smaller tip angle due to the asymetric shape of the droplet.

for better force gradient sensitivity. It also guarantees a better thermalization of the nanowires which permits to use higher optical powers for the optical position readout without damaging the nanowire. The curing can principally improve the crystallinity of the nanowire and thus further enhance thermal conductance and mechanical Q factor. We note that we have observed that the curing process can also evaporate metal on the nanowire, so that materials with an increased vapour pressure at the working temperature such as copper or tin elements should not be used in the oven. After curing, we mount the nanowire on a standardized support in the scanning force imaging setup that is described in the following sections.

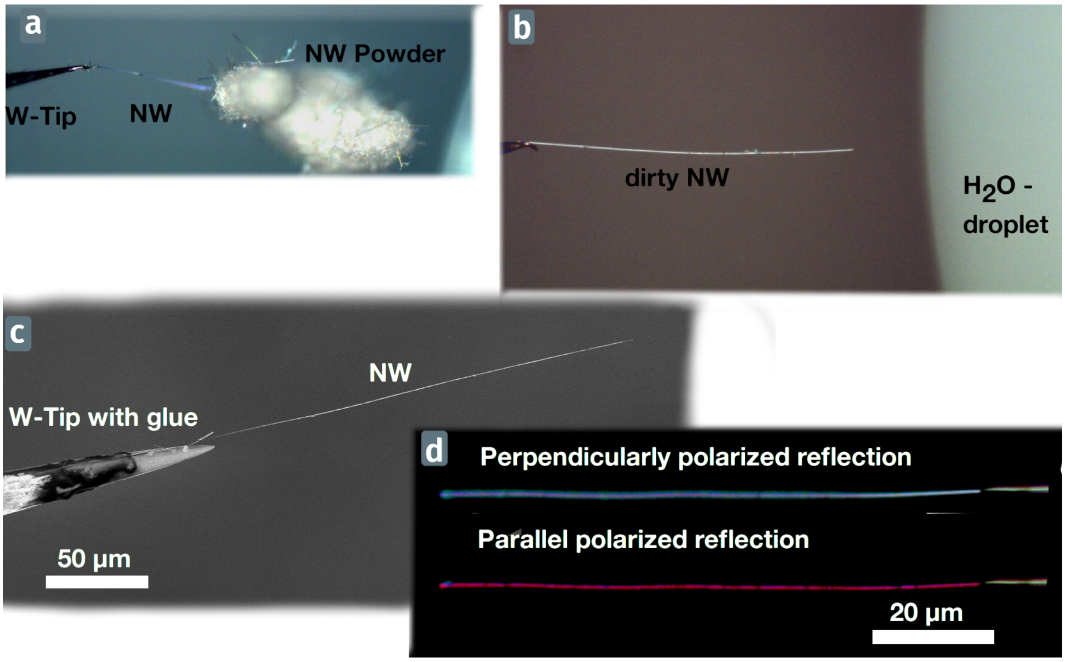

Fig. 1.16: Illustration of the nanowire preparation. A nanowire is selected by its length and color from the nanowire powder and caught with a pointed tungsten tip (**a**). It is then cleand by immersion in a water droplet (**b**) and characterized with optical reflection measurements (**d**) and scanning electrom microscopy (**c**).

1.3 Optical readout of the nanowire motion in 2d

In Section 1.1 we have seen that the mechanical and optical properties of nanowires make them ideal probes for realizing two dimensional force field sensing via the detection of the orientations and frequencies of the two fundamental eigenmodes. In view of the peculiar effects induced by the rotational force fields, which can increase the noise magnitude, it is necessary to employ a 2D readout scheme in order to distinguish the action of a rotational force field to a normal rotation of the eigenmode, which will both change the magnitude of the noise projection on a given measurement channel.

We have already underlined the large optical cross sections of the nanowire, that efficiently interacts with focussed laser beams due to the existence of internal Mie resonances. In this section we will discuss an optical readout technique that allows a measurement of the nanowire's vibration projected along two linearly independent readout vectors (non-parallel). These measurement channels are produced at the separate outputs of a homemade split photodiode amplifier that measures the light reflected from a single nanowire. auto1.17 sketches the detection of light reflected from the nanowire on the split photodiode.

A red probe laser beam is focussed on the nanowire extremity by a microscope objective of 0.75 NA and 100x magnification, modified for vacuum operation. After the objec-

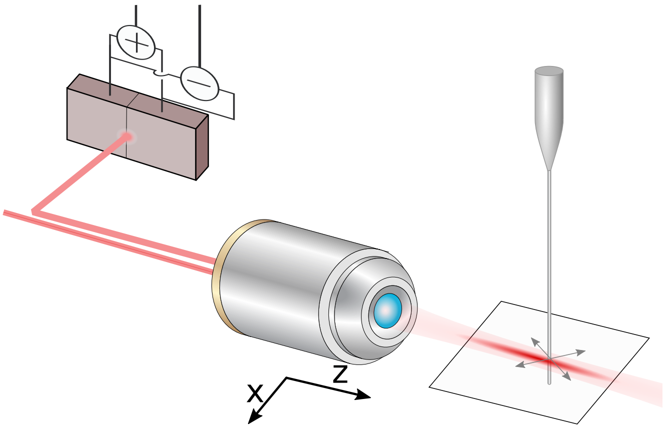

Fig. 1.17: Position readout based on the analysis of the nanowire back-scattered intensity fluctuations. The objective focuses the laser beam to a waist. Placed in the waist the nanowire reflects the light back in the objective that collimates the light into a beam whose intensity is measured on the split photodiode. The registered intensity fluctuations on each half depends on the position fluctuations of the nanowire in the waist area.

tive, the beam waist represents a small spot of high light intensity, with a lateral extension of approximately 500 nm which allows to increase the amount of reflected light from the nanowire. With the objective and thus the laser beam being fixed in space, we bring in the nanowire mounted on a translation stage which is used to piezo-position the nanowire within a 3D volume in the waist area. The objective collects the reflected light scattered by the nanowire and a $^{90}/_{10}$ beam splitter allows 90% of the reflected light to reach the split photodiode that measures the reflected intensity. The detected intensity at the two halves of the photodiode depends on the position of the nanowire in the beam waist such that its horizontal movement is encoded as changes of the two photocurrents measured on left and right halves of the split-photdiode.

1.3.1 The measurement position

With the two signals from the split-photdiode we have access to two linearly independent measurement vectors as we now explain. We calculate the sum and difference of the intensities acquired on the two photodiode halves, which depends on the nanowire position in the optical waist:

$$V_{\ominus,\oplus}(\mathbf{r}_0 + \boldsymbol{\delta}\mathbf{r}(t)), \tag{1.69}$$

where $\mathbf{r}_0$ is the nanowire rest position, which can be piezo scanned, and where $\boldsymbol{\delta}\mathbf{r}(t)$ are the vibrations of its vibrating extremity. Each measurement channel is separated into a low frequency *LF* and a high frequency *HF* output with a typical cutoff of 1 kHz. The low frequency channels will thus record

$$V_{\ominus,\oplus}(\mathbf{r}_0),$$

which permits to image the optical waist with the nanowire and to identify its location in space. The HF outputs of the photodiode will record the rapid nanowire fluctuations, which can be expressed at first order as:

$$\delta V_{\ominus,\oplus}(t) = \boldsymbol{\delta}\mathbf{r}(t) \cdot \nabla V_{\ominus,\oplus}(\mathbf{r}_0). \tag{1.70}$$

As such, each measurement channel realizes a projective measurement of the nanowire deflection along a measurement vector given by:

$$\boldsymbol{\beta}_{\ominus,\oplus} \equiv \nabla V_{\ominus,\oplus}(\mathbf{r}_0) \tag{1.71}$$

Projective measurement

which are simply the spatial gradients of the signals recorded on the DC outputs of the photodiode amplifier. From the expressions defined above, follow the projected quantities

$$\delta r_{\ominus,\oplus}(t) = \mathbf{e}_{\ominus,\oplus} \cdot \boldsymbol{\delta}\mathbf{r}(t) \tag{1.72}$$

with a projection vector $\mathbf{e}_{\ominus,\oplus} = \frac{\nabla V_{\ominus,\oplus}(\mathbf{r}_0)}{|\nabla V_{\ominus,\oplus}(\mathbf{r}_0)|}$.

The colormaps of the two plots in Figure 1.18 show the DC sum and difference signals measured while scanning the nanowire in the transverse horizontal plane. The plotted quantities represent the static reflection signals measured as voltages $V_{DC}^{\oplus}$ and $V_{DC}^{\ominus}$ after calculation and amplification of sum and difference of the signals recorded on the photodiode halves. The quiver plots in Figure 1.18 draw the local measurement vectors of both channels calculated as the gradient of the upper maps. Following the optical axis along a vertical line in the centre of the image, the local intensity gradient of the difference channel is visibly biggest perpendicular to this line, whereas for the sum channel, we can identify two positions just before and after the waist where the variation is strongest along the optical axis. It is this spot which we choose as measurement location for the nanowire due to the perpendicularity of the measurement vectors.

The readout vectors $\boldsymbol{\beta}_{\ominus,\oplus}$ can be expressed in terms of the local intensity gradient in the x,z basis

$$\boldsymbol{\beta}_{\ominus,\oplus} = \begin{pmatrix} \frac{\partial V_{\ominus,\oplus}}{\partial x} \\ \frac{\partial V_{\ominus,\oplus}}{\partial z} \end{pmatrix}. \tag{1.73}$$

Measurement vectors

The lengths of the vectors $|\beta_{\ominus,\oplus}|$ translate the projected displacement $\delta r_{\ominus,\oplus}$ of the nanowire in the direction $\mathbf{e}_{\ominus,\oplus}$ to a change of intensity. The displacements $\delta r_{\ominus,\oplus}$ can then be distorted to reconstruct the nanowire motion projected on the orthogonal (x,z) basis, as:

$$\begin{pmatrix} \delta r_\ominus \\ \delta r_\oplus \end{pmatrix} = \begin{pmatrix} \cos\beta_\ominus & \sin\beta_\ominus \\ \cos\beta_\oplus & \sin\beta_\oplus \end{pmatrix} \begin{pmatrix} \delta r_x \\ \delta r_z \end{pmatrix}. \tag{1.74}$$

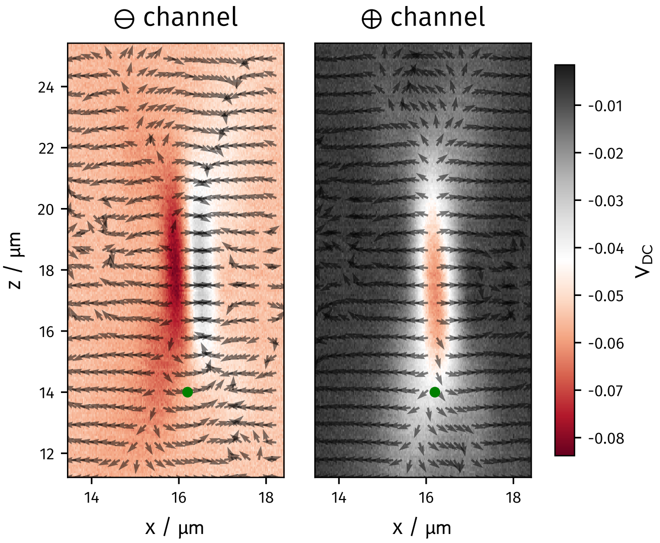

Fig. 1.18: The difference (left) and sum (centre) signals acquired with the split photodiode during a scan of the nanowire through the optical beam waist. The measured light is the reflection from the nanowire as it scans through the waist. The nanowire dwell time is in the order of 10 µs. The right plot (bottom/row) shows the according measurement vector of the two signals. The green spot marks the location where near perpendicular readout vectors can be obtained. This is also the measurement location.

Here, $\beta_{\ominus,\oplus}$ denotes the angle between measurement vector and the x axis. To calculate the projective displacement in the cartesian lab coordinate space we thus apply the inverse transformation of (1.74)

Reconstruction of the NW displacement in x, z

$$\begin{pmatrix}\delta r_x\\ \delta r_z\end{pmatrix} = \frac{1}{\cos\beta_\ominus \sin\beta_\oplus - \cos\beta_\oplus \sin\beta_\ominus}\begin{pmatrix}\sin\beta_\oplus & -\sin\beta_\ominus\\ -\cos\beta_\oplus & \cos\beta_\ominus\end{pmatrix}\begin{pmatrix}\delta r_\ominus\\ \delta r_\oplus\end{pmatrix},$$

which is only defined when the measurement channels are not colinear ($\boldsymbol{\beta}_\ominus \cdot \boldsymbol{\beta}_\oplus \neq 0$). The precise determination of the measurement vectors is an essential ingredient of the signal analysis in 2D. This is the subject fo the following sections.

1.3.1.1 Static determination of the measurement vector

After a coarse positioning of the nanowire in the optical waist, assisted by the maps in Figure 1.18, exactly knowing the local measurement vector requires a finer local estimation since the DC maps can suffer from deformations induced by the system inertia and there can be drifts in the nanowire position with respect to the optical waist. To do so, we realize a local map around the chosen position, of the DC voltages $V_{DC}^{\oplus}$ and $V_{DC}^{\ominus}$ following a technique established in [28, 44]. It is based on a displacement of the nanowire along different discrete positions on a grid around the chosen working point. Figure 1.19 illustrates the positions of the nanowire at which measurements are performed and the trajectory followed by the measurement algorithm, a square-spiral trajectory. The step size can be adapted and is typically of the order of 10 nm to 20 nm.

To decrease uncertainty errors, the trajectory is usually repeated multiple times for averaging. A third order polynomial regression of the two local maps $V_{DC}^{\ominus}(x_i, z_i), V_{DC}^{\oplus}(x_i, z_i)$ yields the local intensity gradients $\nabla V_{DC}^{\ominus}(x_0, z_0)$ and $\nabla V_{DC}^{\oplus}(x_0, z_0)$, which are the above introduced measurement vectors. For an improved estimation of the gradients, the interpolation of $V_{DC}^{\oplus,\ominus}$ is also performed in coordinate frame (x', z') rotated by 45°. From the quantities $\partial_{x'} V_{DC}^{\oplus,\ominus}, \partial_{z'} V_{DC}^{\oplus,\ominus}$, one can then also calculate the gradients in the unrotated frame. The mean of both estimations is finally chosen as measurement vector [44].

When using a reliable and well calibrated piezo positioning stage, the nanowire positions explored during the calibration protocol are reliably known, and the residual error can be limited to the intrinsic optical and physical measurement noises. The measurement uncertainty is different on both measurement channels. Due to the large gradient of the difference signal intensity in the direction perpendicular to the optical axis, this is the signal with smallest slope uncertainty, whereas the smaller slope obtained along the optical axis of the sum channel causes a higher uncertainty on the sum signal. As such, the best SNR are in general obtained on the difference channel, which also presents the interest of suppressing common technical noises.

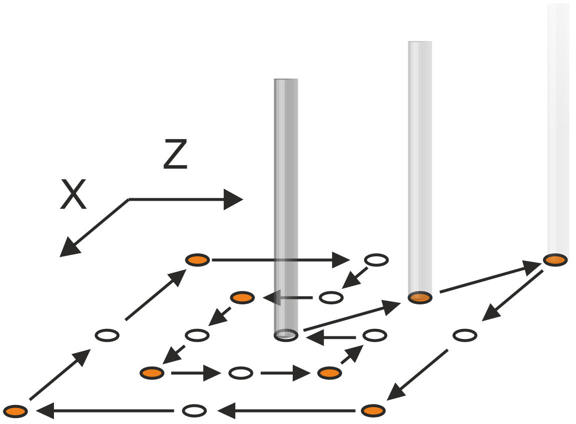

Fig. 1.19: Illustration of the nanowire's path around the central measurement position in the laser beam's waist followed during the readout sensitivity calibration protocol. A measurement of $V_{\oplus}^{DC}$ and $V_{\ominus}^{DC}$ on a spatial grid provides the local intensity gradients from which the measurement vectors are determined.

Several series of the low noise photodiode amplifiers were produced in *Institut Néel* by *Daniel Lepoittevin*, with a conversion gain varying from $2000\,\mathrm{V\,A^{-1}}$ to $2\cdot 10^{6}\,\mathrm{V\,A^{-1}}$, so that we can adapt the detector to the type of power needed in the experiment. For a typical probe laser power of 10 µW to 100 µW the recorded voltages after the photodiode's electronics are in the order of 10 mV to 1000 mV with gradients $\left|\nabla V_{\oplus,\ominus}\right| = 1\cdot 10^{4}\,\mathrm{V\,m^{-1}}$ to $1\cdot 10^{6}\,\mathrm{V\,m^{-1}}$ with an error of about 10 % due to the uncertainty on the sum channel's measurement vector.

The thermal noise of the nanowire, spreading on a few nm (rms), is thus converted into voltage fluctuations of a 10 µV to 100 µV (rms), which can be efficiently sampled, for instance with spectrum analyzers. When, instead, one drives the nanowire, we typically use oscillation amplitudes spanning over 1 nm to 100 nm, which then corresponds to voltage amplitude in the 10 µV to 10 mV range.

1.3.1.2 Dynamic determination of the measurement vector

While the interpolation of the intensities measured at positions close to the measurement location provides a statistically stable estimate of the local readout vectors, the repetitions of the figure of about five times and an acquisition time per point in the order of 10 ms make it too slow to be used as a rapid sensitivity estimator during force field cartography.

In order to have faster access to the local measurement vectors, we implemented a dynamic protocol based on homodyne modulation technique where the piezos controlling the x and z axes are individually driven at two frequencies, $\omega_{\beta,\mathrm{x}}$ and $\omega_{\beta,\mathrm{z}}$, so that the nanowire follows a driven trajectory. $\omega_{\beta,\mathrm{x}}$ and $\omega_{\beta,\mathrm{z}}$ are at low frequencies, around 80 Hz so that they remain inside the transmission band of the photodiode's DC channels,in the flat response band of the piezo drive and at very low frequency compared to the first mechanical resonances, so that the nanowire reacts without undergoing significant deformations. Both frequencies are separated by 10 Hz to 20 Hz in order to spectrally separate the effect of the two driven movements along x and z. Figure 1.20 illustrates the movement of the nanowire during the calibration protocol where the amplitudes $\delta r^{\beta}_{x,z}$ applied on each axis are typically set to an amplitude ranging from 10 nm to 30 nm, where a larger value on the z axis ensures a better measurement of the slower slope along z when using smaller light intensities. The low frequency signals recorded on the photodiode's sum and difference channel are each demodulated at the two driving frequencies to directly obtain the local gradient of the reflection maps, which are encoded in the amplitude of the four demodulated signals:

$$
\begin{aligned}
V_{\ominus,\oplus}\big(\mathbf{r}_0 + \delta r_{\beta,x} \cos \omega_{\beta,x} t \mathbf{e}_x + \delta r_{\beta,z} \cos \omega_{\beta,z} t \mathbf{e}_z\big) \approx \\
V_{\ominus,\oplus}(\mathbf{r}_0) + \partial_x V_{\ominus,\oplus} \cos \omega_{\beta,x} t + \partial_z V_{\ominus,\oplus} \cos \omega_{\beta,z} t.
\end{aligned}
\tag{1.75}
$$

Due to the frequency dependence observed in the response of our piezo actuators (unloaded resonant frequency of approx 500 Hz), a static reference measurement taken as described above, is used to calibrate the dynamic homodyne measurement. The four gradients obtained from this static measurement are compared to those of the dynamic protocol to find a calibration scale for each axis. To obtain the most reliable results, such a calibration should be performed at a position with high signal intensities and a stable static measurement. In addition, the acquisition time for of both calibration measurement (static and dynamic) are increased to 3 s to 4 s for an improved result.

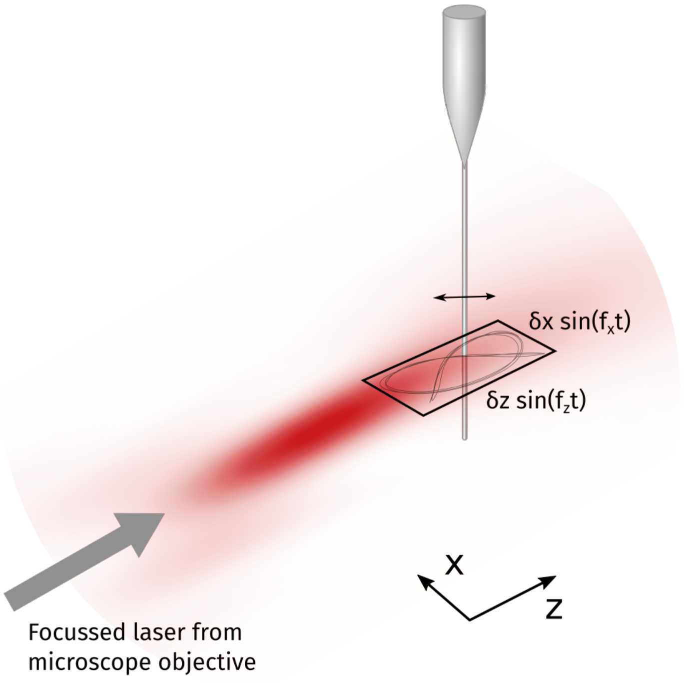

Fig. 1.20: Sketch of the nanowire's trajectory in the laser beam waist for the measurement of the readout vector. The bretzel like shape is a result of a common divider of the driving frequencies along x and z axes and a larger amplitude for the z direction. The size of the drawn trajectory is exaggerated and not to scale.

Thanks to the efficiency of the homodyne measurement, which allows a reliable extraction of the modulated signals strength out of a noise background, the measurement time to determine the readout vectors can be reduced from 5 s to 10 s to some hundreds of milliseconds. The measurement time is limited by the frequency of the sinusoidal drive and the filter bandwidth of the demodulation. Section 1.4.6.2 discusses in detail the measurement and the customized FPGA-based protocol developed for that purpose.

The sinusoidal movement of the nanowire can lead to the apparition of parasitic side peaks on the nanowire's mechanical resonances. Due to their splitting around 100 Hz and the narrow excitation band, the mechanical resonance remains almost unaltered during the dynamic measurement of the readout vectors. Figure 1.21 shows the thermal noise spectrum of a nanowires Brownian motion zoomed on the first mechanical resonance with dynamic readout vector measurement and without. In order to make the side peaks visible the nanowire had to be placed in a central position in the laser beam waist with a pronounced intensity gradient on the difference channel. However, we try to avoid running the dynamical measurement protocol when realizing sensitive measurements. The sensitivity calibration can be rapidly activated during long lasting scripts.

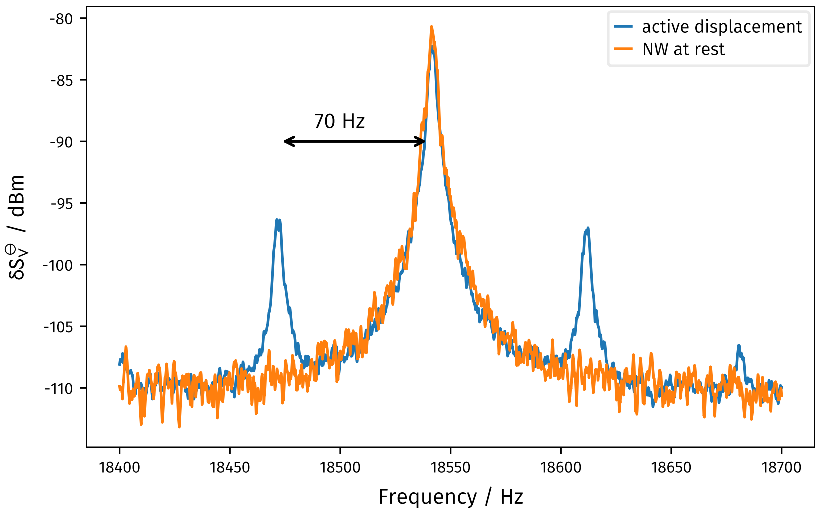

Fig. 1.21: Thermal noise spectrum of one mechanical nanowire resonance. The blue spectrum exhibits side peaks created by the sinusoidal displacement during the dynamic readout vector measurement. The 70 Hz splitting corresponds to the frequency of the displacement along the x-axis to which the difference channel is sensitive. The green curve plots the spectrum at rest.

1.4 Experimental implementation

Beside the optical detection, the scanning force microscopy setup requires a xyz-scanning system to move the sample with respect to the nanowire, a reliable driving force, and signal processing tools. The measurement should further be conducted in an isolated environment under low pressure to protect from external influences such as acoustic noise, temperature fluctuations and electric stray fields. Figure 1.22 outlines the experiment scheme with the described optical detection path and the nanowire and experiment positioning with respect to the laser beam (see Section 1.3) in the upper part of the figure (**a**). The probe laser light, focused by the microscope objective, is scattered by the nanowire that is micro-positioned in the beam waist. The reflected light is captured and rectified by the objective. On its way back, a beam-splitter reflects 90 % of the light onto the split photodiode where the difference and the sum of the photocurrents detected on both halves are calculated and amplified by the homemade photodiode amplifier. In the signal analysis part (**c**), a radar like signal analysis unit computes the projected displacement $\delta r_\mu(t)$ measured along an arbitrary angle μ out of the direct signals $\delta V_{\ominus,\oplus}(t)$ produced by the photodiode outputs. It is realized using the fast signal processing capacity of a field programmable gate array (FPGA). The raw or radar-rotated signals can then be further analysed, for instance in the frequency domain using a vector signal analyser (*VSA*) or recorded on time-sampling devices and employed in a response measurements (lock-in detectors or vector network analyzer (*VNA*)). The measured signal is also used to lock two phase locked loops (PLLs) whose frequencies are locked at the the mechanical resonance of the two nanowire eigenmodes using an external drive, which is in general the optical force that is exerted by the green pump laser (**b**). The nanowire and the

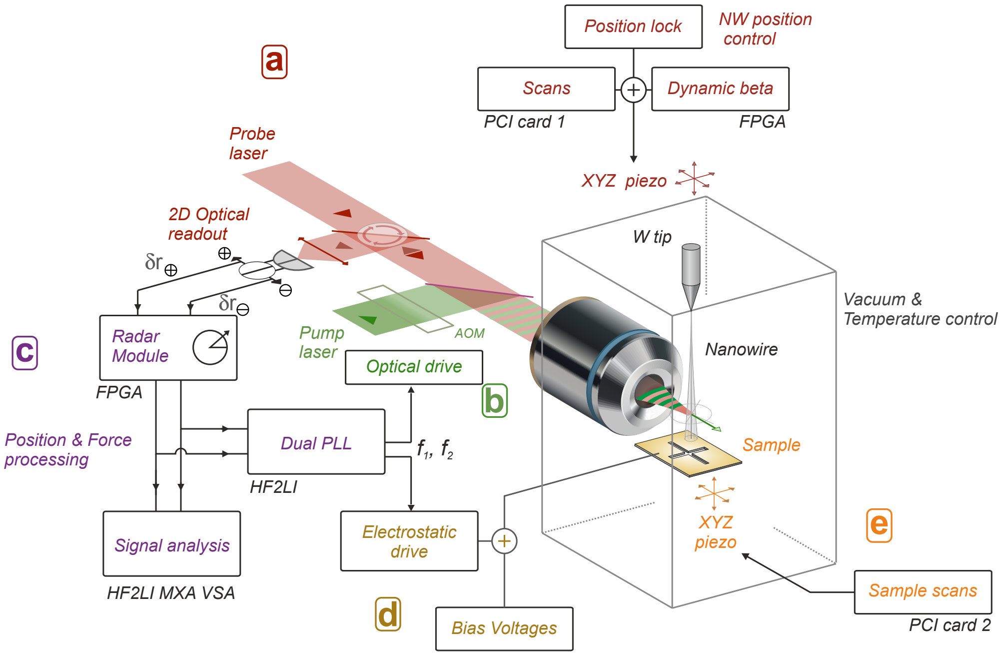

Fig. 1.22: Nanowire force nanoscopy setup with schematic representation of the scanning microscopy block (**a**,**e**), the optical drive (**b**), the homodyne detection and signal analysis block (**c**), and the electrostatic control block (**d**). A versatile control software orchestrates the ensemble of detection and control devices.

sample with their positioning systems (**a**, **e**) are located in a temperature and pressure controlled chamber. Besides positional control, electrodes placed on the nanostructured sample are use to generate, control and analyze the electrostatic force landscape between sample and nanowire (**d**).

This section's discussions cover the different blocks of the experimental setup starting with the optical setup for the optical pump and probe signals (Section 1.4.1). After the optics, Section 1.4.3 gives a description of the mechanical details of the nanowire and sample positioning systems and stabilization measures realized to optimize scan quality. The last three subsections cover the experiment control and data acquisition, emphasizing on the realization of automated scans and measurement scripts with a custom control software (Section 1.4.4) and the technical improvements realized on the base setup during the conduct of this work. In particular we describe the integration of a dual channel multi-frequency lock-in amplifier for realtime force field imaging that Section 1.4.5 covers in detail. Furthermore, the extension of the setup with a flexible FPGA based digital signal processing (DSP) module permits a wider range of measurements such as the continuous monitoring of the readout vector (Section 1.3.1.2), the radar like measurement of $\delta r_\mu(t)$ and the generation of artificial force field gradients (see Chapter 4). The operation principles of the FPGA instrument are subject of Section 1.4.6.

1.4.1 Optical setup

The readout laser is a 632 nm, 15 mW HeNe laser with its intensity adjusted by a half-wave plate and a polarizing beam splitter to discard a portion of the laser power. It is drawn at the left of the optical setup in Figure 1.23. The beam is subsequently widened by an inverse telescope arrangement of two lenses and stray light is removed using diaphragms. An afterwards placed 90:10 beam-splitter lets through only 10 % of the intensity towards the experiment chamber. In the backwards direction it reflects 90 % of the light reflected from the nanowire towards the detector and thus serves as a simple, polarization independent circulator. On the transmitted beam, another half-wave plate controls the probe beam polarization that is set onto the nanowire, before it passes a dichroic mirror used to combine the force driving (pump) and readout beams (probe). The combined beams then enter the vacuum chamber that hosts the experiment via a transparent window with anti-reflection coatings for the visible light on both sides. After passing another diaphragm to remove stray light, a 100×, 0.75 NA *Zeiss* microscope objective modified for vacuum operation with a working distance of 4 mm, focuses the readout beam to an approximately 500 nm wide optical waist in which the nanowire is piezo-positioned. The probe beam is focused to the same spot and we exploit the slight chromatic dispersion of the microscope objective, so that the optical waists' spots of both beams do not match perfectly along the optical axis and the green probe beam waist is around 3 µm before the red waist. This spatial arrangement allows to position the nanowire on the optical axis, just after the red probe waist, to benefit from a slope in the sum channel, while having the nanowire not too close to the green waist. As such, the green optical force is rather homoegeneous in the area an thus does not apply too large force gradients. This remark is also true for the readout beam – one needs to minimize its optical power so that it does not significantly perturb the nanowire eigenmodes.

Part of the reflected light (both, the pump's and probe's light) is collected by the microscope objective and exits the vacuum chamber, counter-propagating with respect to the readout laser. The signals are again spectrally separated by the dichroic mirror, and the probe light again arrives at the 90:10 beam-splitter, where it is deflects at 90% towards the detection units. Filters with a bandwidth centred around the 632 nm of the readout beam serve to suppress the residual green light that could be detected on the photodiode (this suppression is essential, especially when using lock-in detection that can detect a faint fraction of residual green, time-modulated light). After the filters, a (f=200 mm) lens focuses the light onto the split photodiode (*PD1* in Figure 1.23), using fine mirror mounts to balance the intensities on the photo-diode quadrants. A flipable mirror before the filter stage can also be inserted in the optical path to direct the reflected light to a CCD camera for visual alignment of the nanowire and the sample in the vacuum chamber. The propagation path of the readout laser is shown in the lower part of the setup illustration in Figure 1.23.

A second laser in the optical setup serves to exert a time-modulated, spatially homogeneous force to drive the nanowires eigenmodes as described in Section 1.1.3.1. We use a

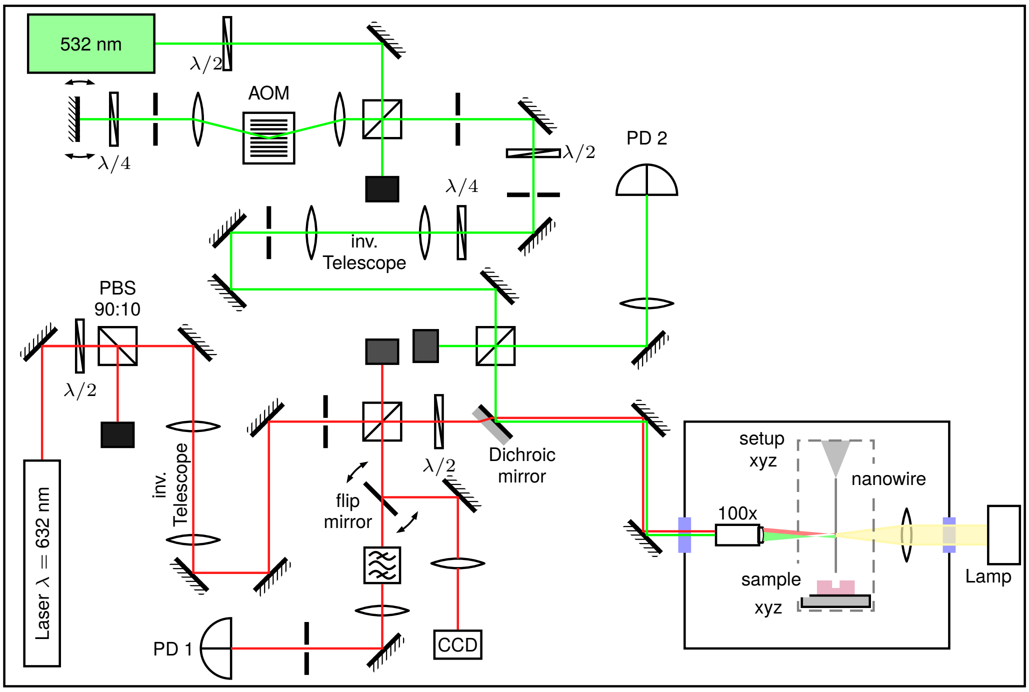

Fig. 1.23: Optical setup with the red readout laser in the lower part. The upper part illustrates the optical path of the excitation laser that is first modulated by a double pass through an AOM working on the first diffraction order. Readout and pump laser are then superposed and focussed by a 100x microscope objective inside the experiment chamber. The reflection of the readout laser is measured on the split photodiode PD1. Optional detection on the reflected green laser beam is possible on PD2.

100 mW green laser with a wavelength of 532 nm that can again be intensity regulated with a half-wave plate and a polarizing beam splitter. The transmitted part of the beam is then intensity modulated to generate a time modulated optical force. To do so, we employ a double pass acousto-optical modulator (*AOM*) scheme. A first lens focuses the light onto the AOM, next a pinhole selects the first order of the light diffracted by the acoustic wave, followed by a second lense which collimates the beam. A final mirror reflects the beam for the double pass configuration of the AOM in order to increase the modulation contrast on the first diffraction order. A quarter-wave plate in front of the mirror turns the polarization into a circular one during the first passage, while it transforms it back into an orthogonal linear polarization during the second passage. As such, the intensity modulated beam that comes back from the AOM, is now reflected by the polarizing cube. The light's polarization can be adjusted with a quarter- and half-wave plates positioned before a telescope that adjusts the beam width to match the microscope's back aperture. Similar to the readout beam, a 90:10 beam splitting cube discards 90% of the beam. The transmitted arm is then combined with the readout beam on the dichroic mirror that only reflects the green pump laser but transmits the red readout laser (cutoff wavelength = 581 nm). The pump beam then shares the same path into the chamber as the readout beam. An additional detection arm for the reflected green

light is installed after the 90:10 beam splitter and allows the collection of the pump light reflected by the nanowire, which then serves for optical alignment and can also be used to perform an optical readout of the nanowire motion. The relative positions of the red and green waists have to be precisely aligned, which can be achieved by adjusting their relative position along the z axis via the divergence of the incoming beams using the telescope lenses.

A white light source located on the right hand side of the vacuum chamber in Figure 1.23 illuminates the nanowire and the sample in the chamber from the back side as seen by the microscope objective. Via the alternative detection path, using the flip mirror, the CCD camera can record an image of the nanowire and the sample that is used for alignment.

1.4.1.1 The split photodiode detector

The dual photodiode detecting the reflected light from the nanowire is a *Hamamatsu* split photodiode that measures the intensity on two active areas **A** and **B,** separated by an inactive zone of 20 µm width. The photodiode has a quantum efficiency around 85 % at 632 nm. A homemade optimized electric circuit, designed and fabricated by *D. Lepoittevin*, splits the photocurrent produced by each quadrant into a high frequency and a low frequency channel using a high and a low pass filtering stage respectively. An additional electronic amplification increases the intensity of the electric signals before the sum and difference signals from the two active areas are created. Figure 1.24 lays out the operational scheme of the photodiode.

In the frequency domain, the conversion from power fluctuations $p^{A,B}[\Omega]$ detected on the two halves of the photodiode to the signals $V_{DC}^{\ominus}[\Omega], V_{DC}^{\oplus}[\Omega]$ for the low frequency and $V_{HF}^{\ominus}[\Omega], V_{HF}^{\oplus}[\Omega]$ for the high frequency channel follows the linear mapping:

$$\begin{pmatrix} V_{DC}^{\ominus} \\ V_{DC}^{\oplus} \end{pmatrix} = \begin{pmatrix} G_{DC}^{A\ominus} & -G_{DC}^{B\ominus} \\ -G_{DC}^{A\oplus} & -G_{DC}^{B\oplus} \end{pmatrix} \begin{pmatrix} p^{A} \\ p^{B} \end{pmatrix}, \tag{1.76}$$

where $G_{DC}^{A\ominus}[\Omega]$ determines the (amplified) contribution of the power registered on area A to the difference signal. The *HF* signal can as well be expressed with the same map as in (1.76), however due to different amplification gains, the conversion factors are different and depend on the analysis frequency.

Calibration The determination of the measurement vectors, as explained before, is performed on the *DC* channels (Section 1.3.1.1), while the dynamic movement of the nanowire is recorded using the *HF* signals. We thus need to calibrate the conversion factors from *HF* to *DC* signals, which do not depend on the analysis frequency. Using Equation 1.76 and an identical conversion matrix for the *HF* channels, we can connect

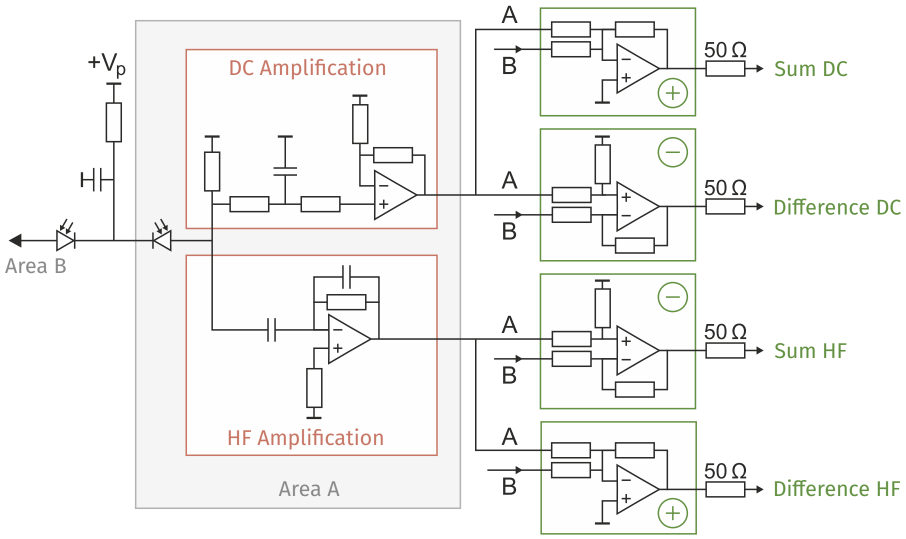

Fig. 1.24: Schematic electric layout of the split photdiode's amplification circuit. The amplification part is shown for area **A**. The same circuit design is used for area **B**. After a signal filtering step followed by current to voltage conversion stages (grey box) the sum and difference signals for low frequency (DC) and high frequency (HF) channels are computed.

how a given power modulation at a frequency Ω would be read out on the *HF* and *DC* measurements channels:

$$\begin{pmatrix} V_{HF}^{\ominus} \\ V_{HF}^{\oplus} \end{pmatrix} = \frac{-1}{G_{DC}^{A\ominus}G_{DC}^{B\oplus} + G_{DC}^{A\oplus}G_{DC}^{B\ominus}} \begin{pmatrix} -G_{HF}^{A\ominus}G_{DC}^{B\oplus} - G_{HF}^{B\ominus}G_{DC}^{A\oplus} & G_{HF}^{A\ominus}G_{DC}^{B\ominus} - G_{HF}^{B\ominus}G_{DC}^{A\ominus} \\ G_{HF}^{A\oplus}G_{DC}^{B\oplus} - G_{HF}^{B\oplus}G_{DC}^{A\oplus} & -G_{HF}^{A\oplus}G_{DC}^{B\ominus} - G_{HF}^{B\oplus}G_{DC}^{A\ominus} \end{pmatrix} \begin{pmatrix} V_{DC}^{\ominus} \\ V_{DC}^{\oplus} \end{pmatrix} \tag{1.77}$$

$$= \begin{pmatrix} \alpha_{--} & \alpha_{+-} \\ \alpha_{-++} & \alpha_{++} \end{pmatrix} \begin{pmatrix} V_{DC}^{\ominus} \\ V_{DC}^{\oplus} \end{pmatrix} \tag{1.78}$$

where the diagonal coefficients α_{++}, α_{--} are the *HF/DC* conversion factors while the off-diagonals α_{+-}, α_{-+} describe systematic acquisition errors due to imperfect electronic signal processing.

The calibration of the conversion coefficients requires a frequency response measurement of the photodiode using a signal of constant intensity p for the two channels *HF*, *DC* and the two active areas *A* and *B*. Here, the characterization of the channels in their respective measurement range of about 0 Hz to 150 Hz for the *DC* channel (used for static imaging, static beta measurements and dynamical beta measurements) and 1 kHz to 100 kHz for the *HF* channel (used for resonant or broadband mechanical readout) is particularly important.

We use the acousto-optical-modulator (AOM) introduced in Section 1.4.1 to modulate the probe laser that is directed and focused on a single half of the split-photodiode. The employed AOM has a flat response in the frequency range of interest (as shown in [28]), and hence the signal intensity at different frequencies can be directly compared.

Figure 1.25 shows a schematic illustration of the optical arrangement for the calibration of the split-photodiode. The AOM is driven by a modulated electrical signal generated by a *Zurich Instruments HF2* digital lock-in amplifier, which can be used as network analyser to realize frequency response scans. The *HF2* is also the main acquisition device for most of the dynamical measurements discussed in this work. It has an optional high-pass input filter and an optional 50 Ω input impedance that affect the measured transfer functions. We therefore perform the calibration measurement with all possible combinations of the input settings and all the photodiodes produced are similarly calibrated.

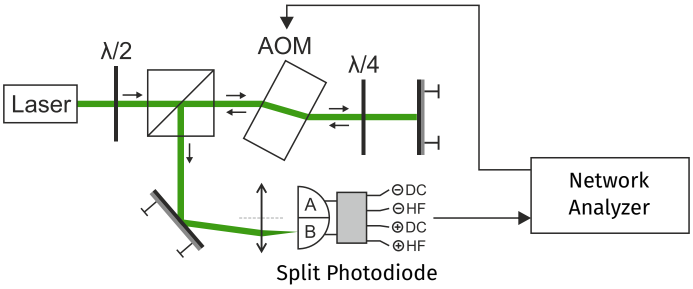

Fig. 1.25: Optical arrangement for the calibration of the split photodiode. The laser beam is modulated by the AOM and a network analyzer measures the response of the photodiode.

Iteratively measuring the response on all four output channels ($A\oplus, A\ominus, B\oplus, B\ominus$) with the laser focused first on quadrant A, then on B, we obtain the eight transfer functions $G^{A,B\oplus,\ominus}_{DC,HF}$ of the photodiode and the signal processing circuit with respect to the constant optical modulation $p[\Omega]$. Figure 1.26 compares the transfer functions for the two photodiode halves measured in the $\oplus$ and $\ominus$ channels using the input high-pass and 50 Ω impedance of the *HF2* for the *HF* channels of the photodiode.

The photodiode's transfer functions exhibit differences between the response to irradiation of areas A and B that are smaller than 1% in the target frequency range. This holds for both, amplitude and phase response of the diode and the electronic circuit, and reflects the quality of the device. We thus regard the photodiode as symmetric and use a single transfer function for both halves A, B per channel $\oplus, \ominus$.

1.4.2 Conversion of the photodiode signal to physical 2D displacement

Bringing together the photodiode response calibration and the measurement vector determination (Section 1.3.1.1), we can convert the acquired voltage fluctuations recorded on the sum and difference channels of the photodiode to a two dimensional displacement.

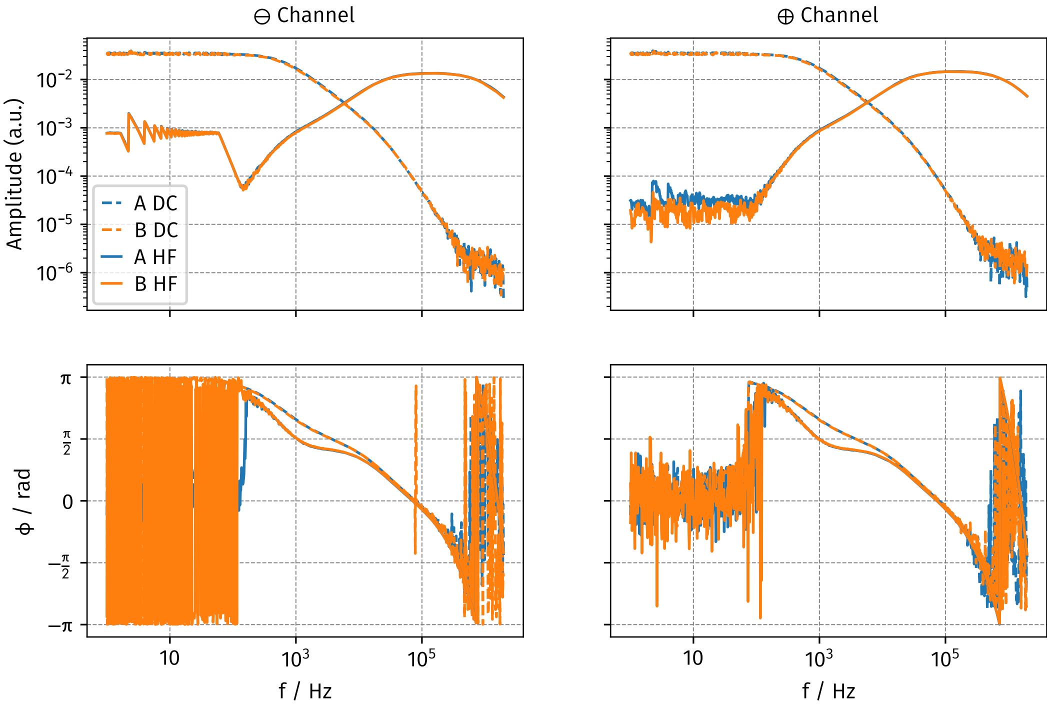

Fig. 1.26: Transfer functions of the split photodiode's output channels for a modulated optical signal on isolated active areas. 180° have been added to the phase of one quadrant on the ⊖ channel to take into account the sign.

In order to do so, the following equation converts the voltage fluctuation recorded on each channel into oscillation amplitudes (in m):

Displacement amplitude in meter

$$\delta r_{\ominus}[\Omega] = \frac{\delta V^{\ominus}[\Omega]}{|\nabla V^{\ominus}_{DC}|_{\omega_\beta}} \frac{G^{\ominus}_{DC}(\omega_\beta)}{G^{\ominus}_{AC}[\Omega]}. \tag{1.79}$$

Here, ω_β is the frequency at which the measurement of the readout vector is realized. It is around 80 Hz to 100 Hz for the dynamical protocol, and is zero for the static protocol. The quotient $HF/DC = G^{\ominus,\oplus}_{AC}[\Omega]/G^{\ominus,\oplus}_{DC}(\omega_\beta)$ is the conversion factor between low frequency *DC* and high frequency *HF* channel of the photodiode. The correction factor for the employed photodiode is shown in Figure 1.27.

The gradient $|\nabla V_{DC}|$ is obtained from the calibration of the measurement vector and corresponds to the length of the measurement vector $|\beta|$. For a measurement of the thermal noise spectrum the formula can be rewritten in terms of the power spectrum:

$$S_{\delta r_{\ominus}}[\Omega] = \frac{S_{\delta V^{\ominus}}[\Omega]}{|\nabla V^{\ominus}_{DC}|^2} \left(\frac{G^{\ominus}_{DC}(\omega_\beta)}{G^{\ominus}_{AC}[\Omega]} \right)^2. \tag{1.80}$$

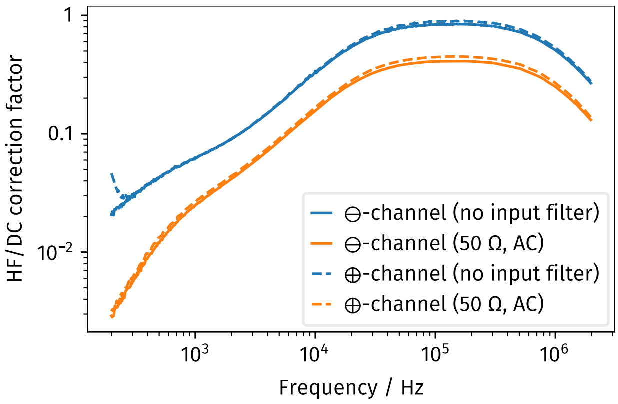

Fig. 1.27: The *HF / DC* calibration curve for the utilized photodiode is shown for the case of no input AC filter on the Zurich Instruments lock-in (blue) and for the most used configuration of 50Ω input impedance plus AC filter. The two quadrants are depicted as solid (⊖) and dashed (⊕) lines. While the flat region with the highest response is not located at the ideal frequency range for the nanowires employed (between 5 kHz to 100 kHz), the photodiode is still one of the devices with the best amplification characteristics available at the time of the measurements.

The calibrated displacements $\delta r_{\ominus,\oplus}$ can be converted to the experimental coordinate system using Equation 1.74. For δr_x we have as complete conversion expression:

Displacement in laboratory coordinates

$$\delta r_x[\Omega] = \frac{\sin\beta_\oplus \, \frac{\delta V^{\ominus}[\Omega]}{|\beta_\ominus|} \frac{G^{\ominus}_{DC}(\omega_\beta)}{G^{\ominus}_{AC}[\Omega]} - \sin\beta_\ominus \, \frac{\delta V^{\oplus}[\Omega]}{|\beta_\oplus|} \frac{G^{\oplus}_{DC}(\omega_\beta)}{G^{\oplus}_{AC}[\Omega]}}{\cos\beta_\ominus \sin\beta_\oplus - \cos\beta_\oplus \sin\beta_\ominus}, \tag{1.81}$$

and a similar one for δr_z.

The preceding paragraphs introduced how a two-channel, optical reflection measurement can provide the positional displacement of a nanowire $\delta\mathbf{r}$ in two dimensions. This technique is used to measure the oscillation trajectories $\delta\mathbf{r}(t)$ in the presence of external force fields. The next section presents a mechanical setup that permits to perform these measurements in a scanning probe microscopy operation mode.

1.4.3 Positioning system

A stable and well controlled nanowire positioning is crucial since the optimal measurement location in the laser beam waist has a size of the order of some tens of nanometers. Thus, the positioning of the nanowire with respect to the laser beam, and independently with respect to the sample require nanometer resolved positioning systems.

The mechanical setup builds around the fixed microscope objective which focuses the laser to a narrow waist in which the nanowire is piezo-positioned. However, the most critical positioning is the relative position of nanowire and sample, also, they need to be moved together during the alignment of the nanowire in the laser beam, so that the force sensing experiment is not altered. Additionally, the sample needs to be positioned and scanned with respect to the nanowire, which requires a second, independent *xyz*-positioning stage. The design of the setup is based on a large three axis piezoelectrical positioning system (*Physik Instrument 733DD*) that supports the nanowire mount together with the second, smaller three axis piezoelectrical positioning system that carries the sample holder (*attocube* positioning stage). The larger stage controls the position relative to the laser whereas the smaller stage can scan the sample beneath the nanowire. When we move the sample, the static force experienced by the nanowire can vary, causing a static deformation, which is compensated by the main piezo so that the nanowire stays at the optimal measurement position (position tracking).

In order to guarantee reproducible translations and mechanical stability over longer measurements, thermal expansion induced by, for instance, day-night cycles needs to be avoided. The support of the large piezo stage and all the scanning probe apparatus is therefore temperature stabilized by four Peltier devices that support the thermalized mounting plate of the positioning system. The Peltier devices' cold sides are connected to a large copper body functioning as thermal load. A PID controller acting on the temperature of the positioning stage stabilizes the systems temperature and compensates fluctuations of the room temperature by applying a controlled current on the Peltier devices. Figure 1.28 illustrates the installation of the Peltier devices and the thermal isolation of the scanning setup.

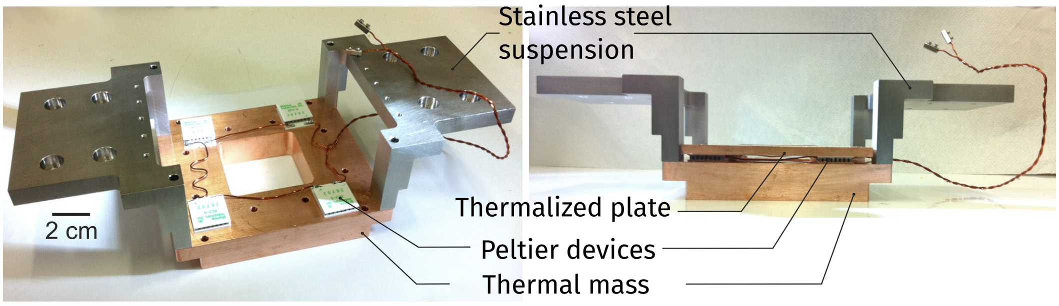

Fig. 1.28: Photograph of the thermal control elements of the experiment. The stainless steel suspension elements are supported by two coarse, motorized, positioning stages. The bottom copper piece acts as thermal reservoir for the four Peltier devices that are glued with their cold sides onto it. The thermally controlled upper copper plate is added in the right side view photograph. This plate supports the two piezoelectrical positioning stages for nanowire and sample so that both systems are thermally stabilized.

Even though the setup is thermally stabilized, changes in temperature, pressure or the static force on the nanowire can lead to a displacement of the nanowire in the laser beam, causing a change of the measurement vectors. We correct for these drift effects by applying a feedback – computed on either amplitude or gradient of the DC signal of the photodiode $V^{DC}_{\oplus,\ominus}$ – on the main piezo stage to stay at a constant relative position. As the width of the laser waist in the range of 500 nm is much smaller than its length (<1 μm), the readout vector along the x-axis (perpendicular to the propagation direction) is much steeper than along the z-axis. Hence, a small displacement in x has a larger impact on the measured signal in the $\oplus$-channel than along the z-axis where the intensity gradients measured on both channels are much flatter. It is therefore mostly sufficient to lock the x position of the nanowire with a stable PID that only acts on the piezo stage along the x-axis.

The whole mechanical setup is shown in the photographs in Figure 1.29 where 1.29a gives an overview of the arrangement of the experimental chamber which contains the microscopy setup and the optical setup outside the chamber. The temperature control stage can be seen in 1.29b where it is mounted on the coarse position control stages, carrying the scanning setup. Panels 1.29c and 1.29d present a closer view on the scanning setup with the nanowire support in front of the microscope objective. The dome like nanowire support permits to correct a nanowire tilt independent of the direction of a tilt within a range of ±15° by rotation of the tungsten tip around its own axis to get the tilt angle in the direction perpendicular to the optical axis, and consequent inclination of the nanowire support following the curvature of the ceramic nanowire mount. This specialized mount has been added to the setup towards the end of this project so not all measurements conducted in this work could benefit from its advantages.

1.4.4 Control Software

Nanowire force microscopy requires the synchronization of different scan and measurement protocols. Since the two-dimensional nanowire force microscopy is a non-standard scanning probe technique, it requires an adapted control software that has been designed and realized in previous projects ([28, 44]) and still is under continuing development.

The main key-requirements for the control program that runs under the internal name *Nano-Imaging Lab* (NIL) are the 3-axis scan with realtime imaging of the acquired data. As scan control device we use a NI USB-DAQ card (connected to a Windows host system[4]) with four analog outputs, three of them controlling the three axis movement, and ten high impedance DC input channels. Furthermore, the software should integrate per point operations, such as spectrum acquisition or response measurements using additional devices as Spectrum and Network analyzers. The low mechanical frequency of the nanowire's oscillations in the kHz regime and their high Q factor often require long acquisition times so that the measurement also needs to be actively stabilized.

The modular program layout consists of three main classes of modules that are organized into three layers: interface, script and instrument layer. For each experimental setup one can use one or multiple instances, adapted to their tasks by activation/deactivation of the required modules. Figure 1.30 illustrates this software layout.

---

[4]

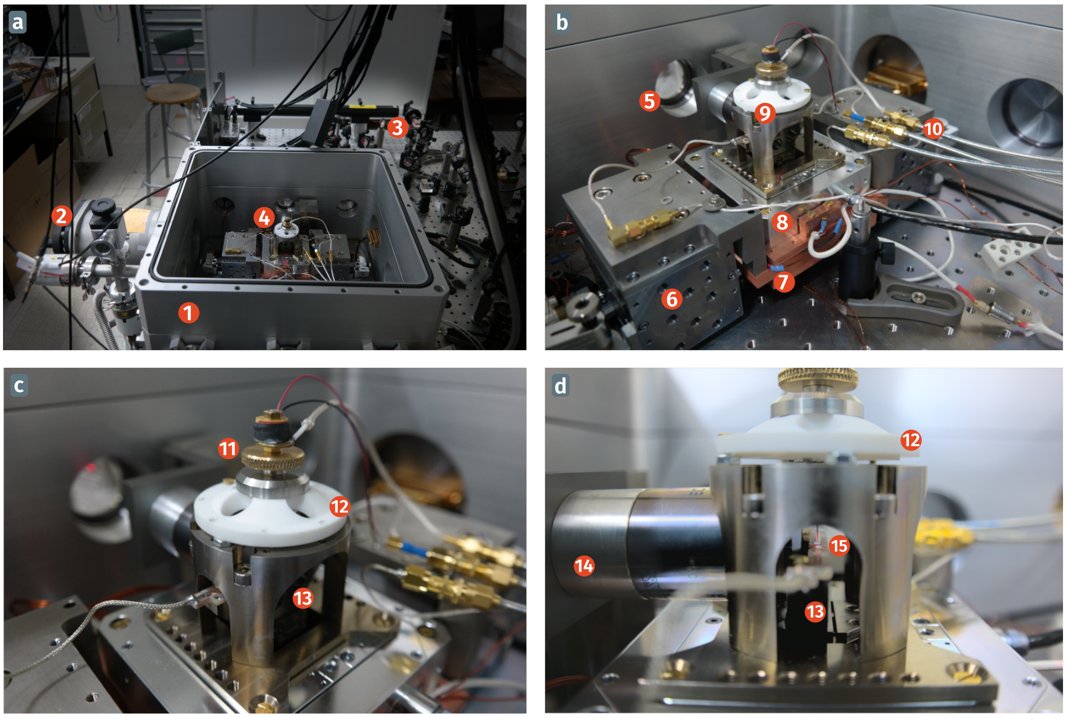

Fig. 1.29: The experiment chamber (1) on the optical table with the detection setup (3) is shown in panel (**a**). At the left, the vacuum setup (turbo pump, gauges and valve) are discernible (2). In the center of one wall of the chamber is a transparent window (4) through which the readout and pump laser are directed onto the experiment. In the chamber one can see the positioning setup with the mounted nanowire holder (round kiosk with the white top), which are shown from closer distance in the photograph in (**b**). In front of the window (5), one sees a part of the microscope objective holder. The coarse positioning setup of the experiment relative to the sample (6) consists of the symmetric arrangement of two *xyz*-micro-positioning stages that carry a central copper block on which the temperature regulating Peltier devices are located (7). The fine positioning is done with the three axes piezo stage (8) that supports the nanowire kiosk (9) and the sample positioning system (not visible as it is in the interior of the piezo stage (8)). The nanowire holder and samples can be electrically biased via electrical feedthroughs to which the cables (10) are connected. Panels (**c**) and (**d**) show a closer view of the nanowire kiosk. The nanowire is mounted at the top and held in place by a special ceramic mount (12) which allows to change the angle of the nanowire while keeping the nanowire centralized and isolates the nanowire mount electrically. The nanowire position is fixed with the big screw (11) which is electrically connected to the tungsten tip and whose potential is controlled via the coax cable that is connected to the screw. At the very top, a piezo is mounted which can act as mechanical drive of the nanowire as alternative to the green pump laser. Here, the nanowire supports needs to be elevated from the kiosk by additional spacers due to a particularly long tungsten tip. The sample holder (13) has space for two samples that can be mounted on each side. In (**d**) one can see how light that is focussed by the microscope objective (14) is reflected from the tungsten tip beneath which the two inversely mounted AFM cantilevers are visible (15).

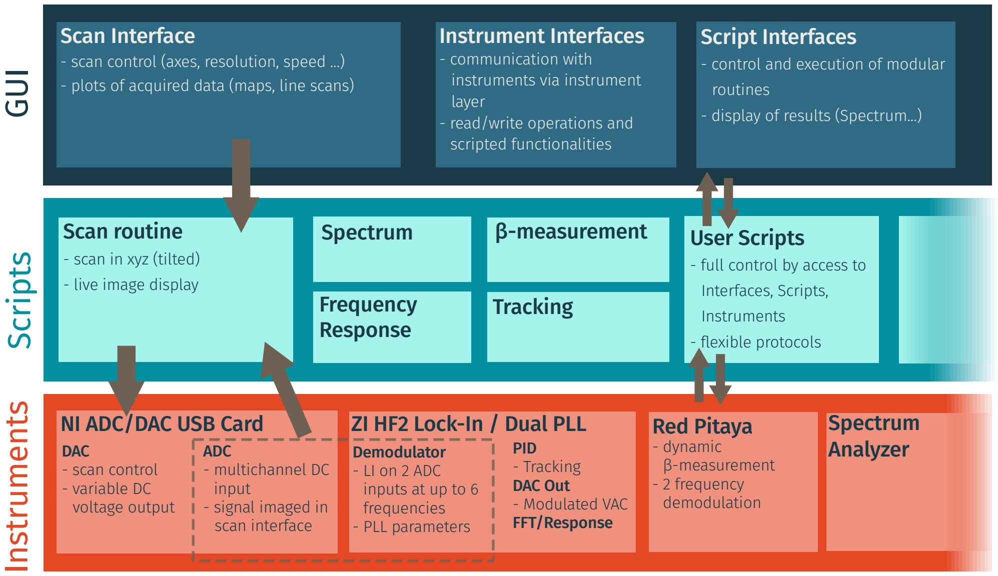

Fig. 1.30: Structural illustration of the three software layers in the experiment control function. The GUI layer contains user interfaces for the main scanning functionality, direct interaction with instruments and the execution of scripts using multiple instruments. The script layer contains scripts for single tasks or user-scripts that can comprise complex measurement protocols and have access to all available instruments and interfaces. The instrument layer is the interface with the devices and makes their functionalities accessible to the interfaces and scripts. The dashed box highlights the instruments that can be used for live imaging during standard scans (illustrated by arrows connecting the scan elements). The arrows from and to the user script block demonstrate its ability to access all available interface and instrument modules.

The *interface* modules contain all user interfaces amongst which the position and scan control interfaces, and the imaging interface form a basis required for all program instances. Depending on the experiment type, the interface layer also contains user interfaces for the used instruments such as spectrum- or network analyser and interfaces for measurement scripts. The *scripts* modules form the second layer of the software and contains measurement scripts for protocols such as different scan types (linear, 2D maps with additional parameter scans, realtime monitoring), the determination of the measurement vector (compare Section 1.3.1.1) or custom user scripts. The user scripts have access to all available interfaces and instruments and can also call other scripts, they are therefore the ideal tool to orchestrate complex measurement protocols. The third layer contains all *instrument* drivers with implementation of communication and measurement protocols adapted to each instrument and use in the experiments.

Each experiment can require a different set of equipment. For this reason the program configuration for a specific experiment needs to be easily adjustable. A *Mother* program generates configuration files that determine the available modules and their configuration for each experiment program. The idea of this modular configuration is sketched in Figure 1.31.

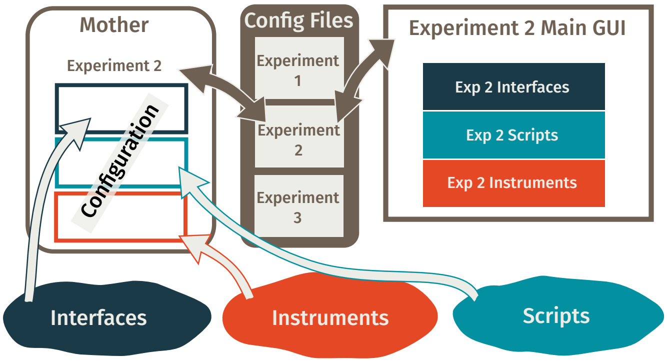

Fig. 1.31: Illustration of the creation process of an instance of the experiment control software. The *mother* program writes a config file based on the available modules in the three pools of interface, instrument and script pools. A standardized main program then accesses the config file and creates the experiment interface.

The typical nanowire force microscopy setup uses two positioning systems as shown in Figure 1.22, one for the positioning of the nanowire and the sample with respect to the readout laser, and one for the actual scan of the sample itself. Two instances of the measurement program control these two positioning systems independently. Figure 1.32 shows a screenshot of the sample control interface, taken after an electrostatic force field measurement at a given bias voltage, above a sharp conical electrode. The realtime display of the force field characteristics such as the divergence (first plot in the screenshot) has been a crucial achievement of this project. The key points of its realization are discussed in the following section.

1.4.5 Flexible resonant acquisition by integration of the HF2LI-PLL

The previous program version described up to this point was limited to the imaging of static signals acquired with the *NI USB-DAQ* card, all the dynamical signal had to be acquired with separate devices, such as network or signal analyzers. During this project we integrated a two-channel lock-in amplifier with demodulation at up to six frequencies (*Zurich Instruments HF2-LI*) into the control software, expanding largely its functional capacities. This added a variety of new measurement possibilities such as spectrum analysis, frequency or parameter sweeps, and frequency tracking with two independent phase-locked loops (PLLs). The software has been modified so that live imaging is now possible using the demodulation results as data, including arithmetical operations and statistics on the acquired data. Together with the dual PLL, this forms the base for two-channel lock-in measurements of the nanowire resonances and realtime imaging of the force field structure described in Section 1.2.

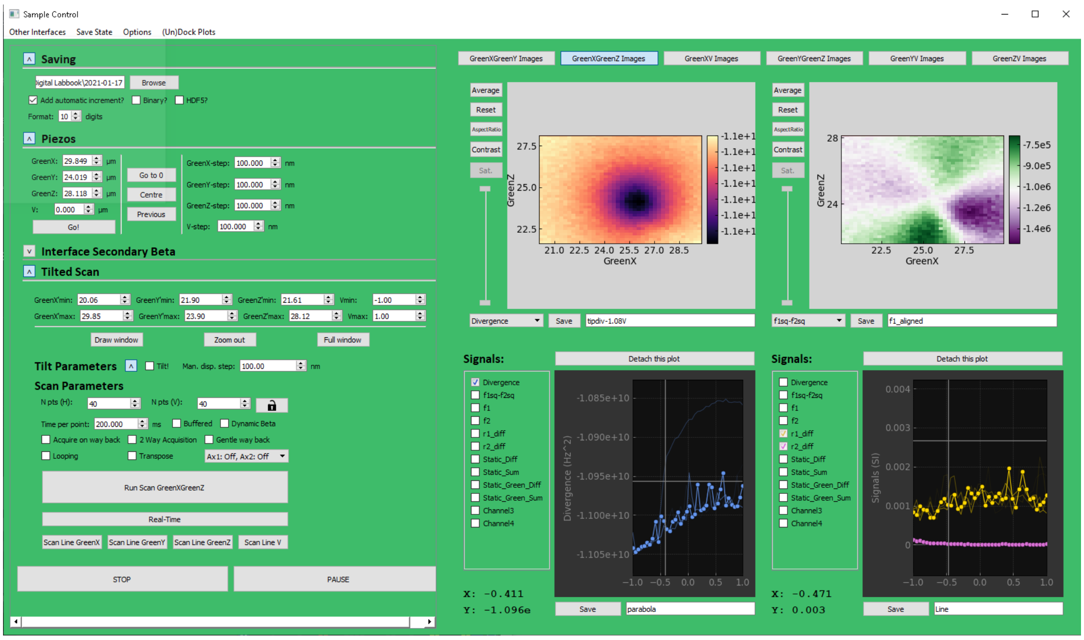

Sample Control

Saving

igital Labbook\2021-01-17

☑ Add automatic increment? ☐ Binary? ☐ HDF5?

Format: 10 digits

Piezos

GreenX: 29.849 µm

GreenY: 24.019 µm

GreenZ: 28.118 µm

V: 0.000 µm

GreenX-step: 100.000 nm

GreenY-step: 100.000 nm

GreenZ-step: 100.000 nm

V-step: 100.000 nm

Interface Secondary Beta

Tilted Scan

GreenX'min: 20.06 GreenY'min: 21.90 GreenZ'min: 21.61 Vmin: -1.00

GreenX'max: 29.85 GreenY'max: 23.90 GreenZ'max: 28.12 Vmax: 1.00

Tilt Parameters ☐ Tilt! Man. disp. step: 100.00 nm

Scan Parameters

N pts (H): 40 N pts (V): 40

Time per point: 200.000 ms ☐ Buffered ☐ Dynamic Beta

☐ Acquire on way back ☐ 2 Way Acquisition ☐ Gentle way back

☐ Looping ☐ Transpose Ax1: Off, Ax2: Off

Divergence Save tipdiv-1.08V

f1sq-f2sq Save f1_aligned

Signals:

☑ Divergence
☐ f1sq-f2sq
☐ f1
☐ f2
☐ r1_diff
☐ r2_diff
☐ Static_Diff
☐ Static_Sum
☐ Static_Green_Diff
☐ Static_Green_Sum
☐ Channel3
☐ Channel4

X: -0.411
Y: -1.096e

Save parabola

Signals:

☐ Divergence
☐ f1sq-f2sq
☐ f1
☐ f2
☑ r1_diff
☑ r2_diff
☐ Static_Diff
☐ Static_Sum
☐ Static_Green_Diff
☐ Static_Green_Sum
☐ Channel3
☐ Channel4

X: -0.471
Y: 0.003

Save Line

Fig. 1.32: Screenshot of the scan interface after having realized a 2D horizontal a scan of the nanowire above a sharp electrode at a given bias voltage. Image plots show the divergence and the difference of the squared eigenfrequencies of the nanowire used for positioning in space and the determination of the eigenmode orientations.

The setup of the main instrument parameters is implemented in the instrument driver and interface layers of the experiment program so that the typical measurements can be quickly performed using the corresponding user interfaces and can easily be used in user scripts. Fine tuning and access to all available instruments parameters remains possible via the devices own web interface. Figure 1.33 shows a screenshot of the device interface with an exemplary response measurement plus spectrum on the right hand plot part, and the setup of the data channels that can be displayed in the imaging plots of the main interface (1.32) on the left hand side.

The possibility of applying arbitrary mathematic operations on the demodulated signals before displaying and exploiting them allows direct imaging of the key force field properties without a time-consuming analysis step. Compared to the previous approach based on thermal noise analysis, the typical measurement time has thus been reduced from the order of days to less than an hour for a regularly sized map. This is firstly due to the faster driven measurement using dual mode tracking with two PLLs that is at least ten times faster than the acquisition of a full spectrum around the mechanical modes, only limited by the mechanical Q-factor and the SNR of the measurement. And secondly, the analysis of the results does not require a complex fitting routine that needs to be adapted for each mechanical system. Instead, the new instrument modules already display first results during the measurement, reducing the necessary time roughly by another factor of ten.

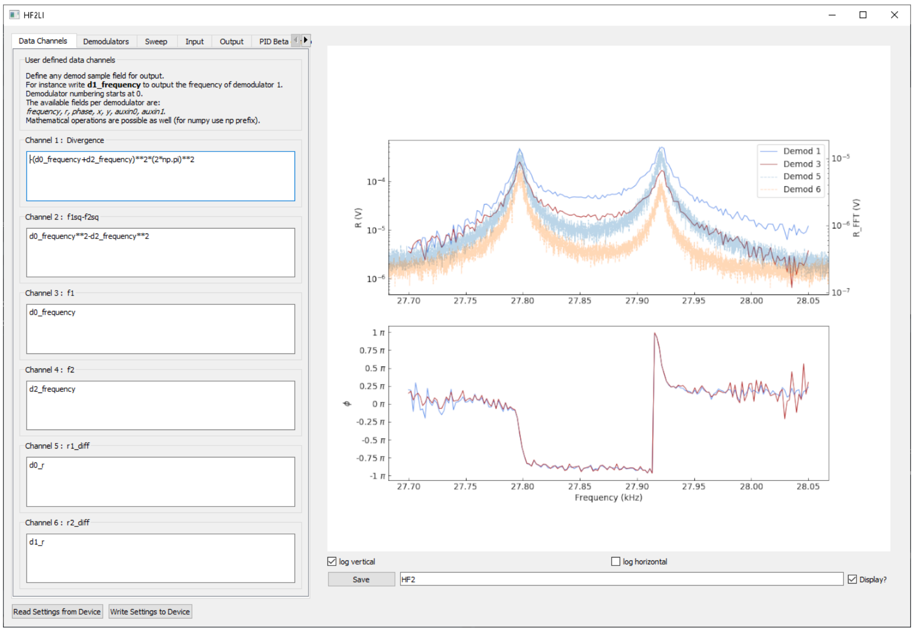

User defined data channels

Define any demod sample field for output.
For instance write **d1_frequency** to output the frequency of demodulator 1.
Demodulator numbering starts at 0.
The available fields per demodulator are:
frequency, r, phase, x, y, auxin0, auxin1.
Mathematical operations are possible as well (for numpy use np prefix).

Channel 1 : Divergence
`-(d0_frequency+d2_frequency)**2*(2*np.pi)**2`

Channel 2 : f1sq-f2sq
`d0_frequency**2-d2_frequency**2`

Channel 3 : f1
`d0_frequency`

Channel 4 : f2
`d2_frequency`

Channel 5 : r1_diff
`d0_r`

Channel 6 : r2_diff
`d1_r`

☑ log vertical
☐ log horizontal
HF2
☑ Display?

Fig. 1.33: Screenshot of the *Zurich Instruments HF2* instrument interface showing the definition of the data channels for realtime imaging (left) and the plot interface for response sweeps with synchronous spectrum acquisition.

1.4.6 Realtime DSP with the Red Pitaya

Digital signal processing provides a fast and flexible way to analyze electrical signals in time and frequency domain. It is a technology that can be found in all recent spectrum and network analyzers as well as in arbitrary waveform generators. Most of these devices are built upon the technology of *field programmable gate arrays* (FPGA), integrated circuits that allow the user to reconfigure the logical operations on the hardware level during runtime. The integration of logical gates and memory on the same chip enable signal processing at the digital clock frequency that typically lies in the range of hundreds of MHz. Also digital processing units do not add additional noise during signal processing, even if the digitization of an analog signal ultimately determines the resolution of the signal processing [102].

The availability of devices that integrate FPGA chips with the peripherical electronics such as digital analog converters and amplifiers with open source code allows end-consumers like the common experimentalist to implement digital signal processing modules on their own. One of these devices is the *Red Pitaya* [92] that comes equipped with a *Xilinx Zynq 7010* FPGA and two 14 bit DACs and ADCs at a clock rate of 125 MHz. Projects like *PyRPL* [80] have used this platform to realize locking of opto-mechanical systems.

The prerequisites for application in our experiments were:

- Integration with the existing software environment
- Components:
    - 2 Input signals (high-pass filtered)
    - 2 Output signals
    - Demodulation at 2 frequencies (4 demodulators) in kHz regime
    - best possible filtering in the Hz regime of the demodulated signal
- Synchronization with other devices, trigger processing

As none of the available softwares for the *Red Pitaya* supports this modus of operation and classic laboratory instruments that fulfil the requirements quickly exceed the budget limits we started the development of a instrument software that suites to our needs. This approach lets us benefit from the expertise of the local electronics department to tailor the development and to get a high level of understanding of the measurement details, which is crucial for correct interpretation of the results. It also permits us to integrate the *savoir faire* of DSP development into our group so that future experiments that rely on rapid digital signal treatment get accessible. One of these is the creation of artificial synthetic force fields based on realtime feedback presented in Section 4.2.

1.4.6.1 The RedPitaya FPGA

The adapted *Red Pitaya* device is designed around the *Xilinx Zynq 7010* system on chip (SoC) that integrates a FPGA unit with a CPU and memory on a single chip. It is adapted to run a Linux based host system that has access to a memory block shared with the FPGA unit. It is via this register memory that commands and data are exchanged between host system and FPGA. The FPGA also has access to the two DACs and two ADCs that are sampled at the clock rate of 125 MHz. Additionally to these main in/out channels there are slow analog and digital io-pins available for access from FPGA and host system. The core of the FPGA is the digital signal processing unit (DSP) that can be programmed at runtime via pre-compiled FPGA architectures called bitfiles. The core DSP of the FPGA has been restructured by *Julien Minet* at Institut Néel to be easily programmable in the laboratory environment.

The host system is a normal Linux operating system that in the supplied version is a Ubuntu based build. It can run any communication server to allow external access for controlling the device such as a web server or a text based communication service via TCP. The manufacturer supplies an open source implementation of an application programming interface (API) [92] coupled with an open source implementation of the SCPI communication protocol that is widespread in laboratory devices. The API and server are written in the C programming language[5], guaranteeing fast interaction between host

---

[5]

system and FPGA. For the customization we kept the SCPI functionality and the overall structure of the API but replaced all special functionalities of the API by our own.

Beside the host system that runs the SCPI server and the FPGA that contains all digital signal processing, a client is implemented on the lab computer. The client is a simple add-on to the existing lab software (see Section 1.4.4). Figure 1.34 gives an overview of the design of the *Red Pitaya* acquisition system.

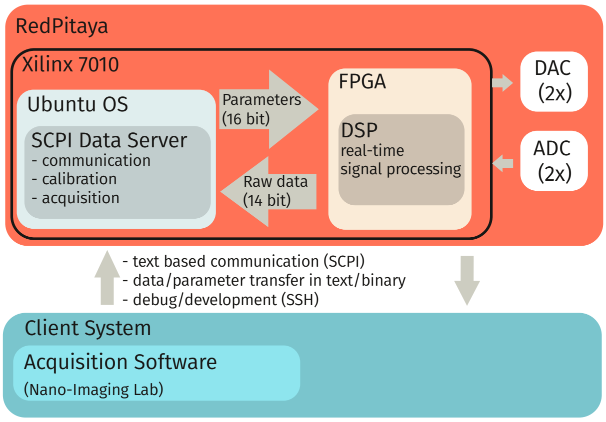

Fig. 1.34: The system design of the *Red Pitaya* acquisition platform with the three main elements client, server and DSP.

The technically most complex part is the data server that runs on the device. It handles communication from and to the client system and from and to the FPGA and therefore requires thorough handling of multiple communication interfaces. Since the acquired data from the FPGA are raw binary numbers, the data server manages all necessary calibration as well, so that the values communicated to the client correspond to physical quantities.

The client system itself is the least complex part. It contains an implementation of the necessary commands to control the device and to submit and accept data. Thanks to the standard text based communication protocol, this condenses to some simple python functions.

The technical most important unit is the DSP on the FPGA itself as here the signals are processed in real time. The next subsection looks into the details of the DSP developed to perform two channel lock-in measurements.

1.4.6.2 Two signals dual frequency lock-in measurements

To realize force field sensing based on driven measurement of both nanowire eigenmodes in two dimensions, we need to perform a lock-in measurement on each signal $V_{\ominus,\oplus}$ of the two measurement vectors for each of the two driving tones which are locked on the two eigenfrequencies. Similarly, the dynamic calibration of the readout vector (Section 1.3.1.2) depends on the simultaneous lock-in measurements of both detection channels at the two driving frequencies which move the experiment along the x and z axis for calibration purpose.

The design for the two-signal dual-frequency lock-in comprises four independent demodulation stages. A schematic representation of the DSP is given in Figure 1.35. For better illustration, the DSP block is divided into the three sections: input signal processing, output signal generation and data acquisition. In the input section, two analog to digital converters (ADC) digitize the voltage input to a 14 bits digital signal that is high-pass filtered in order to remove any residual DC component and low frequency noise. Each signal is then mixed with a harmonic wave at frequency ω generated by one of four available local harmonic oscillators (LO) and the quadratures $\tilde{I}$ and $\tilde{Q}$ are output as real and imaginary part of the mixed signal. For a monochromatic input signal $V(t)$ at frequency Ω and amplitude A, $\tilde{I}$ and $\tilde{Q}$ are connected to the products: $V(t)\cdot\cos\omega t$, $V(t)\cdot\sin\omega t$, which are subsequently combined with a low-pass filter to remove the fast oscillating component. The quadratures are then:

$$I = V(t) \cdot \cos\omega t \cdot F_{\mathrm{LP}}(t) \tag{1.82}$$

$$Q = V(t) \cdot \sin\omega t \cdot F_{\mathrm{LP}}(t), \tag{1.83}$$

where $F_{\mathrm{LP}}(t)$ is the temporal response of the filter whose bandwidth is the so called *demodulation bandwidth*. The complex demodulated signal of a monochromatic signal at frequency Ω (any real signal can be expressed as sum of monochromatic contributions) $V_{\Omega-\omega}(t)$ is thus

$$V_{\Omega-\omega}(t) = I(t) - Q(t) = \frac{A}{2} F_{\mathrm{LP}}(\Omega-\omega) e^{(i(\Omega-\omega)t+\phi_0)}, \tag{1.84}$$

with $F_{LP}[\Omega-\omega]$ being the filter transfer function of the low pass filter. Note that due to the internal multiplication with the pure cosine and sine wave from the LOs, the Q-quadrature has a minus sign in order to write the signal $V_{\Omega-w}(t)$ as positive exponential. We note that this convention for the time evolution is the opposite of the one we employ in the theoretical description of the nanowire mechanics in Section 1.1.

As illustrated in Figure 1.35, the two input channels are symmetric and the employed demodulation frequencies are identical for both signals. The implementation of the instrument however allows to chose any of the two *ADC* signals and any of the LOs as input for each of the four mixers. One signal could therefore also be demodulated at four different frequencies that can be used for multifrequency response analysis. Similarly, all filters can operate as high or low-pass filters with individually set bandwidths.

In order to be sent to the experiment control software, the demodulated signals must first be transferred to the data server of the *Red Pitaya* that runs on the CPU of the device. For communication, FPGA and CPU both share some register and memory resources.

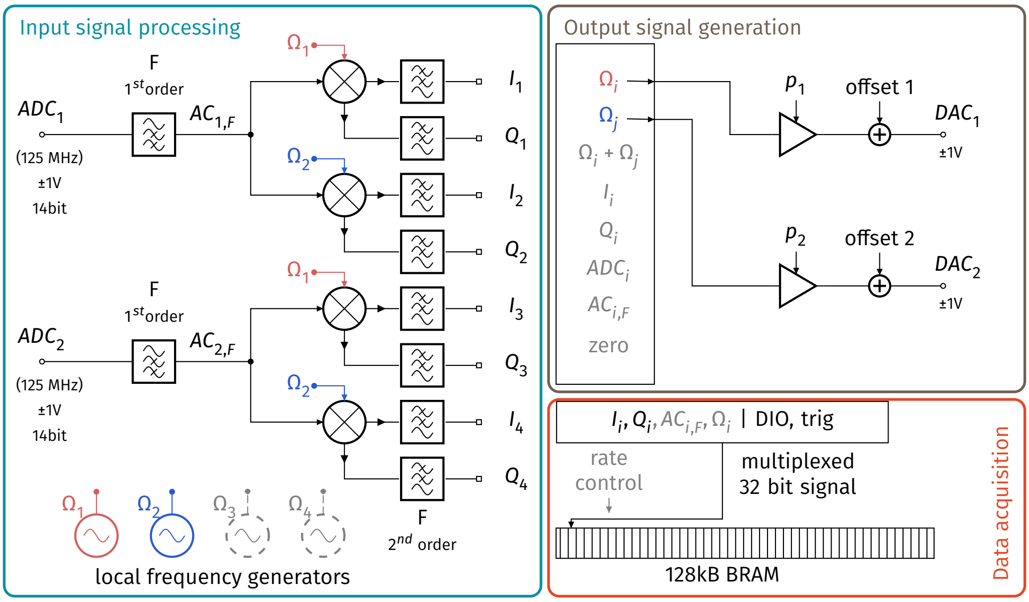

Fig. 1.35: DSP layout of the two channel lock-in measurement implementation on the FPGA. The *input signal processing* block outlines the processing of an analog input signal that is converted into a digital one, then any DC offsets are removed by a digital high-pass before mixing the signal with a local oscillator (LO) wave. For two frequency lock-in measurements two of the four available LOs are used (red/blue). Low pass filters remove the sum frequency signal and narrow the demodulation bandwidth of the in phase (I) and out of phase (Q) quadratures. The two output signals are the two generated waves (other available signals greyed out). An amplifier with gain ($p_{1,2}$) and adder adjust the amplitude and offset of the signal on the two DACs. In the data acquisition block, two measured values (32 bit) per time are written in the shared BRAM memory where data is accessible to the data server.

The interface for data transfer is a 128kB BRAM memory that can receive data as a single 32 bit chunk per clock step at maximum rate. The actual write rate depends on the bandwidth of the filters and the desired acquisition rate, and is limited by the read speed of the program running on the CPU that is slower than the 125MHz of the FPGA. The 32 bit signal can hold two measurement values of each 14 bit length. The remaining 4 bits represent *tag-bits* that mark data, for instance as trigger bits that depend on the presence of an external DIO signal. The data server can then select which data to save and which to discard, depending on the external trigger. Due to the 32 bit length of the transfer signal, writing all eight quadratures to the BRAM requires four clock steps which additionally limits the acquisition rate. With the implemented DSP architecture and the corresponding data server, rates of about 100 kHz to 200 kHz are feasible. The bottle neck for higher rates is the data processing on the CPU side. It is therefore likely that an optimization of the data server program could improve this rate if required. Similar as for the inputs of the mixers, all intermittent signals are accessible for a transfer to the BRAM.

The last part of the DSP is the output signal generation. For the dynamic detection of the readout vector, the position of the nanowire needs to be modulated along the two axes

x and y at two different frequencies. The output signals are therefore chosen to be the waves generated by the two LOs. Other options such as the sum of two harmonic waves are possible as well. The two output signals can be scaled independently via the setting of the two proportionals p_1 and p_2. Additionally, it is possible to add a static offset to the output signal.

The frequency for the dynamic measurement of the readout vectors is typically chosen between 60 Hz to 100 Hz. Firstly, this is a frequency range where the piezo actuators still respond linearly, and which fall in the DC channel bandwidth of the photodetectors. And secondly, the created sidebands on the mechanical peak are far enough from the mechanics so that the measurement of the nanowire resonances is not affected strongly. As demodulation bandwidth we typically choose 30 Hz which is the lower limit at low frequency signals before rounding issues on the FPGA distort the signal. Additional temporal averaging ensures a bandwidth that is small enough to only measure one of the excitation frequencies per demodulator, so that each of them provides an output value propotional to $\partial_{x,z} V^{\mathrm{DC}}_{\ominus,\oplus}$.

1.5 Illustration of a measurement protocol

We illustrate now how to realize a complete measurement, aiming at the mapping of the horizontal 2D force field gradients created by a nanostructured sample in an arbitrary chosen horizontal (xz) or vertical (xy, zy, or any other vertical plane) scanning plane above the sample surface. The electrostatic nature of the force field requires a measurement of its dependence on the bias voltage V_{bias} between nanowire probe and sample. This force field nanoscopy is thus an iteration of individual force gradient measurements on a subset of positions in the four dimensional scan space $x, y, z, V_{\mathrm{bias}}$. The following paragraphs lay out the protocol followed during a measurement.

1.5.1 Preparation

The first step in the measurement preparation is the correct alignment of sample and nanowire to each other. We want the nanowire vertically oriented above the area to explore. A coarse alignment is done with the help of the transmitted laser light after the nanowire, imaged on a paper screen just behind the nanowire. The analysis of the refraction fringes on the screen allows to rapidly bring the nanowire in the centre of the beam's waist. The sample can be similarly positioned, using the transmitted light for a first coarse alignment. This is efficient for tip-like samples, but not sufficient when exploring flat samples.

A finer alignment is then done with the experimental image realized with a white light source on a CCD camera. It provides enough control to adjust the sample to the nanowire in the µm-range using piezoelectric stepper motors. Once the coarse alignment has been performed, we can pump the vacuum chamber and turn on the temperature controller. This creates some micrometer large shifts which we compensate with the piezo stages.

We then position the nanowire at the optimal measurement position in the laser beam using the larger experiment stage. This position provides a good spectral signal of both eigenmodes of the nanowire. In general, we operate with an orientation of 45° between the nanowire eigenmodes and the optical axis, so that it also ensures a good responsiveness to the resonant drive via the optical pressure force of the drive laser, which is aligned along z.

A general prerequisite is a correct calibration of the detection channel as described in Section 1.4.1.1 and Section 1.3.1. This calibration needs to be repeated every time elements in the detection channel are exchanged (including optical elements rearrangements, but also electronic modifications) but remains valid otherwise.

At a position with a good readout signal, with the sample still far enough away from the nanowire (tens of µm) in order to avoid experiencing a significant external force field, we acquire a spectrum of the cold bare eigenmodes of the nanowire. This spectrum provides the orientation and frequencies of the undressed eigenmodes that are used as reference in the calculation of the force field gradients. If the alignment of the eigenmodes with respects to the optical axis is too different from the 45° configuration, we reopen the vacuum chamber and rotate the sample support. The PLLs of the *Zurich Instruments HF2-LI* are then locked to the mechanical modes as described in Section 1.1.3.1, and we can start measuring the variations of the force field experienced by the nanowire.

The measurement software allows recording and plotting of the demodulated signals of both photodiode channels at the two locked resonance frequencies, either in realtime or synchronized with the scan of the output of a *NI-DAQ* ADC/DAC converter that controls the x, y, z-piezo stage moving the sample and the V_{bias} output. Additionally, we can perform mathematical operations on the acquired signals from the demodulators before plotting them and can thus monitor for instance the sum of the squared frequencies $f_{\mathrm{PLL1}}^2 + f_{\mathrm{PLL2}}^2$, a value that is proportional to the force field divergence $\nabla\cdot\mathbf{F} = \frac{1}{M_{\mathrm{eff}}}(g_{11} + g_{22})$. When measuring a structured surface, this quantity reflects the topology of the sample as the largest force gradients usually appear close to edges. Therefore, imaging $f_{\mathrm{PLL1}}^2 + f_{\mathrm{PLL2}}^2$ provides a map of the sample under investigation, and can be used as a control signal while approaching the sample to the nanowire extremity. Since the nanowire is never aligned perfectly perpendicular to the sample, and since the electrostatic landscape above the samples is never completely homogeneous (see Chapter 2), this methods is rather safe, and we can approach the sample to the nanowire extremity without touching. In practice, in this rapid readout mode, we can detect that the nanowire “feels” the force exerted by the surface at a distance ranging from 500 nm to 2 µm above the nanostructures.

These orientation maps can be acquired at much higher speed than detailed force measurements since the detection of frequency shifts is less affected by experimental biases compared to the amplitude measurement that provides the mode orientation. Useful images only require a measurement time $t_{pp} \approx \frac{1}{2}\frac{2\pi}{\Gamma_\mathrm{m}}$, where Γ_m is the mechanical damping of the measured mode.

The first images of the force field divergence are then used to set up the scans. An estimation of the nanowire-sample distance can be obtained by slowly approaching the surface and observing the spectrogram of the mechanical modes. For a flat sample, some tens of nanometer before touching the surface, rotations of the eigenmodes, frequency shifts and RC-induced damping effects typically become so intense that the PLL stops tracking reliably. For vertical scans this distance imposes the lower scan limit, while for horizontal scans, the sample is retracted about 50 nm to 150 nm and the proper operation of the PLL is verified at some random displacements in the scan area and for various voltages V_bias in the planned scan range.

Depending on the structure of the force field under investigation, the nanowire eigenmodes can be subject of intense rotation, especially when approaching electrostatic tips or holes. Those eigenmode rotations are problematic for locking the PLL, since the force and thus the induced projected displacement directly depend on the $(\mathbf{e}_F \cdot \mathbf{e}_i)(\mathbf{e}_i \cdot \mathbf{e}_\beta)$ product. If one of those coefficients changes sign, then the PLL phase setpoint will be changed by 180°. As such, when we realize vertical maps, we try in general to operate in one of the two planes that contain one of the eigenmode. To do so, we employ a “tilted scan” mode which allows us to realize force field mapping in any sub plane of the xyz sample space.

Prior to realizing a sweep of the applied bias voltage, the scan range is adjusted around the minimum value of the force field gradient that is proportional to V_bias^2. In order to detect frequency “jumps” caused by PLL unlocking and to evaluate the hysteresis of the measurement, we perform a bidirectional scan of the voltage range. Furthermore, the demodulated data, which are sampled at a higher rate than the acquisition time per point, are cumulated in each point/voltage, so that the software calculates and records the mean value and the standard deviation. This also helps detecting pathologic measurement points.

Lastly, we verify that the nanowire still is in a good position for the optical readout and apply correction if needed. The position is then locked by a PID controller acting on $V_\ominus^{DC}$ as input and fed back on the x-axis piezo controller of the main setup stage as output as described in Section 1.4.3. Next, the measurement can be started.

In order to let the system reach its steady state, we in general stay some tens to hundreds of ms (more than the inverse mechanical damping rate) at a given position/voltage point. As such, a detailed map made of 100x100 points, where we sample 2×15 voltage values, takes about 5 hours, during which the experimental drifts are in principle well under control. The data are saved in a `hdf5` mixed binary format of an approximate size of 400 MB. In each point, we record the demodulated signals of up to six demodulators per *HF2*-lock-in (the use of multiple devices is supported) that include the central frequency, signal quadratures (I and Q) and the signal at four auxiliary inputs. Out of this data we can reconstruct the force field properties. Additionally to the raw demodulator data, we also save the data as presented as live images in the scan interface where the mathematical operations (for instance the calculation of the divergence from the sum of squared frequencies) are taken into account. The recorded dataset also includes the experimental settings as configured in the control interface or in measurement scripts.

1.5.2 Measurement script

Following on the preparation, the measurement runs automatized by the control program (Section 1.4.4) that follows a user script in which each measurement step is defined. The flow diagram in Figure 1.36 outlines a typical measurement procedure for electrostatic force measurements on a regularly spaced grid in a sub space of the four dimensional (x,y,z,V_{bias}) space.

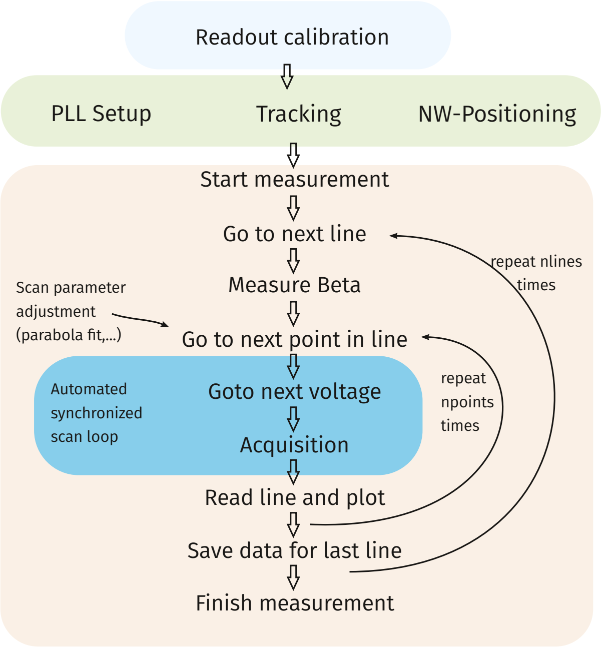

Fig. 1.36: Diagram of the measurement protocol followed during an electrostatic force field measurement in the $(x_i, x_j, V_{\text{bias}})$ space.

The control script also provides the possibility of automatized adaptation of the measurement parameters before each point/voltage. For example, we typically adapt the voltage span of V_{bias} to each point, so that the force field does not induce too large perturbations of the nanowire properties. To do so, we first use a second order polynomial fit to the measured force divergence at the current position, and adjust the voltage span employed for the next position. In doing so, we maintain the same magnitude of the electrostatic force field gradients during the full map. Additionally, the drive strength of the modulating force can be adjusted to guarantee an efficient but not too strong drive of both nanowire eigenmodes independently from the nanowire's location, with respect to the force field, which can generate eigenmode rotations responsible for a variation of the mechanical response to the drive tone. As another automatized parameter control, the central frequency of the PLL can be adjusted programmatically to improve its performance as this allows to limit the available frequency range for each PLL to a few tens of hertz around the resonance. Using larger ranges can lead to a lock on the wrong mode if they are spectrally close to each other. Figure 1.37 shows the additional control interface that is used to set up such advanced scans.

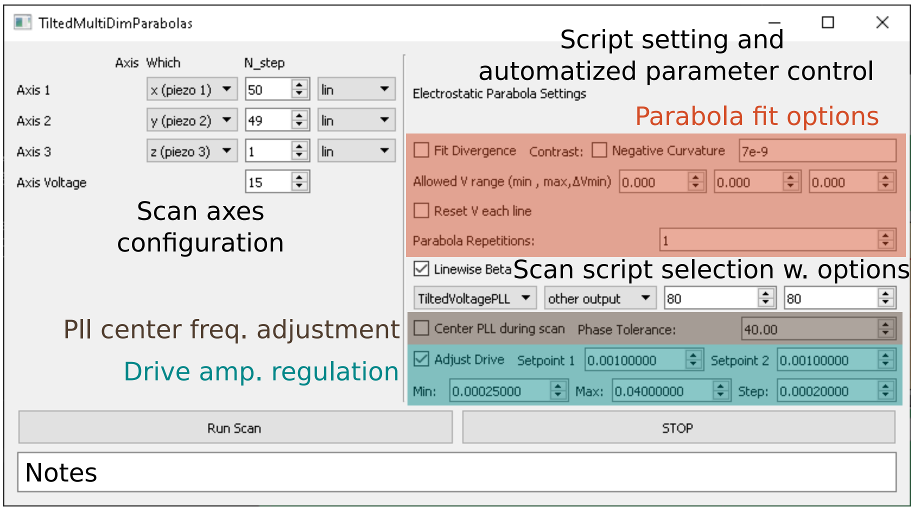

	Axis	Which	N_step	
Axis 1		x (piezo 1)	50	lin
Axis 2		y (piezo 2)	49	lin
Axis 3		z (piezo 3)	1	lin
Axis Voltage			15	

Electrostatic Parabola Settings
☐ Fit Divergence Contrast: ☐ Negative Curvature 7e-9
Allowed V range (min , max,ΔVmin) 0.000 0.000 0.000
☐ Reset V each line
Parabola Repetitions: 1
☑ Linewise Beta
TiltedVoltagePLL other output 80 80
☐ Center PLL during scan Phase Tolerance: 40.00
☑ Adjust Drive Setpoint 1 0.00100000 Setpoint 2 0.00100000
Min: 0.00025000 Max: 0.04000000 Step: 0.00020000

Fig. 1.37: The setup interface for a scan along four axes (spatial + voltage). The left side of the interface serves to define the number of points and a possibly nonlinear sampling of the range that is defined in the main interface (figure 1.32). The right side serves to select the scan script and set options for the different parameter adjustments, parabola fit, PLL center frequency tracking and drive amplitude adjustment.

Additionally, the intermediate processing stage in the script permits to directly calculate the force field gradients if the nanowire's mechanical parameters have been set in the script beforehand, following the measurement principles described in section Section 1.2.1. As such, this permits to directly image the four components of the force field gradients on the scanning interface.

2 Electrostatic force fields above nanostructured surfaces

Having layed out the tools necessary to conduct nanowire based force measurements, the present chapter covers their realizations. The focus of this chapter is on the electrostatic forces created by the electric field above nanostructured metallic surfaces. With gradients in the order of tens of $fN\,nm^{-1}$*, the electrostatic forces are the dominant forces at nano- and micrometric distances. As a consequence, electrostatic forces can be created and tailored almost without effort, so they present an ideal test case for the nanowire microscopy experiment, and additionally, the inevitable presence of electrostatic forces in all kind of nanostructures requires a good knowledge of their nature, in particular in the field of nano-/micro-electro-mechanical-systems.*

We will begin with a discussion of the expected force, felt by the nanowire, based on the Maxwell stress tensor formalism which allows obtaining a more detailed perspective on the electrostatic forces. From the analysis of the different components in the stress tensor, we conclude that the relevant fields which cause the force on a dielectric nanowire are the product of the horizontal and vertical fields at its very apex. This concept is important for the qualitative understanding of the influence of horizontal residual fields – fields that are present due to surface imperfections and do not depend on the sample bias voltage.

After having started the experimental part of the chapter with a presentation of the used samples, we present force divergence measurements as an efficient tool to access the surface topology.
Subsequently, we will discuss the dependence of the electrostatic force $F(V_{\text{bias}})$ *with respect to the applied bias voltage. This allows the separation of the quadratic part which only depends on the topology of the sample surface, from the rest of the measured force. We then discuss the measured quadratic electrostatic force above a selection of nanostructures with particular focus on tip like elevations and holes in the sample surface.*

The contributions to the electrostatic force that are linear in the bias voltage arise from electric fields that do not depend on the sample bias voltage. They are subject of the following sections. Here, we discuss possible origins, such as trapped charges or electrostatic surface patches. We obtain evidence for the latter from close distance force field mapping and identify the SEM imaging of the sample as a source of additional contamination of the sample.

At the end of the chapter we address a combined measurement of the force and force gradient which is possible thanks to the fast measurement protocols introduced in the previous chapter. The force gradients obtained from both distinct measurements present a very good qualitative agreement, which can be regarded as a validation of the force sensing protocols developed in this thesis.

◆

◆

2.1 Electrostatic Maxwell stress tensor

In 1873 Maxwell formulated a general integral expression to calculate the force experienced by an object O enclosed by a surface S due to a surrounding electromagnetic field $\mathbf{E}$ [71]:

$$\mathbf{F} = \oint_S \langle \mathbf{T} \rangle \cdot \hat{\mathbf{n}} \mathrm{d}S. \tag{2.1}$$

This Maxwell stress integral is the surface integral of the time averaged ($\langle ... \rangle$) stress tensor $\mathbf{T}$ on the closed surface S that encloses the object O as illustrated in Figure 2.1a, where $\hat{\mathbf{n}}$ is the outwards pointing normal vector of S.

This section discusses how the stress tensor provides a mean to understand the electrostatic force experienced by a particle immersed in an electrostatic field, and will serve subsequently to analyze the contributions of residual electrical fields and of the vacuum fluctuations of the electromagnetic (EM) field as the origin of the Casimir forces. The description of the force in terms of local fields (of controlled or uncontrolled origin) allows a better understanding of the forces measured with the nanowire force probe.

2.1.1 Formulation

In the so-called Lorentz representation [27, 47] the individual elements of the 3 × 3 Maxwell tensor $\mathbf{T}$ in the cartesian representation are given by:

Maxwell Stress Tensor

$$T_{ij} = \varepsilon_0 E_i E_j + \frac{1}{\mu_0} B_i B_j - \frac{1}{2}\left(\varepsilon_0 E^2 + \frac{1}{\mu_0} B^2\right)\delta_{ij}, \tag{2.2}$$

where E_i are the cartesian projections of the electric field vector and B_i those of the magnetic field. δ_{ij} is the Kronecker delta function. In the static and non-magnetic case, where neither currents nor magnetic dipoles are present, the force only depends on the electric fields and the elements T_{ij} become

$$T_{ij} = \varepsilon_0 E_i E_j - \frac{1}{2} \varepsilon_0 E^2 \delta_{ij}. \tag{2.3}$$

Following the Maxwell stress tensor formalism, we will now discuss the different contributions to the electrostatic force from each face of the nanowire surface, and subsequently the contributions of the different electric fields surrounding the nanowire.

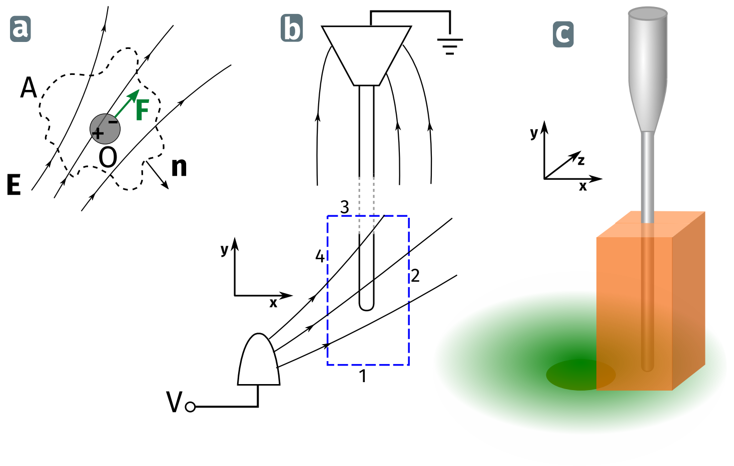

Fig. 2.1: (**a**) A test object *O* in an electric field experiences a force that can be computed by integrating the electromagnetic stress tensor over the surface *A*. (**b**) integration surface on the lower end of the nanowire (blue) that is immersed in the electric field (black lines), created between the grounded NW support and an electrode. The field gradient is strongest close to the tip of the nanowire while the field found at larger height is nearly homogeneous. The same geometry but in 3D is depicted in (**c**).

2.1.2 A qualitative approach to the sources of the electrostatic force

The integration of the Maxwell stress tensor provides the force vector that acts on the enclosed body. For nanowire based force measurements, the horizontal force is of particular interest since it directly impacts the transverse mechanical oscillations of the nanowire, while the vertical component of the force is hardly detected. The latter may cause a stiffening of the nanowire, but the sensitivity to the vertical force is negligible compared to the lateral force gradients. In order to get a better understanding of the field's different contributions, we can decompose the stress tensor integral into the different contributions from each elementary surface (compare Figure 2.1b) surrounding the nanowire:

$$\begin{aligned}\mathbf{F} &= \mathbf{F}_1 + \mathbf{F}_2 + \mathbf{F}_3 + \mathbf{F}_4 \\ &= \int_{S_1} \mathbf{T}\hat{\mathbf{n}}_1 \mathrm{d}S + \int_{S_2} \mathbf{T}\hat{\mathbf{n}}_2 \mathrm{d}S + \int_{S_3} \mathbf{T}\hat{\mathbf{n}}_3 \mathrm{d}S + \int_{S_4} \mathbf{T}\hat{\mathbf{n}}_4 \mathrm{d}S.\end{aligned} \tag{2.4}$$

Here $\mathbf{T}$ is the stress tensor in two dimensions evaluated at each surface and $\hat{\mathbf{n}}_i$ is the outward pointing normal vector of each integration surface. For simplicity, we limit the following discussion to the 2D xy-plane. The contributions for each boundary surface S_i to the total force $\mathbf{F}_i$ in the xy base can then be written as

$$\mathbf{F}_1 = \begin{pmatrix} F_{1x} \\ F_{1y} \end{pmatrix} = \int\limits_{S_1} \begin{pmatrix} T_{xx} & T_{xy} \\ T_{yx} & T_{yy} \end{pmatrix} \begin{pmatrix} 0 \\ -1 \end{pmatrix} \mathrm{d}S = \int\limits_{S_1} \varepsilon_0 \begin{pmatrix} -E_x E_y \\ \frac{1}{2}(E_x E_x - E_y E_y) \end{pmatrix} \mathrm{d}S \tag{2.5}$$

$$\mathbf{F}_2 = \int\limits_{S_2} \varepsilon_0 \begin{pmatrix} \frac{1}{2}(E_x E_x - E_y E_y) \\ E_x E_y \end{pmatrix} \mathrm{d}S \tag{2.6}$$

$$\mathbf{F}_3 = \int\limits_{S_3} \varepsilon_0 \begin{pmatrix} E_x E_y \\ \frac{1}{2}(-E_x E_x + E_y E_y) \end{pmatrix} \mathrm{d}S \tag{2.7}$$

$$\mathbf{F}_4 = \int\limits_{S_4} \varepsilon_0 \begin{pmatrix} \frac{1}{2}(-E_x E_x + E_y E_y) \\ -E_x E_y \end{pmatrix} \mathrm{d}S. \tag{2.8}$$

The contributions to $\mathbf{F}_x$ – the first vectorial component – from the top and bottom (surface 1 and 3) of the integration volume consist in the product of horizontal and vertical fields, while for the left and right surfaces one calculates the difference of the horizontal and vertical fields. If the nanowire is much thinner than the characteristical size of the electric field variations, we can assume that, for a dielectric nanowire, the field on both side surfaces is quasi identical and thus we have $\mathbf{F}_2 = -\mathbf{F}_4$, so that they cancel each other in Equation 2.4. Also, when the top integration surface is far enough from the electrode, its contribution will be negligible. Hence, this very general reasoning suggests that the main contribution to the horizontal force comes from the bottom surface of the nanowire, where the electric fields are maximal when approaching nanostructured surfaces.

The above qualitative analysis can be verified with numerical simulations, as explained in box 2.a.

Panel 2.a: The Maxwell Tensor at the Nanowire Extremity

The electrostatic force exerted on a nanowire, by the field produced by an electrode beneath the nanowire's free end, is purely determined by the fields around its extremity. In order to evaluate the different contributions and to validate this assumption, we performed an electrostatic study in *COMSOL*, where we placed the nanowire above a surface which has a spherical elevation – the electrode. We then simulate the fields around the nanowire's extremity as we apply a voltage (1 V) on the bottom electrode and zero potential at the top surface of the simulation volume. The resulting field is therefore, as in the experimental setup, oriented along the vertical y-direction, with the exception of the regions around the dome and the nanowire tip.

With the calculated fields, we can then evaluate the stress tensor integrals which for the horizontal force F_x are:

$$\begin{aligned} F_x &= \int_S \frac{\varepsilon_0}{2}\big(E_x E_x - E_y E_y\big)\mathbf{n}\,\mathrm{d}S, \text{ for vertical surfaces, and} \\ F_x &= \int_S \varepsilon_0 E_x E_y \mathbf{n}\,\mathrm{d}S, \text{ for horizontal surfaces.} \end{aligned} \tag{2.9}$$

We can then compare the force contribution by each of the lower integration surfaces (the horizontal field at the top boundary is negligibly small due to the geometry, so this surface can be neglected). Figure 2.2 presents the results for the case where the nanowire is close to the dome, so that the electric field is highly inhomogeneous, and for the case, where the nanowire is far away from the dome but still close to the surface.

For both cases, the integrals computed along the vertical side boundaries add up to zero (black curve), which means that the force on the nanowire is dominated by the bottom surface contribution where the field product is E_xE_y. Furthermore, this observation illustrates the fact that the electrostatic force can be regarded as being strongly localized at the nanowire extremity. As such, its impact on the different eigenmodes can be modelled as a point like volumetric force source. In the case of a high field variability – as close to a structured surface –, this product can vary significantly. However, for a larger nanowire-surface distance, the field is more homogeneous, and one can approximate the force by $F_x = -S\ \varepsilon_0\ E_x(x_1, y_1)\ E_y(x_1, y_1)$, where (x_1, y_1) is a point that marks the tip of the nanowire, in order to estimate the order of magnitude of the expected force.

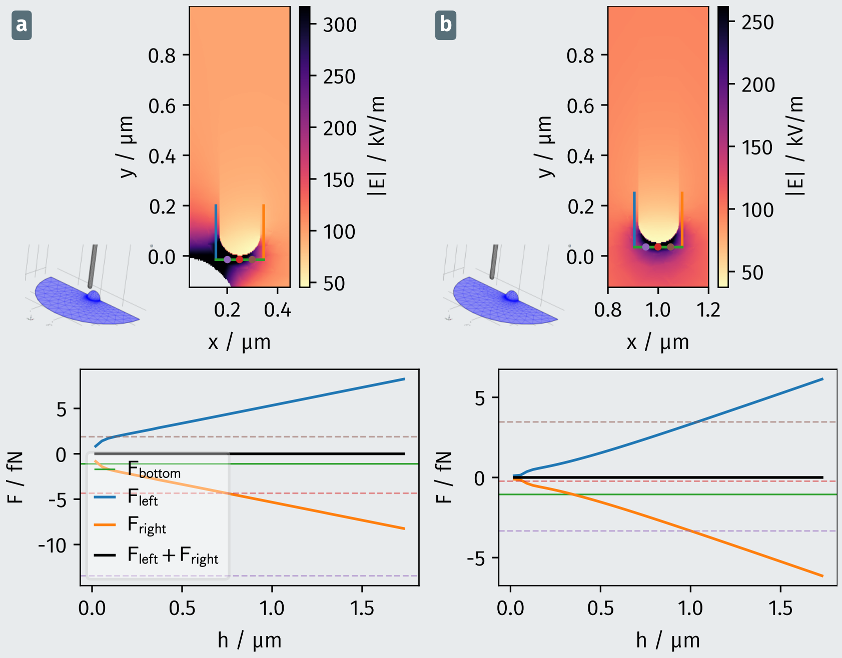

Fig. 2.2: Simulations (*COMSOL*) of the electrostatic field around a dielectric SiC nanowire (with diameter $d = 160\,\mathrm{nm}$) positioned above a flat electrode with a spherical dome. Two situations are simulated, at small distance above the dome ($x = 250\,\mathrm{nm}, y = 0\,\mathrm{nm}$) (**a**), and at larger distance ($x = 1000\,\mathrm{nm}, y = 50\,\mathrm{nm}$) (**b**). The simulation geometry is sketched in the two small insets. The top row illustrates the electric field amplitude around the nanowire tip – the dome is visible as white area in the bottom left corner of the left plot. The integration surfaces for the Maxwell tensor are indicated by the coloured lines placed 15 nm away from the nanowire extremity. The bottom graphs show the result of the force integral for the horizontal force component $F_x = \int_S T_{xj} \mathbf{n}_j dS$, evaluated for different heights h of the side integration surfaces (x-axis). The different colors (blue, orange, green) correspond to each surface indicated in the top row of plots. The black line is the sum of the force integral on left and right side which cancel each other out, so that in the resulting force, only the contribution of the bottom part of the nanowire plays a role. The dotted lines show the force from an evaluation of the Maxwell tensor in a single point $F_x = -S\,\varepsilon_0\,E_x(x_1, y_1)\,E_y(x_1, y_1)$, for the points indicated by the coloured dots in the top images.

Finally, when the electric fields are quasi homogeneous over the nanowire bottom surface, which is the case when the nanowire is not too close to the surface under investigation, the electrostatic force can be approximated by

$$F_x = -\varepsilon_0 S E_x E_y. \tag{2.10}$$

In terms of magnitude, if we position the nanowire above a microsphere with a diameter of 500 nm, the fields at the nanowire's extremity are in the order of $1 \cdot 10^5\,\mathrm{V\,m^{-1}}$, for a bias voltage of 1 V. With a nanowire diameter of 160 nm, this yields a force in the order of few femto-newton.

2.1.3 The role of geometry

We have discussed that the fields at the very end of the nanowire are the main source of the electrostatic force. These local fields depend strongly on the geometry of the sample electrode as illustrated by the comparison of different surface structuration in Figure 2.3. While in the common plate-plate capacitor, we have a constant field $E_x = 0$, $E_y = V_{bias}/d$, the introduction of a structuration, such as a dome (2.3b) or a hole (2.3c), locally reshapes the field. For larger distances to the structured surface, the field perturbations vanish and one retrieves the case of the plate-plate capacitor. At short distances, the field strength can be approximated by the quotient of the voltage and curvature of the surface deformation V/r_{curv}, which can be significantly larger than the quasi homogeneous field found at higher altitudes, especially when approaching nanostructures.

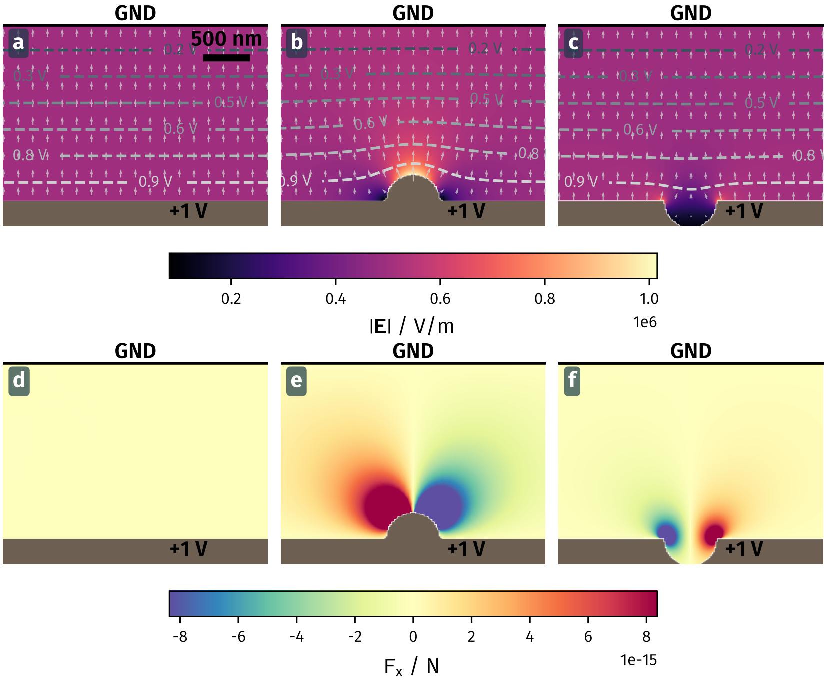

Fig. 2.3: Numerical simulations of the electric field (arrows) and potential found between a biased bottom surface and a grounded top electrode, for three different geometries of the bias sample: (**a**) flat, or with a dome (**b**) and a depression (**c**). In the vicinity of the geometric defect, the strength of the electric field does not depend anymore on the distance to the top electrode, but only on the defect geometry. The bottom row of plots shows the force in x-direction calculated via the approximation $F_x = -S\varepsilon_0 E_x E_y$ (with S the size of the bottom surface of a nanowire with radius 80 nm), for the same three geometries (flat **d**, protrusion **e**, depression **f**).

Thus, the geometric structurations of a surface shape the electric field and are therefore encoded in the electrostatic force experienced by the nanowire. In addition, the trapping or anti-trapping character of the electrostatic force field can directly be attributed to a protrusion or to a depression in the sample potential. The measurement of the electrostatic force can therefore be regarded as a microscopy tool to image the sample topography.

2.1.4 The effect of residual parasitic electrostatic fields

In practice, the electrostatic environment is the sum of many contributions. While the previously described effect from the electric field gradients created by geometric deformations can be controlled via the applied bias voltage, other residual fields are typically present which are independent of the bias voltage, contributing to the stress tensor integral as well. Those are caused, for instance, by the presence of domains of different crystal orientations in the material which change the local material workfunction, or by the presence of locally trapped charges, adsorbed molecules or surface contaminants. Figure Figure 2.4 illustrates these different mechanisms.

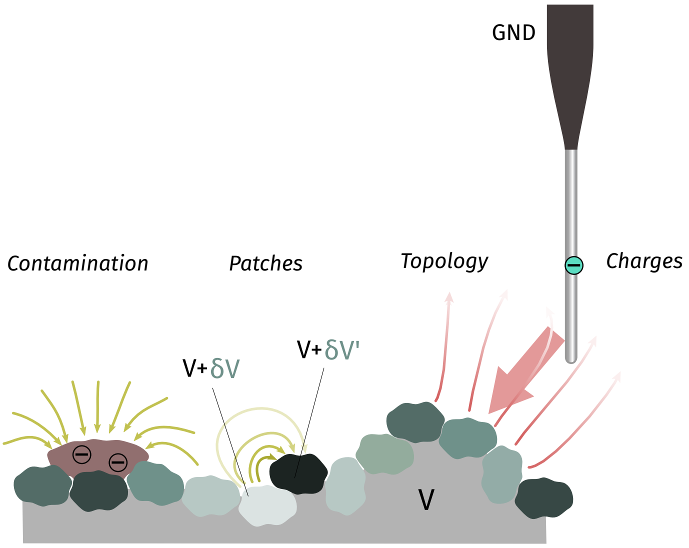

Fig. 2.4: The figure shows an enlarged view on the sources of the electrostatic force when the nanowire (left) is approached to a surface. From left to right these are: Trapped charges on the nanowire. The electrostatic field gradient created by deviations from a perfectly flat plate when a bias voltage V is applied to the sample. Surface patches (illustrated as grain like objects at the surface, corresponding to monocrystalline grains). Contamination of the sample.

The residual fields present a different spatial profile compared to the field created by the electrode. One can write the electric field as a superposition of both, the electrode's field, which linearly depends on the bias voltage V, and the residual fields: $\mathbf{E} = \mathbf{E}_V + \mathbf{E}_\mathrm{p}$. With the approximation from (2.10) $F_x \propto E_x E_y$ for the horizontal force, we now obtain for the force at the extremity of the nanowire:

$$\begin{aligned} F_x &\propto \left(E_{V,x} + E_{\mathrm{p},x}\right)\left(E_{V,y} + E_{\mathrm{p},y}\right) \\ &\propto \underbrace{E_{V,x}E_{V,y}}_{\propto V^2} + \underbrace{E_{V,y}E_{\mathrm{p},x} + E_{V,x}E_{\mathrm{p},y}}_{\propto V} + E_{\mathrm{p},x}E_{\mathrm{p},y}\,, \end{aligned} \tag{2.11}$$

so in total, the horizontal force takes a parabolic dependence of the applied voltage:

$$F_x = \alpha V^2 + \lambda V + \gamma, \tag{2.12}$$

where the quadratic coefficient α is unchanged compared to the ideal case of a perfect sample without residual fields at its surface and only depends on the shape of the field which is created by the electrode. The constant term γ depends only on the residual field, while the linear term λ combines both effects, and shifts the parabola as illustrated in Figure 2.5.

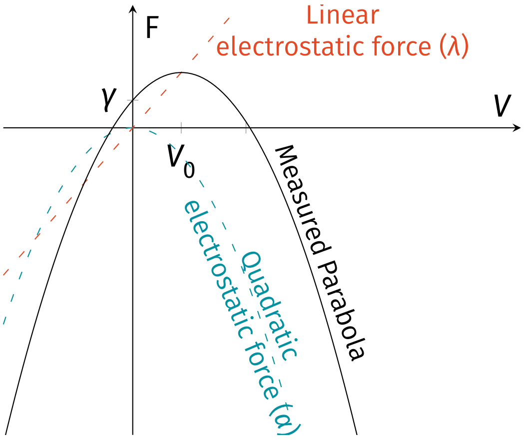

Fig. 2.5: Dissection of the parabolic force (black) in dependence of the control voltage V into its different contributions: The quadratic dipolar term (blue) contributes via the coefficient α (here $\alpha < 0$). The linear force, caused by residual fields E_p introduces the coefficient λ and the offset γ, which displace the parabola along a line. This parabola shift holds for any type of linear effect that causes voltage independent residual fields.

2.1.5 The electrostatic force parabola

The electrostatic force experienced by the nanowire during force microscopy measurements originates from the electric field that permeates the dielectric. The sample topography, the possible residual charge and electrostatic patch distributions, and the applied test voltages affect the electric field that surrounds the nanowire, and thus the experienced force. In the following, we will first be interested in imaging the surfaces by means of the electrostatic force their topography generates. To do so, we will bias the sample under investigation, a metallic nanostructure, and vary the bias voltage. Based on the stress tensor integral, this will cause a parabolic dependence of the force on the applied test voltage, which is described in this section, while the effects of residual electrostatic fields will be described in the second part of the chapter.

In the simplest configuration, an electrode carrying a potential V is positioned close to the dielectric nanowire whose upper extremity is attached to a grounded metallic support. This configuration is outlined in Figure 2.1b. The nanowire presents a very high aspect ratio and thus the distance between the nanowire tip and the electrode is much smaller than the distance between the electrode and the grounded nanowire support. Except for region close to the support, where the mechanical mode profile presents no deformation, the field profile in the upper part of the nanowire is thus quasi homogeneous, and will not contribute to the transverse force experienced by the first eigenmodes, as illustrated in the upper half of Figure 2.1b. This, and the fact that the mechanical motion of the nanowire is maximal at its lower end allow choosing an integration surface that intersects the nanowire at a certain height where the local field gradient is negligible. This approximation would be less valid if some charges are present on the nanowire, but we will consider in the following an electrically neutral, dielectric nanowire.

In absence of any residual electric field at any position, the electric field scales proportionally with the applied voltage $E = -\nabla V$, leading to a quadratic dependence of the stress tensor, and thus of the force on the bias voltage: $T_{ij} \propto \alpha V^2$, so that the force depends quadratically on the bias voltage. One can also understand this dependency by considering the nanowire tip as a voltage biased capacitor, with a capacitance depending on the nanowire position. The electric energy stored in the system thus depends on the nanowire position, which is at the origin of the electrostatic force (the gradient of the stored energy).

With its small diameter of less than 200 nm, we can assume that the nanowire is only polarizable along its length – the y-direction. This polarization over a large part of the nanowire's length (multiple micrometer) causes localized charges at the nanowire extremity.

The curvature of the force parabola solely depends on the electric field structure, which is governed by the geometry of the sample under test and the electric permittivity ε of the nanowire. While the electrostatic force on a neutral polarizable object is purely quadratic in the bias voltage in absence of residual electric fields, there exist different mechanisms that modify this dependency. For example, if a charge q is present on the nanowire, it will experience a Coulomb force $q\mathbf{E}$, which depends linearly on the bias voltage.

Another deviation arises from the difference between the workfunctions of the materials constituting electrode and nanowire. The workfunction is the potential energy difference of an infinitely far placed test charge and the surface fermi-level of a material [59]. It depends on the surface charge distribution in a material and is thus susceptible to crystal arrangement at the surface and the chemical surface properties [5]. Variations between different metals are in the order of few 100 mV, while the exact value in semiconductors depends on the doping level.

This workfunction difference means that there will remain some residual electric fields between the two electrodes even at zero bias, meaning that the condition of zero electric field will be met at a different bias value, V_0. The expression of the force can be recasted into: $F = f_\alpha(V - V_0)^2$ where the quadratic coefficient f_α only contains the geometrical aspects of the field and is not modified by the presence of residual electric fields.

Finally, the above description was restricted to static electric fields. A (slowly) time varying electric field will contribute as a parasitic term in the tensor: when multiplied with the static terms, it will generate a time varying force, which impacts the nanowire, but in principle not its time averaged mechanical properties, which are at the center of the measurement protocols described above. Their quadratic contributions may on the contrary cause a *rms* static force, which cannot be simply mitigated. The specific case of the vacuum fluctuations at the origin of the Casimir forces will be discussed in the next chapter.

2.2 Samples

This section discusses measurements of the electrostatic force field above nano-structured metal surfaces. The structuration of a flat metal substrate is either positive, meaning that the surface has elevated structures, or negative where the metallic surface is removed or drilled into. Electrodes with such nano-structurations create electric field gradients that cause an electrostatic force on the polarizable nanowire.

Samples used in this study are built based on AFM cantilevers that have the advantage to come with a well characterized probe tip that, when mounted inversely – facing the nanowire – represents a quasi-point like electrode. They are also not too extended along their transverse direction (20 µm to 40 µm), which prevents cutting the optical beam, and thus they do not alter the optical readout. For a metallic surface, we either purchase probes made for Kelvin probe force microscopy where the electrostatic force between the AFM tip and the sample surface is measured as function of the bias voltage and the tip itself is electrically contacted, or coat bare Si or SiN cantilevers with a metallic layer using electron beam induced evaporation. The first tip discussed in this section is a pointed, platinum coated tip. The second tip is a rounded tip on a silicon cantilever with 250 nm curvature radius, coated with approximately 30 nm gold layer with a few nanometer of chromium (Cr) as adhesion layer, using a multi angle deposition recipe (60°: 4 nm / 30° : 4 nm / 0°: 16 nm / 30°: 4 nm / 60°: 4 nm ~ 32 nm) realized by *Simon Le Denmat*. Figure 2.6 shows a selection of scanning electron microscopy imaged of the two tips and the processed cantilevers.

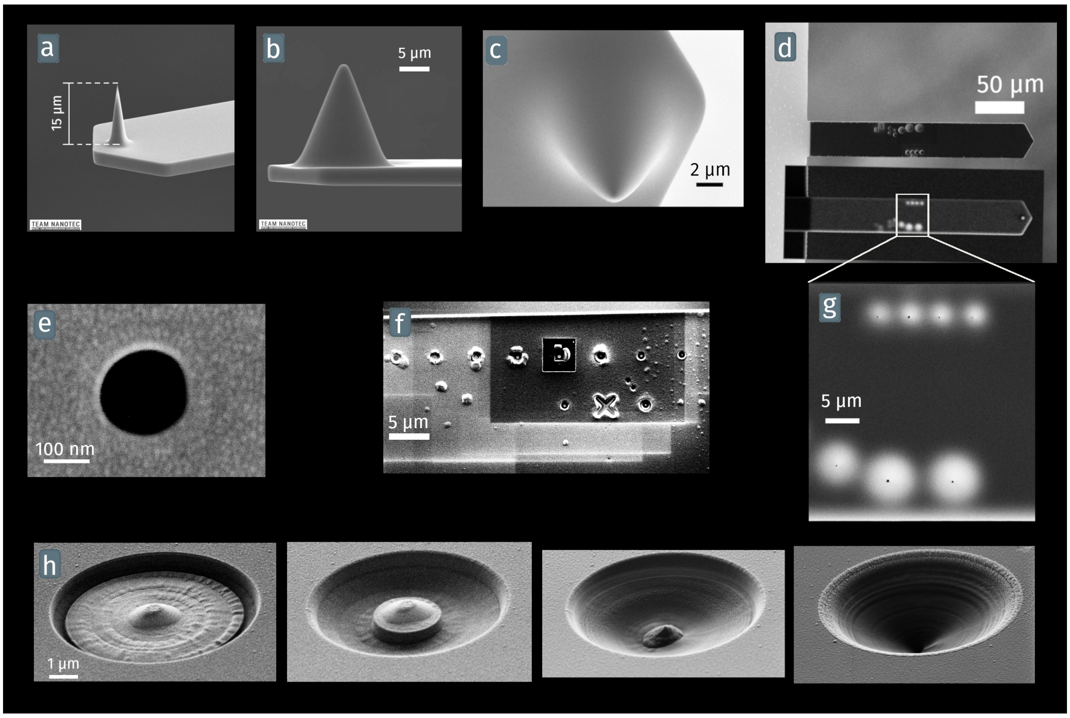

Fig. 2.6: Scanning electron microscope (SEM) images of the sample structures of this study. (**a**) The pointed cantilever probe with a sharp tip. (**b**) Rounded tip with 250 nm radius. (**a**) and (**b**) have been obtained from the manufacturer [2] . (**c**) The round tip after gold deposition and force measurements shows still a homogeneous undamaged surface. (**d**) Cantilever with the pointed tip and the first edition of holes created by FIB. The large image taken with the In-Lens detector of the SEM shows the back of the cantilever with the conically edged holes. The lower inset taken with the secondary electron detector shows the top surface with the visible tip at the cantilever's end. The secondary electron detector has a large collection angle for the scattered electrons at the backside of the sample where the surrounding area of the hole shows up as white halos due to its reduced thickness. This is also visible in the magnified view in (**g**). (**e**) shows a close up image of one of the smaller holes with about 100 nm radius. (**f**) Back side of the second edition of holes in a cantilever. A cross like hole was added as reference. This sample has not been imaged from the front side to protect the surface from electron radiation and contamination. (**h**) Illustration of the successive focussed ion beam etching steps. On the back surface, material is removed in concentric circles with stepwise reduced diameter until the central area is only a thin layer of Si substrate plus the underlying metal surface. A hole with the desired diameter is then etched through this remaining layer.

The negative structures for which metal material is removes from the surface of the cantilever have been fabricated by the *NanoFab* team at Institut Néel (*Jean Francois Motte* and *Gwenaelle Julie*) with focussed ion beam etching, allowing sharp edges as small as 20 nm. The investigated shapes in this work are round holes and trenches that penetrate through the entire cantilever, so that the physics is dominated by the missing metal and not by the possibly underlying semiconductor.

For the final samples, the FIB etching was realized with minimal SEM imaging since we observed that it was responsible for contamination of the samples. To do so, the alignment of ion and electron beams is performed in a separate region on the sample, and SEM imaging is only realized with large field of view to select the processing area before the FIB etching sequences are initiated. Also, the holes are realized from the bottom part of the cantilever so that collisions between scattered ions and the upper metallic surface where the experiments will be conducted are reduced. To dig through the 2μm silicon cantilevers, the process starts by using a large aperture and larger currents to thin down the material, followed by a more precisely controlled step on smaller thicknesses. For further optimization of the fabrication process, one should conduct tests in order to minimize the re-deposition of the etched material on the cantilever. For this work, we realized holes with diameters ranging from 100 nm to 3000 nm.

Panel 2.b: Nanowires

The nanowires referenced in the measurements throughout this thesis have all been mounted under an optical microscope and partly characterized further using SEM imaging. As mentioned earlier, we rather refrain from using this characterization before employing the nanowires as force sensors since we observed significant surface damage and contamination caused by SEM imaging.However, the lifetime of a nanowire as a force probe is indeed pretty long, and we can keep them for months on average, without observing noticeable degradation, even when touching the sample surface unintentionally. They can also be subjected to many pressure cycles without showing appreciable modifications of their mechanical properties. The following table gives an overview of the employed nanowires in this work. Values in red are estimates where a proper characterization, for instance by SEM imaging, has not been performed. Due to nanowire loss during handling and operation, not all nanowires could be imaged subsequent to their use as force probes.

Tab. 2.1: Main nanowires used in this work. The relatively low Q factor of NW3 compared to the others originates from the fact that it has been employed mostly under modest vacuum for the realization and analysis of artificial force fields (chapter Chapter 4) while the others were used as force mapping probes.

	NW1	NW1 2nd mode	NW2	NW3
f_1 / Hz	12681	77460.71	18663	8275
f_2 / Hz	12860	77922.26	26489	8341
Γ / Hz	2.1	15.1	4.8	15.9
Q	6100	5100	4700	500
M_{eff} / pg	4.5		0.8	7.5
L / μm	170	-	130	200 (130)
d / nm	200	-	100	300

2.3 Force field topology from force divergence

In Section 1.1.2.3 we introduced the force field's divergence as an accessible and experimentally robust quantity that reflects the geometric properties of the force field and tells about the underlying sample structure. With the scanning probe setup described in Section 1.4, this quantity can be directly accessed via the nanowire's resonance frequencies, recorded and plotted in realtime with the protocols developed in this work. Figure 2.7 shows a selection of force divergence measurements, taken either for orientation and localization purposes (large view field) or for the refined mapping of the force field's shape. They are taken in a rapid imaging mode, where the full maps are acquired in approximately 1 min to 10 min. All images map the force above different holes drilled in the cantilever surface for a constant bias voltage. While the holes appear as dark spots in most images, there are two cases where the divergence shows ring like features with a bright spot in the hole's center (2.7d, 2.7g).

As the electric field gradient is strongest close to sharp edges, we expect that the force and its divergence are also strongest in vicinity to edges. This is what we see as bright features in 2.7b. Note that the different images are not comparable quantitatively as they are taken above different materials using different nanowires with different vibration frequencies and experimental settings, such as height and applied bias control voltage. However, they represent a valuable amount of information about the sample and the physics.

The presented maps provide an essential tool for orientation and localization of nanostructures on the sample surface so that one can easily choose the scan area for more detailed studies. They also give an insight in the basic phenomenology. The general observation that holes are presented as dark spots with smaller divergence (panels 2.7b, 2.7d, 2.7f and 2.7g) shows that they create a trapping potential for the nanowire as will be discussed later in greater detail. Additionally, the maps contain information about the sample itself. While the sample surface in 2.7b is homogeneous with only a single contamination at the bottom right of the cantilever, the image 2.7a shows different large rectangular areas that do not correspond to physical structures but rather to contamination of the sample surface during the fabrication and SEM imaging process.

2.3.1 Force field at different bias potential

Figure 2.8 displays the measured force field divergence above the round metallic tip at four different applied bias voltages. The first global observation is that the divergence above the tip is smaller than at the edges of the scan area. This demonstrates that the

---

[1] The divergence is here uncalibrated which means that the effective mass of the nanowire's (in the order of picogram) is not taken into account. The presented form is the typical image one gets out of a single horizontal scan at a fixed bias voltage.

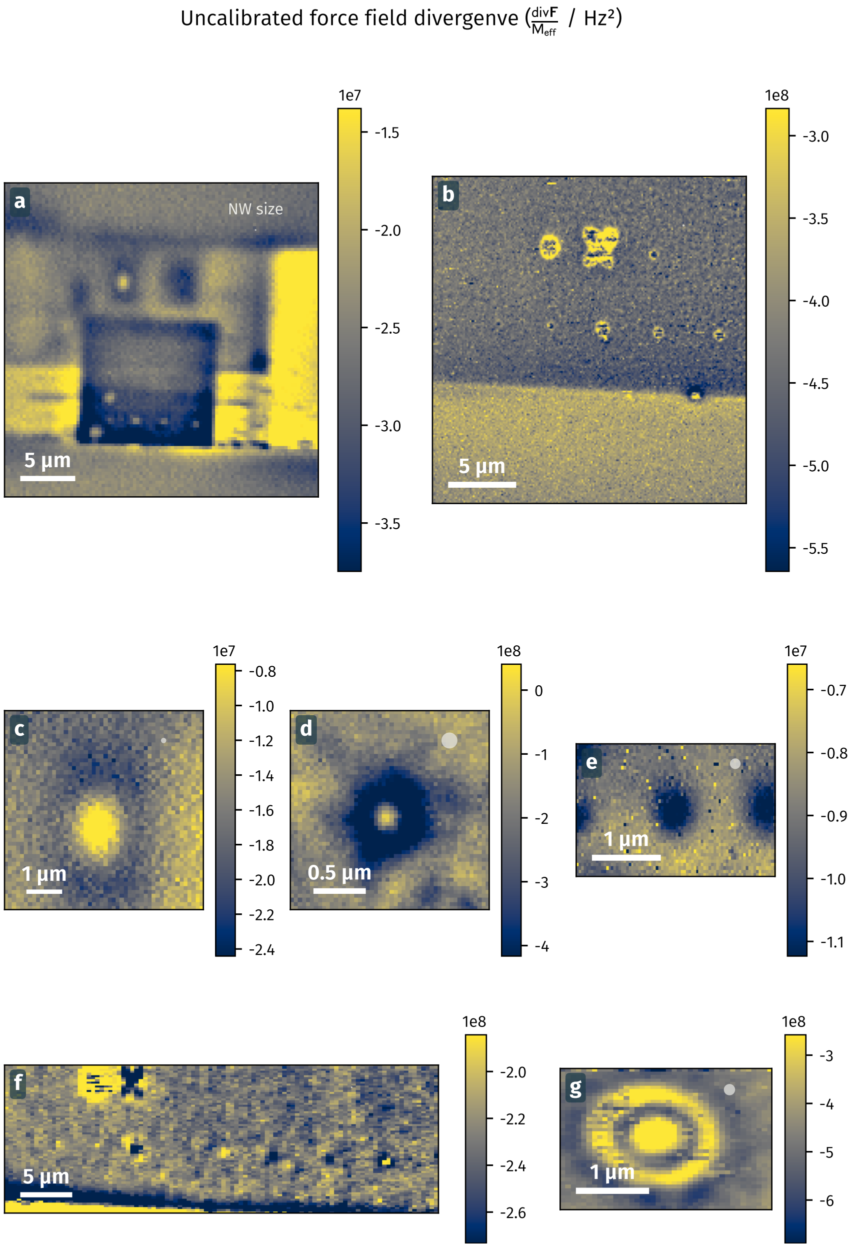

Fig. 2.7: Maps of the uncalibrated force field divergence[1] measured at a fixed values of the applied control voltage for orientation and localization purpose. (**a**) and (**b**) show the processed areas of two nanostructured cantilever beams in which holes were etched by focussed ion beam etching. Image (**c**) in the second row is a close up scan over a hole in the top region of the cantilever in (**a**) and (**d**) represents a scan above one of the smaller holes in the lower part of (**a**). (**e**) shows a row of holes on another sample and (**f**) and (**g**) were taken on the structures shown in (**b**). The different control voltages and local residual fields (as well as nanowire/sample properties) for each map cause a different appearance of similar structures between the images (e.g. high divergence values at hole edges in (**b**) vs dark circles in (**e**)).

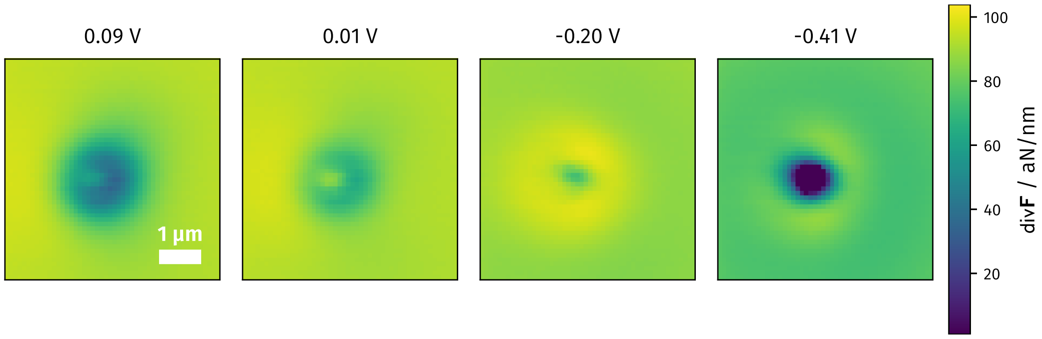

Fig. 2.8: Force divergence measured above the rounded tip at different voltages. While the smaller divergence values (blue), measured above the tip, indicate a trapping force for all applied voltages, the geometric shape of this force changes from a large trapping area for higher positive voltages with a small point of a high divergence via the inverse of this shape at −20 mV to a sharply pronounced circular region of trapping force at the largest negative voltage. The varying shape of the divergence can be explained by force contributions which depend on the position above the sample and that do not scale quadratically with the applied voltage. These contributions are associated to the existence of residual electric fields.

nanowire is attracted towards the stronger electric field above the tip, which means that the force would tend to trap the nanowire above the tip. Figure 2.9 illustrates this reasoning of a trapping potential.

A second observation in the results in Figure 2.8 is that the strength of the trapping (the *blueness*) depends on the voltage and is stronger for higher applied voltages. This effect is associated to the quadratic dependence of the force on the applied voltage.

The probably most important third observation is that the shape of the measured divergence strongly varies with voltage and even shows artefacts such as the small bright spot that appears in the region of small divergence above the tip at high applied voltages. These variations cannot be ascribed to the expected quadratic electrostatic force on the polarizable nanowire but suggests that another significant force contribution is present which scales differently with the applied voltage. In order to access the different force components it is therefore necessary to characterize the voltage dependence of the force field. To do so, we implemented a stable measurement procedure that samples the force parabola at each spatial point for progressively varied bias voltages. The technique and its results are subject of the next section.

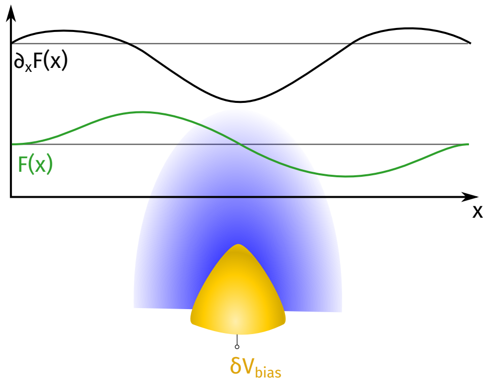

Fig. 2.9: Illustration of the trapping property of the force field above an electrostatic tip. When approaching the nanowire, it feels an attraction towards the increasing field gradient above the tip, thus a positive force $F(x)$. Directly above the tip, the horizontal force is zero but moving towards larger x, the nanowire experiences a force pulling it back towards the tip direction with a negative $F(x)$. Hence, the force is *trapping* the nanowire. The curve of $\partial_x F$ depicts the measured force divergence with a local minimum above the tip.

2.4 Measuring the electrostatic force parabola

To measure the force's dependence on the applied voltage, we add a point wise voltage scan to the measurement sequence (compare Section 1.5) where the applied voltage is swept from a lower limit to an upper limit and back. This bidirectional scan allows excluding hysteresis effects that may arise in presence of too large force gradients for example, and avoids abrupt jumps in the applied voltage. It is possible to perform an automated fit to the acquired divergence parabola and to redefine the voltage limits based on this fit. This is particularly useful during scans realized when approaching the surface. In general, a large voltage excursion, typically in the range of 1 V, needs to be applied in order to create a measurable force field at large distances, while a voltage in the mV regime is sufficient at small distances to create similar force fields.

The measured divergence has the expected parabolic shape as exemplarily shown in Figure 2.10 where the results for three locations above a pierced cantilever surface are presented. Here, we see the three cases with positive, negative and nearly no curvature of the parabolas. A linear shift of the parabolas is not immediately visible but one can observe a vertical offset of the parabolas' extrema. The curve above the hole's center shows a strong deviation of the parabolic shape in the regime of low voltages, which is most likely caused by the effect of a static displacement (compare box 1.a) that becomes significant when operating at larger fields and is characterized by a larger error of the measured divergence due to less stable PLL operations.

Figure 2.11a shows the recorded parabolas above the round tip and Figure 2.11b the divergence parabolas above a hole with a radius of 650 nm estimated from SEM images

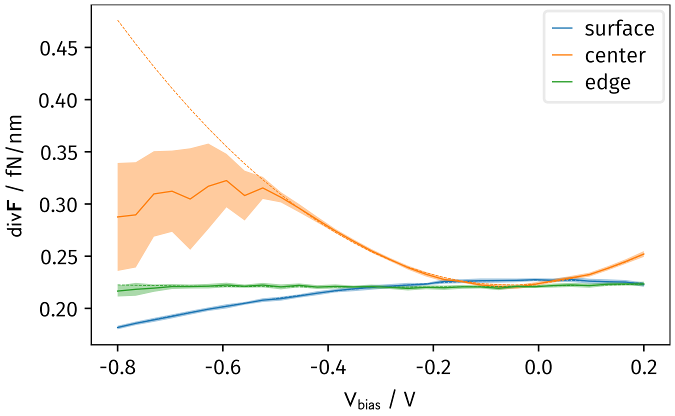

Fig. 2.10: Some of the measured parabolas at different locations above a hole in a metallic surface (see figure 2.11b). The shaded area presents the 2σ interval of the divergence obtained from the statistical error of the PLL. The dashed lines show the fit result of the parabolas. In order to achieve the good quality of the presented fits, we weight the data points by their error and exclude data from the fit where the error is too large or where the PLL phase is far from the lock setpoint.

of the cantilever's back. The colorscale shows the quadratic divergence coefficient that we will further call α. Both scans have been conducted with fixed voltage range with $V \in [-0.2; 0.8]$ V for both measurement.

The curvature of the divergence parabolas above the tip in 2.11a is negative everywhere, indicating that the electrostatic force is indeed purely trapping with its maximum directly above the tip. In this central region, we observe a small deviation from the ideal parabolic shape at the rightmost segment of each parabola. Since the shown data is obtained from the unprocessed resonance frequencies, acquired with the dual PLL frequency tracking, we interpret this deviation as measurement artefact that appears when the frequency lock operates at its limits, which is the case when the forces are strong enough to displace the nanowire statically (as mentioned above) and to rotate its eigenmodes. In practice, the rotation of the eigenmode basis is often the origin of a loss of the PLL lock, due to the reduction of the projected driven signal on the measurement channel. The phase error of the PLLs, as well as the amplitude of the demodulated driven signals – which is also recorded in realtime – represents a criterion to sort out the reliable data points and we typically neglect points where the phase error is larger than an equivalent frequency shift of 15 Hz (around 3 to 10 times the mechanical linewidth Γ) in the processing of the data. Additionally, each measurement at a given position and voltage consists of an ensemble of successive acquisitions performed during the measurement time per point that is in the range between 50 and 200 ms so that we can use the statistical error of this ensemble as weights in the fit routine.

The force divergence above the hole in Figure 2.11b also shows the strongest effects above the structure but instead of a trapping potential the quadratic force field above the hole is anti-trapping. The nearly flat parabolas at points far away from the hole get

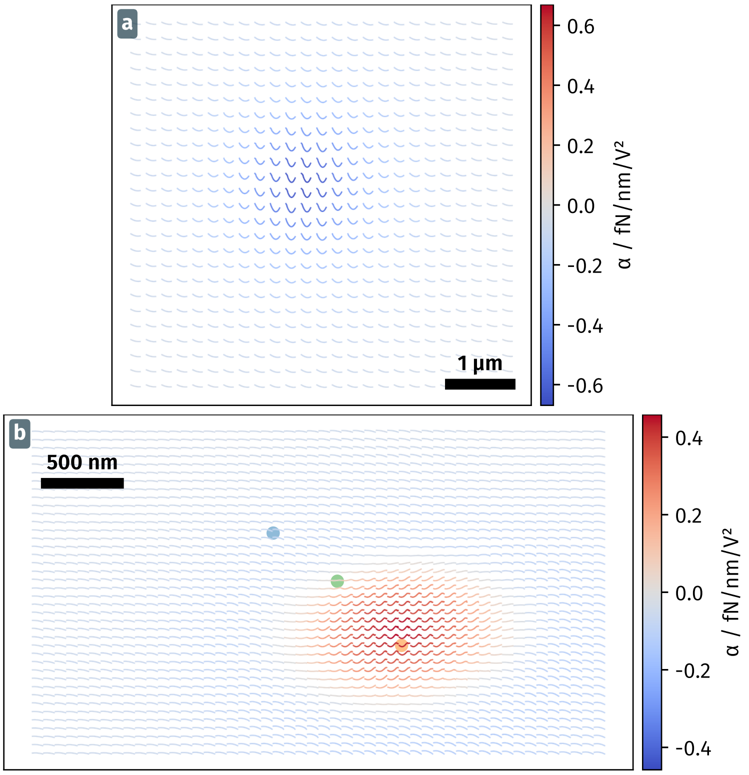

Fig. 2.11: The force divergence parabolas measured at each spatial point above a tip electrode (**a**) and a hole in a metal coated cantilever (**b**). The voltage range for the parabolas in both cases is $V \in [-0.2; 0.8]$ V. The heights of the drawn parabolas are calibrated to the common maximal amplitude, making the comparison between points possible. The color of the parabola indicates the local curvature α which is the term of the force divergence scaling quadratic with the applied voltage.

a clearly negative curvature when approaching the hole's perimeter before the curvature is inverted and reaches its maximum at the hole's center.

2.5 Mapping of the electrostatic force

Figure 2.12 shows the electrostatic quadratic force contribution above four different nanostructures. The force above the tip that has been discussed above is displayed in 2.12a. Compared to the force divergence measured at different bias voltages in Figure 2.8, the here presented α does not show any structuration other than the negative, trapping area above the tip. The map of a circular hole in Figure 2.12b shows a different pattern with a dominant positive α above the hole – meaning that the nanowire experiences an anti-trapping electrostatic force field. It is surrounded by a ring of negative values which indicates a locally trapping force field. This trapping ring is caused by the attractive electrostatic force towards the edge of the hole, where the electric field gradient is the most intense. Seen from the center of the hole, the nanowire is therefore attracted towards all directions since the electric field gradient increases uniformly. Thus, the hole's center represents an unfavourable rest position and the local force field is anti-trapping. The stiffness of the electrostatic anti-trapping force field remains however significantly smaller than the nanowire's restoring force, avoiding bi-stability or so-called lateral "jump to contact".

Measurements above flat sample structures that do not protrude much above the surface, such as the hole geometry, also allow exploration of the force fields originating from the surrounding substrate itself. Here, this can be seen as small irregular patterns that appear in the top part of the image, which are caused by a granular surface structure of the metallic substrate. The fact that these patterns are only visible at one edge of the image tells us that the sample or one of the translation axes is slightly tilted, so that the nanowire is closer to the sample at the top of the map than at the bottom. In order to see the effects from the intrinsic surface structuration, the nanowire-sample distance typically needs to be below 50 nm to 100 nm.

Figure 2.12c shows a structure similar to the hole but in the form of a cross. Again, the force field above the trenches which fully traverse the cantilever, is anti-trapping, which is visible in all four arms. The situation at the cross' center resembles that of a hole with a 2D anti-trapping strength and a larger value of α than for the anti-trapping 1D regions on the arms. We can also identify the attractive edges of the cross as slightly negative regions, surrounding the trenches, that are more pronounced in the right part of the image than on the left hand side which hints to a slight tilt of the scan. As a remark, those measurements are realized with a cross oriented along the uncoupled eigenmode orientations: as such, the structure of the force field along each arms is quasi uniaxial and does not lead to appreciable eigenmode rotations in those areas, which facilitates the measurement.

The intrinsic force map measured above a metallic surface is presented in the map 2.12e. The map, acquired around 50 nm to 100 nm above the surface shows mostly negative α varying on typical transverse dimensions of 100 nm showing a grainy structure. This

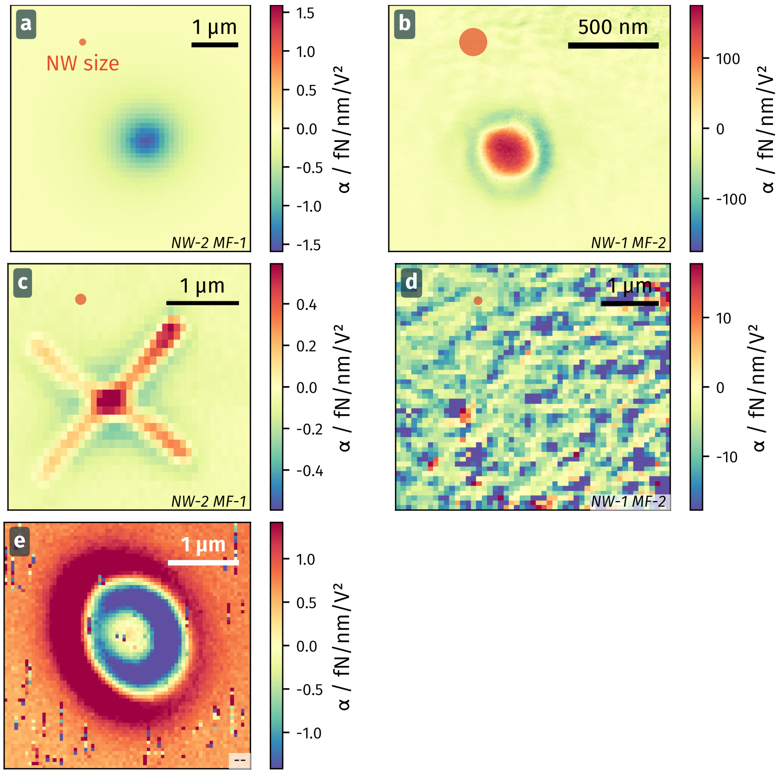

Fig. 2.12: Dipolar force maps above a tip (**a**), a hole (**b**), a cross like hole (**c**), a flat metal coated surface (**d**) and a metal coated disk (**e**). The disk has been measured by *Hugo Weltz* so the nanowire it was measured with is not in the list in box 2.b.

geometry typically recalls the grain structure observed on evaporated metallic layers (see SEM image 2.6e).

We will next focus on the geometrical electrostatic force divergence measured above different holes and take a look at the theoretical expectations for this type of structure obtained from numerical simulations.

2.6 Electrostatic force above a hole nanostructure

A geometric argument predicts that there should exist a region where a vertically polarized dipole is repelled by a hole drilled in a metallic plate: at infinity, the interaction strength is zero and thus the potential energy is identical with that at the position where it is vertically centred in the opening of the hole (here, the dipole field lines are perfectly normal to the opened plane). At distances farther away than the opening of the hole, the plate resembles a closed surface towards which the dipole is attracted, therefore there must be a vertically repelling region at shorter distances [64]. As such, the dipole will experience a vertically trapping point, at the inversion of the vertical force. As a consequence of the Earnshaw 's theorem, the force should be laterally repulsive at that location [47, 64].

While those remarks apply for a dipole and the nanowire is not completely equivalent to a dipole, due to its elongated geometry, it still is expected that it should experience a similar, laterally anti-trapping force field. The above observation of an anti-trapping force field can also be simply understood with the idea that the nanowire is attracted towards the edges of the hole, where the electric field is maximal.

Even though the nanowire probe is not sensitive to vertical forces, a vertically repulsive region implies a detectable non-equilibrium in 3D due to Earnshaw's theorem [47]. The example for a simple dipole indicates that geometrically more advanced sample structures come with more complex phenomena that can be probed with high sensitivity, using nanowire force field microscopy.

In previous setups it has been very difficult to approach surfaces in a safe and controlled manner but the employment of the quasi realtime force field measurement protocols now allows performing scans close to the surface of flat structures such as holes. With their characteristic variation from locally trapping to anti-trapping areas, they present an interesting test case.

Figure 2.13a and Figure 2.13b display the horizontal maps (parallel to the surface) above two holes of different sizes. Both show the same features of an anti-trapping α in the center and a ring with a trapping negative α at the holes' perimeter. This ring is wider for the larger hole (2.13a) which can be also seen in the line cuts shown in panels 2.13c and 2.13d. The first map has been taken at a larger height of about 300 nm, compared to the second map of the smaller hole, which was measured close to the surface between approximately 50 nm to 150 nm. A consequence of the larger distance is that small distinct features smear out.

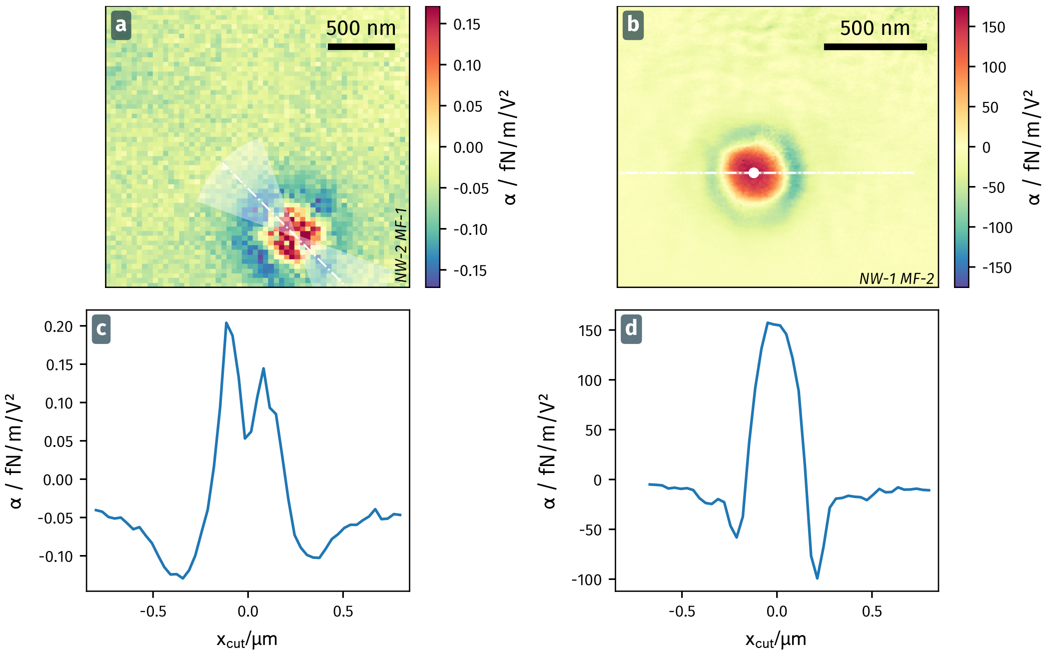

Fig. 2.13: The electrostatic quadratic force measured above two larger holes with ≈ 500 nm diameter (**a,c**) and ≈ 400 nm diameter (**b,d**) is shown as horizontal map and line cut through the hole (bottom). The white dashed lines in the top plot row represents the orientation of the line cuts, the shaded area covers the data points that were averaged in order to reduce the noise in the line cut. The first map has been measured at a height around 300 nm and the second closer to the surface around 50 nm to 150 nm. In both maps the blue colored regions represent the trapping force field around the edges of the holes and the positive α are created by the anti-trapping field in the center of the hole.

Panel 2.c: Measuring with different mode families

In Section 1.1 we discussed the properties of nanowires as force sensors and saw that the second family of eigenmodes, which has one node in its longitudinal oscillation pattern, can be found at about six times higher frequency than the first eigenmode family. Since the force sensitivity scales inversely with the frequency of the oscillator, it is beneficial to work with the first eigenmode family if the maximum force sensitivity is desired. Additionally, the resonant mechanical response of the first mode is six times larger, so that the driven signal is slightly enhanced as well.

However, there are cases that benefit from the use of the second mode since, firstly, it is less sensitive to strong local force gradients and can thus be used to measure at smaller height above the sample where a frequency tracking of the first mode would already fail due to the large eigenmode rotations induced by the force field. Secondly, the higher frequency and the generally larger linewidth of the second mode family allows faster measurements as one can work with a larger bandwidth of the PLL's phase detection. Thirdly, the higher frequencies are also generally associated to a larger frequency splitting $\Omega_2^2 - \Omega_1^2$, reducing the eigenmodes' rotations which scale with the ratio of transverse components g_{ij} ($i \neq j$) to the mode splitting.

In the case of measurements on nanostructured surfaces, one can often benefit from the higher frequencies of the second mode family due to the advantages stated above. The reduced force sensitivity is only a minor drawback since the force gradients measured close ($<$ 500 nm) to the sample are rather strong (in the fN nm^{-1} regime). Therefore, some of the presented results in this section are realized with the first mode family and others with the second mode family. While, conceptually, there are no differences in the mathematical description of the dressed modes of the first or second mode family, an experimental confirmation can underline this point.

Figure 2.14 shows the same vertical force divergence map above a small ((280±10) nm diameter, measured with SEM) hole, measured with the first and second mode family. Notably, the quality of the second mode family scan is better in terms of noisiness close to the surface, while the first mode family scan shows large amounts of noise close to the surface in the lower area of the maps. Still, both maps reveal the same structure of the force field divergence with similar amplitudes.

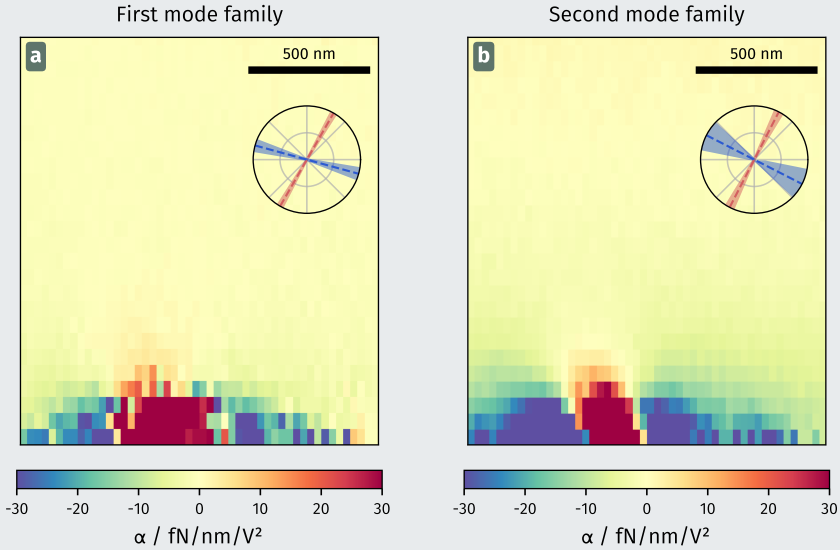

Fig. 2.14: Vertical force divergence map above the same hole measured with the first mode family (12 648 Hz and 12 832 Hz) (**a**) and the second mode family (77 460 Hz and 77 922 Hz) (**b**). The scans were conducted separately. The mode orientations of the eigenmodes of both families that are indicated by the two insets are roughly identical during the measurement. The plotted α are adjusted so that the value measured at the largest height (3.4 µm, out of the shown plot limits) is zero in both measurements.

This comparison between first and second mode family shows that both can be used to measure the force gradient and that one can adapt the used mode family to the measured sample in order to either boost the sensitivity using the first mode or to increase measurement speed and stability with the higher frequency second mode family.

The vertical dependence of α measured above a hole is shown in Figure 2.15a for the first micrometer above the surface. Those vertical maps were taken along the orientation of an uncoupled eigenmode to minimize the eigenmode rotation. The nanowire to sample distance can be determined much easier in such vertical maps since the last few tens of nanometers above the cantilever often carry strong lateral electrical fields that create large force gradients in which the resonance tracking with the PLL becomes instable during scanning. The bottom region in the plot shows such a region of instability, which is not necessarily a sign of a contact between nanowire and sample, as often, the mechanical noise spectra can still be observed in such regions. However, in the right side of the image, the nanowire is probably in contact with the sample. Due to the unstable PLL lock under large eigenmode rotations and the possibility of a contact between nanowire and sample, the scan is performed by progressively approaching the sample in the vertical y-direction for each horizontal point. Thus each line starts at a stable reference height far away from the surface.

We again find the characteristic transition from negative to positive values of α when approaching the hole's center. The negative regions over the attractive edges of the hole vanish more rapidly with distance than the positive central region that at distances above 500 nm is the only remaining sign of the hole. The line cuts in panel 2.15c obtained at two different heights above the surface confirm this observation.

Comparing the two negative regions in the short distance line cut, one can see that the left hand side reaches only one third of the minimum α of the right hand side. This is an effect that can be attributed to the 2.5° inclination of the sample. It is not visible for the larger distance line cut.

The right hand side panels 2.15b and 2.15d show the results of a numeric finite element simulation that we have conducted using the *COMSOL Multiphysics* electrostatics module. The simulation geometry is outlined in Figure 2.16 and consists of a nanowire domain and a model of the cantilever with a circular hole that has a conically increasing diameter from top to back surface. This represents the ion beam etch profile of the hole in the sample, when drilling the hole from the bottom side. The nanowire length is reduced by a factor of ten in order restrict the simulation time to a feasible duration since it scales with simulation volume. While the force calculation is not affected by this approximation since the electric field gradients are strongest at the end of the nanowire, the electric field intensity of the experiment cannot be reproduced exactly. However, the

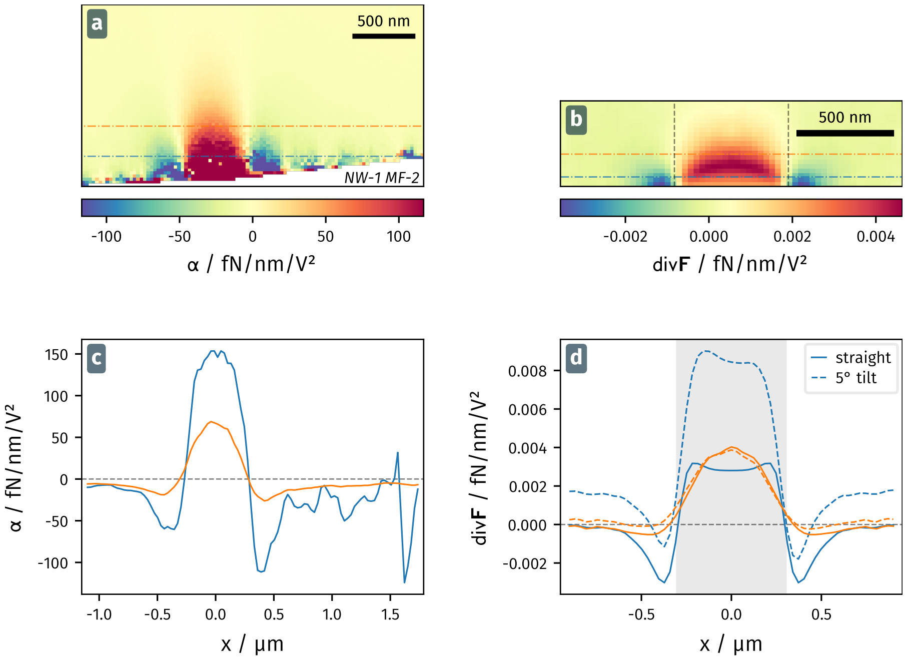

Fig. 2.15: The vertical map of the dipolar force divergence measured above a hole in a cantilever is shown in (**a**) and compared to a simulation (**b**). The lower plots show a linecut at the height of the dashed lines for the experimental (**c**) and simulated (**d**) results. The linecuts for simulation also include the case of a tilted nanowire (calculated based on the projected force simulated for the straight nanowire). While the amplitude fo the force divergence does not match between simulation and experiment, most likely due to the reduced length of the nanowire in the simulation, the curves show good quantitative agreement. Particularly the simulation for the tilted nanowire reproduces the deeper dip on the right of the central positive domain that is observed in the experiment. The tilt in the map in (**a**) is probably caused by two effects, a small tilt of the nanowire with respect to the sample and a tilt of one of the piezo scanning axes.

simulation gives a reliable indication of the shape of the force field and, in general, also an estimation of the expected order of magnitude of the force gradients.

The results in 2.15b show the same shape as for the experimentally measured hole, again with a positive region that extends further into the vertical direction than the two surrounding negative areas. Panel 2.15d presents a horizontal line cut of the simulation results at a distance of 150 nm. The shape of the curve is similar to the experimental results at small height. Adding a 5° clockwise tilt[2] to the nanowire, one obtains the dashed curve that agrees even better with the experimental results. Caused by the setup design, it is only possible to adjust the nanowire's angle to a small degree by mechanically bending the supporting tungsten wire. With the recently implemented improved sample

---

[2] Here we just calculate the horizontal force gradient in the tilted nanowire's coordinates using the simulation results of the straight nanowire, by combining the vertical and horizontal forces simulated in the vertical geometry. Simulation with truly tilted nanowires have shown that up to an inclination of 10°, the measured force can be safely approximated by a linear combination of the force vector simulated in the vertical configuration along the projection of the measured force on the tilted nanowire axis.

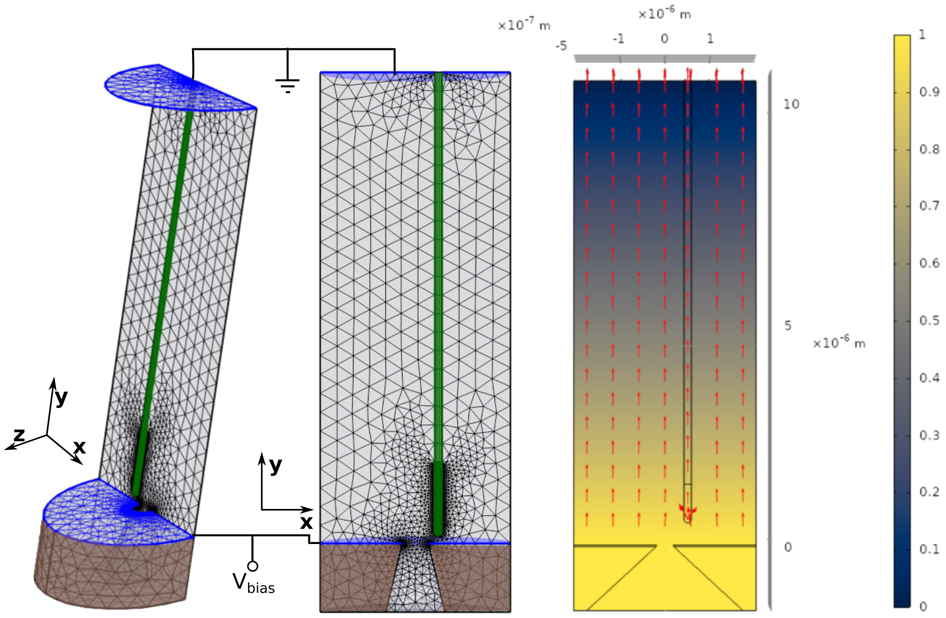

Fig. 2.16: *COMSOL* Simulation geometry for a 3D electrostatic study with force calculation on the 10 μm long nanowire (green) above a hole in a metal coated Si substrate (brown). The electrodes are depicted in blue. The mesh is refined at boundaries with sharp curvatures and at the end of the nanowire. The right image presents an example of the simulated electric potential and field (red arrows).

holder it is now possible to adjust the tilt angle of the nanowire so that measurements will not be affected by this geometric imperfection.

2.7 Electrostatic force above a metallic tip

Figure 2.17a presents the quadratic coefficient of the force gradient obtained from fits to the acquired parabolas. The panels 2.17b and 2.17c show vertical measurements conducted along the black and white dotted lines. The horizontal map has been measured about 200 nm above the tip, indicated by the respective dotted lines in the vertical maps. The horizontal scan direction of the vertical maps follows the eigenmode orientation of the nanowire that is the direction with the least mode rotation. Little rotation means stable readout, orienting the scan direction along the eigenmodes therefore ensures the best measurement conditions. While the divergence coefficient for the horizontal map and the *yz'-scan* have similar maximal intensities, the absolute divergence measured in the *yx'-scan* is smaller and the map shows artefacts at small y close to the tip. These are the effects from measurement instabilities at small sample-nanowire spacings. The smaller amplitude is likely caused by a small offset of the scan with respect to the center of the tip electrode.

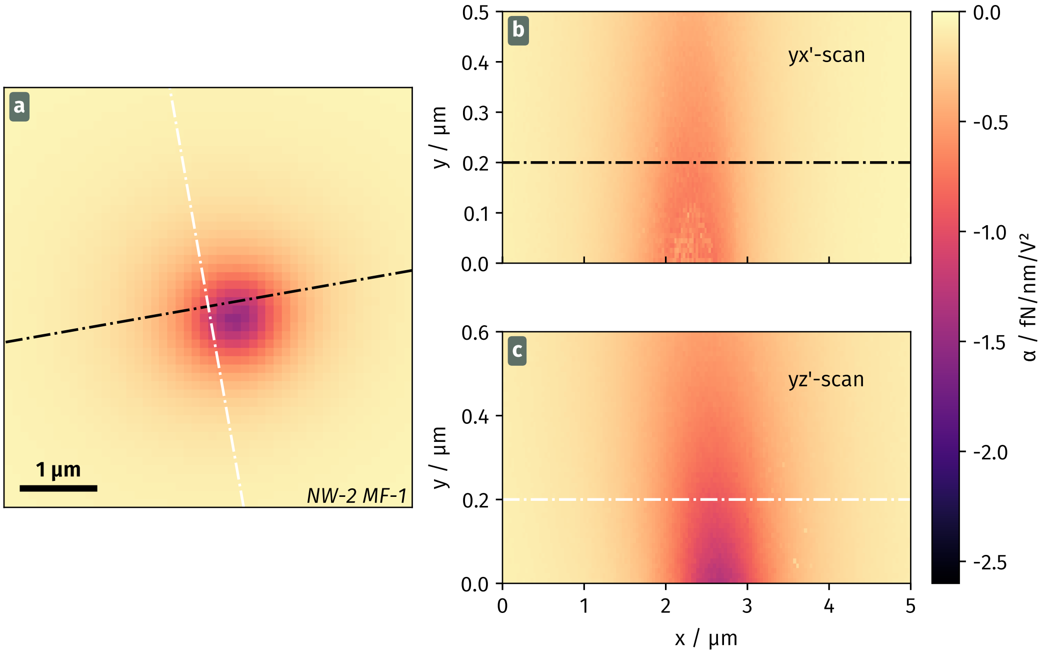

Fig. 2.17: The quadratic force divergence α above a rounded metallic tip (tip curvature radius 250 nm) is measured in the horizontal plane (**a**) and for two vertical cuts along the eigenmode orientation of the nanowire (**b,c**) in the rotated coordinates (x', z').

2.7.1 Comparison with simulations of the electrostatic force

In order to have an estimate of the expected electrostatic force gradient, we perform a finite elements simulation using the electrostatic module of the *COMSOL Multiphysics* simulation software. The electrostatic simulation provides access to the electric fields at each point of the evaluation grid of the simulation and implements the integration of the Maxwell stress tensor over domain surfaces to calculate the electrostatic force on objects. Figure 2.18 outlines the simulation geometry. We model the nanowire with the material properties for SiC that are provided with the software, and the electrostatic tip with the properties of gold. However, since we apply a fixed potential to the tip's surface, its material properties do not affect the simulation result[3]. The blue shade highlights the electrodes in the illustration with the ground electrode being the upper boundary surface of the simulation geometry. An optional charge can be added at the place indicated by the green marker at the end of the nanowire. The simulation space represents one half of the full geometry due to its symmetry, in the simulation we vary the nanowire's position along the x and y directions.

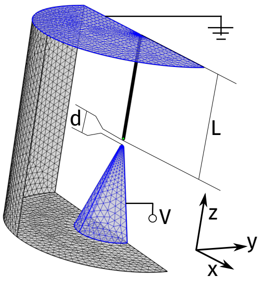

Fig. 2.18: The meshed geometry used in the electrostatic simulation of the force on a nanowire in the electric field created by a conical tip electrode with 250 nm curvature. The simulation axes are different from the experimental axes (y and z are swapped). Simulations are typically performed for a number of coordinated in the *xz* plane.

Panel 2.d: Gradient $\partial_x F_x$ vs divergence $\mathrm{div}\mathbf{F}$

In order to reduce the time needed for simulations, we typically perform linescans of the nanowire above the 3D simulation geometry in the vertical plane. Thus, the measured horizontal force acts only along one axis with the perpendicular force component being zero due to symmetry. From such a measured force F_x, one can easily deduce the force gradient $\partial_x F_x$ along the scan axis. However, the gradient only compares with the force divergence $\mathrm{div}\mathbf{F}$ up to a certain degree as one can see in Figure 2.19 for the simulated force field above an electrostatic tip electrode. In particular, one can make the false assumption that the measured force divergence should inhibit positive regions at the sides of the tip if one only looks at the force gradient. Also, as logical consequence of the symmetry, the maximum divergence is about a factor of two larger than the gradient.

---

[3] Indeed, the material properties matter if one wants to calculate the field in a body. The properties for all metallic objects (where the internal fields are zero), are therefore irrelevant.

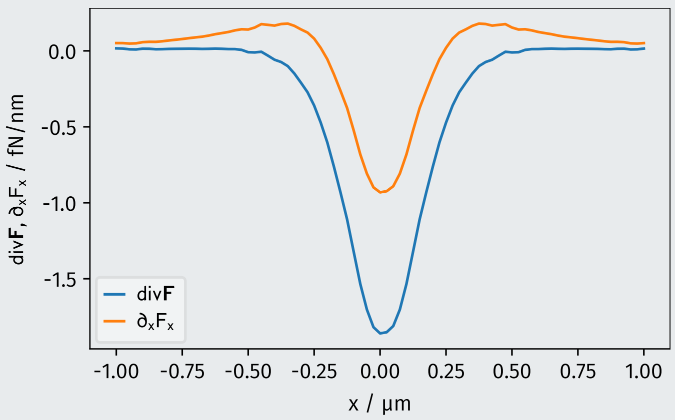

Fig. 2.19: The force gradient and force divergence for a nanowire of 10 μm length and 160 nm length at a distance of $d = 100\,\mathrm{nm}$ above a round tip with 250 nm curvature radius. Both curves show similar features, however, the force divergence does not show positive values, while the gradient does. Even a qualitative comparison of the measured force divergence to the simulated gradient can therefore be misleading.

The force divergence is the most accessible and informative quantity from a force field measurement and one typically wants to compare the experimental results to the simulated force divergence. In order to do so, the divergence can be calculated from the simulated gradient. Exploiting the circular symmetry of most of the regarded nanostructures, one can regard F_x as centric radial force F_r and thus construct a 2D map $F_r(x,z)$ from which one then infers the 2D force field

$$F_x(x,z) = F_r(x,z)\,\cos(\theta(x,z)),\;\; F_z(x,z) = F_r(x,z)\,\sin(\theta(x,z))$$

with $\theta = \tan\frac{z}{x}$. Having calculated F_x and F_z one now has access to the force gradients in 2D and to the force divergence $\mathrm{div}\mathbf{F} = \partial_x F_x + \partial_z F_z$.

Figure 2.20 compares the measured force divergence in the vertical maps of Figure 2.17 with simulation results. Figures 2.20a and 2.20b present linecuts at different heights through the yz' and yx' vertical measurements, where x' and z' are approximately the direction of each eigenmode[4]. While all curves of the yz' map are centralized around the same z', the curves in the yx' map are shifting towards the left for larger heights. This can either be a result of a non-perpendicular constellation between nanowire and sample, or a misaligned movement of the piezo axis. Figure 2.20d therefore shows the simulated force divergence for an inclined nanowire above a tip. While the shift to the left is basically not visible, the divergence at positive x' becomes slightly positive for small distances. This is contrary to the curve in 2.13b, where the divergence on the left side is increasing for decreasing distances. It is therefore likely that a movement of

---

[4] Performing scans along the direction of an eigenmode minimizes the mode rotation and therefore prevents the case where the one of the mode is not detected by one of the measurement channels.

the piezo stage in y also displaces the sample along x'. A reason for this could be the mechanical constrains imposed by the electrical connection of the sample.

Comparing experiment with simulation, one makes the general observation that the horizontal span does not agree. In order to match the simulation to the experimental results, the horizontal size needs to be doubled. We do not have an explication for this difference. One possible, but unlikely explanation is that we conducted the measurement on the wrong electrostatic tip as we worked with two types of samples, having both, tips with a 250 nm and 500 nm curvature radius. However, despite this disagreement in the horizontal size, one can make some qualitative observations.

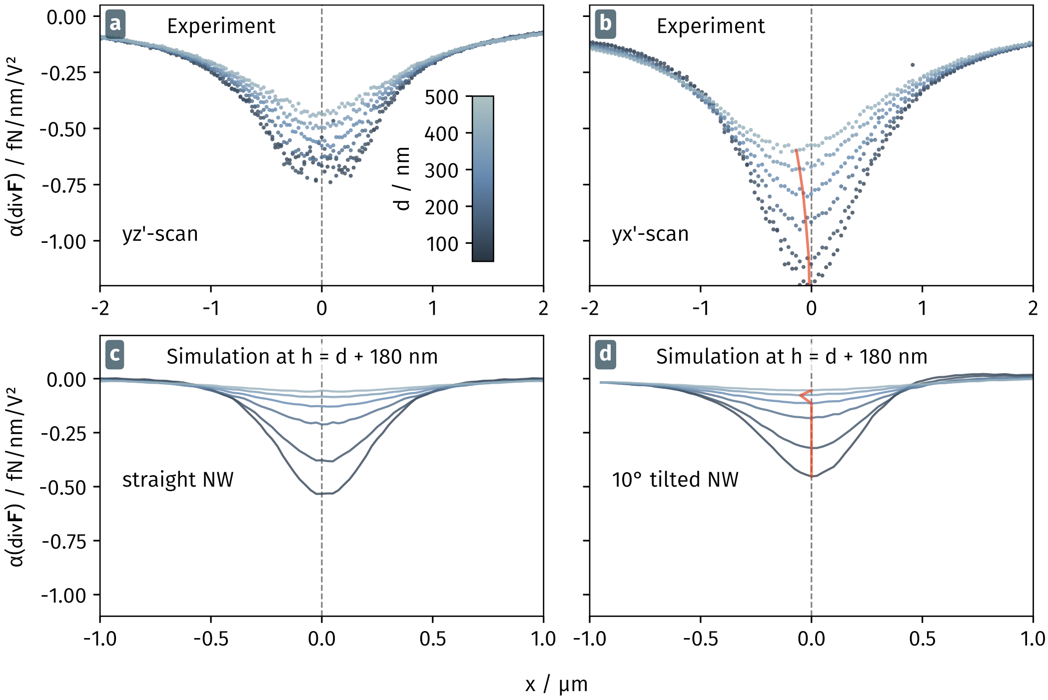

Fig. 2.20: Linecuts through the vertical measurement above the round tip in Figure 2.17 (**a**,**b**) are compared to the simulation of a straight wire (**c**) and a 10° tilted wire (**d**). The horizontal axis of the simulations is stretched by a factor of two in order to match the experimental data, possibly due to a mistake in the measurement (a measurement on a tip with larger tip radius). We retrieve similar shape and amplitude of the simulated data when adding a vertical correction of 180 nm to the simulated results. The measurement in the *yx*′ plane is subject to a non-perfect scan aligment as one observes a shift of the data to the left when increasing the measurement height (highlighted by the orange line).

Firstly, the experimental data is decreasing more strongly when approaching the center from either side, than the simulated curves. This is possibly caused by the cantilever beneath the tip which adds a background field. One would not expect such an effect to appear along two perpendicular axes, but due to the rotation of the measurement coordinates ($x, z \rightarrow x', z'$) in order to match the eigenmode orientation of the nanowire, the force field created by the cantilever can affect both measurements. However, the fact that the decrease towards the center is equally strong for both scans, and the fact that the horizontal map in Figure 2.17a does not show any asymmetry suggest that the difference between simulation and experiment is another one.

Secondly, we point out that, in order to retrieve a similar form of the simulated shape, we need to shift the vertical zero by 180 nm with respect to the measurement. This is an effect of the uncertainty in the experimental vertical zero, which we can only determine as the height where the measurement fails (the PLLs loose track due to extreme frequency shifts). However, this height can still be quite far above the surface. The criteria at which the force gradient get too large fore a linear operation is given by their value compared to the mechanical stiffness $k_m = M_{\text{eff}}\Omega_m^2$of the nanowire. For the two modes of the nanowire this amounts to 11 fN and 22 fN respectively, which is about one order of magnitude larger than the measured force gradients. Still, the stability of the PLL can fail before $\partial_x F_x = k_m$, so that we can assume that the closest curves suffer exactly from this effect and that the real distance to the tip is about $>$ 100 nm larger than the estimation based on the measurement.

More generally, this effect determines a fundamental limit of nanowire force microscopy: If the overall force field is large enough that the force gradient is comparable to the stiffness at small NW-sample separations, it becomes difficult to impossible to resolve smaller, fast decaying forces such as the Casimir force, or small scale local variations of the force field for which the nanowire needs to be very close to the sample.

2.8 Contribution from parasitic fields

We have already seen above, in the stress tensor discussion, that the residual electrostatic fields, which do not depend on the bias voltage, are responsible for both, a linear contribution in the bias voltage to the electrostatic force, and for an additional force, independent on the bias voltage. The first contribution causes measurable effects as they shift the force parabola, so that this offers a possibility to explore them experimentally. This section deals with possible origins of the residual electrostatic fields and of the linear force contributions. Since those residual fields cannot be compensated simply by biasing the sample, they will have an impact in the Casimir force measurements.

Figure 2.21 picks up the force fields measured above the nanostructures presented above in Figure 2.12 and shows the V_0 of the electrostatic force divergence. Here, one observes a variance of up to two volts for measurements close to the sample surface. At the regions where the quadratic contribution α transitions between negative and positive, the V_0 which is calculated as $V_0 = \beta/2\alpha$, becomes infinite. In Figure 2.21 they are marked as abrupt transition from blue to red.

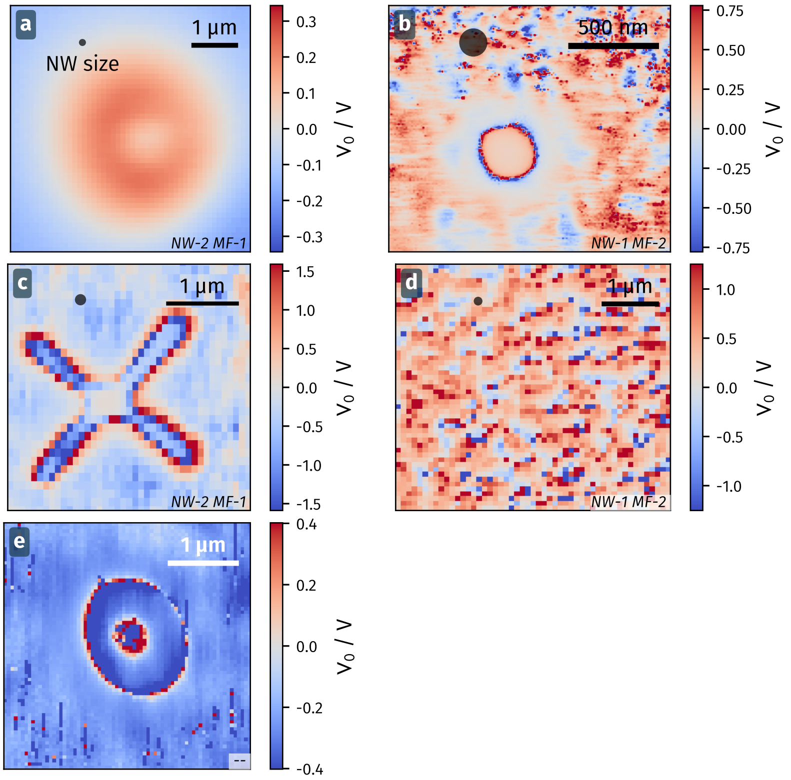

Fig. 2.21: The V_0 measured above the nanostructures presented in Figure 2.12. At those regions where a large positive V_0 changes to a large negative value, the divergence parabolas are nearly flat (α is small). This is the case at the edges of the hole structures in (**b**) and (**c**), as well as for the disk in (**e**). Above the substrate in (**b**) and (**c**), one observes the variations of the measured V_0 that is caused by the surface patches.

2.8.1 Patch effects in the experiment

A first phenomenon that is responsible for force contributions scaling linearly with the applied voltage are surface patches as introduced in Section 2.1.4. A characteristic of surfaces, beside their topography, is their electrostatic contact potential that depends on the crystallinity, surface ligands and impurities of the metallic coating. We call areas that have a homogeneous electrostatic contact potential electrostatic *patches*. However, on a real surface, they are of finite size, which causes spatial fluctuations in the contact potential. Also, since the metallic support tip and the sample are not made of the same material, even when the bias voltage is zero, there will always remain a residual electric field. Above a perfect metallic sample, the former would be spatially homogeneous, so in the following, we will discuss variations around this mean residual field. The method to estimate this mean residual field will be discussed in the next chapter.

The deposition method of the metal influences both parameters, topography and contact potential, up to a certain degree. The samples discussed in this project were partly purchased already coated with a metallic layer or coated by thermal evaporation without special measures to minimize the surface roughness. With the deposited layer measuring only about 20 nm in thickness, we expect variations of a few nanometer around the mean thickness, based on the experience with the local evaporation setup. The spatial extension of these irregularities on the surface is typically in the order of tens to hundreds of nanometers. A better estimate of their topographic variations could be obtained by atomic force microscope cartography of the surface which has not been done on the samples employed in this work at the moment in order to avoid sample contamination. Other studies, using Kelvin probe force microscopy (KPFM), have found that a correlation between topography and contact potential does not necessarily exist [39], hinting towards a contribution from contaminants.

While the quadratic electrostatic force contribution (α) is caused entirely by the topography of the electric field, the linear term (β) presents a mixture of the parasitic fields E_p and the fields created by the sample electrode E_V. The most important origin of parasitic fields are differences in the local contact potential V_{patch} on the sample (see Section 2.1.4), unlike other experimental techniques as Kelvin probe force microscopy (KPFM) we cannot measure this workfunction difference directly, but we can define a similar quantity. Therefore, we rewrite the quadratic expression for the force field divergence in polynomial form

$$\operatorname{div}\mathbf{F} = \alpha V^2 + \lambda V + \gamma, \tag{2.13}$$

as factorized expression

$$\operatorname{div}\mathbf{F} = \alpha (V - V_0)^2 + \gamma'. \tag{2.14}$$

Here we we can define a local offset potential V_0 based on the measured coefficients α and λ[5].

The first two plots in Figure 2.22 show the quadratic coefficient and the offset potential for the force field's divergence above surface areas at different altitudes. The slices shown in 2.22a and 2.22b map an area of the platinum coated surface of one of the purchased AFM cantilevers, in which the holes are drilled. Both, the quadratic coefficient and the local offset potential show a grainy structure that smoothens with increasing distance. A similar grain structure has been observed in *AFM* measurements performed on a gold covered sample (2.22c). The offset potential in 2.22b loses its visible structuration less rapidly with increasing distance than α. The size of the visible domains is similar for α and V_0, their spatial correlation is not clearly evident from the maps. We did not perform a quantitative study to compare the spatial distributions of the different force components due to the difficulty to acquire highly resolved large maps at small nanowire-sample separations. Still, Figure 2.23 presents a linecut through the medium height map, showing the quadratic, linear and static force gradient. Here, a one can see a clear similarity between the three terms with some distinct differences, which is nor-

---

[5] This potential V_0 is a theoretical value which minimizes the measured 2D force divergence. It does not have physical counterpart like the contact potential in classic KPFM which is basically the difference of the workfunctions in the involved materials. This is due to the fact that the nanowire measures the force perpendicular to the electric surface fields. In simulations we have seen that the V_0 measured with a metallic nanowire approaches the contact potential.

mal as the linear term is also related to the voltage dependent fields which determine the α coefficient. The constant term γ, which is about twice as large in amplitude as the other terms, shows that the large part of the measured force originates from linear effects (geometrical, quadratic effects do not affect the constant term).

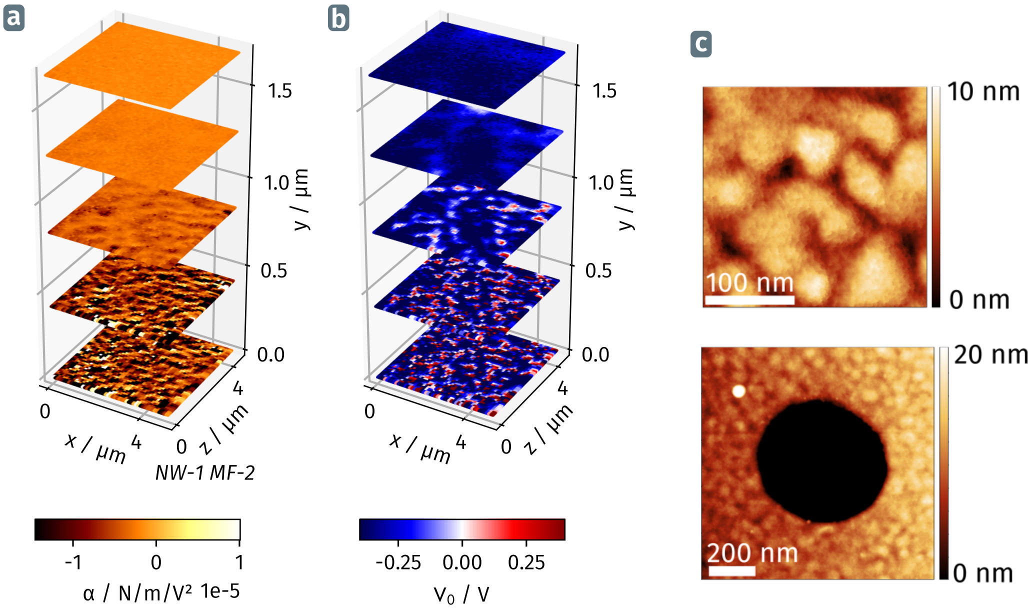

Fig. 2.22: (**a**) The quadratic coefficient of the force field's divergence above a planar metal surface without structuration is shown at five different measurement heigths. (**b**) shows the offset potential V_0 above the same 5 by 5 µm area with 51 by 51 px resolution. Both maps show pattern with a size of a few hundreds of nanometers at small height y that become less distinctive with larger distance. The *AFM* images in (**c**) were measured above a similarly prepared gold surface and show a characteristic size around 100 nm of the surface grains with a structuration in height up to 10 nm.

In Figure 2.24, the panels 2.24a and 2.24b show the same quantities for another area on the surface. The increasing resolution from lower to upper half of the images is due to a slight tilt of the sample. Again, the size of the features in both images is comparable and one observes that the offset potential shows a clearer structuration in the lower half of the image while the variations in α are less pronounced. The sort of vertical line separation, visible on the left third of the image, represents the boundary between two domains, such as those illustrated in 2.24c. Here, we see the force divergence measured at a fixed potential above the section of the cantilever on which holes were etched with focussed ion beam etching. At the lower and upper regions of the map, the edges of the cantilever are visible. The drilled holes are discernible as four holes arranged equidistantly along a line in the lower part of the large dark square. The dark rectangular regions correspond to the areas that have been imaged in scanning electron microscopy after the structuring of the cantilever. During electron beam imaging the bombardment of electrons can

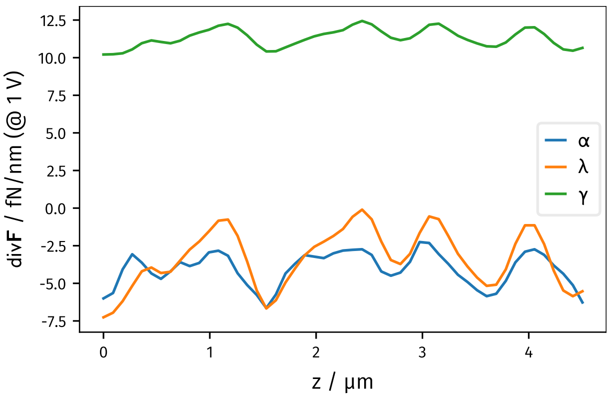

Fig. 2.23: The linecuts through the third measurement in Figure 2.22 (z=0.8 µm) show the quadratic α, linear λ and constant γ force divergence, at a bias voltage of 1 V.

damage the existing surface structure leading to a change of the local offset potential, but they could also start etching the surface, which would increase rugosity.

Another probable cause of surface destructuration is electron beam induced deposition (EBID) of carbon during the imaging. In this process, carbon from evaporated organic molecules binds to the surface at the position of the electron beam [77]. Even in clean environments, organic residues that are the source of the carbon, are present in the vacuum chamber of the microscope or on sample and sample holder. The measurement shown in panel 2.24a and 2.24b has been conducted on the transition from a clean area that had no visible surface contamination due to electron beam imaging on the left hand side, to a contaminated region on the right hand side. While both sides show a similar structuration of quadratic coefficient α and V_0, the contaminated region has a larger amount of areas with positive V_0 than the left hand side.

This potential difference can be caused by a modification of the work function of the material, or by dissimilar contact potentials on neighbouring patches, which is hardly quantifiable using the presented results from the 2D force field measurement due to the absence of external control of those surface fields (see Section 3.5). The only tuning option is, by experimental design, the control voltage V_c applied on the sample which creates a field along the vertical axis between the sample and the grounded nanowire support as illustrated in 2.24d. Horizontal fields, like those between neighbouring patches, can therefore not be compensated directly, so that the measured V_0 is a result of the combined linear effect from the local patch landscape. We also observed that the local offset potential that needs to be applied to get to the parabola's extremum, increases significantly as we approach the surface with the nanowire, even over the values presented in Figure 2.22 up to the order of a few volts. Due to the strong spatial variations, no stable operation of the force measurement scanning setup is possible in this regime and we restricted our use of detailed large area scans to larger sample-nanowire distances.

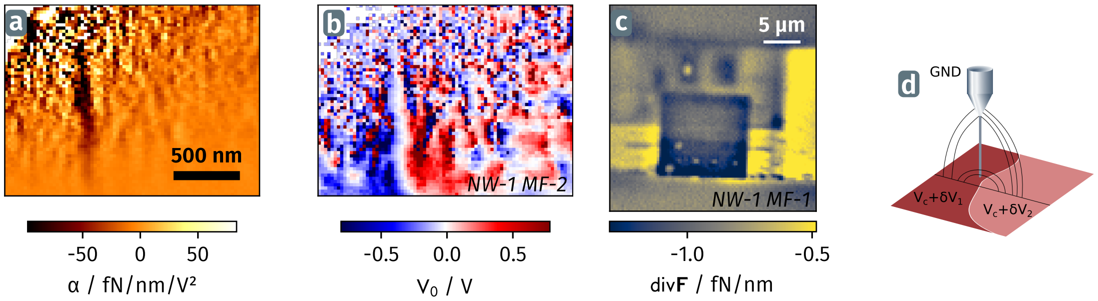

Fig. 2.24: (**a**) and (**b**) present α and V_0 above the boundary between a clean surface area (left part of each plot) and an area that has been exposed to electron irradiation during SEM imaging (right part of each plot) which led to a change in the measured offset potential. A larger spatial overview of the effect of electron beam irradiation is shown in panel (**c**) that plots the force divergence for a fixed applied voltage above the area in which the cantilever surface has been structured. The cantilever traverses the image from left to right with its edges visible in the top and bottom of the image. The dark rectangular areas are correspond to regions imaged in the SEM while the yellow areas have not been exposed to the electron beam. (**d**) outlines the electrostatic field above two patches with the field created by the control voltage V_c that creates a vertical component, while the difference of the patches contact potential δV_1 - δV_2 creates a field which is independent of V_c.

Panel 2.e: Sample degradation

Despite the nanowire force measurement being a principally non destructive measurement technique since contact between sample and nanowire is avoided, other effects can occur during measurements which can degrade the sample. Two important mechanisms are:

1. Induced deposition of particles attracted by the high intensity laser waist
2. Change of the material structure at zones of high electrostatic field

In the first effect, small particles still present in the vacuum environment can pass the laser beam and are accelerated towards the sample where they stick to the surface. In the SEM images in Figure 2.25 they are visible as white spots. When imaging the full cantilever their concentration is larger at the side facing the laser beam which confirms our interpretation of their presence.

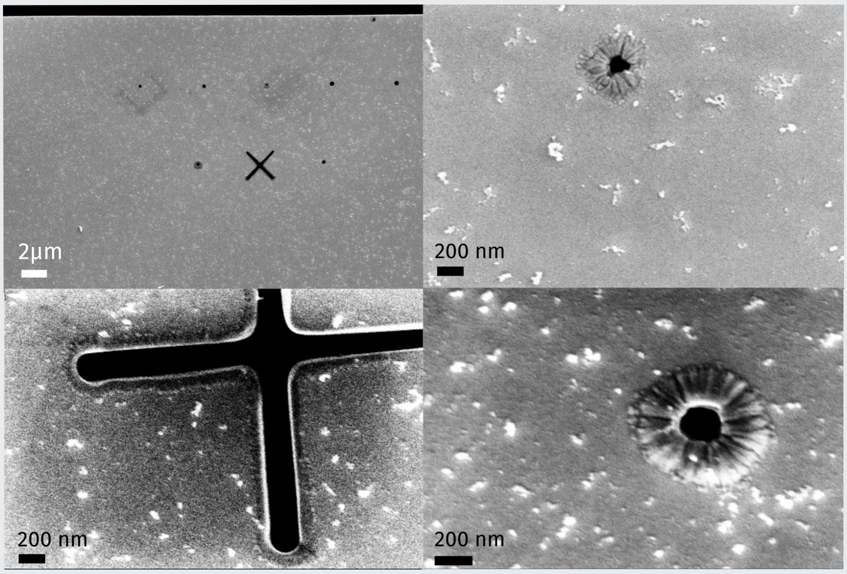

Fig. 2.25: A SEM image of the measured area after force measurements. The top left image shows an overview of the structured area with small debris scattered over the surface whose concentration is larger close to the imaged area. The right images present two different closely studied holes that show some deposition of unclear origin at their perimeters. The cross in the bottom left image presents similar structuration at its edges.

The second effect is more difficult to explain and a detailed investigation is required to understand it better. On the post-measurement SEM images, we observe an additional deposition at the holes that were measured with the nanowire and see similar formations at the edges of the cross. The degradation of holes has already been observed during force measurements but only on some, extensively measured structures. This is confirmed with the SEM images. While only superficially studies holes were not affected those where multiple detailed measurements were performed are most strongly degraded. Comparing the hole sizes pre- and post-measurement, we observe that the holes became smaller due to the degrading effects.

The explanation of the observations remains guesswork up to this point. It is possible that additional material deposits at the regions of strongly confined electrostatic field when the nanowire scans closely above the hole edges. Another explanation would be that a tunneling current can occur when the nanowire is very close to the edges of the hole. Here, the electrostatic field is strong enough to extract charge carriers from the nanowire in which free charges can be created by the green pump laser which has an energy above the estimated bandgap of the SiC nanowires. The resulting current can heat the metal strong enough to transform the surface. A measurement that will provide additional information about the degradation is energy-dispersive X-ray spectroscopy providing its material composition.

2.8.2 Simulation of an electrostatic patch

The interplay between horizontal and vertical electric fields makes it difficult to access the structure of the electrostatic force intuitively. We therefore modelled a single electrostatic patch in a *COMSOL* simulation to get a better understanding of the contribution created by patch effects in a simple geometry. Figure 2.26a outlines the simulation geometry.

We found that, while stable simulations can be run reliably in 3D geometries for the purely dipolar case where no charge or voltage offset is present, the case of a patch that carries the additional potential offset $V_p = 0.05\,\mathrm{V}$ requires very fine meshing around the tip of the nanowire, starting at sizes of 3 nm that rendered 3D simulation unfeasible with respect to time and memory consumption. We therefore changed to a 2D geometry, illustrated in panel 2.26a, where the nanowire is highlighted by a blue circumference and the patch that lies on the bottom boundary is depicted as green line. The entire upper boundary acts as electronic ground while the control voltage V_c is applied to the lower boundary. The potential at the patch electrode is the sum of the applied voltage and the patch potential $V_c + V_p$. We conduct the simulation in the vertical plane and iterate for at least three different control voltages at each point. This allows computing the force gradient for each value of the bias voltage, and thus computing the quadratic term and the offset voltage in each position above the patch.

Panels 2.26b and 2.26c show the quadratic coefficient of the force divergence and the measured offset potential, respectively. The two vertical black lines indicate the limits of the simulated patch which has a length of 400 nm. The nanowire has a diameter of 160 nm which is a realistic representation of the nanowires employed in the experiments. In order to keep the runtime feasible, we restricted its length to 8 µm. This has the side effect that the quantitative comparison of simulation and measurement is less meaningful since the experimental conditions are not mimicked adequately.

The offset potential shows rapid transition from positive to negative values when transversing from surface to patch. The magnitude, more than 25 kV directly above the surface, is much higher than any experimentally measured value, due to the quasi null value of α which displaces the factorized V_1 further apart. It decays rapidly when moving away from the surface and approaches zero for large distances, which is expected as the horizontal field components are strongest directly above the surface.

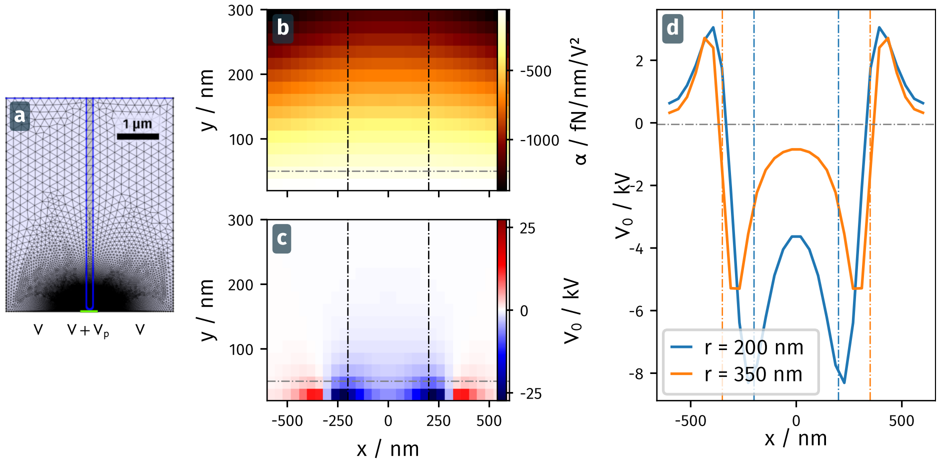

Fig. 2.26: Results of the 2D simulation of the electrostatic force on a nanowire above a patch with the simulation geometry outlined in (**a**). The blue trace highlights the nanowire domain. The green line at the bottom presents the patch modeled by a region to which an additional voltage V_p is applied. The terminal for the control voltage is the entire bottom boundary of the simulation space while the top boundary acts as ground electrode. (**b**) and (**c**) present the quadratic coefficient α and the offset potential of the of the electrostatic force divergence. The vertical black lines indicate the border of the patch and the horizontal grey line at $y = 50\,\text{nm}$ marks the horizontal cut for V_0 (**d**). The line plots in (**d**) compare results from simulations of a patch with 400 nm and 700 nm radius with the patch borders indicated by the respectively colored lines.

Panel 2.26d displays a horizontal line cut through the V_0 map at the height of 50 nm indicated by the grey dashed line and compare the results of the 200 nm radius patch with a larger one at $r = 350\,\text{nm}$. The offset potential in 2.26d is positive outside of the patches and negative on the patch which corresponds to the opposite sign of the additional applied potential $V_p = 50\,\text{mV}$. Another difference between the two patch sizes is that the minimum of V_0 does not fall together with the border of the big patch while it does so for the smaller. Centrally above the patch, V_0 achieves a local maximum that is flatter above the big patch. This is due to the fact that the measured force convolutes the size of the sample geometry with the size of the nanowire. In the case of the small patch, both length scales are comparable so that V_0 varies constantly. For even larger patches with a size of multiple nanowire diameters, the measured V_0 would form a plateau.

The quadratic coefficient in Figure 2.26b varies continuously over the whole simulation area without visible features at the patch borders. The variations are of the order of $100\,\text{fN/nm/V}^2$ which is one order of magnitude larger compared to the measurements. However, it is not intuitive that the flat surface should cause a variation in the dipolar force and we attribute the apparition of a non-zero quadratic term to the finite simulation size and the dynamically adapted meshing. In order to mitigate this effect, we also performed simulations over slightly curved surface ($r = 5.2\,\mu\text{m}$) on whose center the patch is positioned. We now have a real quadratic contribution and we can dissect the different contributions further. Figure 2.27 presents the coefficients of the fitted parabola to force and divergence. Here, we present both, the coefficients of the polynomial form $F/\mathrm{div}\mathbf{F} = \alpha V^2 + \beta V + \gamma$ and the coefficients of the form $F/\mathrm{div}\mathbf{F} = \alpha(V - V_0)^2 + \eta$.

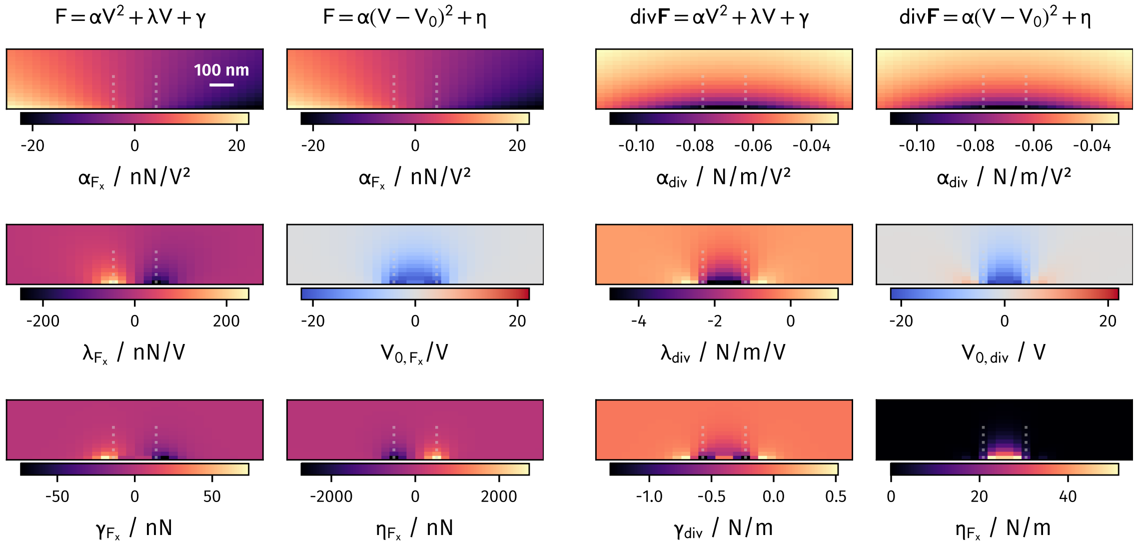

Fig. 2.27: Results from the electrostatic simulation of a single patch with V_p = 50 mV of 200 nm diameter on a curved surface (r = 5.2 µm). The plots show the different contribution to the horizontal force and force divergence experienced by a 8 µm long and 160 nm thick nanowire. On the left side, the contributions for the horizontal force are given. The right side shows the different terms of the corresponding force divergence.

Comparing the amplitudes of the terms α, λ and γ, one notes that the strongest contribution (at 1 V) comes from the linear term, followed by the constant term, both only caused by the presence of the patch. Indeed, one can clearly see the patch's effect in these terms, but the quadratic coefficient is free from it (same holds for the divergence plots). An observation that can also be made in measurements, is that the linear contribution decays less fast with increasing distance than the other terms, a fact that is transferred to V_0. The larger α in this simulation compared to that on a flat substrate decreases the resulting V_0 to maximal values around 20 V, which is close to experimentally obtained valued for close distances. Interestingly, the V_0 for force and divergence are similar, which is a consequence of the quasi-flat geometric curvature employed.

Figure 2.28 presents cuts through the above maps for the force divergence shown in Figure 2.27 and for simulations with a smaller (d = 100 nm) and a larger (d = 700 nm) patch, taken at a height of 75 nm. Again, we present the coefficients of both parabola expressions. The quadratic term is identical for both expansions since it is created by the curvature of the surface that is the same for all simulations. When looking at the other terms, the signature of the features caused by the smaller patches are almost similar as long as the patch dimension remains smaller than the nanowire diameter. When simulating a larger patch, one can identify the correct characteristic size in the curves. Due to the size of the larger patch, the linear and residual terms are small at the patch center, causing a contribution η, that approaches a value much smaller that at the edges and much smaller than for smaller patches.

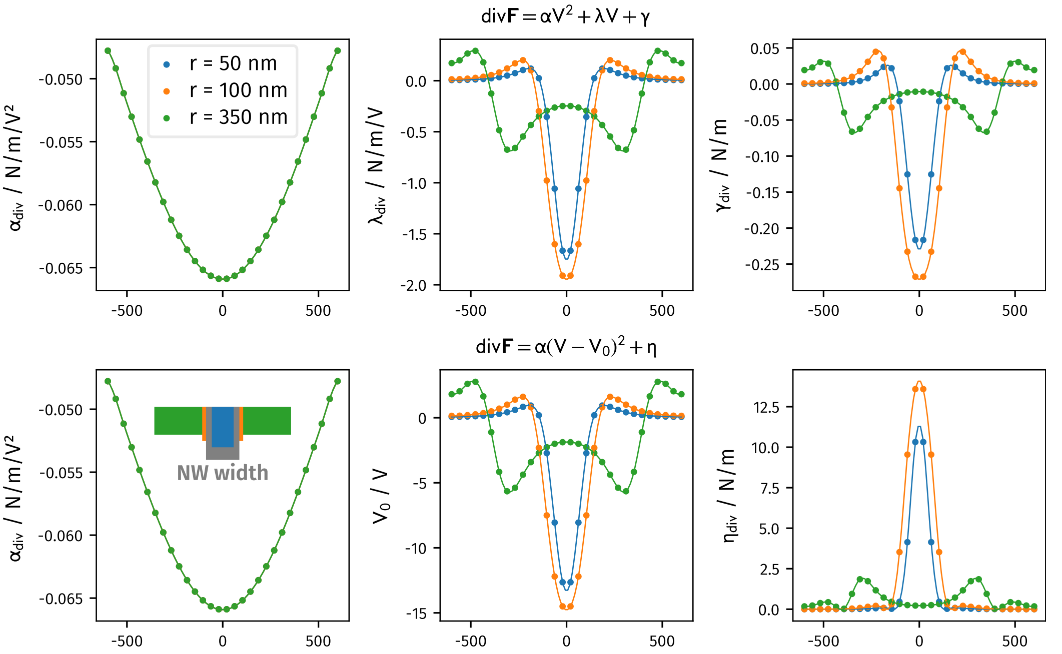

Fig. 2.28: Linecuts through the simulation for three patches of different sizes on a surface with 5.2 µm radius of curvature. Beside the patch size the parameters are identical to Figure 2.27. The inset in the bottom right plot illustrates the size of the nanowire (grey) with respect to the size of the patches (colored).

The simulations, even though their quantitative value is uncertain, show that the nanowire represents a sensitive probe, suitable to investigate the parasitic surface fields, with a resolution largely determined by the size of the nanowire. The facts that the linear and residual terms can be easily separated from the quadratic term and penetrate farther into the space above the surface, while roughly keeping their horizontal extension, clears the road to the exploration of residual surface fields.

We also note that, while the fitting procedure is more intuitive with a $\alpha(v-v_0)^2+\gamma$ curve, the connection to the tensor discussion introduced above are more easily done with the $\alpha V^2 + \lambda V + \eta$ representation. This can be seen in Figure 2.28: the residual contribution presents an attractive quadratic pattern with a negative divergence, as expected for a 50 mV patch offset, while the η term presents an erroneous higher divergence above the patch. Then, the large sample curvature makes that λ and V_0 present identical variations, but this would not be the case for smaller geometric structures ($V_0 = \lambda/2\alpha$).

The large effect caused by the electrostatic patch originates from the presence of horizontal surface fields to which the nanowire is particularly sensitive. This was no hindrance in previous experiments as it has not been possible to approach surfaces close enough [29] to be bothered by this effect. Also, the effects are less pronounced above structures where sharp geometric features dominate over flat surface. The challenge in performing experiments under the presence of strong patch effects is the decreased measurement stability caused by high local force gradients that can shift the nanowire's mode frequencies and rotate the eigenmode orientations. Additionally, the interpretation of the results with respect to underlying force contributions such as Casimir forces gets more complicated if local patch effects cover them.

A measure to mitigate the contribution of strong patch-created horizontal fields can be the employment of metallic nanowires that convey the electric ground to the extremity of the nanowire. The applied control voltage would thus compensate the local electrostatic field close to the nanowire tip and not only by the vertical field between sample and nanowire support in the case of the dielectric nanowire. This has the advantage that the force parabola is shifted less strongly by the linear patch effects. We simulated this case and found that the offset voltage is reduced by a factor of 1000 as presented in 2.29a compared to the dielectric nanowire while both curves show the same qualitative features.

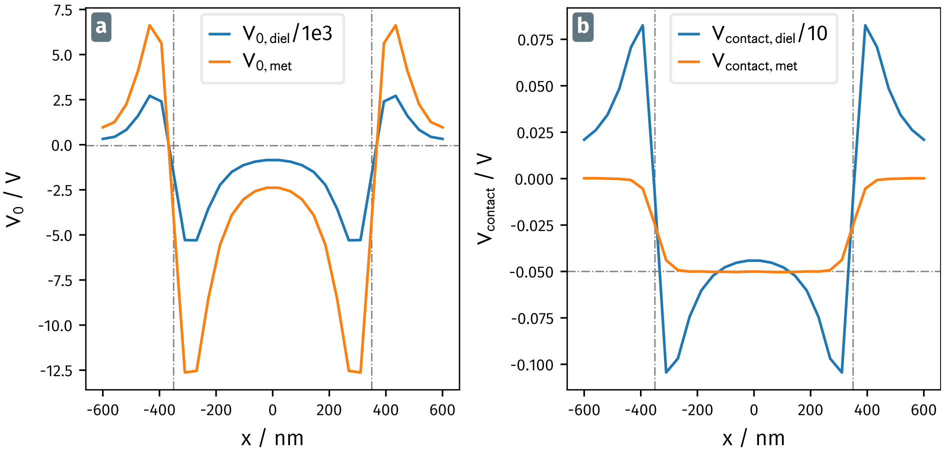

Fig. 2.29: Plot (**a**) compares the offset potential simulated 50 nm above a patch with $V_{\mathrm{patch}} = 0.05\,\mathrm{V}$ via the horizontal force divergence $\partial_x F_x + \partial_z F_z$, felt by a dielectric (blue) nanowire ($L = 8\,\mu\mathrm{m}$, $d = 160\,\mathrm{nm}$) to that simulated for a metallic nanowire with same dimensions (orange). Note that the V_0 for the dielectric nanowire is scaled by a factor of 1/1000 and is therefore about 500 times larger than that measured with the electrostatic nanowire due to the much more localized electric field in that case. In (**b**), the contact potential V_{contact} – the potential measured based on the vertical force gradient $\partial_y F_y$, similar to standard KPFM measurements, but here purely conceptual – is compared for both cases. While the metallic nanowire measures the correct patch potential, the dielectric nanowire measures a value ten times larger and the simulated shape of V_{contact} is different due to the different shape of the electric field in both cases.

The measured variations of V_0 that we retrieve from the force divergence measurements is mostly caused by lateral residual fields, which do not present the same geometry as the bias field. In simulations, we can also access the vertical force gradient $\partial_y F_y$ that is not measurable experimentally and that is dominantly – but in the case of a dielectric nanowire not entirely – caused by vertical fields. This configuration is analog to standard KPFM [81], where a metal coated AFM cantilever is used to measure the vertical force minimizing potential. Figure 2.29b compares the contact potential obtained from the vertical force gradient for both types of nanowires. While, in the metallic case, we obtain the correct contact potential that was applied on the patch region, the dielectric case is still a factor of ten too large and its shape differs significantly, showing the same jump at the patch border also observable in 2.29a. We explain this with the field changing properties of the dielectric which is now placed between the two electrodes. Also, we have noted in Section 2.1, that the electric fields perpendicular to the measured force have an important contribution to it. This has a larger impact on the dielectric case since the field penetrates the nanowire, while in the metallic case the field is confined between the wire's extremity and the surface.

2.8.3 Multiple patches around geometry

Another possibility to use electrostatic simulations to evaluate the effect of patches is to take a look at the electrostatic field above a structured surface on which patches are present. Applying the methods from Section 2.1, we then estimate the expected forces on the nanowire. Figure 2.30 presents the simulated fields above a 2D geometry with a centred hole in a conducting plate. The surface of the plate is structured into different regions resembling surface patches. They are still modelled with a conductive material, but each single one carries an additional potential $V_p \in [-10\,\mathrm{mV}, 10\,\mathrm{mV}]$ in addition to the applied bias potential V on the plate. The height of the patch grains is exaggerated compared to the real surface structurations which we found to be in the range of 5 nm to 10 nm.

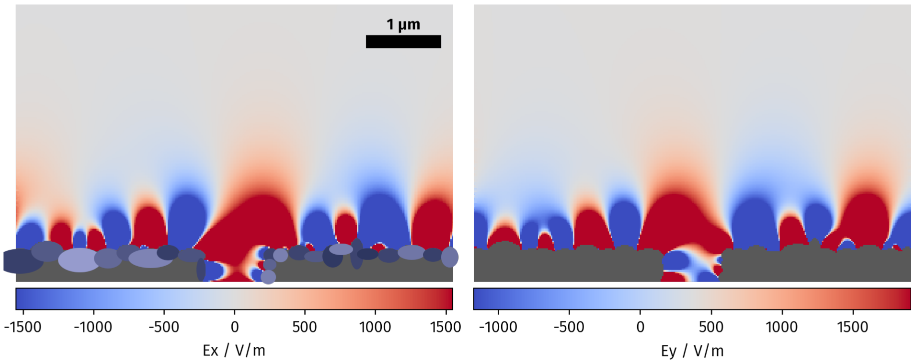

Fig. 2.30: Simulation of the electrostatic fields above a metallic plate with a hole in the center. The plate's surface is structured with oval patches that each have an additional potential to the bias potential applied to the plate itself. The ground level is fixed at the top border of the plot.

One observes that the horizontal fields E_x induce a component that changes sign on the center of the patch grains while the vertical fields change close to the boundaries between patches. This means that the horizontal force which is a result of the product E_xE_y will show domains smaller than the physical domains. This effect is visible in Figure 2.31, where the quadratic, linear and constant terms of the horizontal force are shown above the same structure. The quadratic term contains a significant contribution of the geometric structuration of the surface which is much smaller in the experimentally investigated samples, still, the hole dominated the effect, in particular at distances $> 200\,\mathrm{nm}$. In the linear and residual forces the patches dominate the force field both at close and at larger distance. While the linear force is a mix between the constant residual fields and those created via the applied bias voltage, the constant term γ permits to isolate the effect of the surface patches. Here we observe that the domains with the same sign of the force seem to happen over smaller regions than in the quadratic and residual force terms. Looking at the geometry beneath, one can discern one region of positive and negative sign per grain which is what we expect from the product of fields. The constant force is also much more localized at the surface than the other terms as here, there is no far reaching vertical field that amplifies the structuration of the force field.

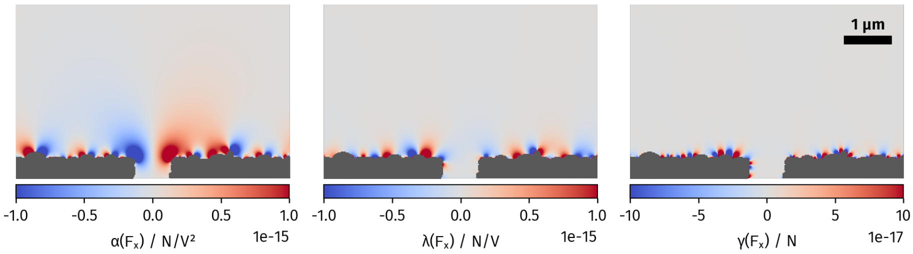

Fig. 2.31: The electrostatic force terms (α-quadratic, λ-linear, γ-constant) obtained from the fields simulated above a grainy surface with a central hole ((2.30)) show the effect granular surface patches have on the overall shape of the force field.

2.8.4 Charges

The probably most direct explanation for a residual electric field leading to a supplementary linear electrostatic force is that the nanowire could carry an electrostatic charge. Since SiC is a wide-bandgap material [14] and the nanowires are additionally covered by a 2 nm to 5 nm oxide layer which makes charge cancellation at the surface and within the wire inefficient, they are easily capable to trap electric charges at their surface.

The force experienced by a charge on the wire that is immersed in an electric field depends on the sample geometry. It is proportional to the electric field and, for a spherical electrode, varies with the inverse square of the distance. In order to estimate the effect from a charge placed at the extremity of the nanowire, we conducted finite elements simulation in *Comsol Multiphysics* where the electrostatic force on a nanowire is calculated 100 nm above a tip electrode with an end curvature of 250 nm. The nanowire carries a single positive electric charge in the center of its extremity. For a positive bias voltage, it is thus expected to be repelled from the tip. Figure 2.32 shows the results for two nanowires of 10 and 50 μm length, respectively. The shorter nanowire in the upper panel experiences a force gradient more than ten times as high as the long nanowire due to the proximity of the electrodes[6]. While the quadratic coefficient (the dipolar force) presents the same trapping characteristics as in absence of charges, the linear coefficient is anti-trapping due to the positive sign of the charge. Comparing both force gradients at a voltage of one volt, the linear contribution is about one sixth of the quadratic contribution in case of the short nanowire. For the longer nanowire, the ratio is about one half and thus about three times as large. Since this is the more realistic case, we can expect a major linear contribution in the usual voltage range of ±1 V if a full charge is present. In experiments, the linear contribution is typically at least a factor of ten smaller than the quadratic term.

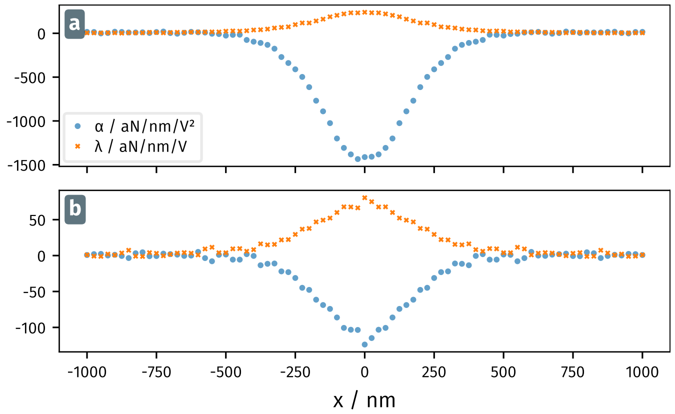

Fig. 2.32: Finite element simulation of the quadratic α and linear λ terms of force divergence as experienced by a 160 nm thick nanowire with a single positive charge at its extremity at a distance (d = 100 nm) above a rounded tip (r = 250 nm) electrode. Panel (**a**) shows the force divergence terms for a short (L = 10 µm) wire and (**b**) the same simulation with a longer (L = 50 µm) wire. The nanowire length directly affects the distance between the tip and ground electrodes and therefore changes the electric fields at a given distance from the tip but does not affect the characteristic trapping α, seen directly above the tip's center with an antitrapping λ for both nanowires. The antitrapping potential is caused by the positive sign of the charge.

The consideration of a single trapped charge at the extremity of the nanowire in simulation leads to force divergences that fall into the range of experimentally measured values. However, during the time our group has experience with SiC nanowires, we only rarely observed discrete jumps during force measurements which could be attributed to charges attaching or liberating from the nanowire. We also performed experiments where we measured the frequency of the nanowire while sweeping the voltage applied to a sharp electrode in the proximity of the nanowire between ±10 V but did not observe a change caused by the emission or collection of electrons. From this experience we assume only little to no effect from changes of the nanowire's charge during experiments.

---

[6] As mentioned before the length and height of the nanowire also determine the distance between electrode and grounded nanowire mount. Simulations for longer nanowires therefore yield the more realistic quantitative results. The nature of the observed effects however does not depend on the nanowire's length in simulation up to the limit where the field close to the ground plate is not homogeneous anymore (the nanowire length is in the order of its diameter).

However, to better evaluate the effect, studies need to be conducted investigating in detail the charges present on the nanowire. These would include a force measurement in a homogeneous horizontal electric field to directly measure the linear force created by a charge distribution in the electric field [78], as well as field emission measurements.

2.8.5 Mixed electro-optical forces

In most experiments, we use a combination of an optical driving force and an electrostatic control of the test force field, which both have static contributions. Hence, there exists a static force that is caused by the combination of the optical electromagnetic field gradient and the electrostatic field gradient and scales with intensity $|E_{\mathrm{opt}}E_{\mathrm{elec}(V_{\mathrm{bias}})}|$. We typically assume that this force presents a constant offset due to the homogeneity of the laser beam. However, if gradients of this mixed force are present they will vary linearly with the applied bias voltage.

Panel 2.f: The effect of large oscillation amplitudes

Nonlinear effects

Nonlinear effects present a cause that perturb the harmonic oscillator approach. The approximation of linearly varying force field gradients at the displacement $\delta\mathbf{r}$ of the nanowire (Equation 1.33) is only valid if the oscillation amplitude is much smaller than the typical length scale l_{FF} over which the force field varies $\delta r \ll l_{\mathrm{FF}}$. For large δr this approximation is not valid anymore and the higher order force gradient terms would need to be taken into account. At the typical oscillation amplitude of the nanowire of some tens of nanometers the observed force fields can be linearized within good approximation. However, with strong modulation forces, one can reach the regime of nonlinear response which can be avoided by appropriate regulation of the power of the optical drive.

Spatial resolution

The question of the ultimate lateral spatial resolution has not really been discussed up to now, since we have only observed rather “large” geometric defects of minimum transverse dimensions around 50 nm to 100 nm. For a nanowire at rest, it depends on the reach of the force field, and how its equivalent volumetric force spreads in the nanowire’s volume. The smallest lateral features we have observed so far, without optimizing for maximal resolution, are around 50 nm. However, beyond this intrinsic limitation on the transverse resolution, one needs to investigate how the nanowire motion impacts the resolution. The nanowire's random thermal noise spreads over 1 nm to 10 nm depending on the nanowire employed, but this always remains small compared to their diameters. Due to the random character of the thermal motion, it is difficult to extract time-resolved informations, so that the main consequence will be a blurring of the force field under investigation. In the case of a force measurement realized using driven trajectories, advanced force sensing techniques based on time-resolved measurements can be implemented, such as measuring the driven displacement at harmonic frequencies of the driving tone, which will allow obtaining informations on the higher order spatial derivatives of the force, and thus a more refined lateral resolution. We have not investigated those types of measurements, but one can estimate the impact of the oscillation amplitude on the measurement employed in this work.

Due to the non-zero oscillation amplitude of the nanowire, the force field measurement is never a singular pointwise measurement but should be though of as a motionally averaged measurement over the oscillation area in 2D. In order to achieve high spatial resolution in the horizontal plane, it is therefore beneficial to choose thin nanowires with small displacement amplitudes (at close distances, the force gradients are sufficiently strong to employ stiffer nanowires) or to thermally cool the nanowire so that its vibrational thermal motion is reduced, which further increases the force sensitivity [36].

For the force sensing measurement based on the driven nanowire trajectories, the most direct parameter to tune in order to reduce the nanowire's oscillation amplitude is the strength of the driving force. At small amplitudes the response to the drive becomes difficult to detect on top of the nanowire thermal noise, while at larger oscillation amplitudes, the system may become non-linear and smooth out the details of the force field. If we reduce the drive too ambitiously, we loose the benefits of a large detection signal strength, which allows determining the oscillation phase more precisely, a prerequisite to ensure a proper operation of the PLLs. For most of our experiments, the stable operation and a large signal are the more valuable criteria while the spatial resolution is only of secondary importance, particularly in the case of "large" sample structures with a characteristic lengthscale ρ larger than the maximum employed nanowire displacement amplitude, which can reach around 100 nm under strong modulation. In practice, we do not overpass such a value, otherwise the optical readout cannot be considered as linear anymore, and one observes some vertical foldings of the response signals.

We now evaluate the motional averaging effect caused by a large oscillation amplitude. We model the spatial variations of the electrostatic force gradient as the one experienced by a polarizable particle in the field of a point charge placed at the origin. The spatial variations of the force gradient $\partial_x F_x$ are illustrated in the inset of figure 2.33. The oscillating nanowire would measure a gradient motionally averaged over its driven trajectory. Given an oscillation amplitude Δr we can calculate this averaged force gradient g_av via

$$g_\mathrm{av} = \frac{1}{\pi \Delta r} \int_0^{2\pi} \mathrm{d}u \, F_x(x + \Delta r \cos(u), y) \cos(u).$$

This formula converges towards $g_\mathrm{av} = \partial_x F_x$ for small oscillation amplitudes, as can be verified by realizing an expansion at first order in Δr of F, prior to realizing the integration. Figure 2.33 compares the effect of different Δr on the measured force divergence.

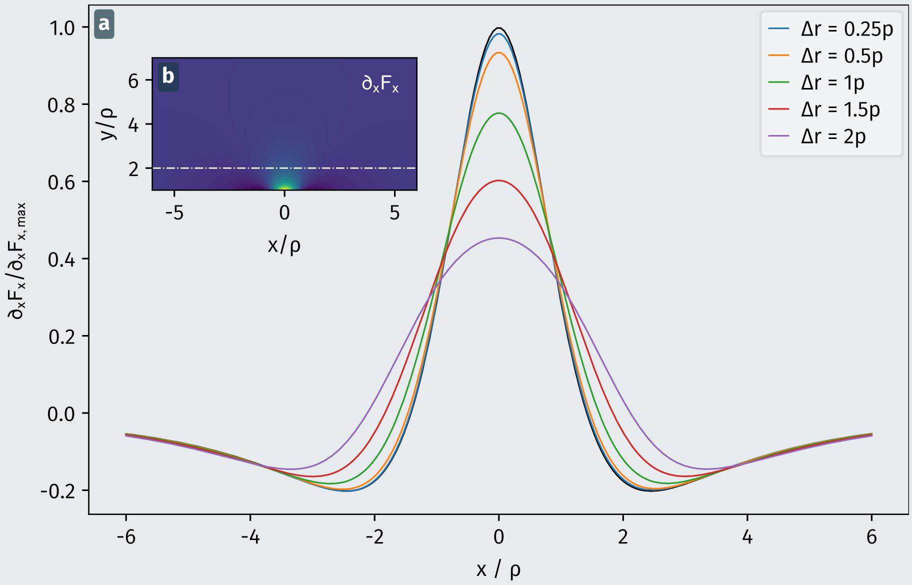

Fig. 2.33: The 1d force gradient created by the electric field of a single charge at the origin measured with different oscillation amplitudes Δr is shown in (**a**). All coordinates are in relation to the characteristic lengthscale ρ of the measured gradient at proximity to the charge. Inset (**b**) plots a vertical force gradient map as measured by a theoretical probe with $\Delta r = 0$. The white line at $y = 2\rho$ indicates the height at which the curves in (**a**) are calculated. With increasing size of the nanowire's oscillation amplitude, the measured shape of the gradient flattens out, with stronger effect for the minima in the beginning, and the present features widen. The black curves shows the theoretical gradient for $\Delta r = 0$.

A practical estimation of the effect from a larger oscillation amplitude can be done by measuring the force above the same nanostructure with different modulation amplitudes of the optical drive and therefore leading to different oscillation amplitudes. Comparing the measured divergence pattern along the same horizontal line measured above an electrostatic tip, we observe that the averaging effect is only present at small separations. For measurement heights typically interesting for horizontal scans, only small effects are visible in the quadratic electrostatic force as illustrated in Figure 2.34.

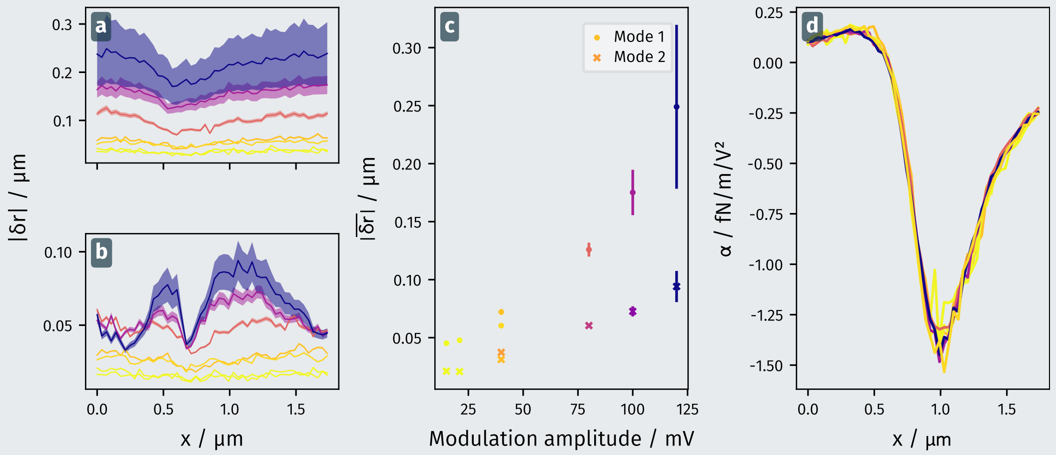

Fig. 2.34: The oscillation amplitudes measured for a horizontal scan approximately 150 nm above an electrostatic tip are plotted for the first mode (**a**) and the second mode (**b**) at different modulation strengths. For each mode and modulation strength we obtain a mean amplitude (**b**) with values up to 250 nm for the first mode that is driven more efficiently. In (**d**) we show the measured force field divergence extracted from the eigenfrequency shifts along the horizontal lines for each modulation amplitude. The curves are barely different, which probably shows that for the measurement height and sample, the characteristic size of the force field variations is larger than the oscillation amplitude of the nanowire. Measurements at closer distance show indeed an effect for larger oscillation amplitudes. The colours in all plots relate data with the same modulation amplitude.

We note that the resolution with which topographic features in the force field map can be imaged correctly depends on the size of the nanowire trajectories. If the spatial features are smaller than the trajectories, they will appear less pronounced in the resulting maps but still show up with slightly increased size. Features larger than the spreading of the nanowire's trajectories can be imaged without a loss of resolution. This means that in practice, if one wants to measure the force above nanostructures smaller than 200 nm, one should verify that the oscillation amplitude is not blurring the measured force pattern.

2.9 Comparison of force and force gradient measurement

In the foregoing sections, most of the measurements of the force field gradients were realized by measuring the perturbation of the mechanical properties of the nanowire under the action of the electrostatic fields. To do so, we used a time modulated optical driving force, which was constantly driving the nanowire's motion independently of the measured force field. Like this, the 2D force field cannot be measured directly but only via the reconstruction based on the spatial integration of the measured force gradients [29]. A different method that permits to measure the force field directly makes uses of a small modulation δV around the tunable sample voltage bias V. By doing so, we directly modulate the electrostatic force, both its quadratic and linear contribution in V. Reproducing such a resonant response measurements at different points above a sample of interest, thus allows to directly image the electrostatic force vectors and represents an interesting complementary analysis of the force field gradients derived from the perturbation of the nanowire eigenmodes. Naturally, this methods cannot be used to obtain direct information on the residual surface forces, but permits to obtain a better understanding of the electrostatic forces which have to be subtracted in order to observe the Casimir forces.

By simultaneously measuring the optical and electrostatic responses at resonance one can reconstruct both, force fields and force gradients. However, the electrostatic forces are rapidly changing in orientation and strength above a sample surface, which causes large mechanical perturbations and also makes it impossible to use them as a reference force in a PLL. We will thus still rely on the optical force to maintain the driving frequencies at resonance, but will alternate between optical and electrical driving tones to preserve the resonant driving condition for both driving tones.

In order to probe the electrostatic force, the electrostatic bias voltage is modulated by a small oscillating voltage so the total voltage that creates the electric field is $V(t) = V_{bias} + \delta V(t)$. If the modulation is sufficiently small, we can linearize the quadratic electrostatic force $\mathbf{F}_{\mathrm{el}}$ around the applied bias voltage V_{bias} as

$$\mathbf{F}_{\mathrm{el}} = \boldsymbol{\alpha} V^2 + \boldsymbol{\beta} V + \boldsymbol{\gamma} \tag{2.15}$$

$$\Rightarrow \delta \mathbf{F}_{\mathrm{el}}[\Omega]|_{V_{\mathrm{bias}}} = 2\boldsymbol{\alpha} V_{\mathrm{bias}}\, \delta V[\Omega] + \boldsymbol{\beta}\, \delta V[\Omega]. \tag{2.16}$$

Figure 2.35 illustrates the idea of this procedure.

The response of the nanowire is then directly related to the driving force via $\delta \mathbf{F} = \delta V \frac{\partial \mathbf{F}}{\partial V} = \boldsymbol{\chi}^{-1} \delta \mathbf{r}$, where

$$\frac{\partial \mathbf{F}}{\partial V} = 2\boldsymbol{\alpha} V_{\mathrm{bias}} + \boldsymbol{\beta}$$

is the local dependence of the electrostatic force on the bias voltage modulation. When using the phase-locked frequency tracking at the eigenmode frequencies Ω_-, Ω_+, one obtains the following equations for the signals measured along the detection vectors $\boldsymbol{\beta}_{\oplus,\ominus}$:

$$\delta F \mathbf{e}_F \cdot \mathbf{e}_\pm \; \mathbf{e}_\pm \cdot \mathbf{e}_{\beta_{\oplus,\ominus}} = -i \Gamma \Omega_\pm \delta r^{\pm}_{\beta_{\oplus,\ominus}}, \tag{2.17}$$

where $\delta r^{-}_{\beta_\ominus}$ is the complex driven displacement amplitude measured at the first resonance frequency on the difference channel of the photodiode, with the other constellations referring to the second eigenmode frequency and the photodiodes sum channel respectively. The above expression permits to reconstruct the driven electrostatic force vector in amplitude and orientation for each measurement point and each voltage bias. Using the signal acquired on both detection channels, one obtains the direction of each

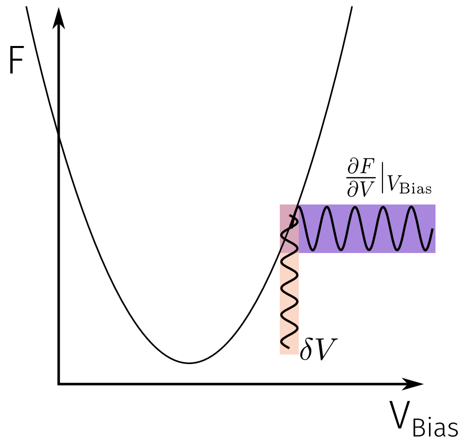

Fig. 2.35: Principle of the direct measurement of the electrostatic force. The small modulation δV around an offset V_{bias} generates a time-modulated electrostatic force, which can be directly detected by using it as a driving tone in a response measurement. Instead of sweeping the drive frequency across the two mechanical resonances, it is possible to only drive the nanowire at its two resonant frequencies, at the condition to ensure that the drive frequency remains at resonance. The modulated force with amplitude $\delta V \frac{\partial F}{\partial V}$ drives the nanowire's oscillation. It presents a linear dependency with the bias voltage, and changes sign accross the parabola extrema.

mode with the definition $\theta_{\pm} = \arctan \frac{\delta r_z^{\pm}}{\delta r_x^{\pm}}$[7]. Subsequently, one can calculate the force vector $\delta \mathbf{F}$:

$$\begin{pmatrix} \delta F_x \\ \delta F_z \end{pmatrix} = \frac{\Gamma}{\cos\theta_- \sin\theta_+ - \cos\theta_+ \sin\theta_-} \begin{pmatrix} \sin\theta_+ & -\sin\theta_- \\ -\cos\theta_+ & \cos\theta_- \end{pmatrix} \begin{pmatrix} \Omega_- \delta r_- \\ \Omega_+ \delta r_+ \end{pmatrix}. \tag{2.18}$$

In theory, we usually assume that the measured force gradient directly derives from the local force and vice versa, that the force field can be reconstructed from the force gradients via integration. Since it is always wise to challenge one's assumptions experimentally – especially if one is convinced of them – a simultaneous measurement of force and force gradient would be an important evidence for this basic operation principle.

Using the modulation of the electrostatic force to measure both, force and gradients has two disadvantages. Firstly, the electrostatic force can be perpendicular to one of the nanowire's modes so that the signal for this mode would be small and one would lose the benefits of resonant detection. Secondly, a change in orientation of the electrostatic force represents a sign change of its phase in the projective measurement, so that a

---

[7] Here, the displacement in the cartesian laboratory coordinates x, z are obtained using the reversed projection on the measurement channels:

$$\begin{pmatrix} \delta r_x \\ \delta r_z \end{pmatrix} = \frac{1}{\cos\beta_- \sin\beta_+ - \cos\beta_+ \sin\beta_-} \begin{pmatrix} \sin\beta_+ & -\sin\beta_- \\ -\cos\beta_+ & \cos\beta_- \end{pmatrix} \begin{pmatrix} \delta r_{\beta_-} \\ \delta r_{\beta_+} \end{pmatrix}.$$

resonance lock using the dual PLL technique would not work for most of the geometries that we explore, which leads to rapidly varying electrostatic forces.

A first approach to circumvent these drawbacks consists in acquiring full response sweeps, for which no PLL must be set up. With typically hundreds of frequencies and a measurement time per frequency[8] of 300 ms such a measurement quickly takes minutes per point, so that maps with 50 × 50 points spatial resolution and 25 different bias voltage values would take several days to complete. In this section we present a technique that performs the electrostatic response measurement as a complementary step to the above described protocols and makes use of the strengths of PLL based, resonant detection described above and flexible scripted measurements. The additional measurement of the force leads to a measurement only about 2.5 times longer than a pure force gradient measurement (caused by additional settling times when switching the driving force). For smaller maps with about 900 spatial points one measurement takes about 10 h to 16 h, a duration over which the experiment can be fully stabilized without suffering too much from spatial drifts.

2.9.1 Protocol

The combined measurement of force field and force gradient had been included in the force field cartography routine by modifying the automated protocol discussed in Section 1.5, so that one can easily change the measurement mode using the graphical interface of our scan control program. With the PLL's locked on the nanowire's resonance frequencies using the optical force as pump, we add for each spatial coordinate the following steps:

1. Set the first value of V_{bias} and wait $\Delta t_1 \approx 1/BW_{\text{PLL}}$ until the mechanical system is adapted to the new conditions (the mechanical damping rate is always larger than the measurement bandwidth)
2. Measure the response to the optical force: the complex amplitudes of δr_β at the 2 driving frequencies Ω_-, Ω_+, on both measurement channels $\ominus, \oplus$
3. Fetch the measured data and calculate the sample averaged resonant frequencies
4. Disable the PLL tracking and set the mean frequencies as demodulation frequencies[9]
5. Turn off the optical modulated force, but keep the same mean optical power in order not to perturb the nanowire mechanical properties caused by the green laser.

---

[8] This is given by the desired resolution of the sweep which is usually smaller than the linewidth of the resonance.

[9] One could also just turn off the PLL and use the last locked frequency. This has the disadvantage that the last value would be affected by any noise in the PLL detection. The averaged frequencies were found to be the better option and the detection sequence, first readout on the optical force, then on the electrostatic force, was thus fixed.

6. Change to the electrostatic driving force with an adapted modulation strength δV based on the previously measured point or initial parameters. Since the driven electrostatic force varies with the sample position, one needs to adapt the electric drive strength. We adapted the two driving amplitudes differently, since the electrostatic force rapidly changes in space and thus in its projection on both eigenmodes.
7. Wait $\Delta t_2 \approx 1/\Gamma_m$ for the system to respond to the new electric drives (2 driving frequencies simultaneously) and measure the resonant driven response to the optical force. In practice, we used a set of three driving tones on each mechanical modes, at frequencies $\Omega_\pm$, $\Omega_\pm \pm \Delta$, with $\Delta/2\pi = 20\,\mathrm{Hz}$. This leads to a combination of 12 demodulated signals that were recorded on two different ZI-HF2 lock ins. Such multiple measurements per peak was used to detect variations in the mechanical quality factors (that cannot be detected using a single driving tone), as well as errors in the resonant frequency driving conditions.
8. Switch off the electric driving forces and turn on the optical driving force
9. Wait $\Delta t_2 \approx 1/\Gamma_m$ for the system to respond to the new drive, and enable the two PLLs
10. Use the results to adjust the amplitude δV of the electrostatic drive and repeat for the remaining values of V_{bias}, then move to next spatial coordinate and start over

Figure 2.36 illustrates this procedure.

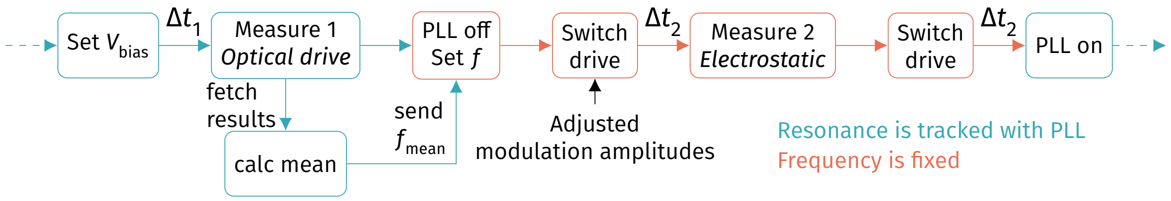

Fig. 2.36: Diagramatic representation of the measurement protocol for the combined force and force gradient measurement for a single spatial point and a single voltage. The element colors indicate if the PLL frequency lock is activated (blue) or disactivated and the demodulation frequencies are fixed (orange). The delay time Δt_1 is used to let the system adapt to the new force gradient matrix created with a new V_{bias} and the time Δt_2 ensures that the measured response is that of the present driving force. The electrostatic drive amplitude is calculated based on the measurement results at the previous position, assuming a smooth and sufficiently slow spatial variation of the force field.

The measurements were performed with a nanowire presenting a rather large frequency splitting, which helps preventing the eigenmode basis from rotating under the action of a too strong external optical or electrostatic force field. During the measurement, the data is acquired in a buffered mode: by ramping up and down the bias voltage. As mentioned earlier, we conduct a bi-directional voltage scan in order to detect possible hysteresis effects possibly caused by a too slow PLL tracking and to ensure that no abrupt jumps occur in the applied voltage.

We will now dissect the combined force/gradient measurement at a given spatial point. Figure 2.37 shows the data for one resonant drive acquired on a single measurement channel (here $\beta_\ominus$) for one voltage scan. The top panel 2.37a presents the measured frequency of the first mode that is tracked with one PLL. The horizontal axis corresponds to a (uncalibrated) timeline with the labels indicating the currently applied V_{bias} that increases towards the center of the plot and then decreased in the second half. The frequency curve f_1 shows a parabolic dependence of V_{bias} for each scan direction that reflects the dependence of the force field gradients $g_{ij}(V_{\text{bias}})$ on the bias voltage. The two wide plateaus in the frequency curve correspond to the values measured during optical and electrostatic drives that are indicated by blue and orange dots respectively. The frequency values are identical since the mean frequency measured via the PLL lock on the response to the optical drive is used as demodulation frequency for the electrostatic measurement.

Similarly, the panel 2.37b displays the detected amplitude of the first mode projected on the measurement vector $\beta_\ominus$. Each line contains the alternating response to the optical and electrostatic force. The response to the constant optical drive is, in the presented case, nearly constant, which indicates that at this particular measurement point no significant rotation of the first mode occurs, as expected from the large frequency split of the employed nanowire. Opposed to that, the response to the electrostatic force (orange dots) varies strongly with the applied bias voltage, showing a linear decrease for increasing bias voltage (and the reversed behaviour in the backward voltage scan). This lineshape corresponds to the affine relation expected from Figure 2.9 with a slope that is determined by the prefactor $2\boldsymbol{\alpha}\delta V$ projected on the eigenmode direction and along the measurement vector orientation. The amplitude of the measured signal is directly proportional to the applied force in the direction of the mode (here mode 1). The phase of the projected displacement in 2.37c is stable for the data obtained with the optical drive that is locked by the PLL and varying for the response to the electric signal that is more susceptible to delays caused by electrostatic retardations and by phase inversion due to a orientation change of the total driven force.

In addition to the demodulated signals at resonance, we also modulate at two sidebands at ±20 Hz on each side of the resonant tones. This multi-frequency measurement permits to measure delayed effects which could change the damping coefficient of the nanowire. Furthermore, an imperfect lock of the PLL can easily be corrected for based on the phase difference between the three measurement tones around each mechanical resonance. Since we need to demodulate 6 frequencies on 2 measurement channels, this measurement requires 12 demodulators that are read out simultaneously at each measurement step.

Analogously to the curves in Figure 2.37, the response signals of both modes on both readout channels are acquired and tangled into two separate sets for the optical and electrostatic drive after the measurement. Using the dataset of the electrostatic drive, one can obtain the electrostatic force field and from the optical drive the electrostatic

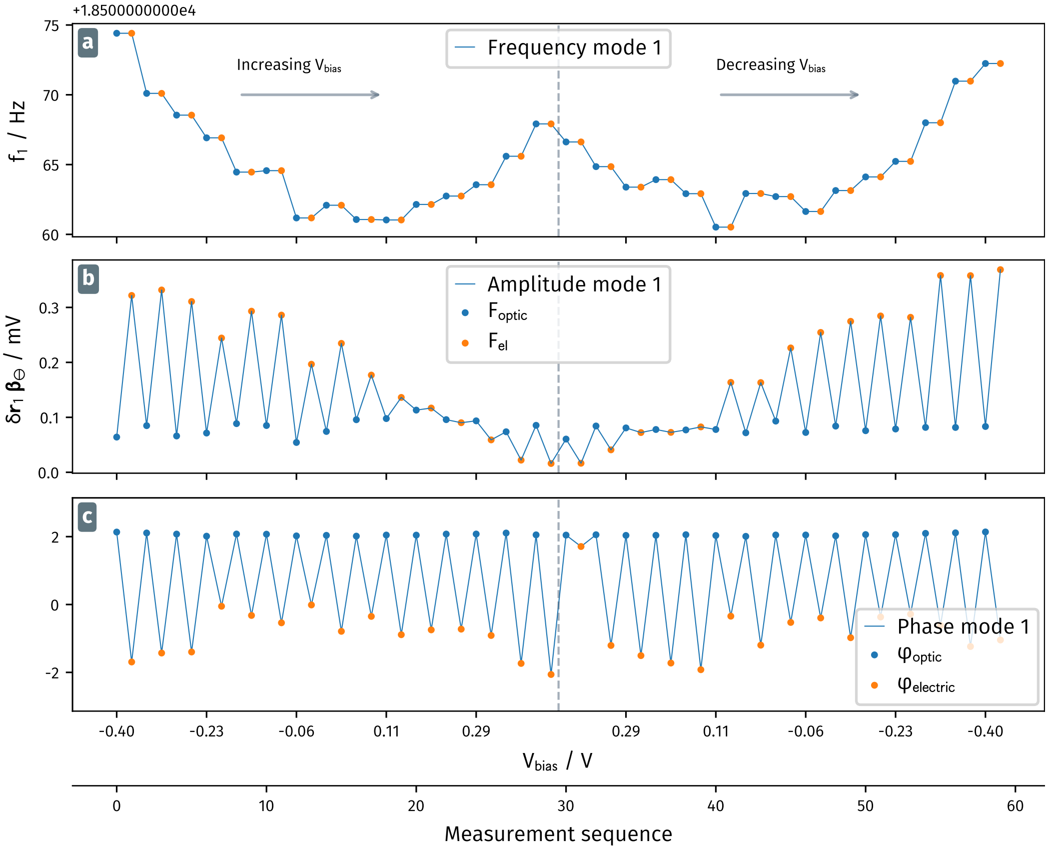

Fig. 2.37: Simultaneous measurement of electrostatic force and gradient for a single spatial point. In (**a**), the measured frequency of the first mode is shown as the applied bias voltage is swept from its minimum (−0.4 V) to its maximum value (0.3 V). Here the x-axis represens a timeline where the voltage is changed periodically and a single point in voltage corresponds to a pair of measured points (blue and orange) since the gradient and the force measurement are performed alternately, with a change of the driving force from optical to electric between blue and orange points (and back between orange and blue) as presented in figure 2.36. The grey vertical line represents the change of the sweep direction from increasing V_{bias} (left) to decreasing (right). (**b**) plots the measured displacement amplitude of the first mode projected onto the ⊖ measurement channel, and (**c**) the phase. The stable value for the phase on the optical drive proves that the PLL lock operates consistently. During the measurement sequence, 12 similar signals were acquired simultaneously (6 frequencies and 2 measurement channels), while the dynamical measurements of the measurement vectors was also activated and measured at each line.

force field gradients. The following section presents the exemplary comparison of both results, realized in a horizontal scan above the rounded electrostatic tip.

2.9.2 Force/Gradient above an electrostatic tip

The central force field of an electrostatic tip is a good test case for the comparison of simultaneously measured force and gradient. The results discussed in this section were obtained from a map with 30 × 35 spatial points taken around 150 nm above a metallized tip, using the first mode family of nanowire 2 (compare box 2.b). At each point, we follow the procedure described above, which consists in scanning the bias voltage from −0.25 V to 0.05 V in 15 steps (and back), leading to 31500 individual force and gradient measurements, each acquiring the data of twelve lock in measurements[10].

Figure 2.38 presents the results obtained in one single position. Here, the modulated forces F_x, F_z are obtained from the amplitude of the nanowire displacement, while the divergence follows directly from its frequency shift. One can clearly identify the linear slope of the force with $\mathbf{F} = 2\boldsymbol{\alpha}\delta V V_{bias} + \boldsymbol{\beta}\delta V$ and the quadratic shape of the force divergence $\mathrm{div}\mathbf{F} = \mathrm{div}\boldsymbol{\alpha}V^2 + \mathrm{div}\boldsymbol{\beta}V + \mathrm{div}\boldsymbol{\gamma}$. Notably, the forces do not share a common zero crossing, nor falls the extremum of the gradient parabola together with the zero crossing of one of the forces. This is expected behaviour as the vectorial forces depend differently on the bias voltage and on the quadratic and linear contributions than the scalar force divergence.

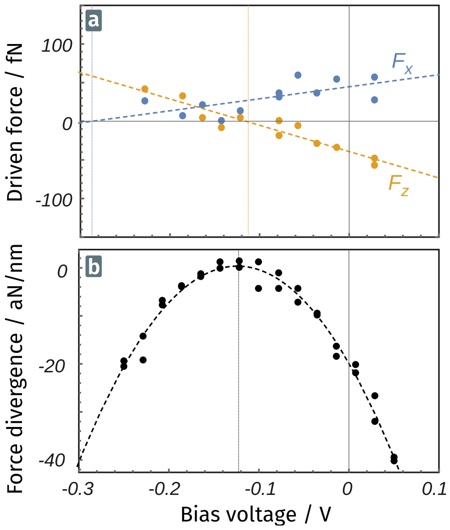

Fig. 2.38: The measured force (**a**) and force divergence (**b**) at a single point of the 2D horizontal map (the middle point in the gray shaded area of Figure 2.40a). The vertical lines mark the point of zero bias voltage (solid black line), and the zero force, respectively divergence extremum (colored dotted lines), which do not fall together. The data has been cleaned by excluding points at which the PLL did not track the peaks reliably due to a reduction in the signal strength possibly caused by an unfavorable projection of the driving force on the eigenmodes or by a problem in the PLL setpoint.

---

[10] We use three frequencies per peak, the central frequency plus a sideband of ±20 Hz in order to detect changes in the quality factor. This makes for six lock-in measurements per measurement channel.

From the measured driven force at each spatial point, we have a direct access to the driven force field at each voltage. The driven force field obtained for three different bias voltages is shown in Figure 2.39. For the smaller and larger voltages, the central nature of the force field is evident with all flashes pointing away from (towards) the electrostatic tip for a small (large) voltage, respectively. This again shows the linear shape of $F_{x,z}(V_{bias})$ as in Figure 2.38, where the data for a point in the upper left quadrant (F_x has a positive, F_z a negative slope) is shown.

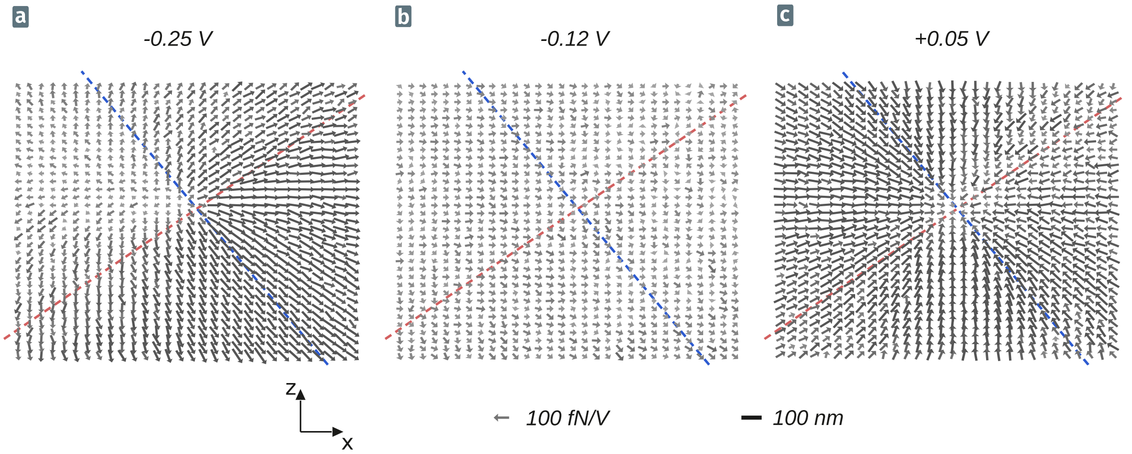

Fig. 2.39: Vector plot of the force field measured at three different voltages above the electrostatic tip. The force is obtained via the modulation of the electrostatic field. The colored lines indicate the orientation of the nanowire eigenmodes (blue: mode 1, red: mode 2), and their crossing the position of the electrostatic tip (minimum divergence point). For the smallest bias voltage (**a**), the field's divergence is positive (all arrows are pointing away from the tip's center), while at the largest voltage (**c**) the inverse is true. The medium voltage (**b**) corresponds to minimal force, where one is not dominated by the quadratic contribution of the electrostatic force.

In order to eliminate bad data points, we clean the acquired data with a criterion based on the phase deviation which indicates failure of the PLL lock. This typically affects the points measured at large bias voltages at which the strong local force becomes comparable to the nanowire stiffness and causes large frequency shifts. As shown in Figure 2.38, we then fit the driven forces at each point with a linear relation and thus extract the linear term $\delta F_{x,z}/\delta V/V$ and the residual term $\delta F_{x,z}/\delta V$. Figure 2.40a presents both terms as vector fields while plots of the measured driven force contributions are shown in 2.40b. Both terms globally show the same characteristics, with the linear term being about ten times larger at $V_{bias} = 1\,\mathrm{V}$. In the presentation as vector fields, one can observe that the central point of the arrow plot is slightly different (in the linear contribution it is shifted slightly to the left). Such a difference in spatial shapes is the origin of the non standard force images that can be obtained at a single voltage (as shown in Figure 2.8)

The combined measurement of force and force gradient permits us to validate the equivalence of both measurements and presents a confirmation of the standard approach which measures the force gradients in order to reconstruct the local force field. To compare the divergence measurements and the force measurements, we now compute the local

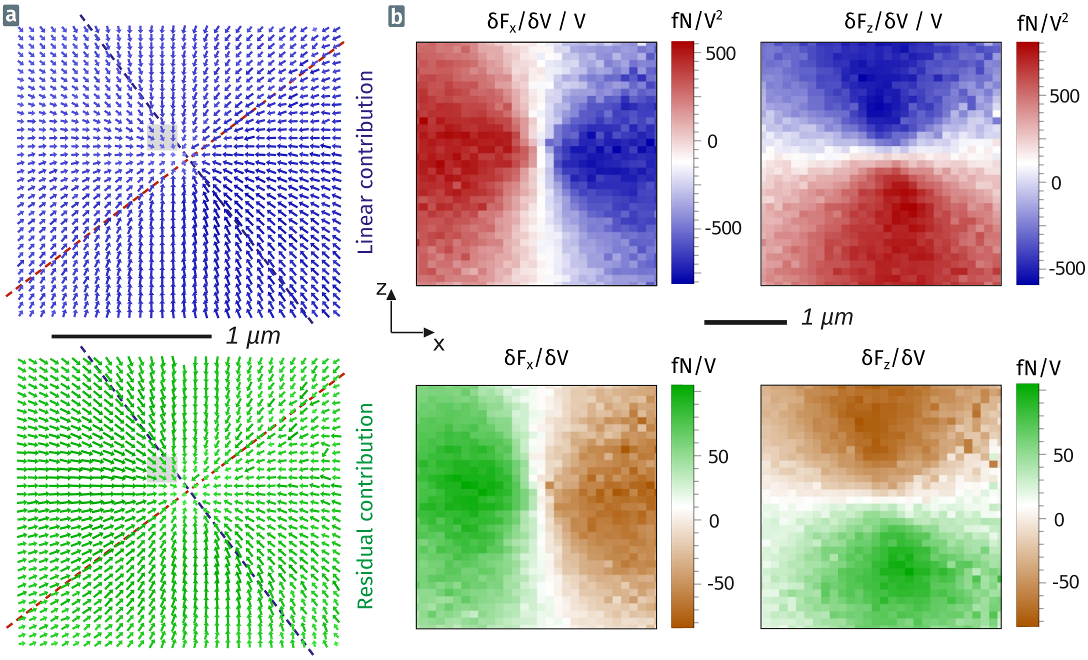

Fig. 2.40: The linear and quadratic contributions obtained with a fit to each local measurement provide the force fields shown in (**a**). The shaded area illustrates the point of the example in Figure 2.41. Using the nearest neighbours to fit the local slope, one obtains the local forces $\delta F_{x,z}/\delta V$ (**b**).

derivative of the measured driven force fields. To do so, we take into account the nearest surrounding points. This provides a 3 × 3 map, where at each point we determine the linear slope $\delta F_{x,z}/V_{bias}$ and the residual offset $\delta F_{x,z}$ of the driven force contribution by a linear fit. Taking the grey shaded area in Figure 2.40 as example, one obtains the local force field shown in Figure 2.41a. We can then fit the linear and residual components at nine points for each force direction with a plane $f_{x,z} = a_1 x + a_2 z + b$, where $a_{1,2}$ are the local gradients along x and z (see Figure 2.41b and 2.41c) of the driven force field.

Note, that due to the linearization $\delta \mathbf{F} = 2\boldsymbol{\alpha}\delta V\, V + \boldsymbol{\beta}\delta V$, the linear term that we derive with this method is twice the quadratic force gradient obtained from the frequency based measurement, while the residual term from the above method directly compares to the linear force gradient from the frequency based measurement. The gradients $\partial_i F_j$ $(i, j = x, z)$ obtained in Figure 2.41 are:

$$\begin{pmatrix} -1.46 & -0.40 \\ -0.72 & -1.32 \end{pmatrix} \mu\mathrm{N\,m^{-1}\,V^{-2}}$$

for the quadratic contribution, so that the half divergence of the quadratic term is: $0.5(dxFx + fzFz) = -1.39\,\mu\mathrm{N\,m^{-1}\,V^{-2}}$, which is in good agreement with the divergence obtained from the parabola fit of Figure 2.38: $\mathrm{div}\alpha = -1.32\,\mu\mathrm{N\,m^{-1}\,V^{-2}}$. The same agreement is obtained on the divergence of the linear term $\mathrm{div}\boldsymbol{\beta}(-0.34\,\mu\mathrm{N\,m^{-1}\,V^{-1}})$ at that given position.

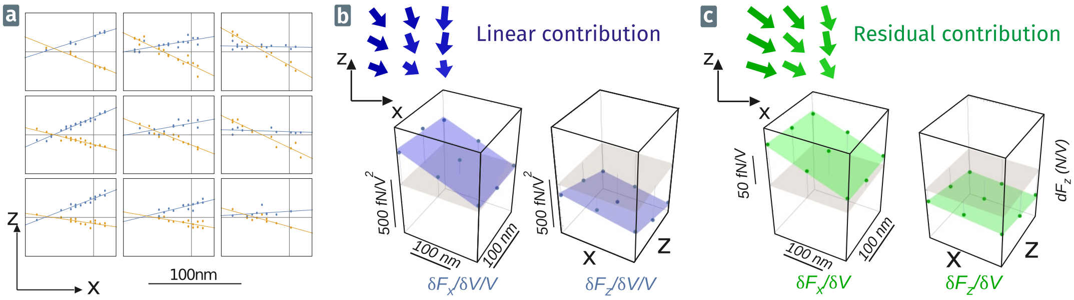

Fig. 2.41: In order to calculate the local gradient of a two dimensional force map, we take the measurements at the nearest neighbours into account. This gives an ensemble of 9 measurements (**a**), for which we individually perform a line fit to obtain the linear (slope) and residual (offset) contribution. We then plot the fitted linear (**b**) and residual (**c**) force in 3D and fit each set of nine points with a plane $f(x, z) = a_1 x + a_2 z + c$. The slope of this plane in x (a_1) and z (a_2) direction are the local force field gradients. The insets in (**b,c**) are an image of the vector flow derived from the fits of the bare measurements shown in (**a**). The central point of (**a**) is identical to the measurement shown in Figure 2.38.

Figure 2.42 presents the complete map of the linear and residual force gradients calculated via the driven force. In both cased $\partial_x F_z \approx \partial_z F_x$, which demonstrates that the measured electrostatic force field is conservative. We also observe the same central shape of the linear and residual contributions. We note that the sign of the maps in both cases has not necessarily to agree since the sign of the residual force depends largely on the direction of the parasitic field E_p which can be inversed when the workfunction difference between nanowire and sample is different. However, in the present case, both terms present a trapping force above the tip.

In Figure 2.43, we compare the force divergence from both measurements. The measured α in both cases agrees in amplitude and size, with the only difference of a higher noise floor on the amplitude based force measurement. We expect this to be the case since the amplitude measurement is limited by the determination of the detection vector and is thus affected much more by noise than the frequency measurement.

The linear term β of the force divergence is compared in Figure 2.44 and in plot 2.43c. Again, both datasets match in shape and amplitudes, with noisier results from the force measurement (2.44b).

This proof of principle measurement thus represents a method to validate the entire measurement chain. For what concerns the electrostatic force measurements, it represents a powerful tool to determine the quadratic and linear contributions of the force on the bias voltage. The greater knowledge acquired on those contributions will, in future, help to properly substract them to observe small residual forces such as the Casimir forces.

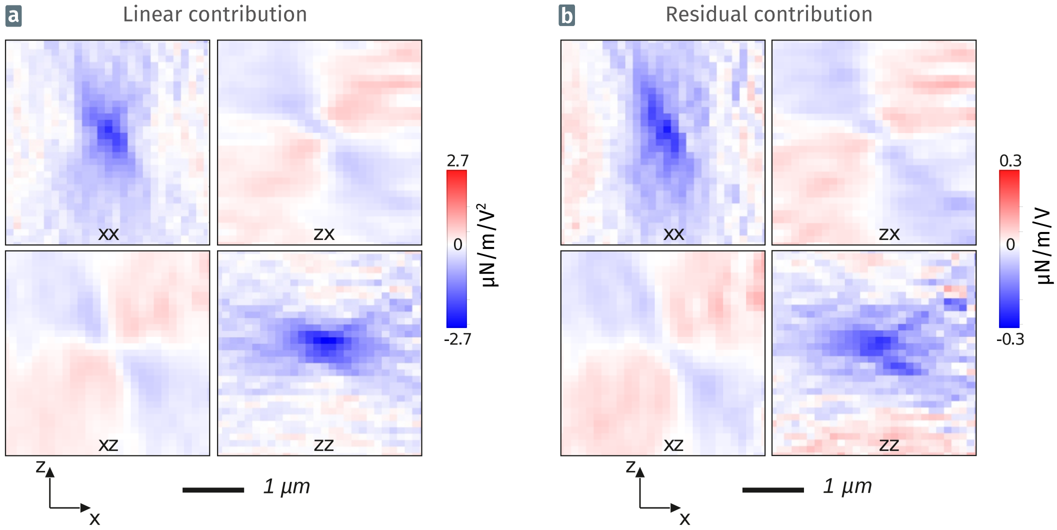

Fig. 2.42: The four force gradients $\frac{\partial\,(\delta F_{x,z}/\delta V)}{\partial x,z}$ of the linear (left) and residual (right) driven force components denoted by the indices x and z (e.g. xz for $\partial_z(\delta F_x/\delta V)$) are shown for the results from the direct force measurement. The linear term gives access to α (the quadratic term from the frequency based measurement) and the residual term comprises the linear term of the frequency based measurement.

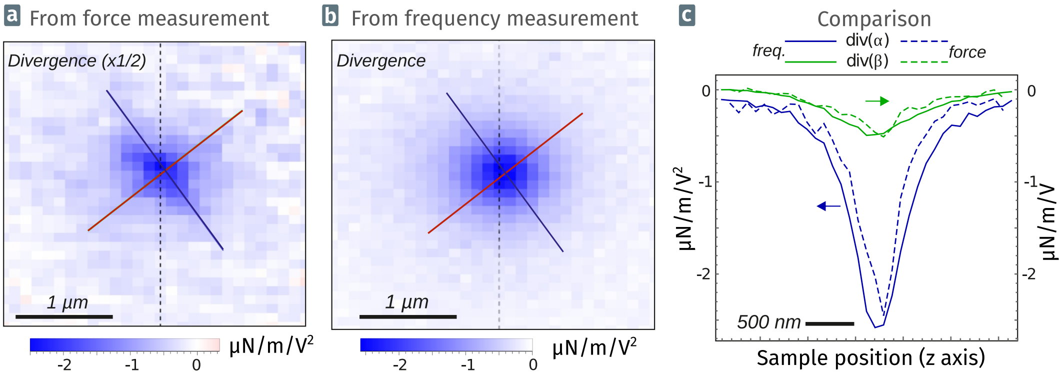

Fig. 2.43: The quadratic part α of the force divergence is obtained from the linearized force (with its slope as 2α) (**a**) and compared to the frequency based measurement of the divergence (**b**). In (**c**), line cuts through both maps are compared, showing a high degree of agreement. The green curve shows the linear contribution to the divergence β, as a result from a cut through the two maps in Figure 2.44. The cross marks the orientation of first (blue) and second (red) nanowire eigenmodes

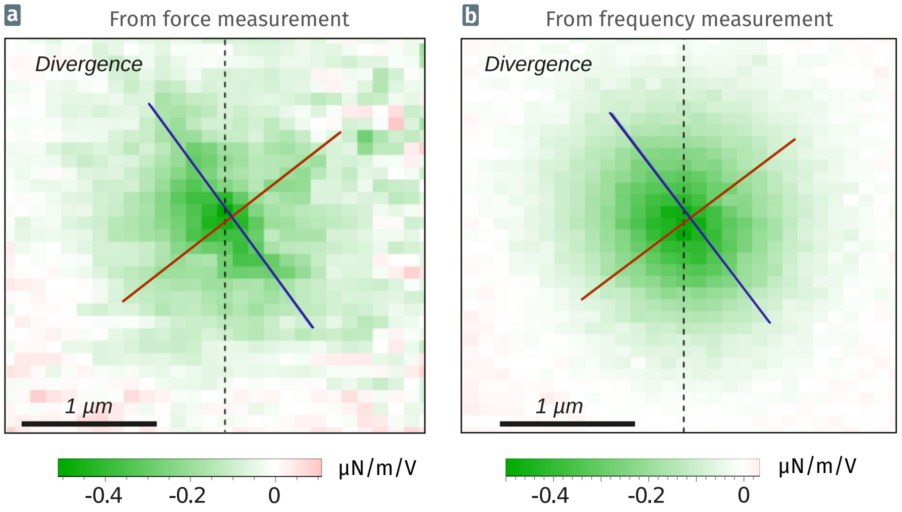

Fig. 2.44: The linear term of the force divergence is compared for the two measurements: The direct, amplitude based force measurement (**a**) and the frequency based measurement of the divergence (**b**). Both measurements give a linear force gradient in the order of 400 nN m^{-1} V^{-1} at the tip's central position.

3 Proximity and Casimir forces

While the electrostatic forces that have been the subject of Chapter 2 are dominant for nanowire-sample separations of hundred nanometers and more, proximity forces start to play a role at smaller distances. The measurement of proximity forces, in particular the Casimir force which originates from vacuum field fluctuations, is the motivation of the present chapter, as well as the description of the experimental limitations which originate from residual electrostatic fields. The latter should be understood and if possible compensated as to operate in a true electromagnetic vacuum. The chapter starts with a brief introduction to proximity forces and the Casimir force in Section 3.1.

In Section 3.2 we adapt the discussion of the Maxwell stress tensor from Section 2.1, introducing the fluctuating fields as origin of the Casimir force. The static, residual electric fields are responsible for two contributions in the force field, linear and independent on the sample bias voltage. We introduce a method that allows for compensating, under certain assumptions, their linear contribution so that the remaining force field can be restricted to the Casimir force field and to the quadratic contribution of the residual electrostatic fields. The linear contribution of the parasitic surface fields are responsible for a large scattering in the electrostatic parabola extrema, which prevents a proper definition of the sample work function, around which the effect of parasitic fields should be evaluated. We introduced a statistical analysis, which allows to retrieve a mean V_0 *value around which the effects of the surface patches can be developed. This method permits to suppress the linear contributions arising from the parasitic fields, so that one can determine the residual force, which do not depend on the bias voltage. It then contains the Casimir forces, as well as the quadratic contributions from the parasitic fields.*

In order to compare the extracted residual force to the expected Casimir force, one needs to estimate the strength of the Casimir force using numeric simulation techniques, which have been adapted in the frame of this work. Section 3.3 picks up the simulations performed in order to better understand the characteristics of the Casimir force in such a non-analytical geometry. We investigate the effects of different geometries and materials. For the geometry of a hole in a metallic surface beneath a SiC nanowire, we obtain estimations for the Casimir force field gradients in the range of tens of $\mathrm{aN\,nm^{-1}}$*, which is within the detection range of the nanowires.*

In Section 3.4, we apply the developed method to extract the residual force from a measurement for the geometry of two crossing trenches, which comes with a reduced dimensionality compared to a measurement above a circular hole. While the magnitude of the thus mea-

sured residual forces are in the same order as the predicted Casimir force and show similar features, they present a different distance dependency. We trace this back to the limitations of the method to extract the residual force, as it cannot remove terms that are quadratic in the parasitic residual fields.

We then finish the chapter by presenting a technique based on the employment of two additional pairs of electrodes positioned in the sample plane, which would allow compensating the parasitic fields along the three directions in space, and hence isolating the Casimir contribution from the parasitic field contribution (Section 3.5). This technique will be subject to future studies and is already tested in our group.

✦

✦

3.1 Beyond electrostatics – Proximity forces

In the previous chapter, we have considered electrostatic forces between two objects – the nanowire and a nano-structured electrode – which are at a distance of a few micrometers or less. At shorter lengthscale, other effects than the electrostatic force, which is long ranging in comparison to those proximity effects, come into play. Contrary to the electrostatic effects discussed above, those forces originate from dynamical interactions, which can be understood either from a material point of view: an interaction between fluctuating dipoles, or from a field point of view: the action of fluctuating electric fields δE. This class of interactions can be divided into three historically grown groups, the *Van der Waals* force, the *Casimir-Polder* force and the *Casimir* force.

The Van der Waals effect is a combination of the interaction between different dipole types (permanent or induced) in matter. The combined effect of all interactions (permanent with induced, permanent with permanent, …) is the resulting Van der Waals force. Figure 3.1a illustrates the example between a fluctuating permanent dipole p_1 that induces a polarization p_2 in a second particle which causes an interaction between both particles.

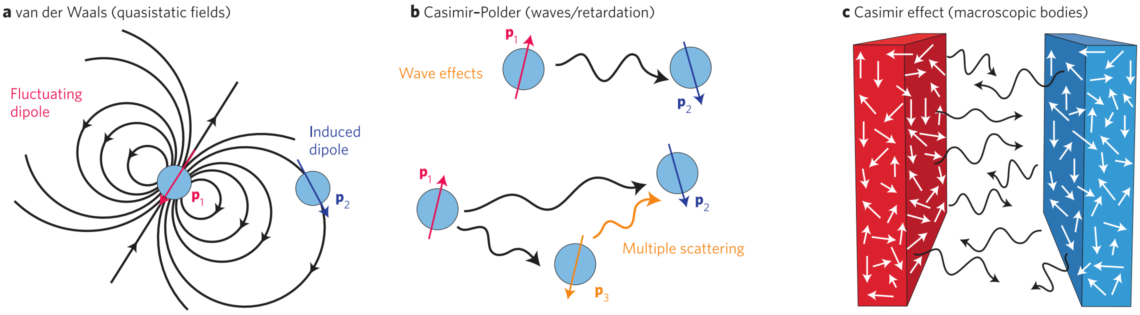
a van der Waals (quasistatic fields)

b Casimir-Polder (waves/retardation)

c Casimir effect (macroscopic bodies)

Fig. 3.1: Illustration of the different types of dipole fluctuation induced forces: Van der Waals force (**a**), Casimir-Polder force (**b**) and the Casimir force (**c**). Taken from [98].

In 1948, *Hendrik Casimir* and *Dirk Polder* integrated a delay in this interaction, originating from the finite speed of light in the description of the Van der Waals force [15]. When solving the problem for a neutral atom in front of a flat metallic mirror, and for two neutral atoms, they found that the delay causes the force to decay more rapidly at large distances than the London-Van der Waals description suggested. This adds a monotonously decreasing prefactor to the static Van der Waals force. The interaction between atoms and neutral objects is therefore often referenced to as *Casimir-Polder* force, however, the physical mechanism – the interaction between fluctuating dipoles – is the same. Figure 3.1b schematically illustrates how delayed effects between dipoles come into play.

In the same year, Casimir also first presented his calculation for an attractive force between two parallel, perfectly conducting plates [16]:

$$F = \hbar c \frac{\pi^2}{240} \frac{1}{a^4}, \tag{3.1}$$

where a is the distance between the plates. While Casimir based his calculations on the change in zero point energy when one introduces the metallic plates in vacuum, more general approaches [32, 66] are based on the fluctuation of the vacuum field. The Casimir force is non-additive and one needs to take into account the combined fluctuation of the dipoles contained in the macroscopic bodies (Figure 3.1c).

In order to precisely predict the outcome of measurements of the Casimir force, more recent works took into account the properties of the real mirrors [40, 63, 96]. These are in particular a finite temperature and the optical properties of the metallic plates which deviate significantly from a perfect metal descriptions at the part of the spectrum which plays a dominant role in the calculation of the Casimir force. With deviations from the theory for ideal mirrors due to a realistic Drude model of the materials, Lambrecht and Reynaud achieved to reduce the deviation between theoretic prediction and experimental results to about 10% [63]. The correct modelling of the material parameters is thus a critical and complex problem in the calculation of Casimir forces, and a correct theoretical model requires experimental data to be tested against, which, however, is rare and difficult to be obtained.

Due to the intrinsic complexity of the calculation of the Casimir force, the original geometry of Casimir, and a few – highly symmetric – other geometries, still represent the standard configurations of Casimir experiments. Already a few years after its prediction, the Casimir force has been detected and other experiments followed up to the current date [26]. However, the increasing calculation efficiency of modern computers and new theoretical approaches [94, 95], allow to take a look at problems without analytic solutions. In particular, vertically repulsive Casimir forces were predicted to be experienced by a finite needle, positioned above a circular hole drilled in a metallic plane. The magnitude of the predicted effect is significantly smaller than the forces measured in traditional experiments, and has not been detected for the moment. The geometrical analogy with our experiment lead us to investigate the possibility to detect Casimir forces above a hole.

3.1.1 Measurements of Casimir forces on the microscale

The traditional Casimir pressure between two parallel plates at a distance of 1 µm is of 1.3 nN mm^{-2}, a force well detectable with modern force measurement techniques. Due to the easier alignment, measurements often use a spherical surface with large radius compared to the object separation, that in theory can be approximated by a superposition of flat rings with successively increasing diameter – the so called proximity force approximation (PFA) [10] –, as illustrated in Figure 3.2a from reference [50].

For these measurements, a spherical, micrometer sized particle which is attached to a vibrating force probe such as an AFM cantilever [50, 79] or a torsion pendulum [54], is approached to a surface and the Casimir force gradient along the oscillator trajectory is measured up to a few percent accuracy via the change of the probe's frequency. These measurements of the gradients of the uniform uniaxial Casimir force permitted exploring the effect of surface patches [38, 39, 58], surface structuration [54] (see example in Figure 3.2b), or the influence of the dielectric surrounding of the bodies [55, 79, 106], which allows repulsive Casimir interactions. However, the requirement of a perfect alignment and the small force per surface area has made it difficult to investigate Casimir forces on a smaller scale. With the growing field of micro- and nano-electro-mechanical systems (*MEMS / NEMS*), the Casimir force will become important when systems miniaturize [98] as the Casimir force is one origin of irreversible adhesion. First experiments [110, 119] already realized on-chip Casimir experiments that exploit the high accuracy of modern nanofabrication (Figure 3.2c). This technique has the advantage that one can measure a large ensemble of the same repeating nanostructures at the same time, thus dealing with higher absolute forces.

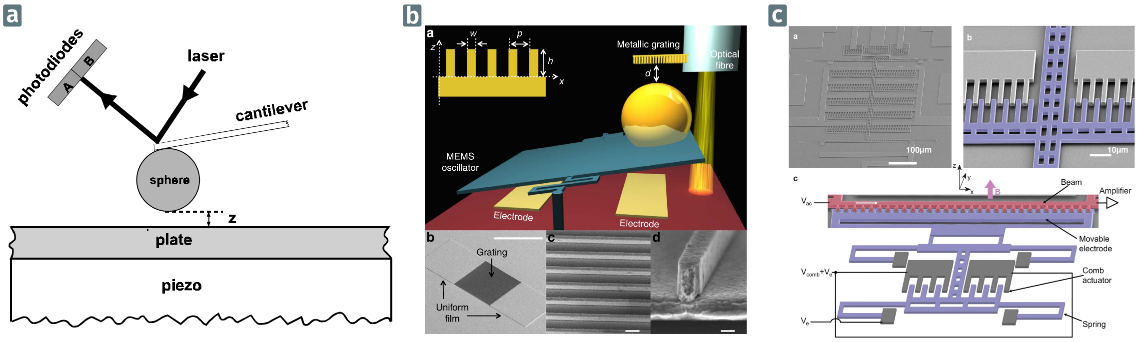

Fig. 3.2: The Casimir force between a plate and a sphere can be traced back to the force between two parallel plates via the proximity force approximation (PFA), and measured via a vibrating cantilever whose position is read optically (**a**) (from Harris et al. [50]). Similar experiments with structured surfaces have been conducted by Intravaia et al., using a more microscopic approach (**b**) (from [54]). Recently, nanomechanical on-chip experiments have been realized to measure non-monotonic Casimir forces (**c**) (from Tang et al. [110]). Here, the repetition of identical nanostructures that cause a certain Casimir interaction allows to enhance the total measured force.

In this chapter, we will discuss how two-dimensional nanowire force field nanoscopy can be used to explore proximity effects above nanostructured surfaces. Dissimilar to the measurements mentioned above, the horizontal force field sensing techniques, developped with the nanowire, allows to measure the lateral Casimir force on a small body, something that has only been done for large, structured parallel plates [19, 34] or for larger cantilevers at separations where the PFA is still valid (the separation is small compared to the radius of the sphere), in order to investigate the effect of non-contact friction in AFM [20, 109]. Additionally, the employment of small probes, such as the nanowire, permits to investigate novel forms of the Casimir effect like a repulsive Casimir force [64, 65, 76, 112], that has been modelled to be in the order of several aN for systems of comparable size to our nanowire (see below). The high sensitivity of the nanowire makes it an ideal candidate for first measurements of Casimir forces on the nanoscale. Also, the quantitative evaluation of the Casimir forces requires to properly take into account the physics of the electrostatic patches. This measurement is however rarely done with the same probe as for the one employed for the Casimir measurements (in particular because one wants to access patch sizes far smaller than the sphere radius). Interestingly, the nanowire can in principle also serve to explore the structuration of the electrostatic patches, as illustrated in the above chapter.

3.2 Detecting the Casimir force with a nanowire

The measurement of Casimir forces requires a sensitive force detection whose principles we layed out in the previous sections. Furthermore, the small magnitude of the Casimir force compared to the electrostatic force requires a good knowledge of the involved materials. We have already mentioned the presence of electrostatic patches in the last chapter, which makes that the nanowire is always surrounded by a residual electric field so that the measurement conditions deviate from the vacuum field required to measure only the Casimir forces. Here, we will first present a basic interpretation of the contributions of fluctuating fields to the electrostatic Maxwell Tensor introduced in Section 2.1, which permits to formalize the nanowire based Casimir measurement. Then, we will discuss an analysis technique accounting for the linear contribution arising from the surface patches. We also briefly discuss the numerical recipes used for simulation of the Casimir force above nanostructures.

3.2.1 The effect of fluctuating field in the Maxwell formalism

In Section 2.1, we have introduced the Maxwell stress tensor to calculate the electrostatic force acting on a nanowire above a structured surface. For the purely electrostatic case, the field around the nanowire's extremity is a sum of the field $\mathbf{E}_V$, which is controlled by the electrode, and parasitic residual fields $\mathbf{E}_\mathrm{p}$, caused by effects like electrostatic patches or charges, which do not depend on the bias voltage. In order to take the fluctuating fields that cause the proximity interaction into account, we add a fluctuating field $\delta\mathbf{E}$, which has a zero time-averaged value, but a non-zero *rms* value and is the origin of the Casimir force:

$$\mathbf{E} = \mathbf{E}_V + \mathbf{E}_\mathrm{p} + \delta\mathbf{E}. \tag{3.2}$$

The investigation of the fields close to the nanowire's tip in box 2.a has shown that the force on a thin nanowire is solely caused by the fields at the bottom integration surface. There, the stress tensor component that gives the force in the horizontal direction is given by $T_{xy} = -\varepsilon_0 E_x E_y$ which, similar to (2.11), yields:

$$T_{xy} = -\varepsilon_0 \big(E_{V,x} + E_{\mathrm{p},x} + \delta E_x\big)\big(E_{V,y} + E_{\mathrm{p},y} + \delta E_y\big) \tag{3.3}$$

Since the force is the integral of the time averaged stress tensor, the first order contributions in δE vanish and only the second order fluctuating term $\delta E_x \delta E_y$ remains, so we obtain for the force:

$$F_x \propto \underbrace{E_{V,x}E_{V,y}}_{\propto V_\mathrm{bias}^2} + \underbrace{E_{V,x}E_{\mathrm{p},y} + E_{V,y}E_{\mathrm{p},x}}_{\propto V_\mathrm{bias}} + E_{\mathrm{p},x}E_{\mathrm{p},y} + \big\langle \delta E_x \delta E_y \big\rangle. \tag{3.4}$$

The quadratic electrostatic term remains again unchanged, as well as the linear term, but the fluctuating forces add a new contribution η to the offset force:

$$F_x = \alpha V_{\text{bias}}^2 + \lambda V_{\text{bias}} + \gamma + \eta. \tag{3.5}$$

We retrieve the same parabolic form for the electrostatic force as before, but now with an offset caused by the linear contribution from the parasitic residual fields plus the quadratic contribution from the fluctuating fields. Figure 3.3 illustrates this shift and the corresponding terms at play.

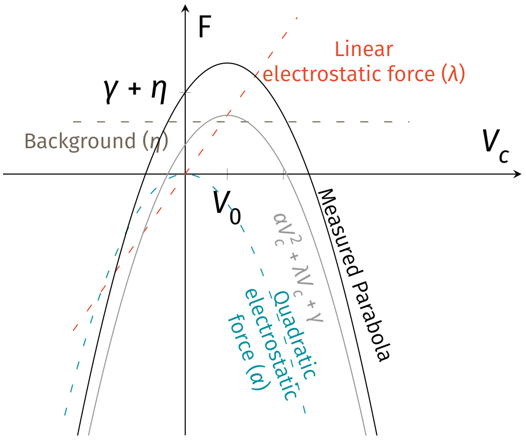

Fig. 3.3: A force measurement at a fixed position in an ideal environment without stray fields would give a force parabola $F(V)$ that is only determined by the quadratic electrostatic coefficient α (blue), whereas parasitic residual fields cause a linear contribution (orange), which creates a shift of the parabola extrema, as well as a modification of the force extremum force. Field fluctuations cause a constant, voltage independent, offset η so that the measured parabola (black) is further displaced vertically. The grey parabola does only show the quadratic and linear contributions. It has the same apex position V_0 as the black curve since the background force does not add a horizontal shift of the parabola.

3.2.2 Extraction of the Casimir contribution

In order to measure the Casimir force, one would ideally measure the voltage dependent quadratic and linear electrostatic forces to try to isolate the voltage independent Casimir effect. From a voltage varying measurement one can infer the terms α and λ without ambiguity, but it is not possible to compensate for the quadratic contribution from the parasitic residual fields, since the products of the fields $E_{V,x/y}E_{\text{p},y/x}$ and $E_{\text{p},x}E_{\text{p},y}$ have a different spatial dependence. To suppress the residual electrostatic fields, we will propose, at the end of this chapter, a method based on the use of external electrodes to compensate the residual horizontal electric field contributions. We believe that, with such a method we could reach a better estimation of the Casimir forces. In the following, we will present a method to partially compensate for the linear voltage contribution in the force, caused by the parasitic fields.

With force gradients expected at the level of a few tens of $\mathrm{aN\,nm^{-1}}$ (see below), the Casimir force is much smaller than the contribution of the electrostatic fields $\mathrm{fN\,nm^{-1}}$, which are maximal when the nanowire is positioned close to the surface. Above an unstructured, flat area, surface patches present the main source of force field variability above the surface, leading to spatially dependent terms $\lambda(\mathbf{r})$ and $\gamma(\mathbf{r})$. In presence of a Casimir term η whose transverse spatial variations are supposed to be small compared to that of the linear terms, which are caused by statistically distributed variations of the surface fields, the parabolas will, on average over the area, have a common crossing point. If the statistic is sufficient, such an averaging process should in principle lead us to an estimate of the average workfunction difference between the two materials. From this point we can infer a statistical value for V_0, which can be used in the subsequent analysis to suppress the linear contributions of the surface terms for the rest of the map. *It is important to note that this V_0 does not represent the workfunction difference as one would measure in KPFM, due to the intrinsic difference to the horizontal force measurement.*

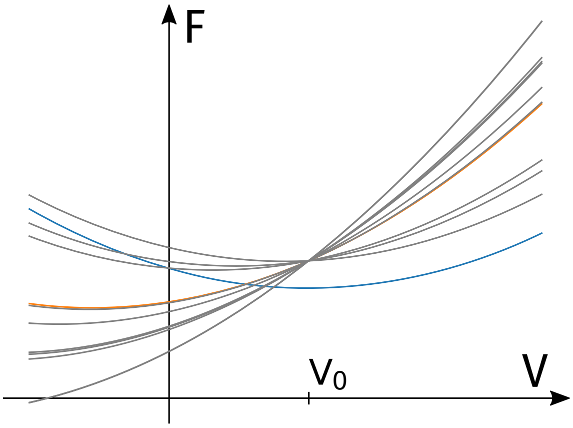

Fig. 3.4: The measured force parabolas on a flat surface, or at sufficient distance from the surface show little to no variations in the quadratic term α and without the presence of residual constant electrostatic fields one would measure the blue parabola whose vertical offset is only due to the Casimir force. The voltage independent residual fields E_p cause a linear contribution due to the product of the fields $E_V E_p$ and a constant term E_p^2 that adds an additional offset to the Casimir contribution η. When the local workfunction on the surface fluctuates around a mean value, the measured parabolas (grey, orange) all cross at a common, mean V_0.

The above principle is based on the fact that for a given α, variations of the parasitic fields will lead to a displaced parabola, but the force at the offset potential V_0, will remain unchanged (see Figure 3.4). Even if the presence of the quadratic parasitic terms ($E_{\mathrm{res},x}E_{\mathrm{res},y}$) may falsify this assertion, they contribute generally only weakly, and finding the “stable” point in the force divergence measurements thus represents a reasonable method to estimate V_0. At this potential, the variations of the force divergence can be supposed to be caused only by the terms $E_{\mathrm{res},x}E_{\mathrm{res},y} + \langle \delta E_x \delta E_y \rangle$. The principle of the estimation of

V_0, and of the linear contribution due to surface fields is illustrated in Figure 3.5, using experimental data.

To obtain the common crossing from the measurements, we fit all the curves div$F(V_{\text{bias}})$ acquired at varying positions, and create a 2D histogram of all fitted parabolas measured on a reference area (i.e. far away from the surface structuration), such as shown as Figure 3.5. We then determine the point where most parabolas overlap by fitting a Gaussian distribution for each line $P_{V_i}(\text{div}F)$ at each voltage V_i. The common crossing is found at the voltage $V_{\text{bias}} = V_0$, where the spreading of the fitted Gaussian is the smallest.

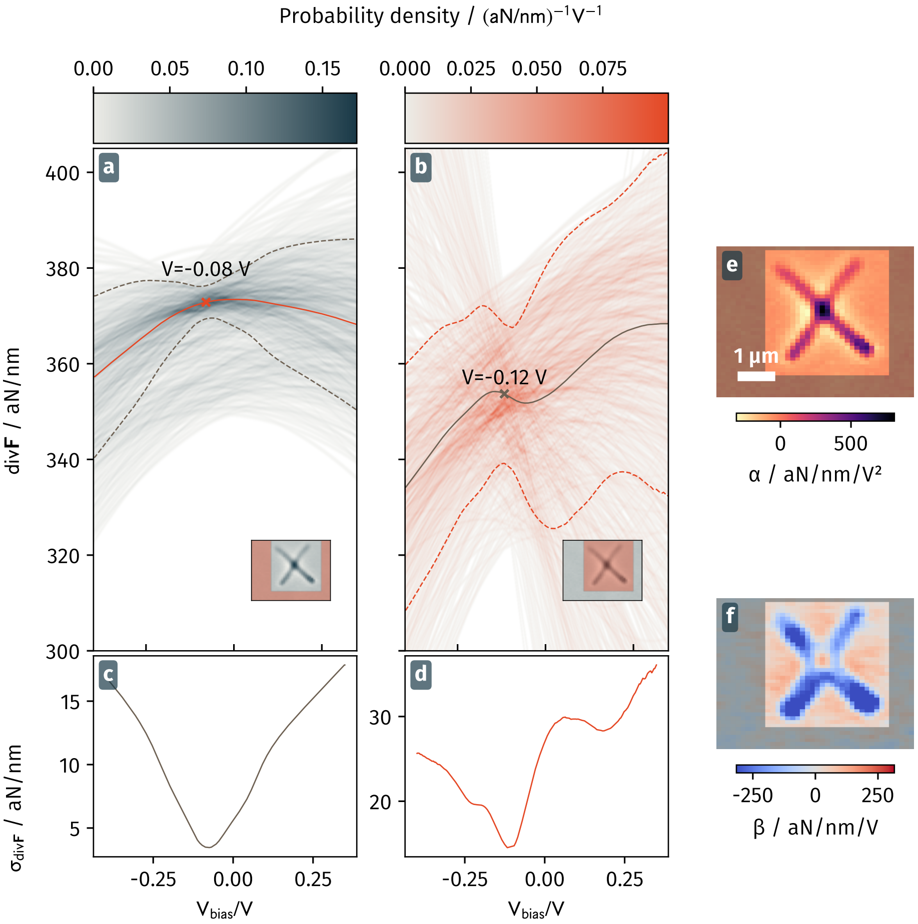

Fig. 3.5: In order to find the common crossing of the force divergence parabolas in the voltage plane, we create a histogram based on the fitted parabolas (**a,b**). In (**a**), we take only neutral points, which means points where the nanowire is far from the test structure (as indicated by the red shaded area in the inset), into account. In (**b**), the area close to the cross is investigated. In the 2D maps, presented in (**e,f**) the quadratic term α (**e**) is relatively constant in the neutral region but the parabolas are shifted by a varying linear term β (**f**). The common crossing is then determined by fitting a Gaussian distribution to each vertical line of the histogram (the orange line marks the center of the distribution, the dotted lines show the standard deviation σ which is also shown in the plots (**c,d**)) and determining the point where this distribution has the smallest width (orange cross), which gives the point of common crossing.

We have found that, for all measurements of better quality (long averaging times, small error in the frequency estimations, ...), the parabolas tend indeed to have a common crossing point, and the assumption of statistically distributed variations of the linear term is therefore plausible. Also, after subtraction of the linear contribution of the parasitic fields, the remaining Casimir contribution η is in the order of magnitude we would expect for the geometries we work with. In the following section we discuss numeric tools used to estimate the Casimir force we can expect and will then present some of the maps of the residual force measured above nanostructures.

3.3 Simulating the Casimir force

3.3.1 Methodology

Since the analytic calculation of the Casimir force is only possible in highly symmetric geometries with nearly ideal material properties, we can not rely on analytic methods to estimate the Casimir force experienced by a nanowire above a structured sample. However, with the increase of nanofabrication craftmanship in the last decades, the demand for numeric methods to calculate the Casimir force increased as well. Due to the similarity between fluctuation induced effects and classical electromagnetic (EM) problems, it has been possible to adapt standard computation methods for EM to calculate the Casimir force for more complex geometries and materials (see Dalvit et al. [26, Chapter 6]). All methods have in common, that one needs to integrate the Maxwell stress tensor on a surface surrounding the nanowire, as introduced above, but by integrating the contribution of **all** frequencies ω, corresponding to a sum of the vacuum energy for all possible modes. We remember that the Stress tensor (in Minkowski representation) is defined as [26, 27]:

$$\begin{aligned}\left\langle T_{ij}(\mathbf{r})\right\rangle_\omega = \varepsilon(\mathbf{r},\omega)\left[\left\langle E_i(\mathbf{r})E_j(\mathbf{r})\right\rangle_\omega - \delta_{ij}/2\sum_k\left\langle E_k(\mathbf{r})^2\right\rangle\right] \\ + \mu(\mathbf{r},\omega)\left[\left\langle H_i(\mathbf{r})H_j(\mathbf{r})\right\rangle_\omega - \delta_{ij}/2\sum_k\left\langle H_k(\mathbf{r})^2\right\rangle\right]\end{aligned} \tag{3.6}$$

The field correlations are given by the *Green's function* $\mathcal{G}(\mathbf{r},\mathbf{r}',\omega)$ that comprises material and geometric properties [26, 67]:

$$\left\langle E_i(\mathbf{r})E_j(\mathbf{r})\right\rangle_\omega = \frac{\hbar\omega^2}{\pi}\Im\mathcal{G}_{ij}(\omega;\mathbf{r},\mathbf{r}')\coth\left(\frac{\hbar\omega}{2k_BT}\right), \tag{3.7}$$

for $T > 0$, and similar for the magnetic field with the corresponding magnetic Green's function. Here, the fluctuation-dissipation theorem relates fields to vacuum fluctuations.

The Green's function represents the electrical response to a localized current source, and thus relates the electric fields to harmonically oscillating source currents $\mathbf{J}(\mathbf{r}, \omega)$.

Due to material and geometric resonances, the field shows a very complicated, oscillating behaviour for real valued frequencies with most frequency contributions cancelling each other out in the Casimir integral, and only a small resulting value that finally gives the Casimir force. One can, however, rotate the integral to the positive imaginary axis where the integrand is usually well-behaved. This is possible since, after Cauchy's integral theorem, the integral along a closed path in the complex plane always values zero if it does not contain poles of the integrand. Since the poles of the Green's functions are only in the negative imaginary plane, the path integral between two points in the positive plane is identical. Instead of integrating over the real ω-axis (the orange curve in Figure 3.6), one is free to chose a path along the imaginary ξ-axis that rejoins the real axis at $\omega \gg 0$ (blue curve). Since $\mathcal{G}$ decays exponentially with $\omega + i\xi$, the integral in this region is zero and one obtains the equality between a path integral along the real and imaginary axis. Such a rotation from real to imaginary frequencies with $\omega = i\xi$ is called *Wick rotation* [26], and the stress tensor integral over the closed surface S becomes [99]:

$$F_i = \mathfrak{I} \int_0^\infty i \, \mathrm{d}\xi \oiint_S \sum_j \langle T_{ij}(\mathbf{r}; \xi) \rangle \, \mathrm{d}\mathbf{n}_j. \tag{3.8}$$

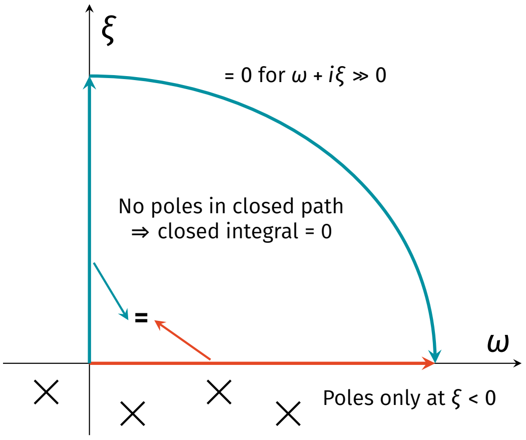

Fig. 3.6: Illustration of the Wick rotation that follows from Cauchy's integral theorem. The integral along the closed curve illustrated by the blue and orange line equals zero as all poles are located at the negative imaginary half space. Since the integrand is zero at large $\omega + i\xi$, the integral along the real ω and imaginary ξ axes are equivalent.

At finite temperature, the integral in (3.8) becomes a sum over the so called *Matsubara* frequencies [26, 32, 67]:

$$\xi_n = \frac{2n\pi k_B T}{\hbar}, \tag{3.9}$$

Matsubara frequencies

which are a consequence of the poles of the Bose-Einstein occupation factor $\coth(\hbar\omega/2k_BT)$ in the fluctuation-dissipation theorem in Equation 3.7, and of the application of the residue theorem to the integral.

In this work we have used two calculation methods for the Casimir force. The first one makes use of the scattered field in the time domain [72, 99], so that finite-difference time-domain (*FDTD*) simulation methods can be used to solve the stress tensor integral numerically. A free FDTD simulation software developed by some of the authors of the methods, coming with means to calculate Casimir forces, is *MEEP* [83]. Due to the complexity of the computation, this approach is effectively limited to simulations of the Casimir force in 2D. After having reproduced some of the predictions for systems similar to our nanowire [65], we switched to a more versatile technique that describes the electromagnetic field in terms of fluctuating surface currents [94, 95]. In this approach, the integral over the Maxwell tensor reduces to a sum over the discretized interaction of surface currents at each imaginary frequency ξ on the test object, which can be solved with less numerical effort (see reference [95] for a detailed theoretic derivation). In contrast to the FDTD approach, this method does not rely on a meshing of the entire geometry, but only of the object surfaces, which reduces the number of calculation steps. Additionally, the force contribution is increasingly small for large ξ_n, so that one only needs to calculate for the first few tens of values of n. We use an implementation of the boundary element method developed for Casimir simulations called *SCUFF-EM* [93].

3.3.2 Implementation

The geometry we are interested in, is in particular that of the nanowire above a hole in a metallic plate since a repulsive force has been predicted for the case of a vertical dipole above a hole [33, 65, 112], as illustrated in Figure 3.7a.

The experimental geometry is different from the ideal proposed cases, in the aspect that we do not have an infinitely thin metallic plate, but a metal layer on a dielectric substrate. Additionally, the nanowire is not an ideal uni-directional dipole as it has a non-zero polarizability in the horizontal plane. We therefore picked up the calculation approach using SCUFF-EM and designed a geometry that reproduces the experimental case. Figure 3.7b illustrates a typical simulation geometry. Similarly to the electrostatic simulation we reduce the nanowire's length in order to save computation time, however, we now do not suffer from accuracy losses since the top part of the nanowire does not add much to the scattering properties of the field confined between the objects. This assumption is confirmed by a comparative study with different nanowire lengths, shown in Figure 3.8. The variations in the Casimir force do not seem to be linked systematically to the nanowire lengths, so that they most likely emerge from small differences in the simulation geometries (the meshing). It is hence important to assure a fine meshing at the opposing faces of the objects with a good resolution at curved regions and edges. The objects and meshes are scripted and then created with the free software *GMSH* [41].

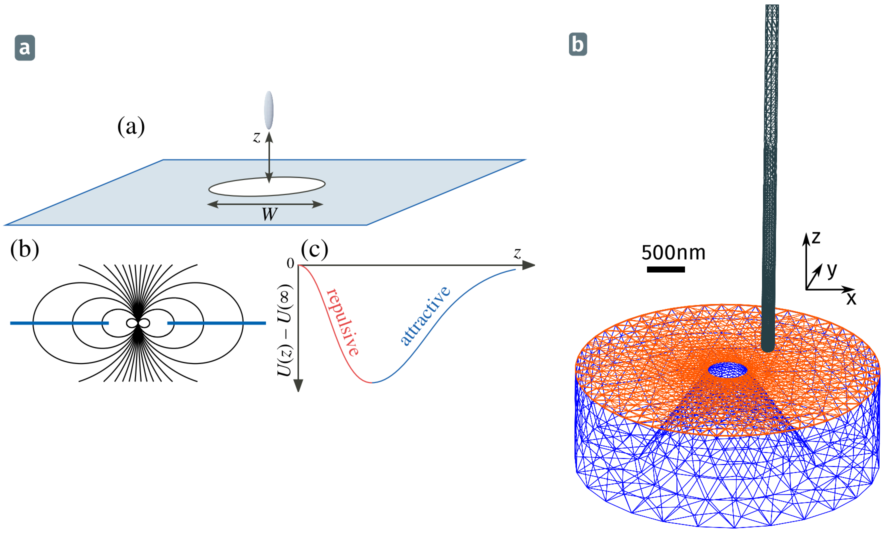

Fig. 3.7: (**a**) An elliptical, vertically polarizable particle is erxpected to be vertically repelled close to a hole drilled in a metallic plate (**a**-a) from [65]. This follows from the argument that, when the particle is positioned centrally in the hole (**a**-**b**), its field lines are perpendicular to the plate, so that no interaction is present between the dipole and the rest of the plane, since the latter cannot be polarized by the perpendicular field due to symmetry. At infinite distance, the particle also experience a vanishing force, however it must be attracted by its image dipole for $z \gg W$, so one obtains a typical potential interaction energy as shown in (**a**-**c**), which is repulsive at small z. (**b**) Sketch of the simulation geometry for the nanowire-hole geometry. The sample represents a conical hole in a silicon cantilever (blue), that is covered by a metallic plate (orange). All surfaces and interfaces between materials need to be meshed for the surface current method. We chose a particular fine mesh on the opposing faces of nanowire and sample (close to the hole), as these faces are the main determinants of the scattering properties.

The above simulations also allows to give an estimate for the Casimir force properties: its magnitude is around some tens of aN, varying on a transverse dimension of hundreds of nm, so that the horizontal force field gradients can be expected at the level of $\partial_x F_x \approx 0.3\,\mathrm{aN\,nm^{-1}}$. This magnitude is rather weak but other geometries studied below will predict force gradients well within the force sensing capacities of the nanowire.

Since the Casimir force strongly depends on the optical properties of the materials, we model all domains with experimental data from optical measurements [84], which is evaluated at imaginary frequencies using the *Kramers-Kronig* relation following the principles layed out by *Reynaud et al.* [26, 63]:

Kramers-Kronig relation

$$\varepsilon\left(i\xi\right) = 1 + \frac{2}{\pi}\int\limits_0^\infty \mathrm{d}\omega \frac{\omega\varepsilon''(\omega)}{\omega^2 + \xi^2}. \tag{3.10}$$

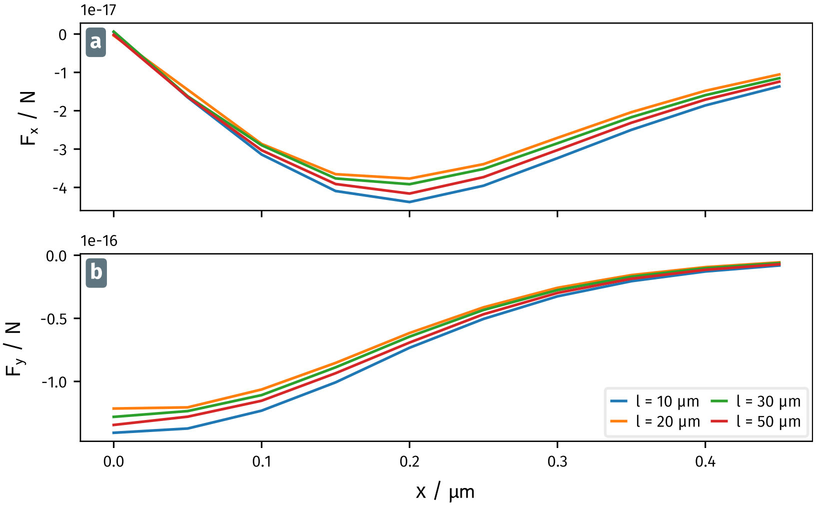

Fig. 3.8: Comparison of the Casimir force between a sharp metallic tip with a curvature radius of 30 nm and a nanowire with diameter d = 200 nm for different nanowire lengths at a height of y = 70 nm. (**a**) presents the horizontal force (parallel to x) and (**b**) the vertical force (in y direction), for a horizontal scan of the nanowire tip with the tip apex located at x = 0. The Casimir force is found to be attractive vertically and horizontally, towards the tip extremity. The nanowire length does not have a systematic effect on the calculated force, and the present differences are likely to originate from different meshing (each nanowire is meshed seperately). The variations can therefore provide an error estimate for the conducted simulations.

3.3.3 The nanowire-hole geometry

We will now discuss the simulated results for the realistic nanowire-hole geometry. While the predictions of a vertically repulsive Casimir force have been obtained for a comparably small object [64, 65], there are no detailed studies of what happens if the particle above the hole is a relatively large object such as our nanowire with a diameter in the order of 1/2 of the hole size. Also, it has been unclear which effect the presence of a dielectric substrate would have on the Casimir force, and what one could expect from a quasi infinite object in contrast to the finite particles employed.

Indeed, in the conducted simulations, we do not find a vertically repulsive force, most likely due to the non-uniaxial polarizability of the realistic nanowire. Figure 3.9a shows the vertical force F_y which is strongly attractive above the surface and goes towards zero in the center of the hole. As the distance between nanowire and sample increases, the force rapidly decreases. Figure 3.9b shows the simulated lateral (parallel to the surface) Casimir force F_x and panel 3.9c the force gradient $\partial_x F_x$ above a 370 nm large hole, experienced by a 4 µm long and 160 nm thick nanowire scanned at an altitude of 200 nm above the hole. In plot 3.9d, the force field divergence $\partial_x F_x + \partial_z F_z$ is presented as calculated from the simulated forces. It resembles the gradient, due to the symmetry of $\partial_z F_z$. The lateral force shows a clear antitrapping profile, corresponding to a pronounced attraction towards the perimeter of the hole, notably, with a the force extrema slightly shifted to the inner side of the hole. This observation is similar to the findings in reference [73], where the vertical, repulsive Casimir force on a cylinder with a diameter much smaller than the hole's is maximal close to the hole's edge. This case is similar to the geometry of a polarizable particle and a single wedge (the hole's border in this case), which is discussed in reference [75]. In a certain way – if the nanowire is small with respect to the hole – one can describe the hole's perimeter as single *wedge*, assuming the nanowire is blind to the effect of the opposite boundary. The corresponding gradient $\partial_x F_x$ shows

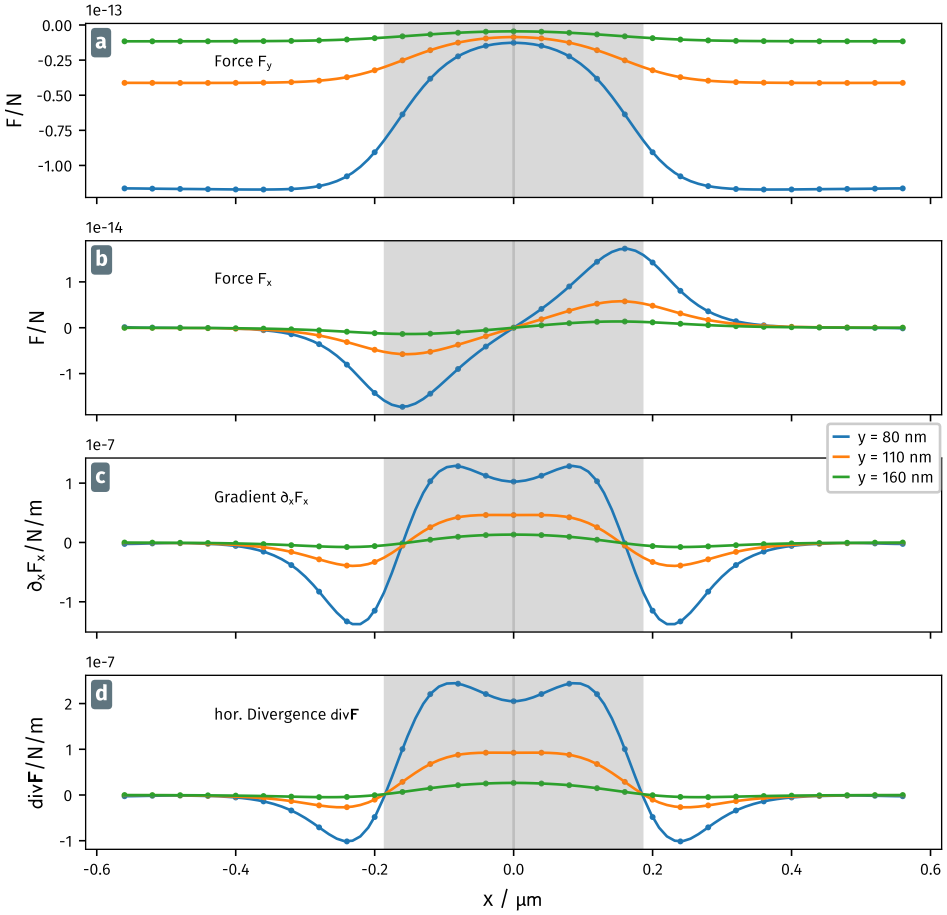

Fig. 3.9: The simulated vertical force F_y on a SiC nanowire with diameter d = 160 nm and length l = 4 µm above a hole in a gold coated Si cantilever with diameter W = 370 nm is shown in (**a**). The other panels show the lateral Casimir force (**b**) and force gradient $\partial_x F_x$(**c**), as well as the 2D divergence $\mathbf{divF}$ in the horizontal plane (**d**). The latter is calculated by assuming a radial symmetry for the Casimir force field. While for the nanowire-hole geometry we do not obtain a vertically repulsive force above the hole, the nanowire experiences an anti-trapping Casimir potential which is strongest close to the edges. The simulation results (points) are connected by a spline for visual guidance.

five local extrema in the horizontal cut for large holes: two are found above the metal surface just before the hole, and two inside. Between the two central maxima, the curve has a dip which is present when the nanowire is close to the surface (blue curve), but disappears for larger distances ($y > 100$ nm) where it forms a flat region.

From these results, we can note three important observations. Firstly, there is the absence of a vertical repulsive force while an antitrapping horizontal force is present. Since we were not able to find a repulsive force with other realistic nanowire-hole geometries, a more thorough study would be needed, which should investigate the limit between the ideal case of a finite metallic plate with a hole and a very thin uniaxially polarizable needle and our realistic case. However, the lateral antitrapping is a particular case lacking experimental investigation.

Secondly, the expected gradient has a highly structured shape, with trapping extrema outside the hole and two antitrapping regions within the hole, which can merge when the nanowire is retracted towards larger distance, or when the hole diameter shrinks.

And thirdly, the Casimir force decays quickly in the vertical direction, and compared to close distances, disappears for distances larger than 150 nm, however, with gradients of tens of aN nm^{-1} and more at distances shorter than 150 nm, they fall well within the sensitivity range of the experiment.

Next, we take a look at the influence of different hole sizes and the role of the underlying substrate. In Figure 3.10a, we compare the force gradient above a hole that is etched cylindrically through the cantilever with one of a conical shape. The force gradient for both cases is nearly identical, with slightly smaller extrema for the straight, cylindrical hole. Thus, the theoretical contribution of the substrate to the Casimir force is rather small. Still, experimentally we may benefit from the conical hole shape, as the dielectric substrate is prone to contaminations and surface effects that can be amplified by the etching process. These parasitic effects could cover the Casimir force, so keeping them away by removing more of the substrate close to the hole is one way to mitigate them.

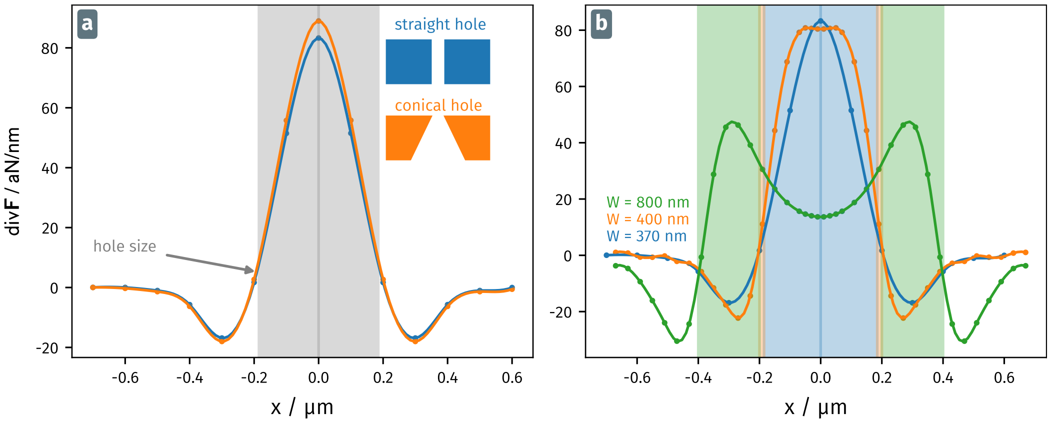

Fig. 3.10: The comparison between a straight, cylindrical hole and a conical one (angle≈24°) in the sample substrate (**a**) shows that the hole shape only plays a minor role for the Casimir force. The objects have the same extents as in 3.9, with l = 4 µm, D = 160 nm, W = 370 nm and a vertical nanowire-hole distance y = 200 nm. Plot (**b**) compares the gradient measured above three differently sized conical holes at y = 200 nm.

Panel 3.10b gives a comparison between different hole sizes. The smallest size corresponds to the hole in the previous plots. For increasing hole diameter, one observes that the central peak quickly becomes the double peak that we have already observed for close distances in 3.9. The maximum value of the force divergence in the antitrapping region decreases (the maxima decline) with larger hole size. A change in hole size does not affect the spatial extent of the individual features above the hole edges, which appear to only depend on the nanowire diameter and the scanning altitude. However in the central area, the maximum antitrapping strength saturates for small holes.

Influence of a tilt

In Section 2.6 we have already discussed that a nanowire tilt changes the force field experienced by the nanowire. It is rather natural to try to predict the influence of such a tilt on the force field experienced by the nanowire, by applying a rotation matrix to the horizontal and vertical forces experienced by a vertically positioned nanowire. However, this approach may fail in a Casimir simulation, so we wanted to verify if and up to which tilt angle such an approximation remains valid. We first describe the projection of the force field calculated in the x, y coordinates onto the coordinates of the rotated nanowire x', y'. Such a counter-clockwise rotation, by an angle α with respect to the x axis is expressed by:

$$\begin{pmatrix} x' \\ y' \end{pmatrix} = \begin{pmatrix} \cos\alpha & \sin\alpha \\ -\sin\alpha & \cos\alpha \end{pmatrix} \begin{pmatrix} x \\ y \end{pmatrix}, \text{ and } \begin{pmatrix} x \\ y \end{pmatrix} = \begin{pmatrix} \cos\alpha & -\sin\alpha \\ \sin\alpha & \cos\alpha \end{pmatrix} \begin{pmatrix} x' \\ y' \end{pmatrix}. \tag{3.11}$$

The projected force $F_{x'}$, which is perpendicular to the nanowire, would be given by:

$$F_{x'} = F_x \cos\alpha + F_y \sin\alpha, \tag{3.12}$$

and we obtain the projected force gradient in the tilted nanowire base by:

$$\frac{\partial F_{x'}}{\partial x'} = \frac{\partial F_x}{\partial x} \cos^2\alpha + \frac{\partial F_z}{\partial z} \sin^2\alpha + \left(\frac{\partial F_x}{\partial z} + \frac{\partial F_z}{\partial x} \right) \cos\alpha \sin\alpha \tag{3.13}$$

At small separations, where the vertical force gradient $\partial_z F_z$ is large, this effect plays an important role. Beyond such a simple evaluation, the tilted nanowire changes the Green's functions and can therefore alter the Casimir force field. In order to estimate the effect of the tilt, we performed simulations in the same geometry as in Figure 3.9, but with a nanowire rotated by α around its extremity, keeping the same scan coordinates.

Figure 3.11a presents the result for a rotation around the z axis – the nanowire is tilted in the scan plane. In order to discriminate between the effect of the projection and the different Casimir force on a tilted nanowire, we plot the approximated force gradient obtained with Equation 3.13, using the force values simulated for a perfectly perpendicular nanowire. The agreement between approximated tilt and real tilt shows the validity of the approximation. The rotation of the nanowire's eigenmode axis in the x, y plane is the crucial factor. For the previous simulations, it has been enough to simulate the space from the holes center towards positive x (due to symmetry), the case of the tilted nanowire requires a simulation of the negative and positive x. With the observation that the projection is the main contributor, we can stick to the faster simulation of a straight nanowire on half the scan range and still obtain meaningful results for a tilted nanowire up to a tilt angle around 20°. At this value, we observed stronger deviations between the approximation and real tilted estimations, which start to be visible as a small offset to the left of the extrema for the real tilt in Figure 3.11a.

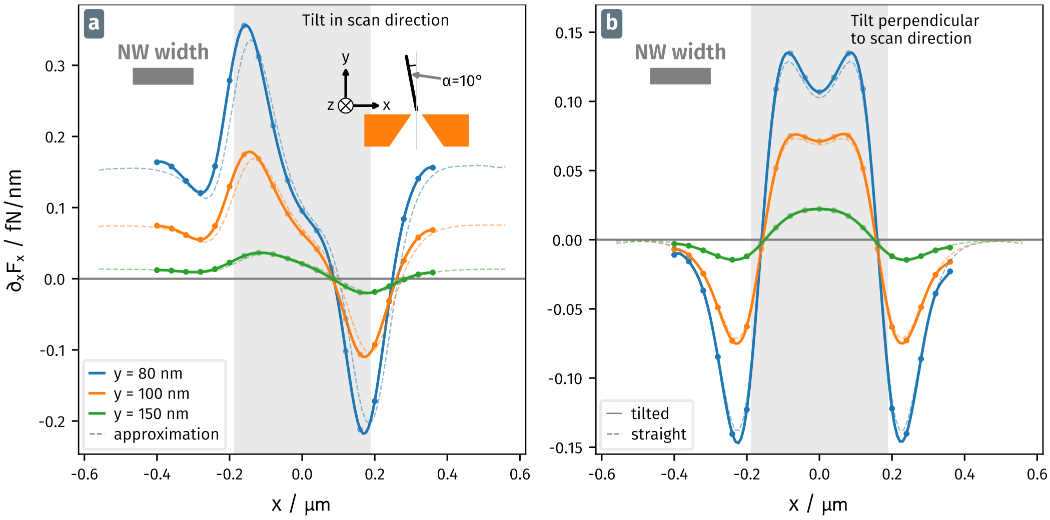

Fig. 3.11: Simulation of the Casimir force for a 10° tilted nanowire above a hole (l = 4 µm, D = 160 nm, W = 370 nm) at different nanowire-hole separations y = 80 nm, 100 nm and 150 nm. In (**a**), the nanowire is tilted within the scan plane which leads to a asymmetric force divergence, and one observes a slight shift of the x-position of the extrema in the direction of the tilt. The solid lines present the simulation of the tilted nanowire, while the dotted lines show an approximation of the tilt by a projection of the simulated force on a straight nanowire along a tilted measurement direction. In (**b**), the nanowire is tilted perpendicular to the scan direction (to the paper-plane), which does not significantly change the force gradient measured along x in comparison to the straight nanowire (dotted lines).

The 10° tilt alters the shape of the force divergence significantly. It adds a constant positive force divergence above the surface, which originates from the fact, that the vertical force F_z is attracting the nanowire – it is negative with a negativity that increases when approaching the surface. When the nanowire displacement $\delta x'$ is positive – the nanowire moves further away from the surface –, F_z has gained in total value, still remaining negative. The gradient $\frac{\partial F_z}{\partial x'}$ is hence positive above the surface. It is also the contribution of this gradient that causes the asymmetry of the gradient at opposing hole borders. Here, it is the displacement in x which significantly increases the negative force F_z when changing from substrate to hole, while on the opposite side, F_z rapidly decreases.

The second tilt configuration is the nanowire tilted out of the scan plane. In that situation, the tilt effect is not impacting the force field measured in the scan plane: the symmetry of the untilted case is preserved as can be seen in the results in 3.11b. Thus, the force gradient experienced by the tilted nanowire is only slightly different from the straight nanowire.

Since the tilt effect is dominated by the projection of the vertical force on the perpendicular direction of the tilted nanowire, we can use the results from the simulation with the straight nanowire to calculate 2D divergence maps for the horizontal plane. Figure 3.12a shows the map for the tilted nanowire, a cut through the center of the hole along the x direction corresponds to the cuts in 3.11a (not that the 2D map shows the divergence, the line cuts the gradient), one along the z direction to those in 3.11b. With respect to 2D measurements of small, rotational symmetric structures, the effect of a tilt can introduce large disturbances in the measured force field, due to the symmetry breaking effect. A 2D map of the force divergence – this also holds for electrostatic forces, as the projection of the force (3.13) is independent from its source – can therefore look very different if the nanowire is tilted and does not necessary reflect the geometry of the horizontal force field. Experimentally, we have introduced the possibility to fine tune the nanowire tilt, by using a home made gimbal nanowire mount, which allows to manually ensure its verticality within a few degrees (see Section 1.4.3).

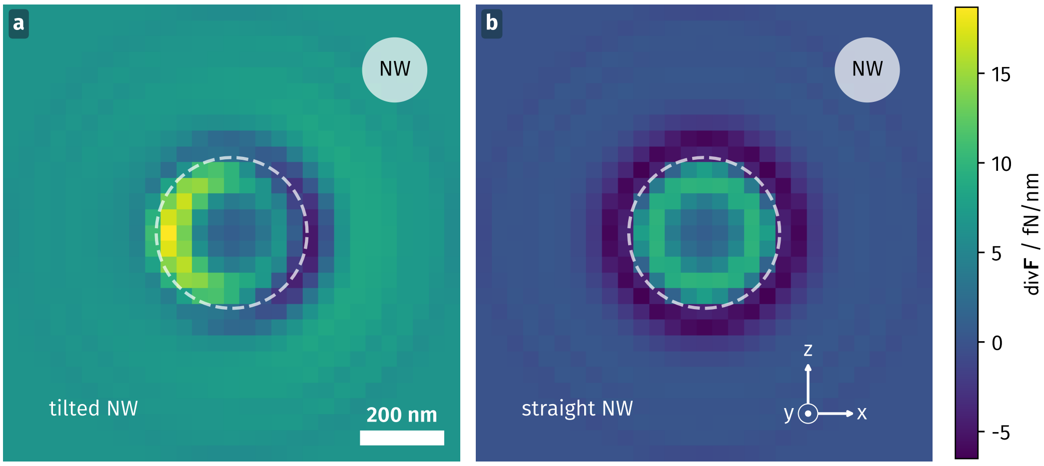

Fig. 3.12: Simulated horizontal divergence from the simulation of the Casimir force for the straight nanowire 80 nm above an underetched hole. In (**a**), a 10° tilt of the nanowire towards the -x direction is presented, (**b**) shows the divergence of the untilted nanowire. The dashed circle marks the edge of the hole and the white circles in the top right corner illustrate the size of the nanowire in the simulation.

3.4 Measured residual force on crossing trenches

We will now discuss the results of the analysis described above on the example of the cross like hole. From the determination of the common crossing point we estimate $V_0 = -0.12\,\mathrm{V}$. This permits to identify the voltage value which compensates for the work function difference from the two electrodes. In a sense, this voltage allows to compensate the average vertical parasitic field (which itself does not depend of the bias voltage). V_0 then represents the value around which one should investigate the impact of the variability observed in the parasitic electric fields.

The parabolas, which were initially fitted with the expression

$$\alpha V^2 + \beta V + \gamma \big(= \alpha (V - V_1)^2 + \gamma'\big),$$

can now be expressed as:

$$\mathrm{div}\mathbf{F} = \alpha (V - V_0)^2 + 2(V_1 - V_0)(V - V_0) + A(V_1 - V_0)^2 + \eta, \tag{3.14}$$

with V_0 obtained via the technique presented in Section 3.2.2. This expression allows to make connections with the expression arising from the tensor analysis given above, $\mathrm{div}\mathbf{F} = \alpha(V - V_0)^2 + \beta(V - V_0) + \eta$. The two first terms now represent the quadratic and linear contributions, while the sum of the last two terms now contains the quadratic parasitic and the Casimir contributions. As stated above, in the present stage, in the measurements we cannot fully discriminate Casimir from quadratic parasitic contributions, but we will describe in greater details the spatial properties of the total residual contributions (η).

Figure 3.13 presents the coefficients of the offset corrected force parabola on a horizontal xz-map. Here, α remains unchanged, but we obtain new linear and constant terms β, η. We first note that the quadratic and linear terms are of opposite signs with a comparable amplitude (at $V_{\mathrm{bias}} = 1\,\mathrm{V}$) but have a different spatial dependence, as can be seen in the central area where α has its maximum, and β is close to zero. Also, the linear force divergence coefficient has a larger spatial extension than the quadratic part. The residual force divergence η has an even larger extension with overall negative values around the cross, and thinner positive regions directly above the trenches of the cross.

We also note that the background of the residual term shows a clear slope from the left to right side. This is likely due to the tilt of the sample surface with respect to the sample stage's xyz-piezo motional axes, which causes the surface to be further away on the left side than on the right side of the plots. As shown in Figure 3.11, an angle between the nanowire and the sample causes a positive, anti-trapping residual force above the surface. This positive offset is comprised in the residual force reference η_0 which is here $37\,\mathrm{aN\,nm^{-1}}$ and has been substracted from the plotted η. It is given by the mean value

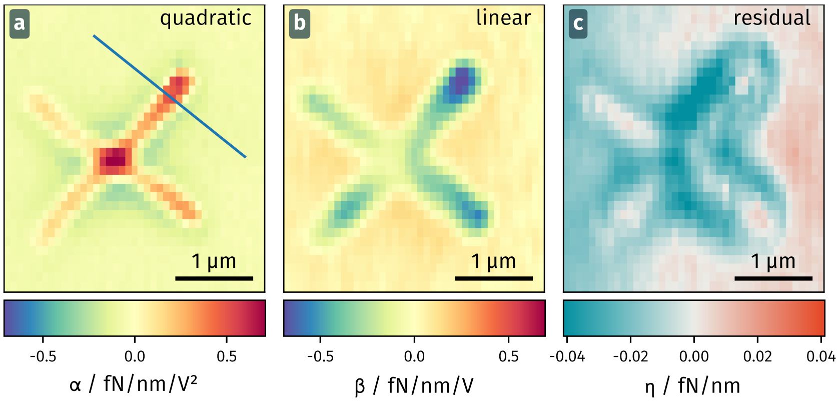

Fig. 3.13: Different components of the electrostatic force divergence above the cross structure assuming a mean V_0 = −120 mV from the common crossing analysis. The horizontal map has been acquired at a height around 200 nm above the surface. The quadratic term (**a**) does not depend on the choice of V_0. The linear term (**b**) shows a trapping force field in the center of the trenches. The residual force divergence (**c**) shows the characteristic transition from trapping at the trench edges to anti-trapping in the center ofthe hole. The gradient in the background on the surface indicates either a tilt of the sample, or a slight tilt of the horizontal scan axes. The line in (**a**) indicates the location of the vertical measurement in figure 3.15.

apart from the cross at the top and bottom of the scan area. This value agrees with the residual force divergence at the common crossing of the parabolas.

Figure 3.14 compares the residual force for the obtained V_0 of −0.12 V and a variation of 0.04 V in each direction. This 40 mV value represents the width of the minimum found in the offset voltage analysis discussed above. While for higher V_0 (3.14c), the positive areas nearly disappear, and both, negative and positive areas, are more pronounced for the smaller V_0. These differences demonstrate the importance of a good estimation of the V_0 and represent the limits of the method. Especially, the choice of V_0 impacts the residual force divergence measured at higher altitudes, where we assume that it vanishes. This analysis thus requires a complete vertical measurement. However, we can still state that, despite the difficulty to fix a V_0 in a horizontal map, we observe an anti-trapping region above the trenches for realistic values of V_0. Furthermore, the magnitude of the measured forces is in good agreement with the simulated values for a nanowire at about 100 nm to 150 nm distance[1] (compare Figure 3.11).

A better estimate for V_0 can be given in the case of a vertical map, since at larger distances, the surface forces become negligible which allows calibrating the reference value of the unperturbed $\Omega_1^2 + \Omega_2^2$. There, the Casimir forces are negligible, so that the parabola shift is purely determined by the parasitic fields. Due to the large distance, they show

---

[1] Note that the simulations have been done for the circular holes, the force divergence is therefore expected to be larger above the hole (as $\partial_x F_x$ *and* $\partial_z F_z$ contribute) than that above the cross. For the Casimir force divergence above a trench one can take div**F** $\approx \partial_x F_x$ from the hole simulation (with $\mathbf{e}_x$ perpendicular to the trench), which has the same amplitude at 100 nm to 150 nm distance as the measured force

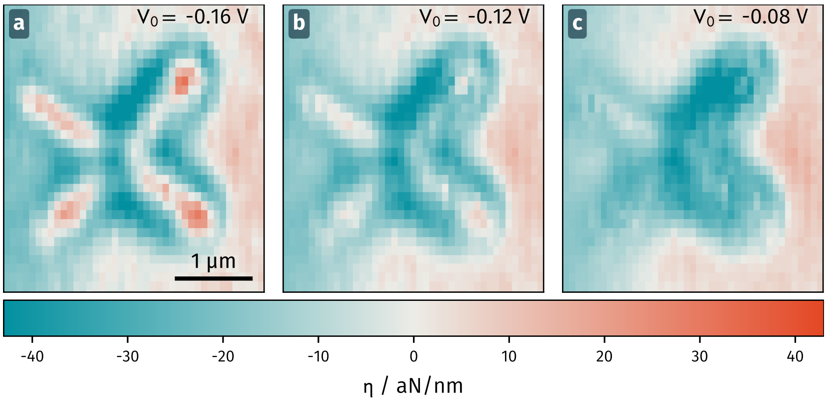

Fig. 3.14: Comparison of the residual forces for different V_0. The central panel (**b**) corresponds to the results in 3.13b. The variation of ±40 mV is larger than the uncertainty of the common crossing technique, however, this technique is only an approximation. In all three cases we observe regions with the expected shape of the residual (Casimir) force divergence.

smooth variations with the sample position. Figure 3.15 presents the results obtained for a vertical cut above one of the cross' trenches, which is indicated as blue line in panel 3.13a. Due to the different scan orientation and a delay of a one and a half months between the measurements, the determined V_0 can not necessarily be compared to each other[2]. The vertical map of the quadratic force divergence in 3.15a shows the same features as the horizontal map, but with more details in the regions close to the surface thanks to the more stable vertical approach of the nanowire. The scans are performed from the top to the bottom, so that the most critical moments (PLL unlocking, touching the surface...) occur at the end of the measurement sequence, such that stable operation

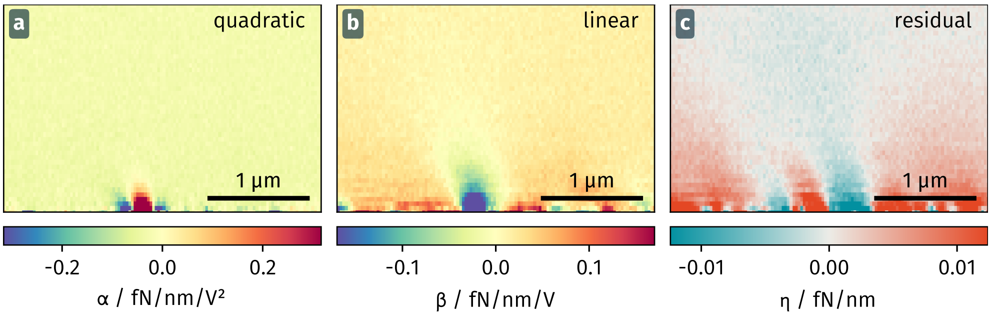

Fig. 3.15: A vertical map, perpendicular to one of the cross' branches is shown for V_0 = −0.39 V. The line in Figure 3.13a indicates the location of the vertical map. The common crossing analysis is performed using the data at large distance from the surface. The asymmetric dependence on the distance (regions with larger values seem to move to the left as one looks at larger distances) can be explained by a deviation from the perpendicular alignment between nanowire and sample. Here, a nanowire tilt towards the right explains the observed shift.

---

[2] We already observed changes of the surface properties over longer times, especially if several air evacuation cycles of the vacuum chamber were performed in the meanwhile.

is guaranteed for as many vertical points as possible. The trapping force component at the edges of the hole is clearly visible in the vertical maps, while it is only slightly pronounced in the horizontal ones, due to its faster decay compared to the anti-trapping force divergence at the trenches center and due to the finer spatial resolution of the map. We also note, that the quadratic divergence is constant above the flat surface on the side of the trench. At these areas, the linear term shows a clear spatial structuration, caused by the horizontal forces due to surface patches. The residual force component for the best fitting V_0 crossing value ($-0.39\,\mathrm{mV}$) shows the expected transition from trapping to anti-trapping divergence when going from the surface towards the trench center.

Regarding the spatial dependence, one has the impression that the residual term decays more slowly with distance than the linear term and the quadratic term, which decays fastest. This can be explained by the parasitic fields $\mathbf{E}_\mathrm{p}$ which extent farther from the sample than the field $\mathbf{E}_V(V_\mathrm{bias})$ created by the electrode. Since the parasitic fields do not contribute to the quadratic term, but to the linear term by a product with $\mathbf{E}_V$ and to the residual term as squared expression, their large extension with height would be reflected most in the residual force field divergence.

In all plots, we observe a tilt towards the left of the vertical evolution of the different terms caused by a physical tilt of the nanowire with respect to the sample. As discussed above, the tilt causes a positive residual force divergence above the surface which means that the nanowire is tilted towards the left[3].

Again, we take a look at the effect of different voltages V_0 on the residual force divergence. Figure 3.16 presents the evolution of η as we vary V_0 by steps of 50 mV. In all cases η keeps its negativity around the edges of the hole whereas smaller values of V_0 cause the positive, anti-trapping region at the trench center to decrease until its barely distinguishable from the background fluctuations. However, these values are largely outside the possible area for a common parabola crossing.

In Figure 3.17, we show cuts at different heights above the sample[4] for the residual term η (3.17a) and the quadratic term α (3.17b). As one can expect, the spatial structuration above the surface averages out at larger distances. The quadratic term in 3.17b is decaying more rapidly with the negative regions disappearing faster than the positive. This can be explained by the same effect as the flattening of the residual divergence above the surface, since the fields at larger distance are an evolution of those present at the surface. A measurement at a larger height thus detects the combined positive and negative areas which sum up to an effective positive divergence at larger distances.

---

[3] The variations of $\partial_x F_x$ in the untilted laboratory coordinates are small compared to $\partial_z F_z > 0$, so that with a left tilted nanowire, the gradient $\partial_{x'} F_{x,}$ is positive.

[4] The zero height is estimated from the height where the PLL lost the lock. The real position of the sample surface is probably 50 nm to 100 nm beneath this level.

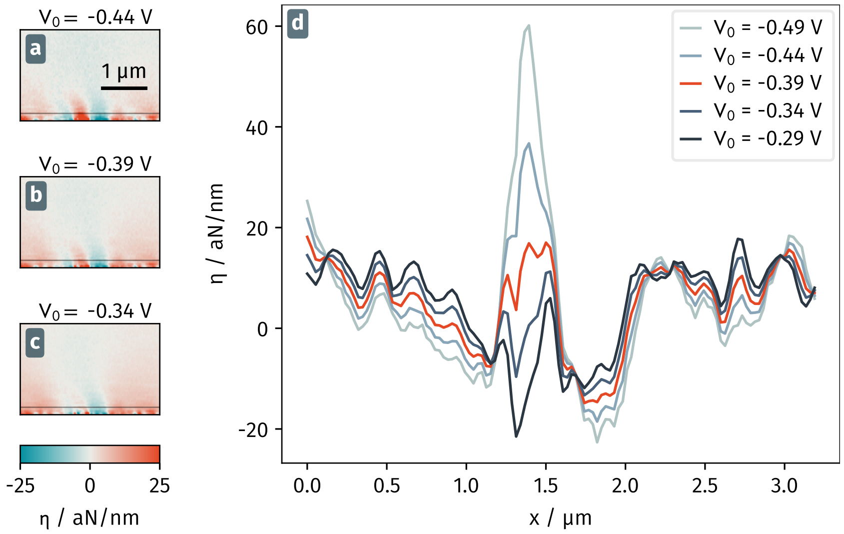

Fig. 3.16: Comparison of the residual force for variations around the $V_0 = -0.39\,\mathrm{V}$ from figure 3.15. For variations of up to +100 mV the trapping (negative) force divergence at the trench's edges remains visible, but the anti-trapping (positive) area at the centre nearly disappears. For smaller V_0, anti-trapping and trapping regions are more pronounces. For all voltages one retrieves a positive residual divergence above the substrate which is caused by a small tilt of the nanowire towards the left side.

Comparing the size of the central feature of the residual and quadratic force divergence in Figure 3.17a and Figure 3.17b, one can observe that the horizontal size of the residual force divergence is slightly larger than the quadratic term. This difference also appears when regarding simulations of residual (Figure 3.9d) and quadratic (Figure 2.15d) force divergence where the residual is zero at the hole boundary whereas the quadratic term has the zero crossing inside the hole.

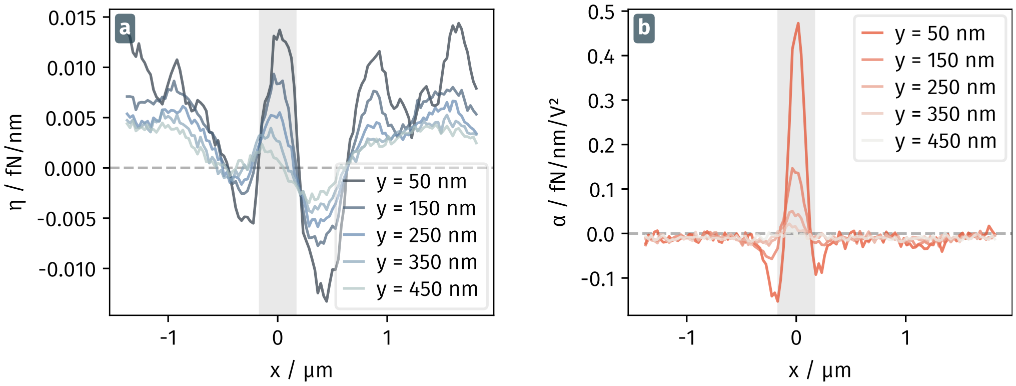

Fig. 3.17: Cuts through the vertical map of Figure 3.15 at different heights for $V_0 = -0.39\,\mathrm{V}$. (**a**) presents the residual force divergence and (**b**) the quadratic term of the electrostatic force divergence. In both terms the offset is corrected by the value at the largest nanowire distance to the sample. The shaded area illustrates the approximate width of the trench.

Assuming that the surface around the cross is perfectly flat, one has no reason to expect a variation of the residual force at those regions, opposed to the residual terms presented in Figure 3.17a. We interpret the presence of these variations as artefacts from the imperfect compensation of the horizontal fields by the *common crossing* technique. Since we are only trying to compensate the statistical mean shift of the force parabolas in order to extract the residual force component, the method ceases to correctly account for the local variations close to the surface. In order to take these variations into account, one would need to compensate the local horizontal fields at each point, the only remaining residual force contribution would then come from the Casimir effect.

In this section we presented a method to estimate the residual force – the force that remains after elimination of the known quadratic and linear electrostatic contributions – from the voltage dependent force field image, by using an average estimate of the offset potential, that allows to estimate and compensate for the work function difference (in other terms, the vertical parasitic residual field). The inferred residual force field, measured on the crossing trenches has a similar shape and magnitude as the Casimir force simulated above a hole of similar dimensions. However, the dependence of the residual force on the vertical distance and the presence of residual variations above a flat surface (as indicated by the homogeneous value of alpha measured on the sides of the trench) show the limits of the mean compensation method. This is expected, since one cannot compensate the effect of a 3D parasitic field with a single electrode. In the next section we will discuss a more advanced measurement, based on the direct compensation of the horizontal fields with additional electrodes, which we plan to conduct in future studies in order to better isolate the horizontal Casimir force field.

3.5 Outlook: 2D force field compensation

As explained above, the existence of parasitic electric fields makes us loose a lot in terms of quantitativeness (uncertain dependence of the residual fields on the distance, variations of the residual force depending on the chosen V_0,...) of the measurement. In principle, they can be compensated using a homogeneous external electric field, which does not create a force directly but serves to partially compensate for the local parasitic field experienced by the nanowire. In a sense, if one wants to measure 2D force fields, it is necessary to control the field in all directions. To do so, we will simply add a set of electrodes at “large” distance from the sample, typically tens of microns, as shown in Figure 3.18. Even with the idea being simple, its interpretation in term of force measurements is not so direct, and is described here.

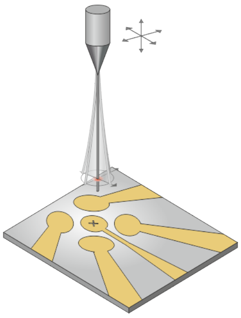

Fig. 3.18: Schematic illustration of the sample design with control electrodes that can create an arbitray, homogeneous field in the horizontal plane. The sample beneath the nanowire is etches into a central electrode that can be used to create a vertical field, analogue to the samples presented in this thesis. The whole structure is positioned on the edge of a Si substrate in oder to avoid a blocking of the readout laser by the sample.

We recall the expression for the horizontal force dependence on the fields at the bottom of the nanowire:

$$\begin{aligned} F_x \propto E_xE_y &= \left(E_{V,x}+E_{\mathrm{res},x}\right)\left(E_{V,y}+E_{\mathrm{res},y}\right)\\ &= \underbrace{E_{V,x}E_{V,y}}_{\propto V_{\mathrm{bias}}^2} + \underbrace{E_{V,x}E_{\mathrm{res},y}+E_{V,y}E_{\mathrm{res},x}}_{\propto V_{\mathrm{bias}}} + E_{\mathrm{res},x}E_{\mathrm{res},y} \end{aligned} \tag{3.15}$$

where the parasitic fields E_{res} cause a shift of the parabola. While it is possible to determine the linear component with measurements of the force's dependence on E_V, one can not directly infer the last term which is independent of the applied voltage. An approach to mitigate this problem is to introduce an additional control field $E_{c,x}$ in the x direction, that is adjusted such that the force is optimized and the parasitic field $E_{\mathrm{res},x}$ can be compensated:

$$\begin{aligned} F_x \propto{} & \left(E_{V,x}+E_{\mathrm{res},x}+E_{c,x}\right)\left(E_{V,y}+E_{\mathrm{res},y}\right)\\ ={} & E_{V,x}E_{V,y}+E_{V,x}(E_{\mathrm{res},y}+E_{c,y})+E_{V,y}\left(E_{\mathrm{res},x}+E_{c,x}\right)+(E_{\mathrm{res},x}+E_{c,x})(E_{\mathrm{res},y}+E_{c,y}). \end{aligned} \tag{3.16}$$

The resulting force, as well as the force divergence, is still quadratic in $E_V \propto V_{\mathrm{bias}}$ but the position of its extremum is now controlled by the additional field E_c. When E_c is varied, one measures the displaced parabolas $\mathrm{div}\mathbf{F}(V_{\mathrm{bias}})$ as presented in Figure 3.19a. The extrema of the parabolas form another parabola (the points in 3.19a) with its extrema localized at the common crossing of the individual parabolas. Without surprise, this phenomenology is exactly the one expected from a parasitic electric field contribution, similar to that produced by the control electrode. When one has to account for and compensate for the three orientations of the parasitic field, the single axis analysis exposed just above is slightly modified: now, one has to find the extremum in a three dimensional space $(E_{c,x}, E_{c,y}, E_{c,z})$. In that situation, the location of compensation will always correspond to a saddle point or to the maximum of an hyperboloid (depending on the signs of the voltage dependent terms $E_{V_{x,y}}$). The force divergence expected in the case where one only needs to compensate for the horizontal parasitic fields with two lateral electrodes

($E_{c,x}$, $E_{c,z}$) is illustrated in Figure 3.19b. Here, the point indicating the best compensation situation is the saddle point. There, the parasitic fields would be compensated best, and one would measure the Casimir force divergence.

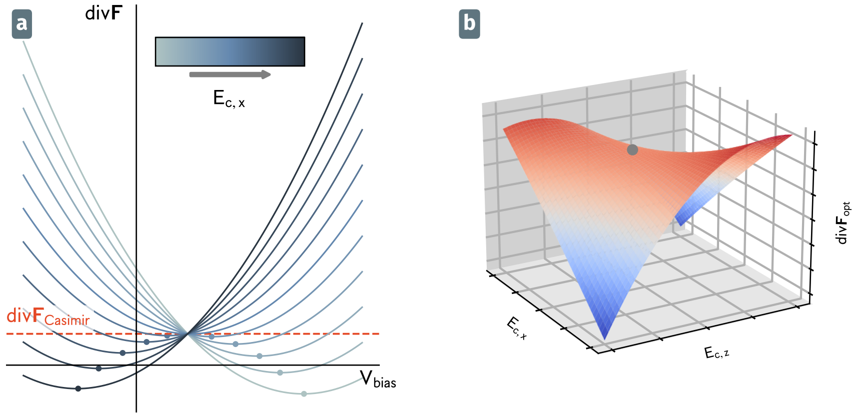

Fig. 3.19: The homogeneous field of an additional control electrode $E_{c,x}$ is shifting the measured parabolas div**F**(V_{bias}) (**a**). The extrema of each parabola again follow a parabolic curve at whose extremum one finds the Casimir force. Figure (**b**) plots the extrema of each parabola for two independent control fields $E_{c,x}$, $E_{c,z}$. Depending on the direction of the fields (thus its sign), the curve either is a hyperboloid (as shown) or a paraboloid. Thus the point where div**F**$_{opt}$ = div**F**$_{casimir}$ is the saddle point, or extrema respectively, here indicated by the grey dot.

While the measurement and analysis protocol presented in this work try to find a mean compensation of the parasitic fields, the control fields should permit to compensate the parasitic field in three dimensions (a symmetric bias voltage applied on all control electrodes can be used to generate a vertical control field). Therefore, in a 2D experimental geometry, one needs to apply two homogeneous, linear independent fields, created for instance by two pairs of electrodes with individually controllable bias voltages such as presented in Figure 3.18. Here, the electrodes are designed to be large enough and remote enough, so that the field created around the nanowire tip and the sample area is uniform. By sweeping the horizontal fields $E_{c,x}$, $E_{c,z}$ and the bias voltage (thus the vertical field $E_{c,y}$), one can acquire the hyperbolic surface of Figure 3.19b and thus infer the isolated Casimir component of the force field. For a perfect patch compensation, one would need to produce a control field presenting the exact same spatial profile as the field at the nanowire extremity which has to be compensated. This is beyond experimental capacities, so that the above described compensation method will only suppress mean field contributions.

We are currently performing the first investigations with samples of this geometry as part of the PhD project of *Hugo Weltz*. Besides the compensation of the horizontal forces in order to get better results for the horizontal Casimir force on the nanowire, the experiments also help to investigate the forces on the nanowire under the presence of strong, homogeneous fields which show non-trivial behaviour due to the modified electronic properties of the nanowire. Additionally, the dual electrode pair configuration permits to apply an arbitrary directional force, that with some adjustments can be used as source for a complete 2D force feedback[5], similar to that realized in Chapter 4.

---

[5] In order to apply a feedback using the electrostatic quadratic force, the applied fields should be inhomogeneous, so that the field gradient creates a force on the nanowire. This is not the case in the center of the field correction electrodes.

4 Creating artificial 2D force fields using realtime active feedback

Up to now, the nanowire was used to investigate external force fields through the modification they induce on its mechanical properties. However this extreme sensitivity can create some practical problems if the force fields under investigation are too large, since they may lead to a rotation of the nanowire eigenmodes with respect to the test force or to the measurements vectors, so that the PLL gets out of lock. It could thus be desirable to have an artificial force field at hand that could help compensating the external force fields, so that the nanowire properties remain unchanged. This idea would be similar to a mechanical balance – which compensates the unknown mass by a known one so that the balance remains at its rest position – at the force field gradient level in our case. To do so, we have developed a method, which allows us to produce artificial force fields, using a realtime feedback in 2D. It is based on the instrumental developments realized on the FPGA card exposed above. By combining the realtime signals from the two measurements channels, it is possible to reconstruct the motion projected along an artificial readout direction, and to generate an artificial force proportional to these voltage fluctuations by feeding them back onto the bias voltage of an electrostatic tip positioned in the proximity of the nanowire extremity. The position of the tip defines the direction along which the artificial force is exerted.

In this chapter, we describe those artificial force fields, the developments realized to ensure their proper implementation and finally their impact on the nanowire movement. We will first discuss the case of uniaxial artificial force fields, where the measurement and feedback force orientations are aligned, and then the transverse case, where the feedback force vector is set perpendicular to the measurement direction. We will also investigate the delayed artificial force fields, where the force is now proportional to the nanowire's velocity projected along one orientation, which is derived from the position fluctuations.

Those artificial force fields also allow generating force fields presenting a pure shear character, for instance with $\delta F_z \propto \delta r_x$, which fall in the class of non-reciprocal (or rotational) force fields. We will show that those synthetic non-reciprocal force fields allow the compression of the nanowire thermal noise in the position and real spaces, and are also responsible for the apparition of a circulation in the noise trajectories. Then, the transverse delayed force fields are shown to bring the nanowire in a non-trivial situation, where the nanowire eigenvectors can become imaginary, traducing a circularly polarized eigenmode. Those artificial force fields thus present an important simulation interest, which will be exposed in the chapter.

◆

◆

4.1 Principle of linear feedback in a two dimensional system

When a single actuation channel is employed, the vectorial feedback force can only be aligned in one direction, with an amplitude that depends on the oscillator position in 2D. In order to mimick any force field in 2D, one should necessarily use 2 actuation channels, with 2 non-parallel feedback force orientations. In the present work we limit ourselves to a single channel feedback force, but the extension to a second orientation is, in principle, straightforward. The four electrode design introduced at the end of the previous chapter could indeed be used for that purpose.

A single directional feedback makes use of an external force acting along $\mathbf{e}_\varphi$ with a tunable magnitude that depends on the nanowire position in 2D. It can be formally written as:

$$\delta\mathbf{F}_{fb}(t) = -M_{\mathrm{eff}}\, f(\delta\mathbf{r}(t)) \cdot \mathbf{e}_\varphi. \tag{4.1}$$

Here, f is a scalar function, with the dimension of an acceleration depending on the nanowire position in realtime. It governs the amplitude of the feedback force that, in the most general case, is a function of the two dimensional resonator position. The angle φ defines the angle of the applied force relative to the direction of the first mechanical mode $\mathbf{e}_1$.

In the case of linear feedback, the function $f(\delta\mathbf{r}(t))$ is a linear function of the displacements δr_μ measured along the direction of measurement $\mathbf{e}_\mu$. Again μ denotes the angle between readout vector and the first mechanical mode. The convention for the naming of the different components is illustrated in Figure 4.1a.

We can write f for an instantaneous linear feedback as

$$f(t) = g_{fb}\, \delta r_\mu(t) \tag{4.2}$$

or expressed in Fourier space

$$f[\Omega] = g_{fb}\, \delta r_\mu[\Omega], \tag{4.3}$$

where g is the feedback gain proportionality factor with the units Hz^2 that is controlled by the experimenter.

One can also make use of a feedback force depending on the velocity ($\delta v_\mu = \delta\dot{r}_\mu$) of the nanowire – we then speak of a delayed feedback. It can similarly be written in the linear case $f(t) = h\delta v_\mu$ so that, since $\delta\dot{\mathbf{r}} = -i\Omega\,\delta\mathbf{r}$, we can express the feedback force processed in the Fourier domain as:

$$f[\Omega] = -i\Omega\, h_{fb}\, \delta r_\mu[\Omega]. \tag{4.4}$$

Such a delayed feedback represents a situation that enables cold damping or heating of the resonator, as often employed in optomechanics, but with the novelty that the force does not necessarily take an uniaxial form. Accounting for the general case of a mixed feedback, $p = g_{fb} + i\Omega\, h_{fb}$ can be regarded as a complex gain factor[1]. Rewriting Equation 4.1 for such a linear feedback yields:

$$\delta\mathbf{F}_{fb} = M_{\mathrm{eff}}\, \underbrace{p\mathbf{e}_\varphi\mathbf{e}_\mu}_{\mathbf{f}} \cdot \delta\mathbf{r}, \tag{4.5}$$

---

[1] We presume that instantaneous and delayed force make use of the same measurement vector and act in the same direction. This is a limiting assumption since instantaneous and delayed force are generally caused by different physical effects that do not necessarily act in the same direction, for instance photon backscattering and local thermal heating in the case of an optical force. The realized feedback is of artificial nature where the experimenter can add an arbitrary delay to the instantaneous force, so that the simplified model of a single complex feedback is valid.

where **f** is the feedback coupling matrix, expressed as a tensorial form comprising the measurement and actuation vectors. In the basis of eigenmodes $\mathbf{e}_{1,2}$ the readout and force vectors are

$$\mathbf{e}_\varphi = \begin{pmatrix} \cos\varphi \\ \sin\varphi \end{pmatrix} \text{ and } \mathbf{e}_\mu = \left(\cos\mu, \sin\mu\right). \tag{4.6}$$

And we can define the feedback's coupling matrix **f**:

$$\mathbf{f} = p\mathbf{e}_\varphi \mathbf{e}_\mu = p\begin{pmatrix} \cos\varphi\cos\mu & \cos\varphi\sin\mu \\ \sin\varphi\cos\mu & \sin\varphi\sin\mu \end{pmatrix} \tag{4.7}$$

$$= \frac{p}{2}\begin{pmatrix} \cos(\varphi+\mu)+\cos(\varphi-\mu) & \sin(\varphi+\mu)-\sin(\varphi-\mu) \\ \sin(\varphi+\mu)+\sin(\varphi-\mu) & -\cos(\varphi+\mu)+\cos(\varphi-\mu) \end{pmatrix}. \tag{4.8}$$

The elements of this feedback matrix have the same unit of Hz^2 as p and the g_{ij} force field gradient terms in Section 1.1.2 and we can interpret them similarly. The diagonal terms represent an independent feedback on the individual modes resulting in a shift of frequencies or a change in individual damping rates whereas the off-diagonal terms cause a cross-coupling between both modes generating a rotation of eigenvectors or a damping matrix that is not aligned with the eigenmodes. Note that with a single feedback force, leading to three tunable parameters p, φ and μ, it is not possible to generate any arbitrary coupling matrix (as mentioned earlier, one would need two actuation channels).

From Equation 4.8 we can define two special cases, namely the *uniaxial* case where $\varphi = \mu$ and the *transverse* case with $|\varphi - \mu| = \pi/2$, which we now describe in greater details..

4.1.1 Uniaxial feedback

In the case of uniaxial feedback where $\varphi = \mu$ (or $\varphi = -\mu$ since one can invert the feedback coefficient without loss of generality), the coupling matrix **f** simplifies and we can write the force as

$$\delta\mathbf{F} = -M_\mathrm{eff}\frac{p}{2}\begin{pmatrix} 1+\cos 2\varphi & \sin 2\varphi \\ \sin 2\varphi & 1-\cos 2\varphi \end{pmatrix}\delta\mathbf{r}. \tag{4.9}$$

A uniaxial feedback where the force vector and the readout vector are identical thus always has a symmetric coupling matrix with equal off-diagonal terms and can only cause a rotation of the modes as a block in the case of an instantaneous feedback. For the special case where the feedback vectors $\mathbf{e}_\mu, \mathbf{e}_\varphi$ are aligned with one of the eigenmodes, the off diagonal terms vanish and no cross coupling nor rotation appears. Assuming alignment of the readout vector with the first eigenmode ($\mu = 0$), the coupling matrix simplifies further:

$$\delta\mathbf{F} = -M_\mathrm{eff}\ p\begin{pmatrix} 1 & 0 \\ 0 & 0 \end{pmatrix}. \tag{4.10}$$

Compared to the g_{ij} force field gradient matrix in Section 1.1.2 an uniaxial aligned feedback represents a single g_{11} term that shifts the frequency of the first mode as $\Omega_{\parallel 1}^{2} = \Omega_1^2 - g11$.

The local force field generated by such a feedback is divergent along one axis as illustrated by sub-figure Figure 4.1b.

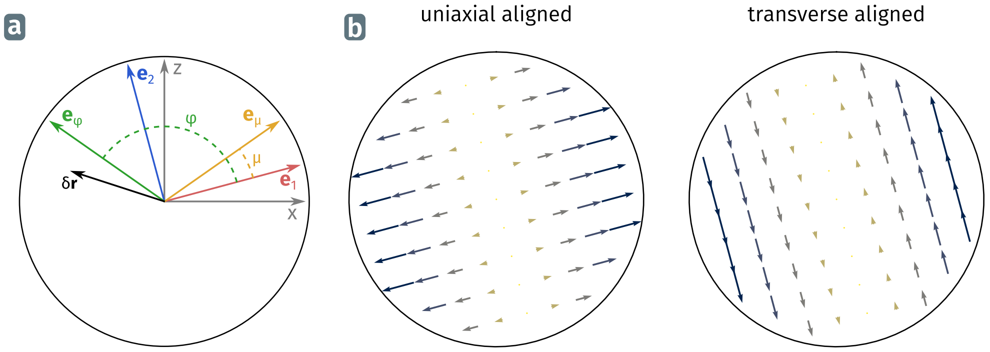

Fig. 4.1: (**a**) Illustration of the conventions used to name vectors and angles. (**b**) Plot of the two dimensional local force field for the uniaxial aligned and the transverse aligned case.

4.1.2 Transverse feedback

For transverse feedback defined by a difference of 90° between the readout and force vector, the coupling matrix $\mathbf{f}$ simplifies as well, and for $\mu - \varphi = \pi/2$ the force writes

$$\delta\mathbf{F} = M_{\text{eff}}\frac{p}{2}\begin{pmatrix} \cos\left(\frac{\pi}{2} + 2\varphi\right) & \sin\left(\frac{\pi}{2} + 2\varphi\right) + 1 \\ \sin\left(\frac{\pi}{2} + 2\varphi\right) - 1 & -\cos\left(\frac{\pi}{2} + 2\varphi\right) \end{pmatrix}\delta\mathbf{r} \tag{4.11}$$

$$= M_{\text{eff}}\frac{p}{2}\begin{pmatrix} -\sin(2\varphi) & \cos(2\varphi) + 1 \\ \cos(2\varphi) - 1 & \sin(2\varphi) \end{pmatrix}\delta\mathbf{r}. \tag{4.12}$$

The second equation shows that the off-diagonal elements can not be equal for any choice of φ. We also note that with a single feedback force it is not possible to generate a purely rotational force ($g_{12} = -g_{21}$), because it would require two actuation channels. The feedback induced coupling between the two modes is therefore non-reciprocal ($\nabla \times F/M_{\text{eff}} = g_{21} - g_{12} \neq 0$) in the case of transverse feedback. In the aligned case, where the readout is oriented along one mode, while the feedback force acts parallel to the other mode, the expression simplifies to

$$\delta\mathbf{F} = M_{\text{eff}}\; p\begin{pmatrix} 0 & 1 \\ 0 & 0 \end{pmatrix}\delta\mathbf{r}. \tag{4.13}$$

Here, we assume a force acting along the first mode $\varphi = 0$ and a readout in the direction of the second mode $\mu = \pi/2$.

A transverse aligned feedback represents a pure shear force causing a rotation of one mode while leaving the second mode unaffected. Figure 4.1b illustrates the local force field generated by the transverse aligned feedback.

From (4.14) above, we can obtain an estimate for the necessary gain that needs to be applied for a mode rotation of $\Delta\theta_1$

$$\cos(\Delta\theta_1) \approx \frac{g_{21}}{\Omega_2^2 - \Omega_1^2} \approx \frac{g_{21}}{2\Omega_m \Delta\Omega}, \tag{4.14}$$

where, in the second approximation, Ω_m denotes the mean mechanical frequency and $\Delta\Omega$ the mode splitting.

4.1.3 Delayed feedback force

In the above discussed uniaxial and transverse feedbacks, we assumed an instantaneous feedback which only depends on the position $\delta\mathbf{r}$ of the nanowire. It is also possible to apply a feedback that depends on the nanowire's velocity $\delta\dot{\mathbf{r}}$, computing the derivative of the position signal prior to feeding it back onto the actuation force. We will come back later on its implementation in the experiment.

The complete equation of motion that takes into account the retarded forces acting as viscous damping is then

$$\delta\ddot{\mathbf{r}}(t) = -\boldsymbol{\Omega}^2 \cdot \delta\mathbf{r}(t) - \boldsymbol{\Gamma} \cdot \delta\dot{\mathbf{r}}(t) + \mathbf{h} \cdot \dot{\mathbf{r}}(t) + \mathbf{g} \cdot \delta\mathbf{r}(t) + \frac{1}{M_{\text{eff}}} \delta\mathbf{F}_{th}(t), \tag{4.15}$$

where $\boldsymbol{\Omega}^2, \boldsymbol{\Gamma}$ are the restoring force and (isotrop) damping matrices of the unperturbed nanowire and $\mathbf{g}, \mathbf{h}$ are the instantaneous and delayed feedback matrices:

$$\boldsymbol{\Omega}^2 \equiv \begin{pmatrix} \Omega_1^2 & 0 \\ 0 & \Omega_2^2 \end{pmatrix}, \quad \boldsymbol{\Gamma} \equiv \begin{pmatrix} \Gamma & 0 \\ 0 & \Gamma \end{pmatrix}, \quad \mathbf{g} \equiv \begin{pmatrix} g_{11} & g_{21} \\ g_{12} & g_{22} \end{pmatrix} \text{ and } \mathbf{h} \equiv \begin{pmatrix} h_{11} & h_{21} \\ h_{12} & h_{22} \end{pmatrix}. \tag{4.16}$$

The g_{ij} in the above equation can be regarded analogously to the force field gradients in the other experimental chapters of this thesis. Their intrinsic difference is that here we speak of artificial force gradients created by an active feedback. The force field gradients native to the nanowire's environment can still be preset as well. Both contributions add up linearly, so g_{ij} can be regarded as the sum of feedback created artificial force gradient and physical force gradient at any point, in order to account for the effects of an external background field that is independent of the applied feedback.

The Fourier transform of (4.15) gives the equation of motion in the frequency domain:

$$-\boldsymbol{\Omega}^2 \cdot \delta\mathbf{r}[\Omega] = -\left(\boldsymbol{\Omega}^2 - \mathbf{g}\right) \cdot \delta\mathbf{r}[\Omega] - i(\boldsymbol{\Gamma} - \mathbf{h})\Omega\delta\mathbf{r} + \frac{1}{M_\text{eff}}\delta\mathbf{F}_{th}[\Omega] \tag{4.17}$$

$$\Leftrightarrow \delta\mathbf{r}[\Omega] = \frac{1}{M_\text{eff}}\begin{pmatrix} \Omega_1^2 - g_{11} - \Omega^2 - i(\Gamma - h_{11})\Omega & g_{21} - i\Omega h_{21} \\ g_{12} - i\Omega h_{12} & \Omega_2^2 - g_{22} - \Omega^2 - i(\Gamma - h_{22})\Omega \end{pmatrix}^{-1} \cdot \delta\mathbf{F}_{th} \tag{4.18}$$

$$= \boldsymbol{\chi}_{fb} \cdot \delta\mathbf{F}_{th}$$

Combining the undressed eigenfrequencies with the diagonal feedback terms $\Omega_{\parallel 1,2}^{\,2} = \Omega_{1,2}^2 - g_{11,22}$, the susceptibility matrix is then

$$\boldsymbol{\chi}_{fb} = \frac{1}{\det \boldsymbol{\chi}_{fb}^{-1}}\begin{pmatrix} \Omega_{\parallel 2}^{\,2} - \Omega^2 - i(\Gamma + h_{22})\Omega & -g_{21} + ih_{21}\Omega \\ -g_{12} + ih_{12}\Omega & \Omega_{\parallel 1}^{\,2} - \Omega^2 - i(\Gamma + h_{11})\Omega \end{pmatrix} \tag{4.19}$$

with

$$\begin{aligned} M_\text{eff}^{-1} \det \boldsymbol{\chi}_{fb}^{-1} =& \left(\Omega_{\parallel 1}^{\,2} - \Omega^2 - i(\Gamma_1 + h_{11})\Omega\right)\left(\Omega_{\parallel 2}^{\,2} - \Omega^2 - i(\Gamma_2 + h_{22})\Omega\right) \\ & - (g_{12} - ih_{12}\Omega)(g_{21} - ih_{21}\Omega) \end{aligned} \tag{4.20}$$

$$=Y_-[\Omega]Y_+[\Omega], \tag{4.21}$$

where we have introduced the complex admittances $Y_\pm[\Omega]$, whose expression are

$$Y_\pm[\Omega] \equiv \frac{\Omega_1^2 + \Omega_2^2 - f_{11} - f_{22}}{2} - \Omega^2 - i\Omega\Gamma + \frac{1}{2}\sqrt{(\Omega_2^2 - \Omega_1^2 - f_{22} + f_{11})^2 + 4f_{12}f_{21}}$$

using $\mathbf{f} \equiv \mathbf{g} - i\Omega\mathbf{h}$.

4.1.4 Dressed eigenmodes for a single linear feedback

With the general form for **f** in Equation 4.8 we can write $\boldsymbol{\chi}_{fb}$ in the eigenmode basis $\mathbf{e}_{1,2}$ as

$$\begin{aligned} \boldsymbol{\chi}_{fb}^{-1}[\Omega] =& \frac{1}{\det \boldsymbol{\chi}_{fb}^{-1}[\Omega]} \\ & \begin{pmatrix} \Omega_2^2 - \Omega^2 - i\Gamma\Omega + p\sin\varphi\sin\mu & -p\cos\varphi\sin\mu \\ -p\sin\varphi\cos\mu & \Omega_1^2 - \Omega^2 - i\Gamma\Omega + p\cos\varphi\cos\mu \end{pmatrix}, \end{aligned} \tag{4.22}$$

with

$$\begin{aligned} \det \chi^{-1}[\Omega] =& (\Omega_1^2 - \Omega^2 - i\Gamma\Omega + p\cos\varphi\cos\mu) \\ & (\Omega_2^2 - \Omega^2 - i\Gamma\Omega + p\sin\varphi\sin\mu) - \\ & p^2\cos\varphi\sin\varphi\cos\mu\sin\mu. \end{aligned} \tag{4.23}$$

Using the following analogy to the g_{ij} matrix from Section 1.1.2

$$\begin{aligned} g_{11} &\to -p\cos\varphi\cos\mu & \qquad g_{21} &\to -p\cos\varphi\sin\mu \\ g_{12} &\to -p\sin\varphi\cos\mu & \qquad g_{22} &\to -p\sin\varphi\sin\mu \end{aligned} \tag{4.24}$$

we can use Equation 1.40 to obtain the dressed eigenfrequencies of the nanowire with active feedback:

$$\begin{aligned} \Omega_\pm^2 =& \frac{\Omega_1^2 + \Omega_2^2 + p\cos\left(\varphi_{fb} - \mu\right)}{2} \\ & \pm \frac{1}{2}\sqrt{\left(\Omega_2^2 - \Omega_1^2 - p\cos(\varphi + \mu)\right)^2 + p^2 \sin 2\varphi \sin 2\mu}. \end{aligned} \tag{4.25}$$

And similar to (1.42) the dressed eigenvectors are

$$\begin{aligned} \mathbf{e}_- &= \frac{1}{\sqrt{p\sin^2\varphi\cos^2\mu + \left(\Delta\Omega_\perp^2\right)^2}} \begin{pmatrix} \Delta\Omega_\perp^2 \\ -p\sin\varphi\cos\mu \end{pmatrix} \\ \text{and} & \\ \mathbf{e}_+ &= \frac{1}{\sqrt{p\cos^2\varphi\sin^2\mu + \left(\Delta\Omega_\perp^2\right)^2}} \begin{pmatrix} p\cos\varphi\sin\mu \\ \Delta\Omega_\perp^2 \end{pmatrix}. \end{aligned} \tag{4.26}$$

Here, we introduced for visual simplicity the quantity

$$\begin{aligned} \Delta\Omega_\perp^2 \equiv \frac{1}{2}\Bigg(& \Omega_2^2 - \Omega_1^2 - p\cos(\varphi + \mu) + \\ & \sqrt{\left(\Omega_2^2 - \Omega_1^2 - p\cos(\varphi + \mu)\right)^2 + p^2 \sin 2\varphi \sin 2\mu}\Bigg). \end{aligned} \tag{4.27}$$

4.1.5 The projected thermal noise spectrum

Following the proceeding described in Section 1.1.2.4, we can calculate the projected thermal noise spectrum for an arbitrary linear feedback. Equation 1.65 becomes the more general expression

$$S_{\delta r_\mu}[\Omega] = \frac{S_{F_{th}}}{\left|\det \chi^{-1}\right|^2} \begin{pmatrix} \cos^2\mu\left(\left|\chi_{11}\right|^2 + \left|\chi_{12}\right|^2\right) \\ + \sin^2\mu\left(\left|\chi_{22}\right|^2 + \left|\chi_{21}\right|^2\right) \\ +2\cos\mu\,\sin\mu\left(\Re(\chi_{11}^*\chi_{21}) + \Re(\chi_{12}^*\chi_{22})\right) \end{pmatrix} \tag{4.28}$$

Where the asterisk is the complex conjugate and $\Re$ is the real part of a complex quantity.

4.1.6 The parasitic role of the measurement noise

The experimental realization is never an ideal replica of the theory, here, the readout channels add additional noise $\delta\rho_{\ominus,\oplus}^{\text{noise}}$ to the measured displacement noise $\delta r_{\ominus,\oplus}$ of the nanowire. This parasitic noise is then injected into the feedback loop and causes an excess of force noise. This section gives a more detailed description of the feedback process, taking these additional noise into account.

Writing the measured positional estimator as $\delta\rho$ and the real position of the nanowire as $\delta\mathbf{r}$, the measured signal along the detection vectors $\mathbf{e}_\ominus, \mathbf{e}_\oplus$ is:

$$\begin{aligned} \delta\rho_\ominus &= \delta\mathbf{r}\cdot\mathbf{e}_\ominus + \delta\rho_\ominus^{\text{noise}} \\ \delta\rho_\oplus &= \delta\mathbf{r}\cdot\mathbf{e}_\oplus + \delta\rho_\oplus^{\text{noise}}. \end{aligned} \tag{4.29}$$

As before, those projective measurements are used for the signal reconstruction in the x,z coordinates, so we reconstruct the noise contaminated trajectories $(\delta\rho_x, \delta\rho_z)$ from the projected signals:

$$\begin{pmatrix}\delta\rho_x\\ \delta\rho_z\end{pmatrix} = \frac{1}{\sin(\theta_\oplus - \theta_\ominus)}\begin{pmatrix}\sin\theta_\oplus & -\sin\theta_\ominus\\ -\cos\theta_\oplus & \cos\theta_\ominus\end{pmatrix}\cdot\begin{pmatrix}\delta\rho_\ominus\\ \delta\rho_\oplus\end{pmatrix}. \tag{4.30}$$

The projected trajectory along a measurement vector $\boldsymbol{\mu}$ with the angle μ to the x-axis is then given by

$$\delta\rho_\mu = \cos\mu\,\delta\rho_x + \sin\mu\,\delta\rho_z, \tag{4.31}$$

and we can separate the projected real displacement δr_μ from the projected noise $\delta\rho^{\text{noise}}$ as

$$\delta\rho_\mu = \delta r_\mu + \underbrace{\cos\mu\,\delta\rho_x^{\text{noise}} + \sin\mu\,\delta\rho_z^{\text{noise}}}_{\delta\rho_\mu^{\text{noise}}}. \tag{4.32}$$

Inserting the expressions for $\delta\rho_{x,z}$ from (4.30), we obtain $\delta\rho_\mu^{\text{noise}}$ in terms of the measurement noise $\delta\rho_{\ominus,\oplus}$ as

$$\delta\rho_\mu^{\text{noise}} = \frac{1}{\sin(\theta_\oplus - \theta_\ominus)}\left(\sin(\theta_\oplus - \mu)\delta\rho_\ominus^{\text{noise}} + \sin(\mu - \theta_\ominus)\delta\rho_\oplus^{\text{noise}}\right) \tag{4.33}$$

The uniaxial active feedback applies an artificial force that is thus proportional to the projected actual displacement δr_μ and the projected noise:

$$\delta\mathbf{F}_{\text{fb}}[\Omega] = M_{\text{eff}}\,p_{\text{fb}}\bigl(\delta r_\mu[\Omega] + \delta\rho_\mu\bigr)\mathbf{e}_{\text{fb}}, \tag{4.34}$$

so that the equation describing the dressed nanowire trajectory becomes:

$$\delta\mathbf{r}[\Omega] = \boldsymbol{\chi}[\Omega]\cdot\bigl(\delta F_{\text{th}} + M p_{\text{fb}}\delta\rho_\mu^{\text{noise}}\mathbf{e}_{\text{fb}}\bigr), \tag{4.35}$$

where the dressed susceptibility matrix $\boldsymbol{\chi}[\Omega]$ in the $\mathbf{e}_{1,2}$ basis is defined as in Equation 4.22. From this equation, we see that the measurement noise acts as an artificial noise source, oriented along the feedback force direction. When we now measure the nanowire trajectory along another measurement vector β, we get:

$$\begin{aligned} \delta\rho_\beta &= \mathbf{e}_\beta \cdot \delta\mathbf{r} + \delta\rho_\beta^{\text{noise}} && (4.36)\\ &= \mathbf{e}_\beta \cdot \boldsymbol{\chi}[\Omega] \cdot \delta\mathbf{F}_{\text{th}} + \chi_{\beta F}[\Omega] M_{\text{eff}} p_{\text{fb}}\, \delta\rho_\mu^{\text{noise}} + \delta\rho_\beta^{\text{noise}}, && (4.37) \end{aligned}$$

where $\chi_{\beta F} = \mathbf{e}_\beta \cdot \boldsymbol{\chi} \cdot \mathbf{e}_F$. The last two terms in (4.37) contain only readout noise for the two involved detection vectors. The first term is enhanced by the mechanical susceptibility, while the second one represents the readout noise along the measurement direction (which is generally spectrally flat). Both noise terms are linear combinations of the readout noises ($\delta\rho_{\ominus,\oplus}^{\text{noise}}$). Since all noise sources in this equations (Langevin and readout noises on each measurement channel) are uncorrelated, they will add up incoherently in the noise spectra. We can write $\delta\rho_\beta^{\text{noise}}$ (the last two terms) in terms of the noises seen on each readout channel:

$$\delta\rho_\beta^{\text{noise}} = \frac{1}{\sin(\theta_\oplus - \theta_\ominus)} \begin{pmatrix} \big(\sin(\theta_\oplus - \beta) + \chi_{\beta F}[\Omega] M_{\text{eff}} p_{\text{fb}} \sin(\theta_\oplus - \mu)\big)\delta\rho_\ominus^{\text{noise}} \\ +\big(\sin(\beta - \theta_\ominus) + \chi_{\beta F}[\Omega] M_{\text{eff}} p_{\text{fb}} \sin(\mu - \theta_\ominus)\big)\delta\rho_\oplus^{\text{noise}} \end{pmatrix}. \quad (4.38)$$

The measured noise spectrum is then

$$S_{\delta\rho_\beta} = S_{\delta r_\beta} + \frac{1}{\sin^2(\theta_\oplus - \theta_\ominus)} \begin{pmatrix} \left|\sin(\theta_\oplus - \beta) + \chi_{\beta F}[\Omega] M_{\text{eff}} p_{\text{fb}} \sin(\theta_\oplus - \mu)\right|^2 S_{\delta\rho_\ominus^{\text{noise}}} \\ +\left|\sin(\beta - \theta_\ominus) + \chi_{\beta F}[\Omega] M_{\text{eff}} p^{\text{fb}} \sin(\mu - \theta_\ominus)\right|^2 S_{\delta\rho_\oplus^{\text{noise}}} \end{pmatrix}, \quad (4.39)$$

which can be simplified if the readout vectors are perpendicular ($\theta_\oplus = \theta_\ominus + \pi/2$):

$$\begin{aligned} S_{\delta\rho_\beta} = S_{\delta r_\beta} &+ \left|\cos(\beta - \theta_\ominus) + \chi_{\beta F}[\Omega] M_{\text{eff}} p_{\text{fb}} \cos(\mu - \theta_\oplus)\right|^2 S_{\delta\rho_\ominus^{\text{noise}}} \\ &+ \left|\sin(\beta - \theta_\ominus) + \chi_{\beta F}[\Omega] M_{\text{eff}} p^{\text{fb}} \sin(\mu - \theta_\ominus)\right|^2 S_{\delta\rho_\oplus^{\text{noise}}}. \end{aligned} \quad (4.40)$$

As a first criterion for a proper measurement of the mechanical displacement noise, we require a good signal noise to background noise (SNB) ratio $S_{\delta r_\beta} \gg S_{\delta\rho_{\ominus,\oplus}^{\text{noise}}}$ for the frequency range of interest. The main noise contribution then comes from the mechanically enhanced noise and we obtain as a second criterion:

$$\begin{aligned} && p_{\text{fb}}^2 M_{\text{eff}}^2 |\chi_{\beta F}|^2 S_{\delta\rho_{\ominus,\oplus}^{\text{noise}}} \ll S_{\delta r_\beta} && (4.41)\\ \Rightarrow && p^2 \ll \Omega_m^2 \Gamma_m^2 \frac{S_{\delta r_\beta}}{S_{\delta\rho_{\ominus,\oplus}^{\text{noise}}}}, && (4.42) \end{aligned}$$

where we evaluated the susceptibility close to the mechanical resonance. We note that the noise level at frequencies far from resonance remains almost constant.

One objective of the active feedback is to compensate the mode rotations of the nanowire using the transversal configuration. If we want to compensate a rotation of $\pi/4$, we need to apply a feedback gain of $p_{\mathrm{fb}} > \Omega_m \Delta\Omega_m$ with the mode splitting $\Delta\Omega_m$. This imposes a minimum SNB of:

$$\frac{S_{\delta r_\beta}}{S_{\delta \rho^{\mathrm{noise}}_{\ominus,\oplus}}} \gg \frac{\Delta\Omega_m^2}{\Gamma_m^2}. \tag{4.43}$$

Thus, for an eigenmode splitting of 100 Hz with 10 Hz mechanical linewidth, the required SNB is 20 dB while for a high Q nanowire with 1 Hz linewidth, it is 40 dB. The higher required SNB originates from the fact that the mechanical response increases when Γ decreases, but the mode rotation is not affected. Since in practice, the SNB scales with Q, this should not be a too critical criterion, but it sets an upper bound for the gain of the feedback architecture. We note that we have assumed that the driving force does not add any additional noise, but it could be treated using the same formalism.

4.2 Implementation of a tunable linear 2D force feedback

In order to realize a linear force feedback scheme in two dimensions as described in the previous section, two criteria must be fulfilled. Firstly, the position δr_μ needs to be measured and fed back in realtime, meaning with a computation time significantly faster than the evolution of the oscillator position. This requires a signal processing protocol that converts the projected signals along the two readout directions (compare Section 1.3) into a feedback measurement signal, proportional to the motion projected along an artificial direction vector $\mathbf{e}_\mu$. Secondly, the direction of the feedback force must be tunable in order to adapt φ while the feedback force should be efficient enough so that the feedback mechanism can act sufficiently on the nanowire dynamics. This tunability criterion makes it difficult to use the optical force which drives the nanowire in order to lock the PLL on the mechanical response, since the direction of this force cannot be sufficiently tuned due to the static optical montage. Instead, by using one of the metal-coated AFM tips used for force measurements, we have a movable point source of an electrostatic force with good controllability in term of orientation as the nanowire is attracted by the tip, and an extremely efficient actuation: a biased tip located at 100 nm generates a typical force of 100 fN for $V_{\mathrm{bias}} = 1$ V, a value that largely overwhelms all other forces at play in the nanowire dynamics.

4.2.1 Linear electrostatic force

A single electrode creates a central attractive force field in absence of parasitic electrostatic field. By positioning it correctly with respect to the nanowire extremity, the direction of the force can be finely tuned. Since the electrostatic force on a polarizable object is quadratic in voltage, we can get a working point where $\delta F(\delta V)$ is linear if we add a static bias voltage and the feedback voltage fluctuations. A metal coated AFM cantilever electrode has already been investigated in the previously conducted force measurements, we naturally chose such a tunable force for our feedback purpose.

4.2.1.1 Linearity

We recall that the electrostatic force exerted on a dielectric nanowire generated by an electrode follows

$$\mathbf{F}_{el}(V) = \alpha(V - V_0)^2\mathbf{e}_F, \tag{4.44}$$

where $\mathbf{e}_F$ is oriented towards the electrostatic tip and α, V_0 are the position dependent quadratic force coefficient and offset potential. We here neglect any contribution of a constant background force that does not contribute to the feedback. In the experiment we will apply a voltage fluctuation δV to modulate the force added to a static bias potential V_1, then the electrostatic force can be expanded as

$$F_{el}(V_1 + \delta V) = \alpha(V_1 - V_0)^2 + 2\alpha(V_1 - V_0)\delta V + 2\alpha\delta V^2. \tag{4.45}$$

The first static contribution can displace the nanowire rest position and is responsible for a dressing of the nanowire's mechanical properties. When the bias voltage is large enough, the nanowire eigenmodes will naturally get aligned with the electrostatic tip direction.

Equation 4.45 tells that the linear term dominates the voltage fluctuations if $|V_1 - V_0| \gg |\delta V|$ and we can hence approach a linear regime by operating at a working point V_1 far enough from V_0. Experimentally, too large V_1 will create static force field gradients that are too extreme for the nanowire to remain in the linear regime: if it moves away from its rest position, the actuation force will not remain identical. This practically imposes an upper limit for $|V_1 - V_0|$ of about 1 V, a value which depends as well on the distance between the nanowire and the electrode. This distance is chosen not to small to accomplish that the nanowire evolves in a spatially homogeneous actuation force (the nanowire thermal noise trajectories typically spread over 1 nm to 10 nm). With typical amplitudes of δV ranging from a few mV to tens of mV, sufficient to produce fluctuating electrostatic forces which significantly dominate the nanowire dynamics, we verified that the force modulation remains linear with δV by realizing response measurements without detecting any deviation from the linear response regime.

4.2.1.2 Feedback force orientation

The electrostatic force created by a biased tip is radially symmetric. It thus suffices to know the direction of the eigenmodes and to position the tip accordingly in order to have the force direction acting in a well determined direction φ. In practice the direction of the eigenmodes can be obtained either from a fit of the acquired spectra along two measurement directions or by measuring δr_μ in a radar like measurement for multiple angles μ.

In order to determine the correct position of the electrode, one needs to take into account that the obligation to work around an offset V_1 adds a static force field with non-negligible gradients. This central force induces a rotation of the eigenmodes as a block due to the conservative nature of the electrostatic force (Section 1.1.2.3), up to the limit that the lower frequency eigenmode will align towards the electrostatic tip. This observation is an advantage since it allows the electrostatic force to be directly aligned with the dressed lower eigenmode ($\mathbf{e}_- \rightarrow \mathbf{e}_\varphi$).

We could therefore use a high V_1 to create a bias force field that aligns the first fundamental eigenmode basis with the force field. Due to the mentioned experimental difficulties at large offset potentials, where one loses the spatial homogeneity of the feedback force. We adopted a compromise where the electrostatic tip is already oriented in direction of the undressed low frequency mode and the static electrostatic force field improves the force alignment.

Another effect that influences the choice of the force angle φ is the tilt of the nanowire with respect to the cantilever/tip which breaks the isotropic symmetry of the force and the force gradients, the latter being responsible for eigenmode rotations. For a straight nanowire, the only parameter that determines which eigenmode is affected by the applied force is the relative alignment between the nanowire and the electrode. For a nanowire tilted along the x-axis for example, the electrostatic force will not be symmetric when moving the electrode around the nanowire, and will present a force field pattern with a large bias of the vector flow along the x coordinate. The force gradients can also be biased along that orientation. In such a situation, it is important to position the tip in the x direction (along the tilt direction), and to use a bias voltage strong enough in order to align the eigenmodes along the x axis.

4.2.2 Feedback architecture on an arbitrary measurement direction

With the first prerequisite for a two dimensional linear feedback being fulfilled by the use of a mobile single electrode, one still needs to modulate the feedback voltage signal proportionally to the projected displacement amplitude δr_μ measured along $\mathbf{e}_\mu$. Since the latter does not necessarily coincides with one of the two initial measurement vectors ($e_{\ominus,\oplus}$), this requires a realtime projection of the measured signal $\delta\mathbf{r}$ that first must be reconstructed from the measured signals $\delta V_{\ominus,\oplus}$ on the two linearly independent measurement vectors $\boldsymbol{\beta}_{\ominus,\oplus}$.

In order to achieve a realtime signal processing condition while keeping a high degree of flexibility we use the customized *Red Pitaya* FPGA device that was introduced in Section 1.4.6 to create the feedback signal. To do so, the functionalities of DSP and data server have been adapted as will be discussed in the remainder of this section.

4.2.2.1 Realtime digital signal processing

The feedback FPGA unit needs to be able to rebuild the signal $\delta\mathbf{r}$ from the measured signals along two measurement vectors that are not necessarily perpendicular, nor of equal sensitivity, and project this signal onto the chosen measurement vector $\mathbf{e}_\mu$. The device should therefore be fed with the three parameters $\boldsymbol{\beta}_\ominus, \boldsymbol{\beta}_\oplus$ and μ which are the two readout vectors and the projection angle as inputs.

Breaking down the conversion from measured signals $\delta V_{\ominus,\oplus}$ to projected displacement amplitude δr_μ, we first start with the signals projected on the two readout channels $\ominus, \oplus$

$$\delta r_{\ominus,\oplus} = \mathbf{e}_{\beta_{\ominus,\oplus}} \begin{pmatrix} \delta r_x \\ \delta r_z \end{pmatrix}. \tag{4.46}$$

Since both measurement channels have an individual sensitivity, the measured voltages at the detector are

$$V_{\ominus,\oplus} = |\beta_{\ominus,\oplus}| \delta r_{\ominus,\oplus}. \tag{4.47}$$

To obtain the projected displacements from the measured signal we can therefore just divide by the lenghts of the measurement vectors:

$$\begin{pmatrix} \delta r_\ominus \\ \delta r_\oplus \end{pmatrix} = \begin{pmatrix} \delta V_\ominus / |\boldsymbol{\beta}_\ominus| \\ \delta V_\oplus / |\boldsymbol{\beta}_\oplus| \end{pmatrix}. \tag{4.48}$$

For the reconstruction of $\delta\mathbf{r}_{xz} = (\delta r_x, \delta r_z)^T$ from $(\delta r_\ominus, \delta r_\oplus)^T$ we use the transformation from Equation 1.3.1. The product $\mathbf{e}_\mu \cdot \delta\mathbf{r}$ then yields the projected signal δr_μ that is proportional to the displacement $\delta\mathbf{r}$ of the nanowire in direction of $\mathbf{e}_\mu$. We can combine these steps into one equation:

$$\begin{aligned} \delta r_\mu &= s \left(\frac{\cos\mu \sin\beta_\ominus - \sin\mu \cos\beta_\ominus}{|\boldsymbol{\beta}_\ominus| \det \boldsymbol{\beta}} \delta r_\ominus + \frac{\sin\mu \cos\beta_\oplus - \cos\mu \sin\beta_\oplus}{|\boldsymbol{\beta}_\oplus| \det \boldsymbol{\beta}} \delta r_\oplus \right) \\ &= p_1 \delta r_\ominus + p_2 \delta r_\oplus \end{aligned} \tag{4.49}$$

where

$$\det \boldsymbol{\beta} = \cos\beta_\ominus \sin\beta_\oplus - \cos\beta_\oplus \sin\beta_\ominus, \tag{4.50}$$

and where we have also introduced the scaling factor s that ensures that the digital multiplications on the FPGA use large numbers (without digital saturation) in order to make use of the highest digital resolution we can achieve. This will also scale up the output signal in amplitude that can be subsequently attenuated electronically without loss of resolution. The two coefficients p_1 and p_2 do not depend on the measured signal and result only from the input parameters $\boldsymbol{\beta}_\ominus, \boldsymbol{\beta}_\oplus$ and μ. They do not require realtime arithmetics and are therefore calculated on the data server of the FPGA device before being used in the realtime process. As a last operation, the gain of the feedback loop is adjusted by a multiplication with a tunable factor p that can be positive or negative.

Figure 4.2 outlines the DSP configuration of the FPGA. Before any of the above arithmetics is performed, the input signals are filtered by two consecutive first order filters (low and high pass). In combination, they allow to restrict the signal to a frequency range around the mechanical resonances. In practice, the filters also serve the purpose of phase adjustment of the feedback signal. This is necessary because the electrical amplification and filtering steps of the recorded signal realized by the photodiode amplifier add a significant artificial delay to the signal due to the frequency splitting between the DC and HF outputs. It is necessary to compensate this artificial delay in order to create a truly instantaneous feedback signal. In the first versions of the DSP architecture, we did not implement a dedicated delay block and therefore use the digital filters to adjust the phase of the output signal, while relying on external electronic filters for data cleaning. Figure 4.3 shows the amplitude and phase response of a theoretical first order low-pass filter. The phase transition from 0 to $-\pi/2$ allows to correct a phase delay on the input signal by choosing a cut-off frequency ω_c such that the filter has the proper phase delay at the frequency of the mechanical resonances. These are in general very close to each other so that the residual slope does not play a significant role. The downside of this

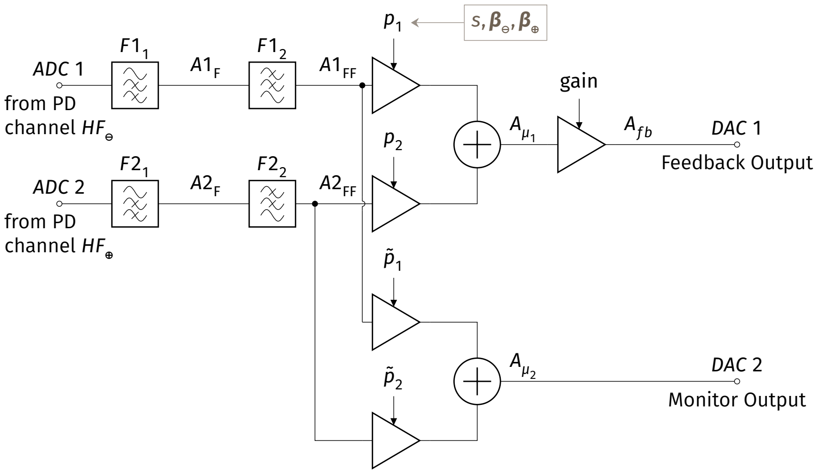

Fig. 4.2: Internal signal processing circuit of the *Red Pitaya* feedback module. The input signals from the photodiode's channels are filtered by two first order filters $Fi_{1,2}$ that can operate as high or low pass filter. A multiplication of the filtered input signals $A1_{FF}, A2_{FF}$ with the proportionals $p_1, p_2, \tilde{p}_1, \tilde{p}_2$ creats a readout singal $A_{\mu_{1,2}}$ for arbitrary readout angles. The proportionals are calculated based on the photodiode channels' readout vectors $\boldsymbol{\beta}_{\ominus,\oplus}$ and a digital scaling factor s. The calculation is performed at runtime in the *C* controlling module that runs on the operating system of the device. Each block represents a module in the FPGA. A variable gain on the feedback output *DAC*1 allows to programatically change the feedback strength.

method is that the signal is necessarily attenuated which comes with a loss of digital resolution that can neither be compensated by subsequent amplification nor the signal can be amplified before, given that the signal already fluctuates on the entire sampling range. In order to correct a phase of opposite sign, this delay module can be configured as a high-pass filter that produces a phase change of opposite sign. Instead of utilizing the module to correct a previously existing dephasing, we can also apply it in order to create a retarded signal required for the creation of delayed feedback introduced in Section 4.1.3.

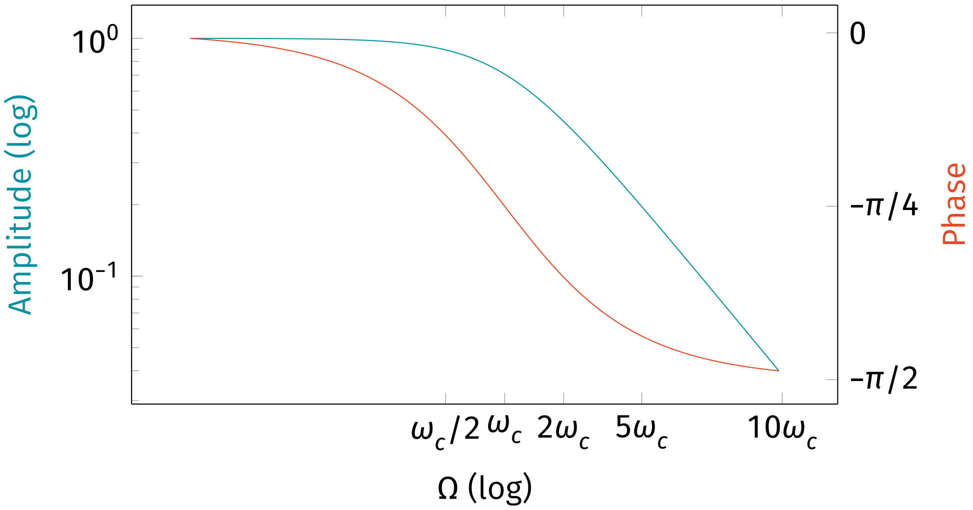

Fig. 4.3: Amplitude and phase for a low-pass filter of first order with a cut-off frequency ω_c.

After both filters, the input signal ($A1_{FF}$, $A2_{FF}$ in 4.2) is split and the signal projection of Equation 4.49 is performed on two separate channels with the coefficients $p_{1,2}$ on one and $\tilde{p}_{1,2}$ on the other channel. The first output serves as the feedback channel, and is subsequently amplified by a controllable gain factor while the second output serves as a monitor channel to realize vibration signal analysis in any desired orientation. It measures the signal at an arbitrary angle μ_2 that is different from the projection angle of the feedback channel with $\mu_1 = \mu$. Those numerical channels, are then converted into analog voltages on a ±1 V range with 14 bit resolution at a sampling rate of 125 MHz.

The FPGA module is the core element of the experimental setup that combines feedback creation with different measurement protocols. Therefore, all parameters employed in the feedback architecture can be modified via the server installed on the *RedPitaya* (compare Section 1.4.6.1), for example when realizing radar like measurements via the monitoring channel, the measurement angle can be adjusted and rotated step by step using automated protocols.

While the presented architecture only supports linear feedback operations it is easily feasible to extent the range of arithmetics in order to create nearly arbitrary non-linear force fields in 2D (where the force can become any function of the oscillator position), being only limited by the computation capacities of the FPGA. The presented linear feedbacks create oscillator responses that represent interesting applications and that can be modelled using the standard linear descriptions of our nanowire system. It is therefore an ideal test case.

4.2.2.2 Experimental implementation

The experimental setup that implements the two dimensional linear feedback measurements resembles the force measurement experiment with the addition of the feedback architecture and of the corresponding analysis tools. The setup's main components are schematically laid out in Figure 4.4. The optical and scanning probe setup are similar to the ones described above. We employ a nanowire of dimensions 300 nm by 200 µm, oscillating around 8277 Hz and 8337 Hz, with quality factors up to 8000 in vacuum, oriented along a direction $\theta_1 = -20°$. The effective mass is measured at the level of $7{\cdot}10^{-15}$ kg. The quality factor of the nanowire can be lowered by increasing the air pressure, as we will do in some of the following experiments.

On the signal processing side, the raw signal from the split-photodiode is sent to the *HF2* two channel lock-in amplifier that records data such as the nanowire's Brownian trajectories and the position noise spectra on both measurement channels. It is also used to lock the dual PLL on the mechanical resonances that are always present in the raw measurement signals $V_{\ominus,\oplus}$, but not necessarily in the radar signal V_μ when the measurement orientation becomes perpendicular to one of the eigenmode. Additionally, the instrument can perform response sweeps using the same drive channel as the feedback signal, measuring amplitude and phase responses of the nanowire, that allow to determine the electrostatic force vector as described above, and to precisely align it with one of the eigenmodes orientations as used later in Section 4.2.3.

On the feedback generating part, the raw signal is band-pass filtered between 0.3 kHz to 100 kHz by a second order filter and amplified by a factor of 200 using two *SRS SR560* low-noise preamplifiers. The amplification ensures that the signal is large enough to fill the whole span of the two analog to digital converters on the *Red Pitaya* (±1 V). Monitoring the amplified signals on an oscilloscope prevents saturation of the inputs. A *Zurich Instruments MF* single channel lock-in amplifier reads the signal on the monitor output (DAC_2 in Figure 4.2) of the feedback FPGA, the radar output, that permits to measure the nanowire trajectory projected along any orientation. Sweeping the projection angle μ_2 on this monitor channel, we can thus realize radar like measurements, acquiring either a full spectrum at each μ_2 or using a resonant measurement by adjusting the demodulation frequencies of the *MF* device to the frequencies of the eigenmodes (or any other), which can be determined by the 2 PLLs of the *HF2* while driving the nanowire with either optical or piezoelectric actuation. The measurement at an arbitrary angle also allows to monitor the effect of the feedback force along a given direction.

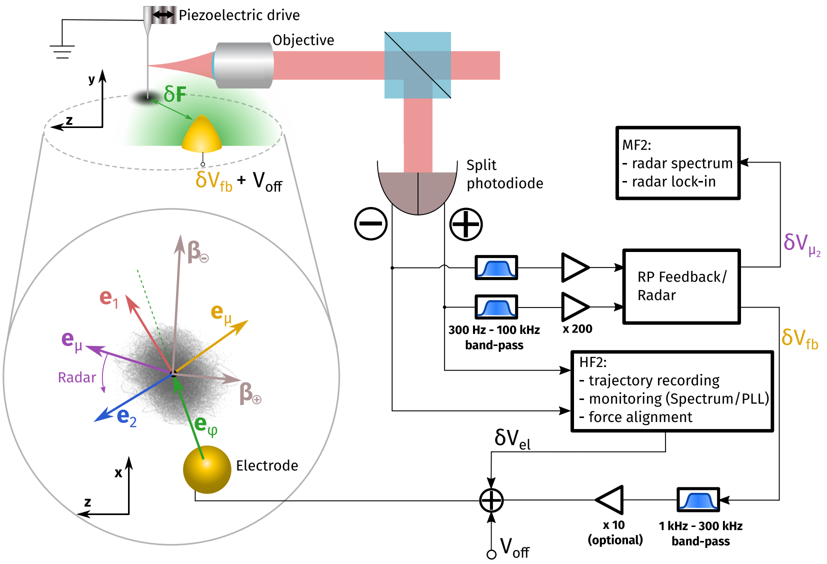

Fig. 4.4: Experimental configuration scheme for artificial force feedback generation. On the right signal processing side, the reflection signals on the ⊖, ⊕-channels of the split photodiode are realtime processed by the *RedPitaya* Feedback/Radar module. Analog band-pass filters and amplifiers on the photodiode signals ensure that the whole dynamic range (±1 V) of the *RedPitaya*'s ADCs is used. The two output signals produced by the FPGA correspond to two independent readout directions e_{μ_1} and e_{μ_2} where the feedback signal has a tunable proportional gain. Raw signal and radar signal are monitored on the HF2 and MF2 instruments, respectively. The feedback signal δV_{fb} is filtered to remove low or high frequency noises and optionally amplified before being added to the offset potential V_{off}. The left part of the figure outlines the generation of an electrostatic force in direction e_{F} proportional to the nanowire's position fluctuations measured along e_{μ}. The vectors $\mathrm{e}_{1,2}$ denote the direction of the mechanical eigenmodes in absence of feedback. The green laser (not shown) or a piezo stack can be used to drive the nanowire to independently probe its mechanical susceptibility dressed by the 2D feedback loop.

The feedback signal passes a combined electronic filter/amplification device that has been manufactured in house by *Kevin Chighine* and *Daniel Lepoittevin* at *Institut Néel*. Here, a band-pass filter at 1 kHz to 300 kHz removes a possible AC offset and high frequency noise that may have been added by the *RedPitaya*'s electronics. The amplifier can be used in the case where the force modulation achieved with the ±1 V output span of the *Red Pitaya* does not create a sufficient mechanical drive. An active homemade adder adds up the feedback signal to the output signal of the *HF2* lock-in and to an adjustable voltage offset that displaces the working point in the force parabola as described in Section 4.2.1. The offset can be used as a sort of amplifier, while its value with respect to V_0 determines the sign of the feedback force.

The electrode's tip that generates the electrostatic field and thus the driving force field is freely positionable in the horizontal x, z plane and along the vertical y axis. It is depicted by the yellow cone in the sketch of the experimental configuration in the upper part of Figure 4.4. The cut in the x, z plane highlighted by the circle illustrates the arrangement of the electrode and the nanowire, here presented as black dot in the centre. The direction of the unperturbed nanowire's eigenmodes are shown as blue and red arrows. The force vector follows a straight line between electrode and nanowire, following the direction of the electric field. The projected signal onto the measurement vectors $\mathbf{e}_{\ominus,\oplus}$ is detected at the two photodiode channels $\oplus, \ominus$. The two readout vectors $\mathbf{e}_{fb}, \mathbf{e}_{\mu}$ correspond to the two output channels of the FPGA module and can be freely rotated in a radar like way. The illustrated configuration corresponds to a nearly ideal arrangement for the generation of a pure shearing force that is topic of Section 4.3.3.

4.2.3 Force alignment

The orientation of the cold nanowire eigenmodes does not affect the generation of the feedback force field that only depends on the measurement and the force vectors' geometrical arrangements. However, the equations simplify and the interpretation of the results becomes easier if the feedback force is aligned to a mechanical mode. In particular, this configuration is necessary if one wants to generate a pure shear force field in the uncoupled eigenmode basis. Aligning the first mechanical mode with the feedback vector mitigates also the induced mode rotation due to a static external field mentioned in Section 4.2.2.2.

The first step of the measurement preparation is the precise determination of the undressed eigenmode orientations. Even if thermal noise measurements always allow determining such an orientation, they are less precise in practice than methods based on the use of external forces. One possibility is to perform a force field gradient measurement above a sharp electrode by monitoring the frequency shifts of the two eigenmodes. As described in the section on electrostatic force fields, the electrode's central force field affects the frequencies of both modes differently depending of the postition of the nanowire. When the nanowire is positioned along a straight line from the tip, in the direction of an eigenmode, only the frequency of this mode will shift while the second mode remains stable. This creates a characteristic pattern in the plot of $f_{1,2}$ that can be used to determine the uncoupled mode orientations.

Another technique to define the mode orientations is the radar measurement realized using the second output of the feedback FPGA module. It can be employed to analyse either the resonant response of the nanowire, or its thermal noise. In the resonant case, we measure the mechanical response δr_{μ} of a nanowire along the vector $\mathbf{e}_{\mu}$, whereas in the noise based case, we acquire a spectrum $S_{\delta r_{\mu}}$ for multiple angles of measurements. The two PLLs of the *HF2* locked on the nanowire's response to the piezoelectric drive (compare Figure 4.4) ensure that the modulation follows the nanowire resonances. Since the lock signal is independent from the detection vector $\mathbf{e}_{\mu}$, we do not risk to loose the PLL's lock when detecting at a direction where the projected displacement for a mode $\delta r_{\mu}(\Omega_{1,2})$ is zero. The *MF* lock-in amplifier performs the demodulation readout of the projected signal, with its demodulation frequencies synchronized to the ones determined by the PLLs of the HF2 device (via the auxiliary inputs and outputs). Due to the large signal intensities, a full radar measurement as shown in Figure 4.5, made of 180 angles, only takes about ten to twenty seconds. The main requirement here is to let the measurement proceed for a duration larger than a few inverse filter bandwidths of the final demodulator, all the other time scales in the signal processing chain being faster than that.

For the noise based measurement, the active drive used to frequency lock the PLLs is deactivated and the *MF* lock-in amplifier operates as spectrum analyzer, registering a spectrum for each projection angle μ. This technique is slower than the resonant measurement but does not require an active drive and additionally provides a better overview of the full mechanical mode spectrum.

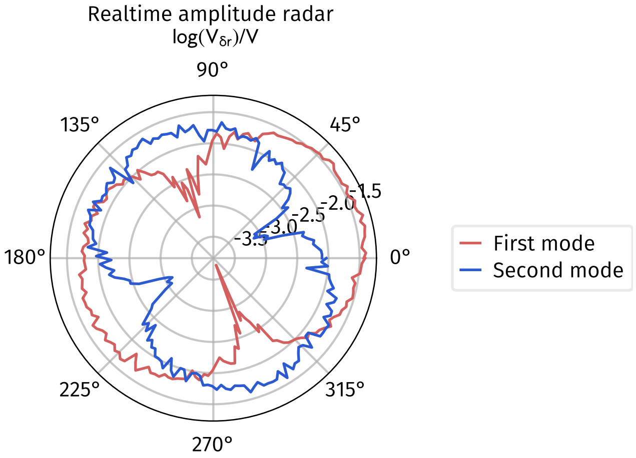

Fig. 4.5: Amplitude radar measurement $\delta r_\mu[\Omega_\pm]$ of the two mechanical modes obtained by scanning the projection angle μ. Two PLLs lock the driven tone at resonance using a piezoelectric actuation on the raw signals $V_{\oplus,\ominus}$ of the photodiode. The amplitudes are acquired at modulation frequencies on the rotating signal V_μ on the second output of the Red-Pitaya feedback module, they are shown in volts, integrated over the filter resolution badwidth (in log scale)..

Compared to the method based on a test force map, the radar measurements have the advantage that the raw mode orientation can be determined without suffering from the effects from interaction with the electrodes and can hence be realized at any offset voltage. The effect of the latter on the mode orientations at a given electrode position can thus be finely evaluated. Both techniques together are important to ensure good force-mode alignment for the feedback measurements.

Once the orientation of the modes is known, the electrode is positioned in the direction of the first eigenmode. To ensure that the electrostatic force only drives a single eigenmode, we measure the electrostatic force response to determine the force's magnitude and its orientation. To do so, the *Hf2* lock-in modulates the electric bias voltage around the chosen static offset and detects the mechanical response of the nanowire. Ideally, when perfectly aligned, the response curve would only show a mechanical response from the first mechanical mode. The upper plots in Figure 4.7 present the response curves for

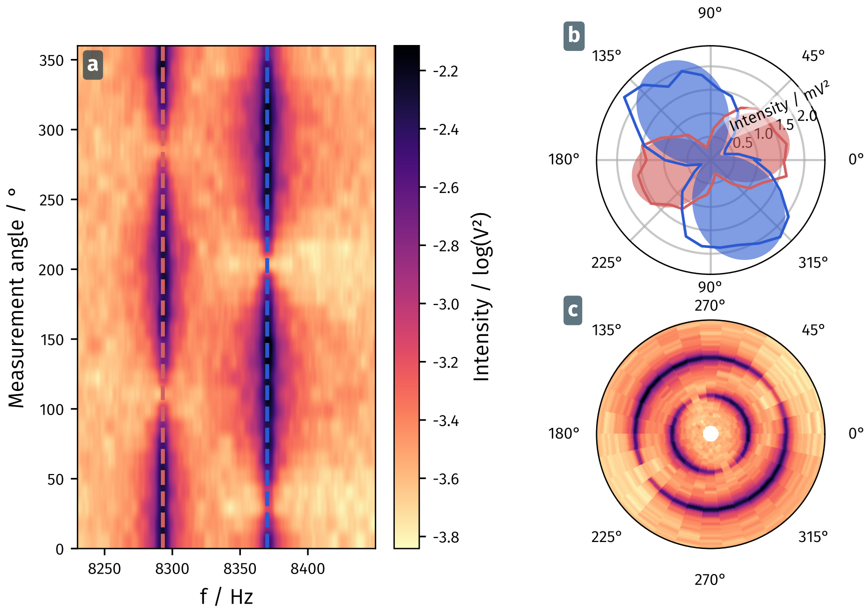

Fig. 4.6: Spectro-angular tomography $S_{\delta r_\mu}[\Omega]$ obtained by recording noise spectra while sweeping the measurement angle μ on of the RedPitaya feedback module (**a,c**). The data is acquired using the second output of the FPGA module, for which the calibration factor from volt to meter has not been determined as the final measurements will be conducted using the known output from the photodiodes. The top polar plot (**b**) shows the angular dependency of the two resonance amplitudes $S_{\delta r_\mu}[\Omega_\pm]$ obtained by sampling the noise value along the line cuts indicated by the dashed lines in the left graph. The bottom 2D polar plot (**c**) reproduces the measurement of panel (**a**) in a spectro-angular representation, which permits to visualise the orientation and frequency of the two modes. The radial axis corresponds to the frequencies plotted in the left image. Both 2D plots share the same colorscale.

an aligned configuration (left) and a slightly off positioned electrode (right). In the non-ideal plot, the second resonance clearly shows a response to the electrostatic drive which is not the case for the aligned configuration. The typical distances between the nanowire and the electrode are in the order of micrometers. Such a large distance is chosen so that the local electrostatic force field gradients remain small ($\approx 1 \cdot 10^{-8}\,\mathrm{N\,m^{-1}\,V^{-2}}$) compared to the artificial force field gradients ($\approx 1 \cdot 10^{-6}\,\mathrm{N\,m^{-1}\,V^{-2}}$) generated by the position dependent feedback. In a such a position, the artificial force field gradient can be modulated efficiently with small modulation voltages in the range of a few millivolts (modulation efficiency around $1 \cdot 10^{-4}\,\mathrm{N\,m^{-1}\,V^{-1}}$).

If the electrostatic force is not well aligned with the eigenmode direction or if the cold eigenmodes are not perpendicular (due to a light induced warping of the basis), both mechanical resonances will appear in the response measurement. To further investigate the effect of a small misalignment we use the fact that if the feedback force is sufficiently homogeneous and is well aligned with one mode, it cannot perturb the seconde mode. To verify that this is the case, we performed a sweep of the feedback readout angle $\mathbf{e}_\mu$ from 0° to 360° with the feedback gain constantly activated, and acquire a spectrum along

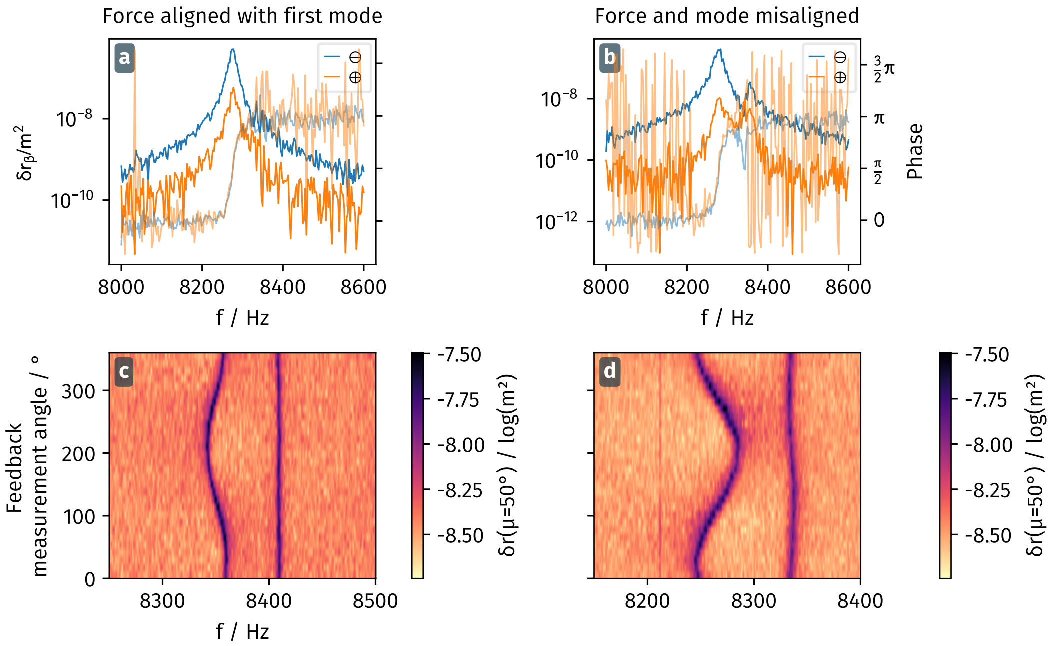

Fig. 4.7: Measurements realized to adjust and verify the force alignment with the first mechanical mode. The top row shows the response of the nanowire to a modulation of the electrostatic bias voltage, with well aligned (left) and slightly misaligned electrical force. The misaligned case shows a response of the second mode in addition to the stronger response of the first mode. The bottom plot row displays noise spectra $S_{\delta r_\beta}[\Omega]$, measured at an angle $\beta = 50°$, with the active feedback loop turned on (instantaneous feedback) working at a constant gain value, acuired for different feeback measurement angles ($\mathbf{e}_\mu$). In the misaligned case, the frequency of the second resonance is also affected by the feedback, showing that the feedback force is not properly aligned with the first eigenmode. On the contrary, in the well aligned situation, the feedback force cannot act on the second mode (if $\mathbf{e}_F \cdot \mathbf{e}_2 = 0$ and if the electrostatic force field is homogeneous, then $g_{12} = 0$ and g_{22}=0), neither by rotating its orientation nor shifting its frequency.

a given direction for each feedback readout angle. The resulting spectra are shown in the lower plot row of Figure 4.7. When perfectly aligned (left plots), as expected, only the first peak is affected by the feedback, with a maximum frequency deviation observed when the measurement angle is parallel to the first mode, while the second is stable. In the misaligned case, both peaks change their frequencies (and their amplitude as well, traducing a rotation induced by the artificial force field).

The detection angle sweep also allows to investigate if the force is instantaneous or delayed. In the case of a delayed force contribution, feedback gains of different sign (i.e. two angles separated by 180°) will cause a damping for negative force $g \propto -i\delta r_\mu$ and an antidamping for $g \propto i\delta r_\mu$, which can lead to a dynamical instability if it is strong enough to compensate the intrinsic damping of the nanowire. If the overall delay is not properly tuned to zero, then the force will not be perfectly instantaneous and then the peaks' amplitudes and linewidths would not be symmetric for positive and negative gains (i.e. for opposite feedback measurement vector orientations). If it is the case, the bandwidth of the FPGA filters which control the overall delays in the loop needs to be adjusted as described above.

4.2.4 Trajectory acquisition

The trajectories were initially recorded using a fast sampling, multichannel acquisition card (*GagePro*), saving the direct outputs of the HF channels of the photodiode. However this method produced a large amount of data, since it was necessary to sufficiently sample the mean oscillation period while simultaneously acquiring many mechanical decoherence times to record a sufficient amount of thermal noise realizations. We then turned to a demodulation technique which allows to only sample the slow variations of the oscillations envelopes. To do so, we record the quadrature signals (X and Y) on both measurement channels $\ominus, \oplus$ named $X_{\ominus,\oplus}$ and $Y_{\ominus,\oplus}$ measured with respect to the same internal clock. The sampling times t_s are also recorded. The data is converted from voltage quadratures ($\delta V(t)$) to projected position quadratures of ($\delta r_\beta(t)$) via

$$\begin{aligned} X_{\ominus,r} &= X_{\ominus,V}/\mathrm{HFDC}_\ominus/|\boldsymbol{\beta}_\ominus| \\ Y_{\ominus,r} &= Y_{\ominus,V}/\mathrm{HFDC}_\ominus/|\boldsymbol{\beta}_\ominus| \\ X_{\oplus,r} &= X_{\oplus,V}/\mathrm{HFDC}_\oplus/|\boldsymbol{\beta}_\oplus| \\ Y_{\oplus,r} &= Y_{\oplus,V}/\mathrm{HFDC}_\oplus/|\boldsymbol{\beta}_\oplus|, \end{aligned} \tag{4.51}$$

where we make use of the measurement slopes (β_i) and of the dynamics vs static conversion factors associated to the photo-amplifier ($HFDC_i$).

4.2.4.1 Plain Trajectory

The recorded trajectory is recorded in terms of quadratures of the demodulated input signal V_t[2] From the two quadratures calibrated to units of meters, the measured absolute displacement is obtained with

$$\begin{aligned} \delta r_\ominus &= \sqrt{2}\big(\cos(t_s\omega_r)X_{\ominus,r} - \sin(t_s\omega_r)Y_{\ominus,r}\big) \\ \delta r_\oplus &= \sqrt{2}\big(\cos(t_s\omega_r)X_{\oplus,r} - \sin(t_s\omega_r)Y_{\oplus,r}\big) \end{aligned} \tag{4.52}$$

where the multiplication with $\sqrt{2}$ transforms the root-mean-square (RMS) value that is saved to the *ZI* device to an amplitude. We note that this definition of the quadratures is

---

[2] For a monochromatic test signal $V_t = V_0\cos(\omega_t)$ that is multiplied with the reference signal $V_r = \sqrt{\oplus}\exp(-i\omega_r t)$ the quadratures are

$$X = \frac{V_0}{\sqrt{2}}\cos((\omega_s - \omega_r)t), \quad Y = \frac{V_0}{\sqrt{2}}\sin((\omega_s - \omega_r)t).$$

associated to a time evolution of $e^{+i\Omega t}$, which is the opposite convention of the formulas employed before, but they follow the measuring device conventions.

The velocity can similarly be expressed as:

$$\begin{aligned}\delta v_\ominus &= \sqrt{2} f_r(-\sin(t_s\omega_r)X_{\ominus,r} - \cos(t_s\omega_r)Y_{\ominus,r})\\ \delta v_\oplus &= \sqrt{2} f_r(-\sin(t_s\omega_r)X_{\oplus,r} - \cos(t_s\omega_r)Y_{\oplus,r})\end{aligned} \tag{4.53}$$

where f_r is the reference frequency in hertz. And the conversion to the lab coordinates is done by

$$\begin{aligned}\delta r_x &= \delta r_\ominus \frac{\sin\beta_\oplus}{\det\beta} + \delta r_\oplus \frac{-\sin\beta_\ominus}{\det\beta}\\ \delta r_z &= \delta r_\ominus \frac{-\cos\beta_\oplus}{\det\beta} + \delta r_\oplus \frac{\cos\beta_\ominus}{\det\beta}\text{ , with}\\ \det\beta &= \cos\beta_\ominus\sin\beta_\oplus - \cos\beta_\oplus\sin\beta_\ominus,\end{aligned} \tag{4.54}$$

where the measurement angles β_i are defined with respect to the x-axis. For the velocity, a set of similar relations is used.

Figure 4.8 shows the recorded trajectory along the x and z directions during a short fraction of the total acquisition time. The magnified section to the left shows the thermal noise of the nanowire oscillating around its mean eigenfrequency around 8340 Hz. On larger timescales, one can see a beating pattern at the frequency difference of the two eigenmodes around 60 Hz, as well as the mechanical coherence time of the nanowire (15 Hz here), reflected by the slowly evolving envelope of the thermal motion.

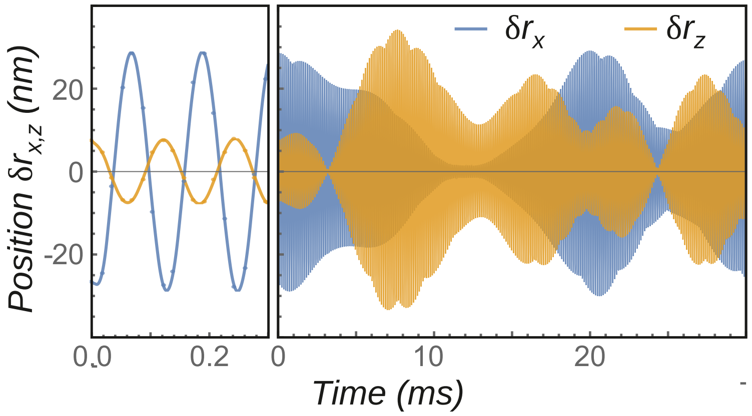

Fig. 4.8: A subset of the recorded nanowire trajectory in the laboratory *xz* coordinates. On short timescales (left) one observes an oscillation at the eigenmode frequency, on longer timescales this oscillation is modulated by the frequency difference between both nanowire eigenmodes which leads to a beating patter, while the nanowire coherence time appears as a longer amplitude modulation.

We will use analyses of the recorded trajectory in time and Fourier space. The details of the conversion from time sampled data to a frequency spectrum is given in Appendix B.

4.2.4.2 Spectrally filtered trajectory

The selected demodulator bandwidth is quite large (hundreds to thousands of hertz) and the trajectory therefore contains a large amount of readout noise, which is larger on the $\oplus$-channel compared to the $\ominus$ one due to common noise rejection. As a visible consequence, for small SNR, this can lead to an asymmetric shape of the displacement histograms in the 2D space. Since the motion signal is mainly encoded at the mechanical resonance, it is possible to spectrally filter the data in Fourier space, in order to remove the out of resonance readout noise, and to thus obtain 2D histograms in better agreement with the theoretical description. We note that this filtering does not suppress the readout contribution “below” the mechanical peaks.

We perform a discrete Fourier transform (DFT) on the demodulated complex data. Since, after filtering, we also apply the inverse DFT:

$$\delta\mathbf{r}_{t_n} = \frac{1}{N}\sum_{k=0}^{N-1} \delta\mathbf{r}_k e^{i2\pi\frac{nk}{N}}, \tag{4.55}$$

we do not need to take sample spacing into account. This holds because both transformations are the mutual inverse to each other.

The filtering itself is achieved by setting all $\delta\mathbf{r}_k = 0$ outside of rectangular window that is defined by frequency $f_c - \Delta f/2 < f_k < f_c + \Delta f/2$ with f_c as central frequency that is chosen to be the mean frequency of the mechanical modes at zero feedback, and Δf the width of the spectral filter.

From the back transformed data we obtain the trajectory in realtime by multiplication with the cosine and sine of $f_{\mathrm{demod}}\, t_s$ as in Equation 4.52 in Appendix B.

4.2.4.3 Spectrum analysis

In order to fit the spectrum we first identify the resonance peaks on the spectra read out along the x and z axes, using a peak search algorithm. The angular tomography of the resonance noise power $S_{\delta r_\beta}[\Omega_\pm]$ follows a squared cosine law with the measurement angle β. We use the recorded and calculated complex displacement spectra $\delta r_{x,z}[\Omega]$ to calculate the noise power spectrum $\left|\delta r_\beta[\Omega]\right|^2$ for β varying from 0 to 2π. Selecting the data points lying close to the identified peaks and calculating the mean as a smoothed value for the resonance height, we obtain the amplitude tomography and the mode orientations $\theta_{1,2}$ by fitting a squared cosine function:

$$A(\beta) = A_0\big(\cos(\beta - \theta_{1,2})\big)^2 + A_{\text{background}}. \tag{4.56}$$

Knowing the mode orientations, we calculate the amplitude spectra

$$S_{\delta r_{1,2}} = \frac{|\delta\tilde{r}_{\theta_{1,2}}[\Omega]|^2}{2\pi} \tag{4.57}$$

and fit a single lorentzian to each resonance, using the frequency from peak detection as first guess for $\Omega_{1,2}$ and the peak heights as guess for $a_{1,2}$:

$$A_{1,2}[\Omega] = \frac{a_{1,2}^2\Gamma_{1,2}^2\Omega_{1,2}^2}{\left(\Omega_{1,2}^2 - \Omega^2\right)^2 + \Gamma_{1,2}^2\Omega^2} \tag{4.58}$$

Since for a normal lorentzian oscillator we have

$$S_{\delta r_{1,2}}[\Omega] = \frac{2\Gamma_{1,2}k_B T M_{\text{eff}}^{-1}}{\left(\Omega_{1,2}^2 - \Omega^2\right)^2 + \Gamma_{1,2}^2\Omega^2}, \tag{4.59}$$

the fit thus provides the preliminary guess for the damping coefficients $\Gamma_{1,2}$ and the effective mass M_{eff} that can be calculated

$$M_{\text{eff}} = \frac{2k_B T}{a_{1,2}^2\Omega_{1,2}^2\Gamma_{1,2}} \tag{4.60}$$

Also, the lorentzian fit provides a better determination of the resonance frequencies. Once the above steps are performed, we in general have a good starting point to realize a final fit using the complete fitting function in Equation 4.28.

4.3 Measurements

We now turn to the experimental analysis of the impact of artificial force fields on the nanowire dynamics. We operate using a single feedback force actuator, exerted in a direction $\mathbf{e}_F$, in the particular case where it is aligned with one of the nanowire eigenmode (in our case $\mathbf{e}_F = \mathbf{e}_-$). This choice permits to simplify the theoretical analysis since the artificial force gradient matrix presents the natural symmetries of the nanowire's restoring force matrix. Having set the tip position, ensuring that the electrical force is aligned with the first mechanical mode, we now start the measurements by adjusting the detection angle μ of the feedback.

This section presents two cases, the uniaxial feedback case with detection and force vectors oriented along the same axis, and the transverse feedback case with a detection angle perpendicular to the feedback force orientation. The uniaxial feedback configuration is expected to create a conservative force field with a nonzero force gradient only in the g_{11} component of the gradient matrix when the uniaxial feedback configuration is aligned with mode 1. The transverse feedback configuration presents a feedback force oriented along the first mode, proportional to the displacement measured along the second. This corresponds to a pure shearing force field where only $g_{21} \neq 0$.

The calibration of the detection angle which is used for the feedback signal requires a good optical readout and a precisely determined readout vector for the feedback. The effects of readout noise associated to the probe laser should be negligible compared to motional signals so that we work with increased injection laser power of around 200 µW for which the SNR reaches at least 15 dBm on each measurement channel. This lower SNR is also due to the fact that, compared to force field microscopy experiments, we increased the pressure of the vacuum chamber to decrease the eigenmodes' mechanical quality factors and reduce their coherence times. This largely reduces the time needed to acquire a certain number of independent oscillation cycles of the nanowire's thermal noise. Another advantage is that a smaller quality factor pushes the dynamical instability thresholds towards a larger force gradients of artificial or physical origin. In particular this concerns topological instabilities as investigated in [44, p. 119][43] that occur when the force field has a nonzero rotational, which is the case when the measurement, eigenmodes and force vectors are not properly aligned. Lowering the Q factor also increases the power needed to generate a self oscillation of the nanowire, in presence of an anti-damping caused by delayed force fields gradients (similar to anti-damping). We now summarize the different results obtained in the different canonical cases.

We first investigated the uniaxial feedback mechanism where the feedback measurement and force vectors are aligned with the first mechanical mode. In this situation, when the feedback force is instantaneous, the artificial force field causes a shift of the resonance frequency of the first mode, and the artificial force gradient matrix only has a g_{11} component. Its effect is therefore easily observable on a spectrum analyser, allowing a good test system for an artificial linear feedback. Then we will investigate the case of a delayed uniaxial feedback, which allows control of the damping rates of the nanowire eigenmodes.

The second type of feedback discussed in this work is the transverse feedback case described in Section 4.1.2. It is a more involved test case as the off diagonal component g_{21} of the susceptibility matrix couples both mechanical modes. It can therefore not be realized in one dimensional systems, and represents a key ingredient of active feedback techniques in 2D. In the last two parts of this section we will explore both, the instantaneous and the delayed configurations of the transverse feedback.

4.3.1 Instantaneous uniaxial feedback - adjusting the nanowire's asymmetry

With the force direction aligned with the first mechanical mode, the feedback's detection angle μ is chosen to have the same orientation as the exerted force. The radar measurements (Figure 4.5) provide a good orientation analysis to find the best angular settings. Additionally, we use the second output of the FPGA module as a monitor signal with the same detection angle as the one employed for the feedback. By setting the detection angle such that only the first mode's peak appears in the signals frequency spectrum we thus ensure the correct alignment, presuming that the modes are perpendicular at the beginning of the measurement. Perpendicular eigenmodes imply that no rotational background force should be present. This excludes unwanted parasitic effect caused by the constant electrostatic field offset, which produces a residual force field of conservative nature. However, the optical field of the readout laser has regions with a non-zero rotational [43], whose effects can be reduced by choosing a readout position on the optical axis where the Poynting vector of the electromagnetic field is homogeneous and parallel to the optical axis.

Starting at zero feedback gain we record the demodulated signal of the two raw measurement channels $\ominus, \oplus$ at a frequency of $\omega_d = 8300\,\mathrm{Hz}$ during a measurement time of one minute using the *HF2* and its *Python* API. The sampling rate of the acquisition is 57.6 kHz and the demodulators fourth order low-pass filter is set to a bandwidth of 500 Hz, sufficient to capture both transverse modes (initial splitting around 70 Hz).

As explained above, we reconstruct the nanowire trajectories in realtime from the recorded quadratures measured on both measurement channels. Additionally, we compute the noise spectrum of the projected spectrum of the nanowire displacement. After the acquisition, the gain is increased stepwise and the measurement is repeated. The measurements are automatized by a collection of *Python* scripts that control the FPGA module and manage the acquisition. Having finished the measurements for positive gains, we invert the sign of the feedback proportional and perform the measurements for negative gains. Splitting the measurement in two parts has two advantages. Firstly, a repeated measurement of the zero feedback setting permits to identify drift effects and other changes that could appear during the scan of positive gains. Secondly, it is possible that instabilities occur at large positive or negative gains, and it is thus more comfortable to progressively increase the gain strength starting from zero for both directions.

The left subplot 4.9a shows the spectrum measured at an angle of 20° for the combined negative and positive feedback gains. As expected from theory, since we produce a uniaxial force field gradient (a pure g_{11}), the first mode is shifting in frequency while the second mode remains unaffected by the artificial force field. We observe that positive gains generate a negative frequency shift for mode one ${\Omega_{\parallel 1}}^2 = \Omega_1^2 - g_{11}$ ($\Omega_-^2 = \Omega_1^2 - g_{11}$) corresponding to positive g_{11}. For negative feedback proportionals, the first resonance frequency approaches the second until it comes to a crossing before the former low-frequency mode becomes the high-frequency mode at sufficient feedback strength.

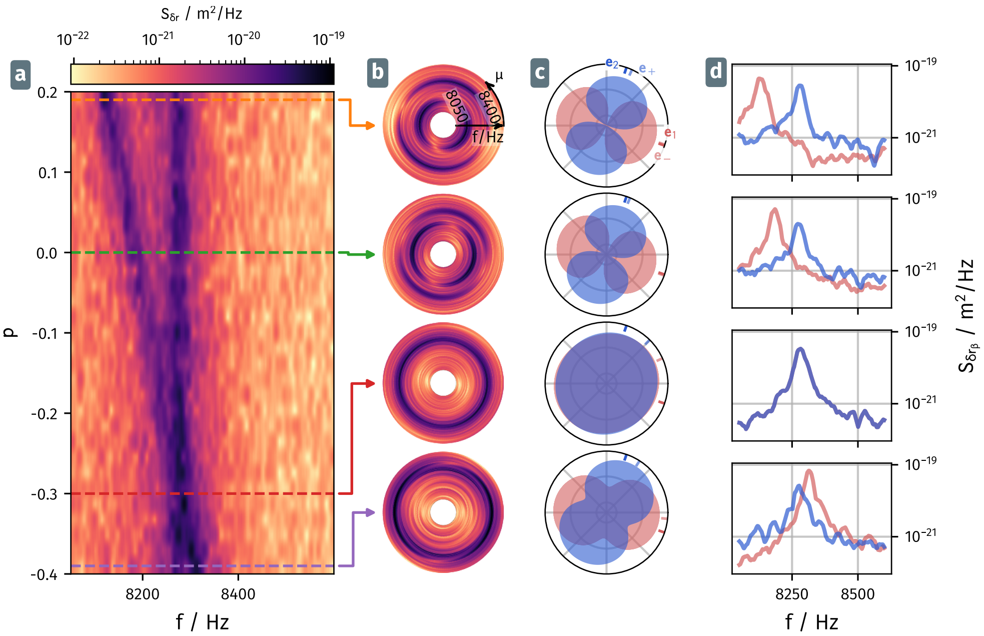

Fig. 4.9: Implementation of the instantaneous uniaxial feedback. Panel (**a**) shows the measured spectrum for the different applied gains at a readout angle of 20° for which both modes are visible. Bare mode orientations are -20°, 70° respectively. The mode resonances are visible as dark lines (high amplitude) and a mode crossing can be observed around a gain of p = -0.3. The coloured lines depict the four cases of no gain (green), high positive gain (orange), high negative gain (purple) and frequency crossing (red). The subplots shown at the right rowwise present for each case: Spectro-angular tomography $S_\delta r_\beta[\Omega]$ (**b**), resonant angular tomography $S_\delta r_\beta[\Omega_\pm]$ allowing to determine the mode orientation (**c**) and spectra measured along the mode direction $S_\delta r_{\theta_\pm}[\Omega]$ (**d**). The spectro-angular tomography draws the spectra measured along 180 readout angles μ sampled between 0 and 2π on a polar axes whose radial axis takes the frequency values around the mechanical resonances and the orthoradial axis takes the angular values of the measurement vector. The four plots in (**b**) share the same scales and their colorscale is identical to panel (**a**). The polar representation of the modes' amplitudes in (**c**), with redish colour representing the first and blueish color the second mode, reveals their orientations $\mathbf{e}_{-,+}$. The mode orientations marked as lightly couloured bars at the plot's perimeter only vary slightly from the orientation of the bare eigenmodes $\mathbf{e}_{1,2}$ indicated by heavily coloured marks, especially when the modes remain sufficiently split in frequency. The spectra in (**d**) thus show a smoothed linecut along the directions $\mathbf{e}_{-,+}$ through the spectro-angular tomography. From top to bottom one observes the transit of the first mode's resonance across the higher frequency mode while keeping the same amplitude.

The four coloured lines mark four gain values of special interest, high positive gain ($p = 0.19$), zero gain ($p = 0$), the frequency crossing ($p = -0.3$) and a high negative gain ($p = -0.39$). Here, we show exemplary the analysis that is done for each gain value at each of these four particular gains. The first column of plots 4.9b connects the mode's frequency crossing with their spatial orientation. The polar density plots of Figure 4.9b present the spectra measured for readout angles μ between 0 and 2π on a polar axis with frequencies on the radial axis and readout angle on the orthoradial axis. This *spectro-angular tomography* permits to observe the mode's behaviour in frequency and orientation at the same time. The following column 4.9c presents a polar plot of the noise spectral densities at each resonance, presenting the expected squared cosine dependence of the measurement angles. These two representations demonstrate that the mode orientation remains stable, while the eigenfrequency is shifted, except for the crossing situation where the two modes become indistinguishable, which biases the angular analysis. The next column 4.9d presents the spectra measured along the two eigenmode orientations for each gain. The fact that only one peak appears in each spectrum, again shows that the modes remain nearly perpendicular for the different feedback gains employed.

Using the full equation of the theoretical noise spectrum in presence of a force field (1.65), we fit the acquired data and thus obtain the properties of each mode as well as the equivalent force gradient matrix created by the feedback. The plot 4.10a in Figure 4.10 presents the mode frequencies of the dressed modes f_- and f_+, showing a shift of the first mode, linear with the artificial feedback strength, and a mode crossing at a gain of approximately $p_{\mathrm{fb}} = -0.3$. The plot also demonstrates that the second mode's frequency f_+ is unaffected by the feedback.

Figure 4.10b reports the relative variations of the mode orientations $\Delta\theta_{-,+}$ with respect to the undressed orientations. The plot confirms the observed trend that both modes remain stable in their orientation for varying proportional gain until the frequency crossing. There, the determination of the mode orientations is difficult because the signals are not discriminant on that parameter, even with a full model fit. Furthermore, the determination of the eigenvectors has a larger error as when the frequencies are wide apart. Still, the first eigenmode appears to slightly change its orientation when approaching the crossing which can be attributed to a non-perfect alignment of the detection angle that causes a non-zero g_{21}. In particular, these transverse components of the force fields that are responsible for the eigenmode rotations have an impact on the eigenvectors that scales with the ratio $g_{21}/(\Omega_2^2 - \Omega_1^2)$. It is hence clear that any residual transverse component will have a larger impact when the partially dressed eigenmodes are quasi frequency-degenerated (the denominator approaches zero).

The fit also allows deduction of the local force field gradients g_{ij} created by the feedback mechanism shown in panel 4.10c. In agreement with the theoretical model, only the component g_{11} shows a systematic dependence on the feedback gain. Again, the more difficult fit of the data around the crossing causes larger uncertainties in this region. However, except for the gain $p = -0.3$ corresponding to the exact mode crossing, the force field gradients correspond to a uniaxial linear feedback which acts on the first mechanical mode.

From the fitted force field gradients shown in Figure 4.9, we can now reconstruct the local map of the force field variations, evaluated over the size of the nanowire's Brownian

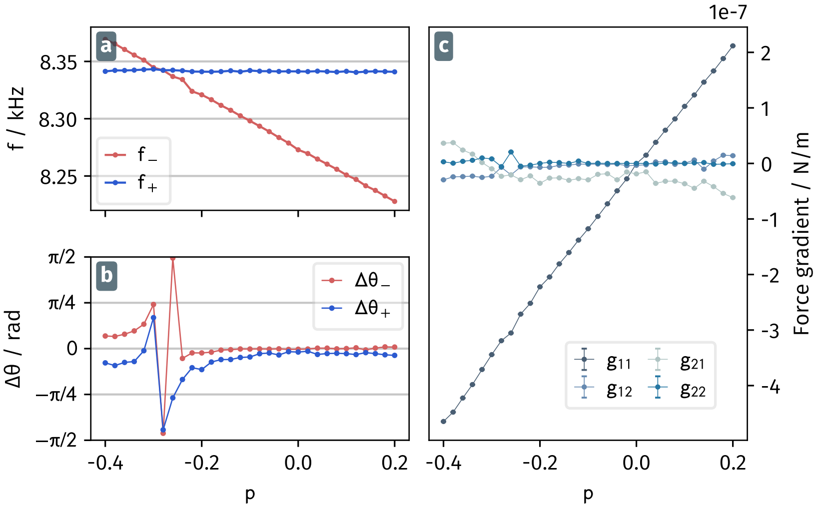

Fig. 4.10: Results of the fit of the dressed 2D oscillator model to the acquired trajectories for each feedback gain. Panel (**a**) shows the resonance frequencies of the two modes – and + with the mode crossing clearly visible at $p_{\mathrm{fb}} = -0.3$. The relative mode rotations $\Delta\theta_{-,+}$ are drawn in (**b**). Panel (**d**) displays the force field gradients responsible for the observed frequency shifts and mode rotations with all term except g_{11} centered around zero.

motion[3]. It corresponds to the vector field $\mathbf{g} \cdot \delta\mathbf{r}$. Figure 4.11 shows the local force field mapped over the recorded trajectory for each of the cuts in Figure 4.9. The colorscale represents the actual force acting on the nanowire at each position while the arrows indicate the direction of the local force field gradient.

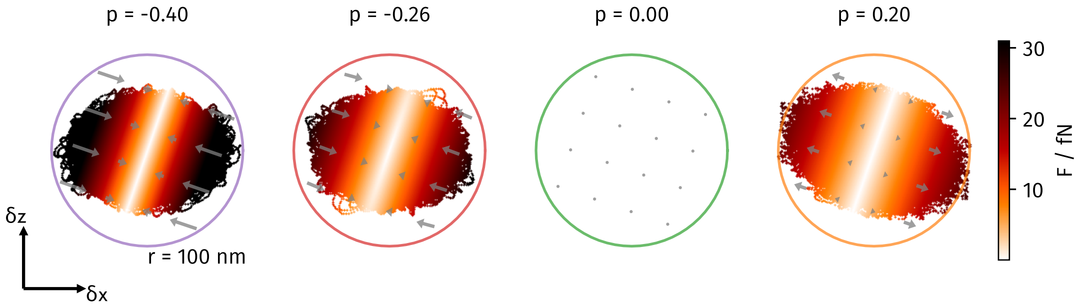

Fig. 4.11: Local force field for the four cuts from figure 4.9. The plots show the whole trajectory acquired for one minute, the 2σ region of the Gaussian distributed position is about half the size of the shown trajectory.

As a conclusion, a purely instantaneous feedback, aligned with one eigenmode permits to adjust the nanowire frequency splitting and in particular to cancel it entirely. This can be of importance when the exploration of weak shear force fields or when a purely two dimensional central force field is desired.

---

[3] We recall here that all the above measurements are done while analysing the thermal noise of the nanowire.

4.3.2 Delayed uniaxial feedback - cold damping

Delayed uniaxial feedback makes use of a force $\delta\mathbf{F} = M_{\text{eff}}\, h\dot{x}\mathbf{e}_x$ which introduces an additional damping $-h$ in the direction of interest. If the latter is aligned with one eigenmode, than its effective damping becomes $\Gamma = \Gamma_m - h$. One speaks of cold damping as the damping can be enhanced without adding additional fluctuations, so that the effective temperature of the oscillator can be reduced artificially. Such a delayed feedback has been proposed in 1998 [70] as a technique to reduce the mechanical noise of cavity mirrors in ultrasensitive experiments such as the gravitational wave detectors *LIGO* and *VIRGO*. Afterwards multiple groups realized the concept on macroscopic [24, 88, 108] and microscopic [4] cavity mirrors, cantilevers [90], and trapped levitating particles [111]. A very recent, conceptual similar experiment [11] realizes cold damping of SiN membranes using electrostatic feedback in 1d. In this section we will discuss the realization of a cold damping feedback on a single mode of the nanowire, using the same experimental configuration as in the uniaxial and aligned architecture covered by the previous section.

As an introductory remark, we note that the artificial damping matrix created by the delayed feedback creates a non-isotropic damping. If the eigenmodes also get coupled by the artificial feedback, then they will partly rotate and find a non homogeneous damping along their oscillation trajectory. This situation of non homogeneous damping has been studied in our group before [105], in the case of a graphen membrane deposited on a vibrating SiN support. We observed that the normal mode expansion is not valid anymore, the Lorentzian shapes can become asymmetric, however the fluctuation dissipation relation was preserved. Here, we first restrict ourselves to the simple situation where only one mode is affected by the cold damping mechanism, and will later study the case of a pure traverse delayed feedback.

After having adjusted the nanowire position and the readout vector as described above, the realization of an uniaxial delayed feedback on the first mechanical mode requires to add a phase delay of $\pi/2$ to the signal employed in the direct feedback case since $\dot{x}[\Omega] = -i\Omega x[\Omega]$. Such a phase is adjusted via the digital filters at the inputs of the *Red Pitaya* (see Section 4.2.2.1). In the previous Section 4.3.1, we have compensated the phase added by the photodiode's high-pass filters via the cut-off frequency of the digital low-pass filters in the FPGA. We now adapt this cut-off frequency accordingly to create the desired phase delay in the signal. We note that these delays are defined with respect to the mechanical oscillation period and thus remain small compared to the inverse mechanical damping Γ_{m}^{-1} of the oscillator. Monitoring the frequency spectrum during the phase adjustment steps helps to find the correct filter settings: If, under active feedback, the first mode's frequency does not deviate from its value at zero feedback, we do not apply an instantaneous feedback anymore, and have reached the $\pi/2$ delay configuration. In presence of a correctly delayed feedback force, one should observe a change in the peak's amplitude but not in frequency.

Once the phase is adjusted properly, we acquire the demodulated quadratures of the lock-ins on the two detection channels as it was done for the instantaneous feedback case. The recording time for each measurement point is 30 s at a sampling rate of 57.6 kHz and a demodulation frequency of 8320 Hz. The fourth order demodulation low-pass filter has a bandwidth of 500 Hz. Again, the sign of the overall feedback gain splits the measurement into two parts where the gain is increased stepwise and a trajectory is recorded for each gain before we switch the proportional's sign and repeat the measurement in the opposite direction. Due to the fact that one direction of the feedback is increasing the effective noise temperature while anti-damping the mechanical dynamics [24], we restrict the number of points in this direction that corresponds to a negative gain in the experimental setup.

We realize the Fourier analysis of the temporal trajectories as described in Section 4.2.4.3 and fit the noise spectra with the full model of the noise spectrum (4.28). By doing so, we can determine the properties of the mechanical modes, which are displayed in Figure 4.12a. They don't show large deviations for the applied feedback gains. Only the frequency of the first mode is shifting over ≈ 10 Hz due to a remaining nonzero instantaneous feedback contribution, while the mode alignment is stable and only suffers from the measurement uncertainty of about ±5° to ±10°.

For a moderate feedback gain, we obtain a noise reduction of the first mode larger than 20 dB in peak height. With increasing gain, the damping coefficient Γ_1 linearly grows while the effective mode temperature, calculated from the area of the Lorentzian fit to the first mode, is decreasing from 300 K to below 50 K. The noise spectra restricted to mode 1 are adjusted with $\Gamma_{fb} = \Gamma_0 - h_{11}$ [24]:

$$S_{\delta r_1}[\Omega] = \frac{1}{M_{\text{eff}}} \frac{2\Gamma_{\text{fb}} k_B T_{\text{fb}}}{(\Omega_1^2 - \Omega^2)^2 + \Omega^2(\Gamma_0 - h_{11})^2} \tag{4.61}$$

This corresponds to the mechanical noise spectrum of an oscillator at thermal equilibrium at the effective temperature T_{fb}:

$$T_{\text{fb}} = T_0 \frac{\Gamma_0}{\Gamma_0 - h_{11}}, \tag{4.62}$$

which can be enhanced or decreased, depending on the sign of the delayed feedback strength h_{11}. Figure 4.12b plots the damping coefficient and the effective temperature as function of the feedback gain for both mechanical modes. While the damping coefficient and temperature for the second mode (blue) only show statistical fluctuations around a constant mean value, the increasing feedback proportional enhances the damping roughly linearly and decreases the effective temperature inverse proportionally.

The inconsistency at $p^{\text{fb}} = 0.16$ where the frequency suddenly jumps up 10 Hz and the damping coefficient Γ jumps from 70 Hz to less than 10 Hz is a fit artefact that originates from asymmetric noise squashing where the feedback is not only acting on the

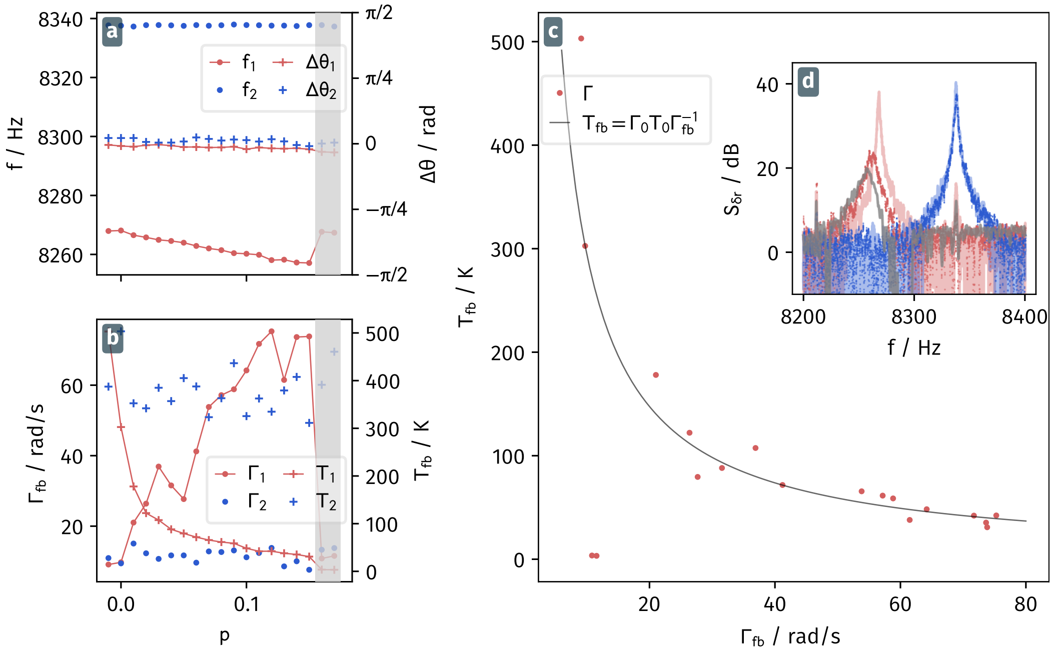

Fig. 4.12: Results for cold damping by a delayed uniaxial electrostatic force field on the nanowire. (**a**) Dependence of the eigenfrequencies (dots) and the deviation from the cold mode orientations on the feedback gain for both mechanical modes. (**b**) The damping coefficient Γ for the first mode increases nearly linearly while the effective mode temperature decreases. The mechanical noise of the second mode is not affected. The grey shaded area in (**a,b**) marks points where noise squashing has been observed. In (**c**), the effective mode temperature is drawn as function of the damping coefficient. The experimental values follow the $1/\Gamma$ dependency 4.62 drawn as black line. Inset (**d**) shows the spectra measured along the eigenmode direction (red: first, blue: second mode) for deactivated feedback (light lines), and a proportional of 0.08 (saturated lines). The grey line shows the asymmetric noise squashing at a gain of 0.15.

Brownian noise of the nanowire but searches as well to compensate the detection noise [90]. While in the perfectly aligned case noise squashing appears after the mechanical noise has been fully damped, a non-perfectly adjusted phase delay can cause a slightly asymmetric damping and background squashing. This is visible in inset 4.12d where the spectra measured in direction of the two eigenmodes are compared for no feedback (lightly colored lines), active cold damping (colored dots) and the noise squashing (grey line). The simple fit model of two Lorentzians which is employed to retrieve frequencies and mechanical linewidths does not account for this effect, but by using the previously applied model that contains the complex force gradients (4.28) it is possible to account for the underlying causes. We restrain from showing the detailed fit results at this point in order to keep the comparability of the data with common representation of cold damping in literature. Also, the affected data only presents a small subset of the results and does not change the validity of the experimental principle, but it highlights the importance to correctly align and adjust the feedback architecture in the case of a quasi frequency degenerated resonator.

The good agreement of the above relation between the effective temperature and the mechanical linewidth in Equation 4.62 in Figure 4.12c with the experimental data confirms that the experiments operates in the regime of cold damping. With this simple realtime feedback mechanism, we decreased the mode temperature by a factor of six from 300 K to less than 40 K. Improving the retardation and alignment of the feedback signal, while increasing the SNB by increasing the readout power, it should be possible to avoid the asymmetric noise squashing and thus to achieve larger cooling factors at higher gains.

Figure 4.13 illustrates the two dimensional Brownian trajectory of the nanowire in the real space measured for different feedback gains. We note that the initial trajectory is not perfectly circular due to the force field background created by optical forces from the readout laser, whose power was intentionally increased to obtain a sufficient signal to background ratio. The arrows illustrating the strength of the additional damping vector field show the increasing viscous feedback with increasing proportional that decreases the spatial extension of the Brownian motion in the direction of the feedback while its extension in the direction of the second mode remains constant.

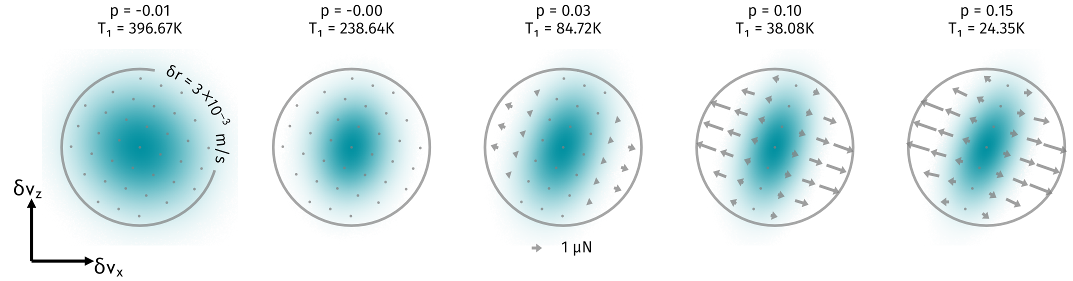

Fig. 4.13: The speed distribution of the Brownian trajectory recorded for five different feedback gains p is shown in the velocity space (v_x, v_z). The transparency of the distribution encodes the probability density for each plot so that the displayed size represents the actual distribution size (not showing the extreme trajectories with largest velocities). The nanowire's movement at zero feedback gain is slightly dressed by the optical force of the probe laser and the noise distribution is therefore not perfectly circularly shaped. The arrows indicate the damping force caused by a nonzero h_{11}. With increasing gain the extension of the distribution spreading is reduced in the direction of the first mode (the axis of the arrows) while remaining constant in the perpendicular direction. The distribution for the negative gaine (left) increased in size, caused by a heating of the nanowire.

Up to now, we have used the artificial feedback architecture in its simplest uniaxial form, and we have shown that it can be used to control and adjust some of the nanowire properties (frequencies, damping rates, effective temperatures) without altering the eigenvectors. The uniaxial mode was used in an aligned configuration, where the feedback force was aligned with one eigenmode for simplicity. The situation would be different if the feedback force was not aligned with the eigenmode basis: in the case of an instantaneous uniaxial feedback, the artificial force field could also generate a rotation of the eigenmode basis, if placed at 45° of the mode for example, but it will always behave as a conservative force field ($g_{12} = g_{21}$). We will now turn to the more exotic situation, where the artificial force field generates a non-reciprocal interaction between the eigenmodes.

4.3.3 An instantaneous pure shearing force field

The force orientation is aligned with the slow mechanical mode, in a similar manner as in the above described parallel feedback case, but now the measurement vector employed for the feedback is turned by +90° by the *FPGA* card, so that it is aligned with the orientation of the second mode in absence of an external force field. Like before, the measurement direction is optimized by monitoring the spectrum measured along this direction via the second output of the *FPGA* module. To verify that the measurement vector is properly oriented, it is also possible to vary it while applying a weak feedback, similar to Figure 4.7c. When one generates a pure shear force field ($g_{12} = 0$), that means the measurement vector is well aligned with the second mode, then the nanowire frequencies are not modified compared to the situation in absence of feedback.

4.3.3.1 Realization and measurement

For the following measurements, we also wanted to record the nanowire trajectories in realtime, in order to subsequently analyse them in real space (discussed later). To do so, we progressively increase the feedback's gain starting at zero and record one minute of the nanowires trajectory at each gain value. The acquisition is then repeated for gain values of opposite signs. We choose the maximum gain such that the nanowire's movement does not become instable, which can arise when the feedback architecture is not perfectly aligned, or when there exists a residual delay in the force application.

From the fit of the noise tomography with Equation 4.28, we deduce the resonance frequencies and the mode orientations in 4.14a as well as the feedback created force gradients g_{ij}, drawn in subfigure 4.14b. The constant value around zero for all components other than g_{12} and the linear slope of it confirm that we operate in a quasi purely transverse feedback configuration, emulating a pure shear force field. In this situation, we recall from the last part of Section 1.1.2.3 that the eigenfrequencies are not modified, as well as the orientation the mode 1 is not modified, and the angular separation between of the modes is given by

$$\cos(\theta_+ - \theta_-) \approx \frac{-g_{21}}{\Omega_+^2 - \Omega_-^2}. \tag{4.63}$$

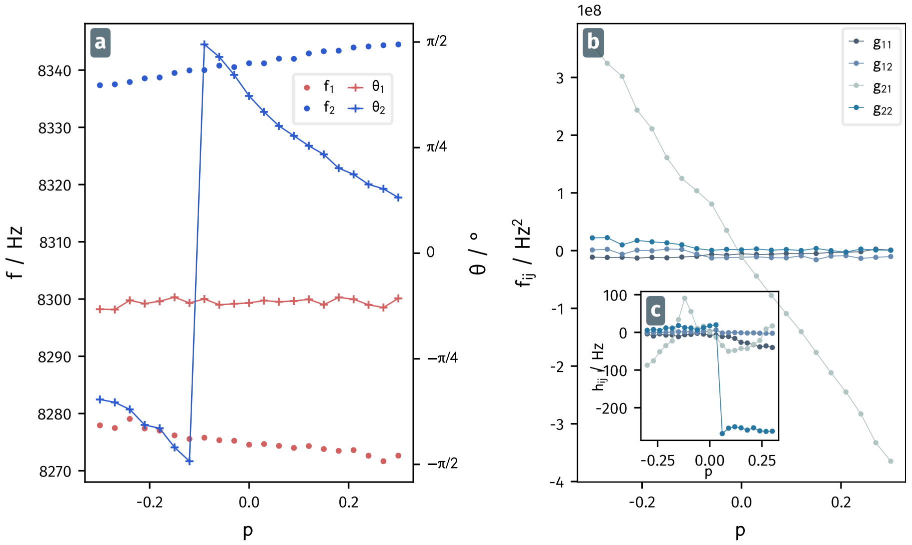

Fig. 4.14: Figure (**a**) presents the resonance frequencies and mode orientations obtained from the fit of the theoretical oscillator model to the recorded trajectories for different gains (p_{fb}). The force gradients real g_{ij} and imaginary parts h_{ij} are plotted in panel (**b**) and inset (**c**) respectively.

Here, the rotation is only determined by the ratio of g_{21} to the squared frequency splitting and we can define a dimensionless force rotational parameter ξ that allows a better quantitative comparison between the measurements:

$$\xi \equiv \frac{g_{21}}{\Omega_2^2 - \Omega_1^2}. \tag{4.64}$$

Figure 4.15 maps the rotational parameter to the applied feedback gain for two measurement series performed in the configuration of the transverse feedback. Both series have

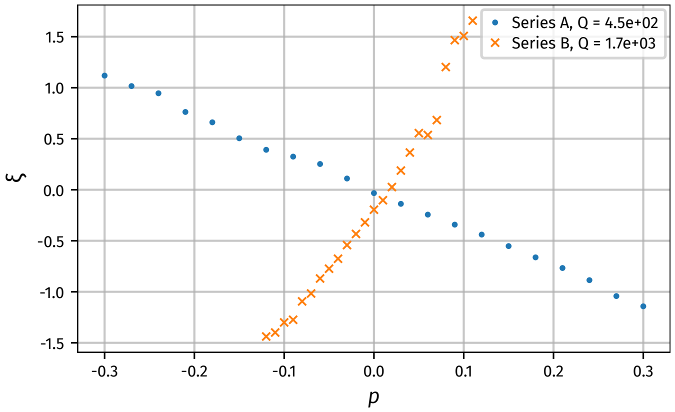

Fig. 4.15: The connection between applied feedback gain and the force rotational parameter ξ for the two measurement series discussed in this section. The difference between the two measurements resides in a different positioning of the electrostatic force, so that the electronic gain does not has the same efficiency, and a different ambient pressure which affects the intrinsic mechanical damping of the nanowire.

been conducted on the same nanowire but under different vacuum levels. The Q-factor of the nanowire's resonances in series B is thus about four times higher than that in series A, which increases the sensitivity of the oscillator to destabilizing effects, such as delayed force contributions or noise in the readout channels employed for the feedback (see Section 4.2.2.2). The measurement results for series A can in principle be realized up to larger feedback strength, due to their improved dynamical stability. Most of the results in this section are obtained from series A if not stated differently.

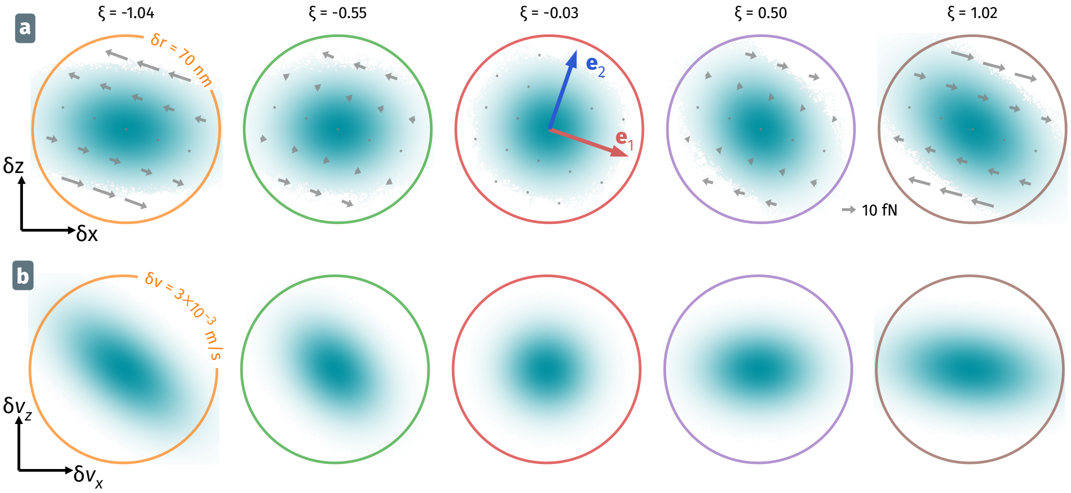

Fig. 4.16: The representations in the first row (**a**) illustrate the thermal movement of the nanowire in artificial force fields created by the active feedback mechanism for different rotation parameters ξ. The transparency of the trajectory represents the positional probability density so that the perceptual size of the Brownian cloud is a good estimation of the effective spatial extension of the nanowire's oscillation. The arrows show the force field calculated for the represented area. Their length is proportional to the applied gain and thus to the rotation parameter, while their direction is inversed with the sign change of ξ. The noise maps in (**b**) show the displacement noise in the v_x, v_z coordinates.

The first row in Figure 4.16a represents the 2D histogram of the measured trajectories for five different feedback amplitudes (positive and negative) and the created local force field for each case. In the central case of zero feedback, no feedback force is present and the noise distributions is quasi circular. Larger gains generate a shearing force field (g_{21} like) where the force is oriented towards the first eigenvector. It distorts the circular shape of the thermal cloud of the Brownian motion in positional and velocity space (shown in 4.16b) as it drives a rotational movement of the nanowire.

In Figure 4.17, the map of the locally averaged angular momentum $\mathbf{e}_y \cdot \langle \mathbf{r} \times \mathbf{v} \rangle$ of the recorded trajectory visualizes the circular movement. At zero feedback, there are is as much clockwise (blue) as anticlockwise (red) rotation as the movement is driven by the purely statistical Langevin force vector. When increasing the feedback gain, the nanowire experiences a shearing force that biases the orthoradial speed distribution and favours the counter-clockwise rotation while a negative gain enhances anticlockwise rotation.

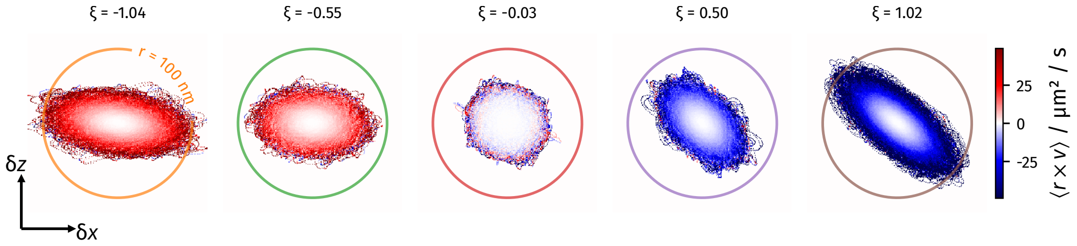

Fig. 4.17: The transverse feedback causes an acceleration with a preferential directionality depending on the sign of the gain. The plots present the mean value of the angular momentum $\mathbf{e}_y \cdot \langle \mathbf{r} \times \mathbf{v} \rangle$ with clockwise rotation (red) for negative ξ and counter-clockwise rotations (blue) for positive values.

From the Fourier analysis of the recorded trajectory we obtain the spectral density $S_{\delta r_\beta}$ that is shown for five different feedback gains in Figure 4.18a. These spectro-angular

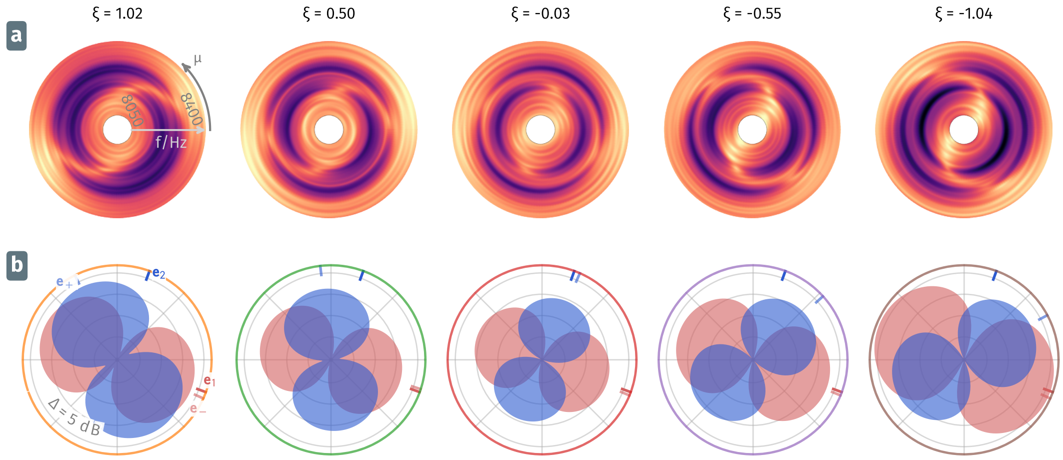

Fig. 4.18: (**a**) Spectro-angular tomography of the trajectories measured around the mechanical mode frequencies for five different rotation parameters ξ. The frequency increases with the radius while the ortho-radial direction corresponds to the measurement angle μ. Compared to the central plot where $\xi = 0$, the outer mode turns in anti-clockwise (clockwise) direction for negative (positive) ξ. The bright S-shaped (inverse S-shaped) regions that appear at large $|\xi|$ are caused by anti-resonant contributions from both mechanical modes. The visible rings are artefacts from the smoothing of the spectrum. The bottom line in **b** shows the amplitude (in logarithmic scale) of the resonances from (**a**) plotted against the measurement angle. The direction of maximum amplitude per mode defines the mode orientation $\mathbf{e}_{-,+}$ and is indicated as tick on the perimeter of plots. The marks for $\mathbf{e}_{1,2}$ indicate the directions of the eigenmodes without external force field.

tomographic maps provide a visual access to the mode orientation that can be identified in the different noise spectra, obtained for each measurement direction. In the central plot, without feedback, the first mode (the inner resonance oscillating at a lower frequency) has its intensity maximum at about -20° where no signal can be measured at the frequency of the second, outer mode. For increasing gain, we observe that the second mechanical mode turns clockwise. The visualization of the amplitudes of first (red) and second (blue) mechanical modes in Figure 4.18b shows that the first mechanical mode keeps its initial alignment. For a negative proportional, we observe the inverse behaviour – the second mode is turning clockwise until it becomes nearly aligned with the first mode. While the orientation of the second mode turns over more than 90°, considering negative and positive feedback gains, the resonant frequencies, depicted in Figure 4.14a, only change by less than ten hertz. We thus reproduce with the artificial feedback scheme, what was realized with the rotational force field of a focussed laser beam.

Even though a pure shearing force does, in theory, not induce additional noise in the system, we observe that the maximum amplitudes of the lobes in Figure 4.18a increase in presence of active feedback. This signal increase can be explained by two principal mechanisms. First, there is the injection of readout noise by the feedback loop by which noise, created during the detection process enters the feedback loop together with the signal that encodes the nanowire's position. The second mechanism that increases the system's noise amplitude is the delayed feedback originating from imperfect phase adjustment, which is able to add energy to the oscillation. The fact that the shearing force field induces correlations between both modes, can be seen at large gains (see for example at $\xi = -1.02$) in the spectro-angular tomography plot where an anti-resonance dip appears showing a dark inversed-S like shape. From the theoretical description, this is a direct consequence that the unperturbed Langevin force is now driving both eigenmodes of the nanowire, thus causing the typical cancellation profiles observed in the response measurements to a coherent force drive.

4.3.3.2 Noise squeezing

In the trajectory plots shown in Figure 4.16a, we observe that the Brownian cloud's diameter is reduced along a measurement angle of roughly 45° for negative and 90°for positive gains. Perpendicular to this noise reduction, the spreading of the thermal cloud elongates, the 2D oscillator is hence squeezed in the plane of motion. Furthermore, the same noise reduction appears in the velocity space in Figure 4.16b, where similar noise compression and enhancement is observed along the same orientations.

Compared to the uniaxial cold damping case discussed in the previous section, where the noise along the direction of the feedback is reduced in the position and speed spaces but the transverse noise is unaffected, we observe a noise increase in both spaces, in the perpendicular direction. We also note that, here, the damping rate of the nanowire is unchanged. This phenomenon can be easier visualized by comparing the width of the position histograms without feedback and with strong feedback in Figure 4.19. The axes correspond to the directions of strongest squeezing and anti-squeezing so that the lateral cuts illustrate a reduction/increase of the variance of the noise trajectory when projected along the transverse directions.

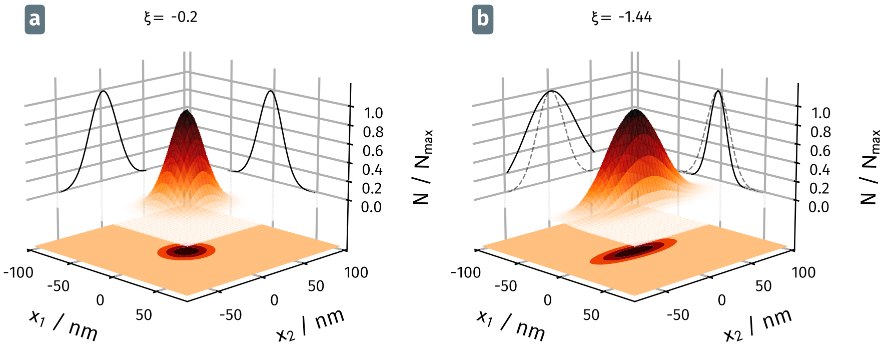

Fig. 4.19: Squeezing and anti-squeezing illustrated on the spatial distribution of the Brownian noise. (**a**) displays the spatial trajectory's histogram without active feedback, (**b**) a case of strong feedback. The distributions are rotated in the horizontal x,y plane to align the direction of largest (x_1) and smallest (x_2) extension. The distribution's height is normalized independently for better comparison of the spatial extension. The grey dashed lines in (**b**) re-display the projected distribution of (**a**) in order to highlight the squeezing (on the x_1,N-plane) and anti-squeezing (x_2,N-plane).

Theoretical description We point out that the above plots (Figure 4.16, 4.17) represent the histograms of the trajectories followed by the nanowire extremity in the position or speed spaces. In the following, we will investigate the noise in the measurement channels δr_μ or δv_μ, and in particular their variances $\sigma^2_{\delta r_\mu}$ and $\sigma^2_{\delta v_\mu}$ and their evolution with the measurement angle, which is not identical to what can be seen in the complete histograms shown above (for a Gaussian distribution, both quantities will match along the main orientations of the ellipse but not in between). However, the recording of the complete realtime trajectories, $\boldsymbol{\delta}\mathbf{r}(t)$ allows reconstruction of the projected signals along any direction and thus to estimate the corresponding variances.

A measure to quantify the squeezing and anti-squeezing of the position noise is the variance $\sigma^2_{\delta r_\mu}$ of the gaussian distributed noise trajectory. Experimentally, we can calculate the variance from the recorded trajectory and compare them to the theoretical definition

$$\sigma^2_{\delta r_\mu} = \int \frac{d\Omega}{2\pi} S_{\delta r_\mu}[\Omega] \tag{4.65}$$

Note that denominator of $S_{\delta r_\mu}$ in Equation 4.28 is a complex fraction with poles at frequencies $\Omega/2\pi$ where $|\det \chi[\Omega]|^2 = 0$. The integration therefore requires the application of the residual theorem and is rather lengthy. Appendix Appendix C discusses this calculation in more detail. For an instantaneous force field the solution of the integral is

$$\sigma^2_{\delta r_\mu} = \sigma^2_{\delta r,cc} \cos^2 \mu + \sigma^2_{\delta r,ss} \sin^2 \mu + 2\sigma^2_{\delta r,cs} \sin \mu \cos \mu, \tag{4.66}$$

where μ is the angle between the measurement vector $\mathbf{e}_\mu$ and $\mathbf{e}_1$, and with the three coefficients

$$\begin{aligned}
\sigma^2_{\delta r,cc} &= A\frac{\left(\Omega_{\parallel 2}^{\,4} + \Omega_-^2\Omega_+^2 + g_{21}^2\right)\left(\Omega_+^2 + \Omega_-^2 + 2\Gamma^2\right) - 4\Omega_{\parallel 2}^{\,2}\Omega_+^2\Omega_-^2}{\Omega_+^2\Omega_-^2} \\
\sigma^2_{\delta r,ss} &= A\frac{\left(\Omega_{\parallel 1}^{\,4} + \Omega_-^2\Omega_+^2 + g_{12}^2\right)\left(\Omega_+^2 + \Omega_-^2 + 2\Gamma^2\right) - 4\Omega_{\parallel 1}^{\,2}\Omega_+^2\Omega_-^2}{\Omega_+^2\Omega_-^2} \\
\sigma^2_{\delta r,cs} &= A\frac{\left(g_{12}\Omega_{\parallel 2}^{\,2} + g_{21}\Omega_{\parallel 1}^{\,2}\right)\left(\Omega_+^2 + \Omega_-^2 + 2\Gamma^2\right) - 2\Omega_+^2\Omega_-^2(g_{12} + g_{21})}{\Omega_+^2\Omega_-^2},
\end{aligned} \tag{4.67}$$

where

$$A = \frac{k_B T/M_{\text{eff}}}{\left(\Omega_+^2 - \Omega_-^2\right)^2 + 2\Gamma^2\left(\Omega_+^2 + \Omega_-^2\right)}.$$

Again, the names g_{ij} and f_{ij} can be used interchangably as real and artificial force field gradients are physically equivalent. Without external force field where $g_{ij} = 0$ for all i, j, the first two terms correspond to the thermal noise variance for the two eigenmodes:

$$\sigma^2_{\delta r,cc} = \frac{2k_B T}{M_{\text{eff}}\Omega_1^2},\ \sigma^2_{\delta r,ss} = \frac{2k_B T}{M_{\text{eff}}\Omega_2^2},\ \sigma^2_{\delta r,cs} = 0 \tag{4.68}$$

When the measured variance falls below this limit, we speak of noise squeezing. We note that the initial variances are not completely isotropic but this is nearly the case when the nanowire is quasi frequency degenerated. The situation is simpler in the velocity space.

A similar calculation can be done to obtain the variance of the velocity $\sigma^2_{v_\mu}$ using that $S_{\delta v_\beta}[\Omega] = \Omega^2 S_{\delta r_\beta}[\Omega]$. With a similar application of the residues theorem, the speed variance obtained from spectral integration writes

$$\sigma^2_{\delta v_\mu} = \sigma^2_{\delta v,cc}\cos^2\mu + \sigma^2_{\delta v,ss}\sin^2\mu + 2\sigma^2_{\delta v,cs}\sin\mu\cos\mu, \tag{4.69}$$

with the three coefficients

$$\begin{aligned}
\sigma^2_{\delta v,cc} &= \frac{k_B T}{M_{\text{eff}}}\left(1 - \frac{2g_{21}(g_{12} - g_{21})}{\left(\Omega_+^2 - \Omega_-^2\right)^2 + 2\Gamma^2\left(\Omega_+^2 + \Omega_-^2\right)}\right) \\
\sigma^2_{\delta v,ss} &= \frac{k_B T}{M_{\text{eff}}}\left(1 + \frac{2g_{12}(g_{12} - g_{21})}{\left(\Omega_+^2 - \Omega_-^2\right)^2 + 2\Gamma^2\left(\Omega_+^2 + \Omega_-^2\right)}\right) \\
\sigma^2_{\delta v,cs} &= \frac{k_B T}{M_{\text{eff}}}\frac{(g_{12} - g_{21})\left(\Omega_{\parallel 2}^{\,2} - \Omega_{\parallel 1}^{\,2}\right)}{\left(\Omega_+^2 - \Omega_-^2\right)^2 + 2\Gamma^2\left(\Omega_+^2 + \Omega_-^2\right)}.
\end{aligned} \tag{4.70}$$

In absence of external force field gradients, the two first expressions converge towards the isotropic case: $\sigma^2_{\delta v} = k_B T/M_{\text{eff}}$.

We have shown experimentally, that the transverse feedback is indeed creating a purely shearing force field with the only nonzero force field gradient being g_{21}. In this case, the above equations simplify and we can write the coefficients of (4.67) as

$$\begin{aligned}
\sigma^2_{\delta r,cc} &= \frac{k_B T}{M_{\text{eff}}\Omega_1^2}\left(1 + \frac{g_{21}^2}{\Omega_2^2}\frac{\Omega_1^2 + \Omega_2^2 + 2\Gamma^2}{\left(\Omega_2^2 - \Omega_1^2\right)^2 + 2\Gamma^2\left(\Omega_2^2 + \Omega_1^2\right)}\right) \\
\sigma^2_{\delta r,ss} &= \frac{k_B T}{M_{\text{eff}}\Omega_2^2} \\
\sigma^2_{\delta r,cs} &= \frac{k_B T}{M_{\text{eff}}\Omega_2^2}\frac{-g_{21}\left(\Omega_2^2 - \Omega_1^2 - 2\Gamma^2\right)}{\left(\Omega_2^2 - \Omega_1^2\right)^2 + 2\Gamma^2\left(\Omega_2^2 + \Omega_1^2\right)}
\end{aligned} \tag{4.71}$$

and those of (4.70) as

$$\begin{aligned}
\sigma^2_{\delta v,cc} &= \frac{k_B T}{M_{\text{eff}}}\left(1 + \frac{2g_{21}^2}{\left(\Omega_2^2 - \Omega_1^2\right)^2 + 2\Gamma^2\left(\Omega_2^2 + \Omega_1^2\right)}\right) \\
\sigma^2_{\delta v,ss} &= \frac{k_B T}{M_{\text{eff}}} \\
\sigma^2_{\delta v,cs} &= \frac{k_B T}{M_{\text{eff}}}\frac{-g_{21}\left(\Omega_2^2 - \Omega_1^2\right)}{\left(\Omega_2^2 - \Omega_1^2\right)^2 + 2\Gamma^2\left(\Omega_2^2 + \Omega_1^2\right)}.
\end{aligned} \tag{4.72}$$

When one varies the measurement angle, one can determine the extrema of $\sigma^2_{\delta r_\mu}$, as well as the extremum angle μ_{extr} which is given by:

$$\tan 2\mu_r^{\text{extr}} = \frac{2\sigma^2_{cs}}{\sigma^2_{cc} - \sigma^2_{ss}} \tag{4.73}$$

Notably, the noise in direction of the second eigenmode, here corresponding to the sine coefficient, is not squeezed in the case of a pure transverse feedback of the g_{21} type, since the force is oriented along the first mode and has no impact on the nanowire dynamics projected along $\mathbf{e}_2$ despite the alteration of the eigenvector. Since the rotation of the second eigenmode depends on how g_{21} compares to the splitting of the modes' frequencies squared, we use the dimensionless rotation parameter ξ (introduced in Equation 4.64), which we also call the *circulation strength*:

$$\xi \equiv \frac{g_{21}}{\Omega_2^2 - \Omega_1^2} \tag{4.74}$$

and the dimensionless dissipation coefficient γ:

$$\gamma = \frac{2\Gamma^2\left(\Omega_2^2 + \Omega_1^2\right)}{\left(\Omega_2^2 - \Omega_1^2\right)^2}. \tag{4.75}$$

This permits to express the extreme speed variances in a rather simple expression:

$$\begin{aligned}\sigma^2_{\delta v,\min} &= \frac{k_B T}{M_{\text{eff}}}\left(1 + \frac{\xi^2 - \xi\sqrt{1+\xi^2}}{1+\gamma}\right)\\ \sigma^2_{\delta v,\max} &= \frac{k_B T}{M_{\text{eff}}}\left(1 - \frac{\xi^2 - \xi\sqrt{1+\xi^2}}{1+\gamma}\right).\end{aligned} \tag{4.76}$$

If the force field coefficient g_{21} is much larger than the splitting of the squared frequencies, thus $\xi \to \infty$ the minimum speed variance approaches the limit

$$\lim_{\xi\to\infty} \sigma^2_{\delta v,\min} = \frac{k_B T}{M_{\text{eff}}}\frac{1+2\gamma}{2+2\gamma}, \tag{4.77}$$

while the maximum variance continuously increases with ξ^2. The optimum squeezing of a factor of 1/2 or 3dB can be obtained for an oscillator with spectrally well resolved mechanical peaks in absence of a force field.

Position and speed noise squeezing in the motion plane The orientation dependent variance $\sigma^2_{r_\mu}$ is directly obtained from the recorded trajectory $\delta\mathbf{r} = (\delta r_x, \delta r_z)$, sampled over N points, via:

$$\sigma^2_{\delta r_\mu} = \frac{1}{N}\sum_{k=1}^{N} |\delta r_{\mu,k} - \overline{\delta r}_\mu|^2, \tag{4.78}$$
$$\text{with } \delta r_{\mu,k} = \delta r_{x,k}\cos\mu + \delta r_{z,k}\sin\mu.$$

where $\overline{\delta r}_\mu$ is the ensemble average of the projected points $\delta r_{\mu,k}$, and k being the sampled points ($\overline{\delta r}_\mu$ should ideally always remain very small since we use a spectrally filtered readout, which, however, can suffer from residual offsets in the measurement). Using similar expressions, one obtains the variance for the projected velocity distribution. The projected displacement variances computed from the recorded trajectories are shown as continuous lines in Figure 4.20a and the projected velocity variances are shown in Figure 4.20b. The blue curves represents the variances of the Brownian trajectory without feedback, while the orange curves are the ones obtained in presence of active feedback.

The curves for no feedback are, in both cases, not perfectly circular which can be caused by two effects. Firstly, the readout laser's optical force creates a background force field that can couple the eigenmodes by its off-diagonal terms. Secondly, the sensitivity of the two readout channels differs by a factor of about ten which translate into an asymmetric numerical amplification of the readout noise creating a small asymmetry in the measured displacement variances. We attempt to reduce this latter effect by applying a 160 Hz wide filter in the Fourier space of the trajectory before we calculate the variance (see Section 4.2.4.2).

The dashed lines present the variance as calculated from the theoretical expressions given above, when using the g_{ij} parameters extracted from the perturbed mechanical properties of the nanowire. Their deviation from the variance calculated directly from data is likely caused by the asymmetric readout noise as well. In case of active feedback (green curve), the variance is reduced below the orange equilibrium curve by about one third along a specific direction which is the force feedback dependent angle of maximal squeezing. Along the perpendicular axis, the variance is increased to about three times the equilibrium value. The velocity's variances are squeezed (anti-squeezed) by about the same amount in the same directions. This squeezing in the position and velocity planes is one of the main differences to other mechanical noise squeezing experiments where the noise is squeezed in quadrature space [91, 101].

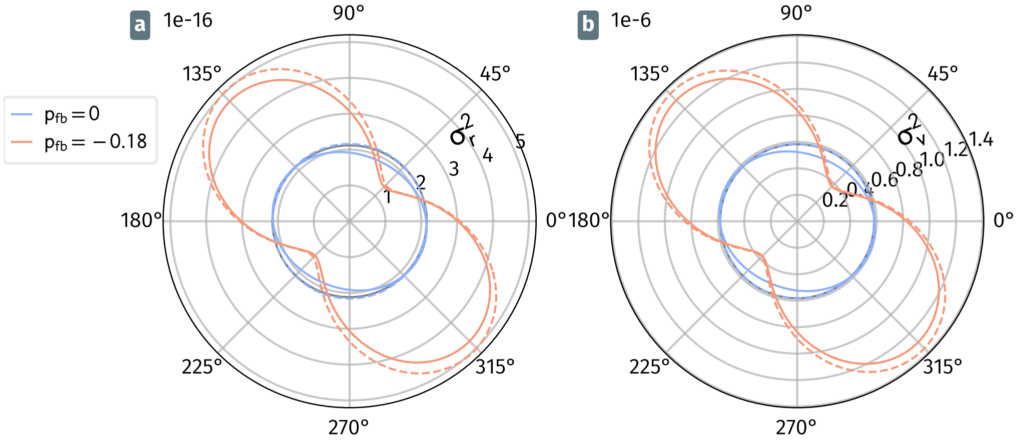

Fig. 4.20: Variance measured and theoretically predicted as a function of the measurement direction, in the position (**a**) and speed spaces (**b**), with and without feedbback (greens, reds). The directions of maximum squeezing are the same in both cases.

Maximum noise reduction Figure 4.21 summarizes the squeezing and anti-squeezing strengths achieved with the transverse feedback method for the same measurement set as presented above. The continuous lines again correspond to the variance obtained directly from the recorded displacement while the dashed line is the variance calculated using the fit results, which serve to determine the g_{ij} parameters. The data points correspond to the angle of minimal variance for both methods. Graph 4.21a shows good agreement between the two approaches. We first note that the symmetry of the variance changes as a function of the feedback gain. The squeezing efficiency does not depend on the sign of the shearing force term f_{21}. The maximum variance is increasing with a power law dependence while the minimum approaches a limit of about three quarters of the initial variance. The gap between minimum and maximum variance at $p = 0$ originate from the asymmetry of the recorded trajectory discussed above. The angle of minimal variance jumps by 90° when changing from negative to positive proportional. The velocity's variance in subplot 4.21b exhibits the same properties as the positional variance.

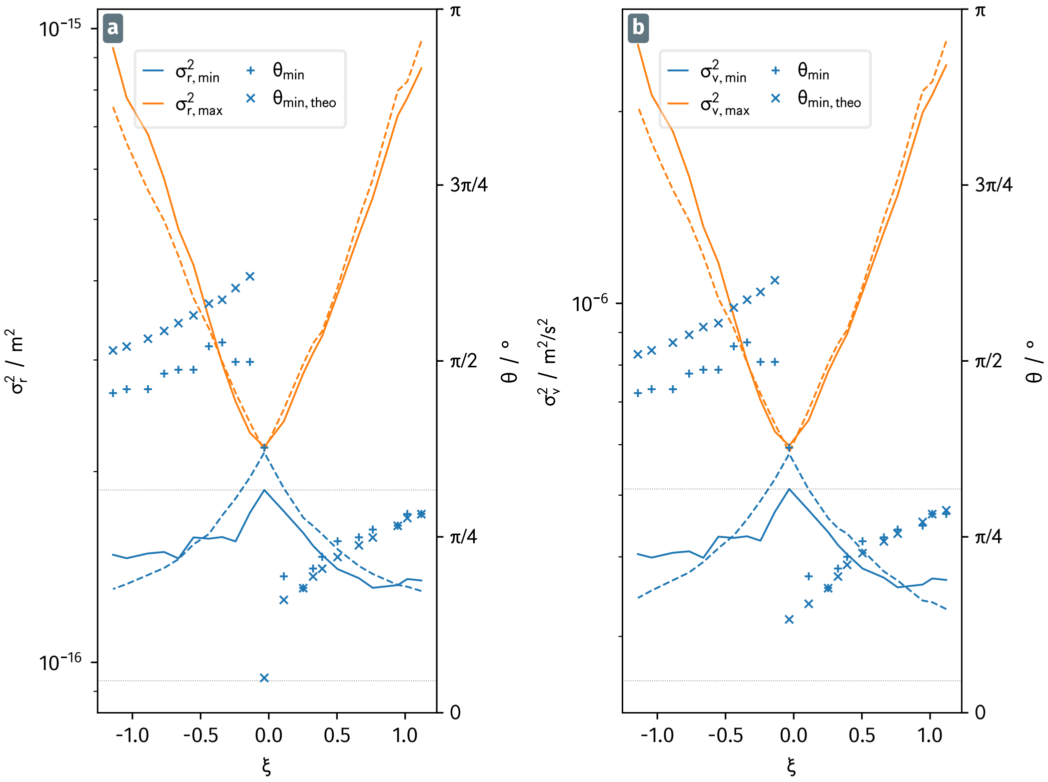

Fig. 4.21: The line plots show the minimum (blue) and maximum (orange) squeezing for position (**a**) and speed (**b**). The dashed lines are obtained from the variance calculation via the spectral noise integration while the continuous lines represents the variance calculated directly from the spatial trajectories. The crosses trace the angles of minimum variance (maximum variance at ±90° of this angle) calculated from data (+) and theory (*x*). The grey lines highlight mark the variances of zero squeezing and maximal achievable squeezing values.

The maximal achieved squeezing is relatively far from the theoretically possible squeezing of 3 dB (Equation 4.77) for a resonator with high Q factor and small mode splitting, which is indicated by the dashed lines in Figure 4.21. A measurement that comes closer to this limit is that of series B (see Figure 4.15) with a Q factor about three to four times larger. Figure 4.22 presents the results of this measurement. The squeezing of the positional variance shown in 4.22a is close to the limit which even seems to be surpassed by the variance obtained directly from the noise trajectory. In this interpretation one must be careful, since the higher Q factor also requires a larger acquisition time in order to record multiple realizations of the oscillation trajectory. Here, this is not guaranteed with the measurement time of one minute. The variance obtained from the fitted g_{ij} (dashed lines) presents a more realistic estimate. The achieved damping is still smaller than the 3 dB, but approaches this limit for small ξ.

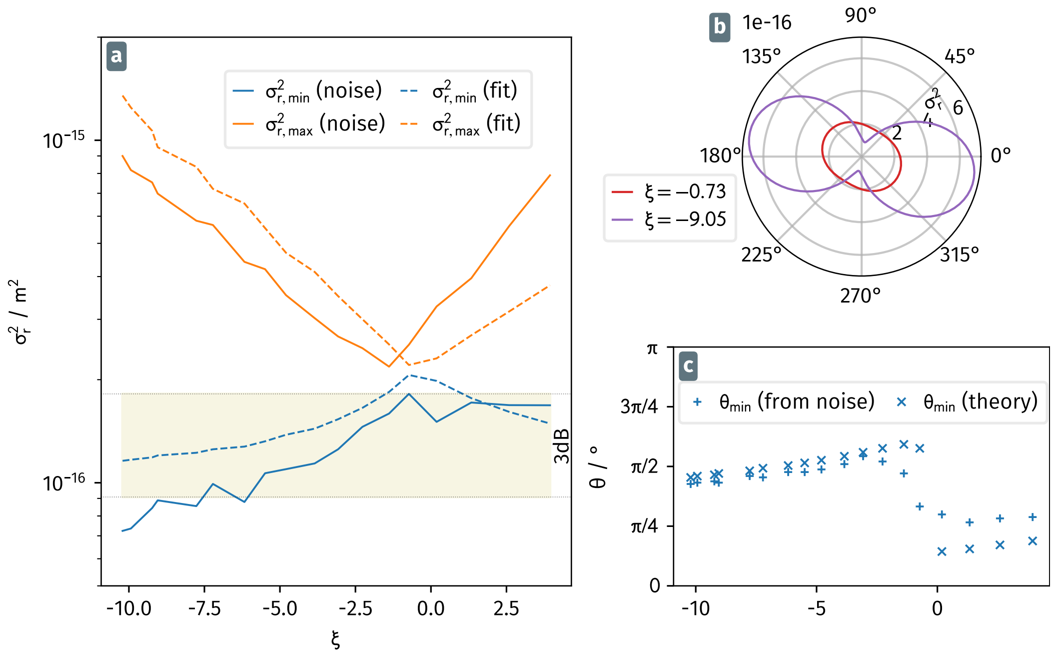

Fig. 4.22: The experiment realized with a higher Q resonance (*series B*) and a larger gain generates a larger squeezing efficiency. Using the same conventions as Figure 4.21, panel (**a**) shows for both, the variance of the recorded noise trajectory and the variance calculated based on the fit to the noise spectrum. The agreement between both is reduced compared to the low *Q* case, probably due to too short sampling of the mechanical motion with respect to the timeconstant $1/\Gamma_\mathrm{m} = 0.2\,\mathrm{s}$ during the acquisition time of one minute. This is also the reason why the variance of the noise trajectory surpasses the *3dB* theoretical limit (shaded area). The polar plot in (**b**) presents the positional variance in dependence of the measurement angle of the cases with smallest rotational parameter and at a feedback with strong squeezing, which has a visibly smaller variance $\sigma_{r,\mathrm{min}}$. The change of the angle of minimum squeezing is depicted in (**c**).

The polar representation of the variance obtained from the noise trajectory in 4.22b shows a small rotation of the angle of minimal variance and a clear reduction of σ_r below the value of $\xi \rightarrow 0$ ($|\xi|_{\mathrm{min}} = 0.73$). Similar to the low Q series in 4.21, the angles of minimal squeezing obtained from noise trajectory and via the theory and the fitted g_{ij}'s are in good agreement with each other but match better for a negative sign of the applied feedback gain.

Orthoradial velocity The squeezing of the nanowire's Brownian noise in 2D positional and velocity space is caused by a nonzero orthoradial acceleration of the nanowire. As a consequence, this modifies the distribution of the orthoradial speed, as opposed to the case of a conservative force field. One can illustrate this effect by plotting the trajectory-averaged angular velocity $v_\theta(\mathbf{r})$ at each spatial point as in Figure 4.23. At zero feedback, in each position, one records as many positively and negatively circulating trajectories so that the locally averaged orthoradial speed is almost zero. This can be seen almost everywhere in the 2D plot, except at the most distant positions, but there

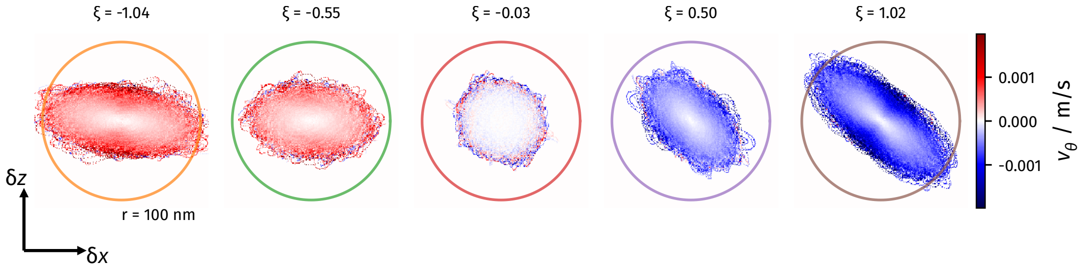

Fig. 4.23: The transverse feedback causes an acceleration with a preferential directionality depending on the sign of the gain. The plots present the mean value of the orthoradial velocity $v_\theta(x, z)$ at each position of the recorded trajectory with clockwise rotation (positive, red) for negative ξ and counter-clockwise rotations (negative, blue) for positive values. When no feedback is present (central plot), there are an equal number of clockwise and counter-clockwise rotating trajectories and the mean v_θ is zero.

one lacks of statistics since it represents rare cases. With applied feedback, the locally averaged v_θ gets a clear preferential direction that depends on the sign of the applied feedback. In all cases the nanowire has a larger orthoradial velocity at larger distances $|\delta\mathbf{r}|$ to the center and for larger ξ, one observes two zones of particular large velocity values in the direction of maximum squeezing (the smallest width of the noise distribution).

Panel 4.a: Fokker Planck

The probability density of stochastical Brownian process in phase space ($\mathbf{x} = (r_x, v_x, r_z, v_z)$ is determined by the Fokker-Planck equation [113]:

$$-B_{ik}\,\partial_{x_i}\Big(x_k\, p_{st}(\mathbf{x},t)\Big) + \frac{D_{ij}}{2}\,\partial^2_{x_i x_j} p_{st}(\mathbf{x},t) = 0. \tag{4.79}$$

with the following definitions:

$$\mathbf{B} = \begin{pmatrix} 0 & 0 & 1 & 0 \\ 0 & 0 & 0 & 1 \\ -\Omega^2_{1||} & g_{21} & -\Gamma & 0 \\ g_{12} & -\Omega^2_{2||} & 0 & -\Gamma \end{pmatrix} \quad \text{et} \quad \mathbf{D} = \frac{2\Gamma k_B T}{M}\begin{pmatrix} 0 & 0 & 0 & 0 \\ 0 & 0 & 0 & 0 \\ 0 & 0 & 1 & 0 \\ 0 & 0 & 0 & 1 \end{pmatrix}. \tag{4.80}$$

It has a solution $p_{st}(\mathbf{x})$ of Gaussian shape [113]:

$$p_{st}(\mathbf{x}) = \frac{1}{N} exp\Big[-\sum_{i,j} A_{ij}\, x_i\, x_j\Big], \quad \mathbf{A} \equiv \frac{1}{2}\begin{pmatrix} 2a_{r_1r_1} & a_{r_1r_2} & a_{r_1v_1} & a_{r_1v_2} \\ a_{r_1r_2} & 2a_{r_2r_2} & a_{r_2v_1} & a_{r_2v_2} \\ a_{r_1v_1} & a_{r_2v_1} & 2a_{v_1v_1} & a_{v_1v_2} \\ a_{r_1v_2} & a_{r_2v_2} & a_{v_1v_2} & 2a_{v_2v_2} \end{pmatrix}, \tag{4.81}$$

with the normalization coefficient N^{-1} obtained from integration over the entire phase space:

$$N = \int_{\mathbb{R}^4} \mathrm{d}^4\mathbf{x}\, \exp\Big[-\sum_{i,j} A_{ij}\, x_i\, x_j\Big]. \tag{4.82}$$

The coefficients of the matrix solution $\mathbf{A}$ of this equation for the 2D nanowire oscillator are given in Appendix D.

In order to find the probability density in the space (r, v_θ) as shown in Figure 4.24, we apply the substitution from cartesian coordinates to polar coordinates:

$$r_x = r\cos\theta, \quad z = r\sin\theta, \quad v_x = v_r\cos\theta - v_\theta\sin\theta, \quad v_z = v_r\sin\theta + v_\theta\cos\theta. \tag{4.83}$$

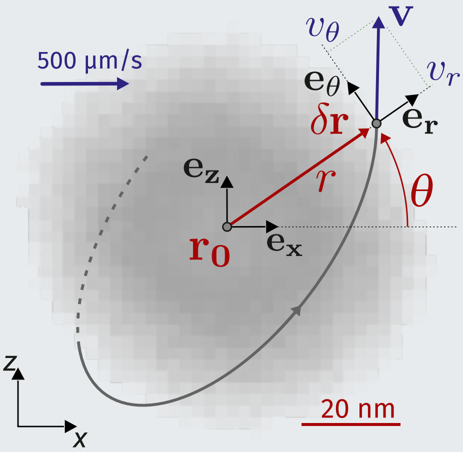

Fig. 4.24: The convention for the transformation fromcartesian laboratory coordinates to a polar coordinate system in which the probability density $P(r, v_\theta)$ is calculated from the Fokker-Planck equation.

In order to obtain the probability density in the space (r, v_θ), one needs to integrate the resulting expression over θ and v_r. The integration over v_r can be done analytically and yields an expression that contains first order Bessel functions. The integration over θ then needs to be done numerically. We therefore perform a combined numerical integration over both variables. The results discussed in this section are obtained from such a numeric integration of the Fokker-Planck equation in the polar phase space.

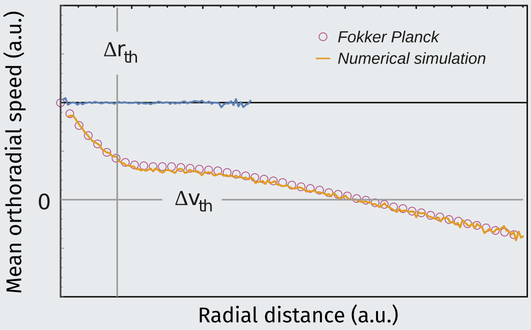

Fig. 4.25: Comparison of Fokker Planck predictions to numerical simulations for a theoretical nanowire. The dependence of the mean orthoradial speed $\overline{v}_\theta(r)$ with the radial distance is calculated after numerical integration of the analytic solution of the Fokker Planck equation (circles), and from the fits of the (v_θ, r) histograms such as the one shown in Figure 4.26.

Then, we also realized numerical simulations of the nanowire trajectories using a dual random Langevin force vector and a *Runge Kutta 4* propagation algorithm. In both cases, the undressed mechanical properties of the nanowire are obtained from experimental parameters (frequencies, damping rate, mass, eigenmode orientation), while the force field parameters are deduced from the dressed mechanical properties. Both numerical methods give results in very good agreement, and furthermore they perfectly reproduce the experimental results obtained. Figure 4.25 represents a typical result of the simulations. The good agreement between both methods allows to validate the numerical simulations, which are less time-consuming.

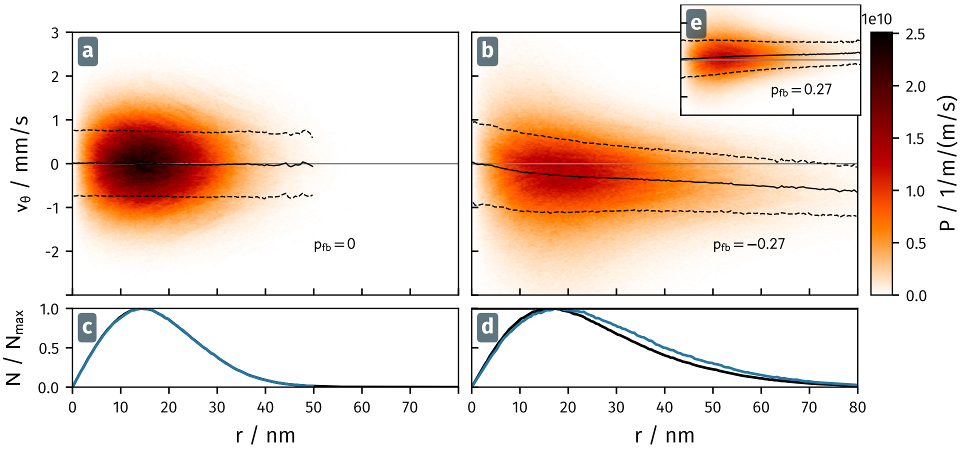

Fig. 4.26: The distribution $P(r, v_\theta)$ of the orthoradial velocity vs the radius without (left) and with (right) a circulating force field. The solid black line represents $\overline{v}_\theta(r)$, the mean orthoradial speed at a distance r ,while the dashed lines indicate the width of the distribution. The lower plots represent $P(r, \overline{v}_\theta(r))$. The inset (**e**) shows the case of a feeback as strong as in (**b,d**) but with opposite sign.

One can prolongate this analysis of the orthoradial speed by inspecting its dependence with the radial distance r towards the center of the distribution. To do so, one can first represents all the recorded data points in the (v_θ, r) space, see Figure 4.26, where the density of probability $P(r, v_\theta)$ is shown. The distribution is symmetric in v_θ in absence of a circulating force field, while it becomes biased when the feedback is activated. The black lines represent the mean orthoradial speed $\overline{v}_\theta(r)$ as well as the distribution width, for each radial distance. The maximum of the distribution $P(r, \overline{v}_\theta(r))$ is plotted in the lower panels. One notices that the mean orthoradial speed increases monotonously with r, while following a non-standard evolution, which is linear at short distances, and is followed by a sort of plateau at larger distances.

As described in box 4.a, we also performed numerical simulations of the noise distribution at the presence of a force field that corresponds to the experimental case. The results shown in Figure 4.27 show very good agreement with the measurements in Figure 4.26.

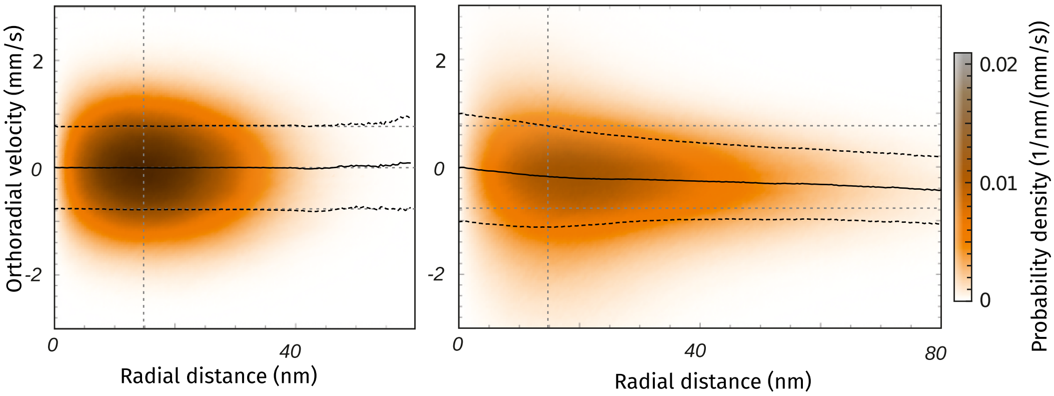

Fig. 4.27: Results from numerical simulations of the distribution of the orthoradial velocity v_θ with respect ot the radial distance r, without (left) and with an pure g_{21} shear force field. The gray dashed lines represent the *rms* spreading in the position and velocity spaces: $\sqrt{k_B T / M \Omega_m^2}$ and $\pm\sqrt{k_B T / M}$. The black lines mark the center value of $\overline{v}_\theta(r)$ (solid line) and the width of the distribution (dashed line). The numerical simulations are recorded during 10 s with a time step of 3 μs, for an oscillator with eigenfrequencies $\Omega_{1,2}/2\pi = 8277\,\mathrm{Hz}, 8337\,\mathrm{Hz}$ and a damping rate of $\Gamma = 123\,\mathrm{Hz}$, and $g_{21} = -5 \times 10^8 \mathrm{rad}^2$.

We can then reproduce a similar analysis for all feedback gains employed and plot the integrated probability density as function of the radius (Figure 4.28). The dependence of the mean orthoradial speed profiles $\overline{v}_\theta(r)$ are shown in Figure 4.29. We observe that the circulating force field is responsible for a bias of the orthoradial speed, which increases with the distance towards the center of the distribution. Similar effects are observed with rotational force fields produced by a focused laser beam, but they are absent when using conservative force fields.

As a concluding remark of this section, one can draw a connection to the orthoradial speed anomaly found in galaxies when investigating the dependence of the orthoradial

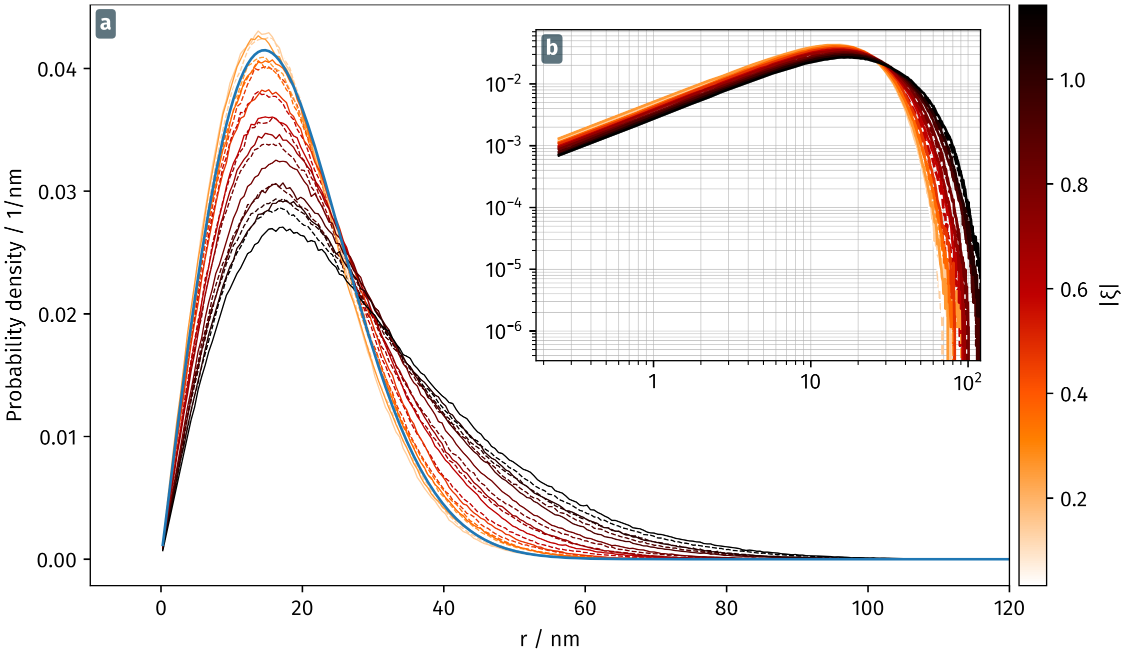

Fig. 4.28: The radial probability density $P(r)$ obtained from the distribution in Figure 4.26 after integration along the $v_\theta$axis. Inset 4.28b shows the density function on a logarithmic scale. The colorcode corresponds to the absolute value of the force rotation parameter ξ (4.64) .

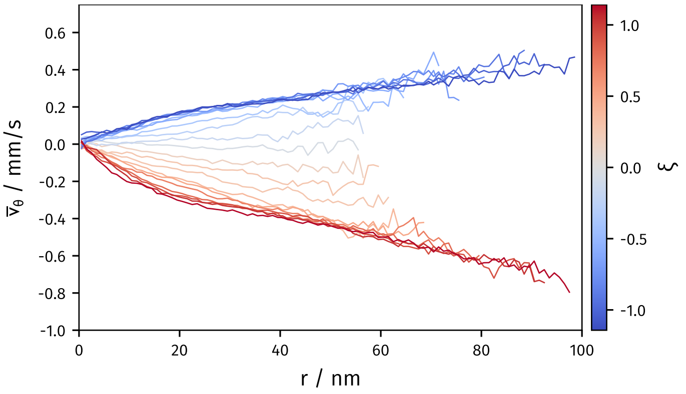

Fig. 4.29: The mean orthoradial velocity $\bar{v}_\theta$ obtained from gaussian fits to the histogram slices as in 4.26 for all measurements. The colorscale encodes the force rotational parameter whose amplitude is larger for stronger feedback.

speed with respect to the distance towards the galactic center. When pointing a telescope towards a certain position in a galaxy, one can infer via doppler spectroscopy on the 21 cm^{-1} hydrogen line, the local speed distribution and report the maximum orthoradial velocity as a function of the distance. One would expect to measure a reduction of the orthoradial velocity at large distances, but instead the measurements show that it converges towards a non-zero value at large distances. To ensure a stable trajectory, one would need to increase the radial acceleration experienced by the most distant stars, but the measurements show that the visible mass cannot explain the observed increase of the orthoradial speed. Those observations on the orthoradial speed anomaly are also called *missing mass curves* and are at the origin of the dark matter hypothesis. Our observations show that an orthoradial acceleration are also responsible for an increase of the mean orthoradial speed with the distance towards the distribution center. The question that naturally arises is whether such a mechanism could be present on a galactic scale (such as a rotational flow in an “extragalatic wind”...). There are obviously many open questions here.

4.3.4 Delayed transverse feedback

We now finish the description of artificial force fields, by describing the situation of a transverse delayed force field, which adds non-diagonal terms in the damping matrix. We use the artificial feedback scheme to generate a damping term along $\mathbf{e}_1$, proportional to the speed measured along $\mathbf{e}_2$ so that we add a dissipation force: $\delta\mathbf{F} = h\delta v_2\mathbf{e}_1$.

Again, for the adjustment of the force delay, we use the filter settings of the FPGA module as described in Section 4.3.2. From the configuration of the delayed uniaxial feedback, we get to the delayed transverse configuration by rotating the readout vector by 90°. In the ideal case, this feedback corresponds to a pure h_{21} term in the susceptibility matrix. Supposing a purely delayed feedback, we replace $g_{21} \rightarrow -ih_{21}\Omega$ in the dressed susceptibility matrix and calculate its eigenvector with Equation 1.42. They now depend on the frequency, and $\mathbf{e}_+$ ($\mathbf{e}_-$ remains unchanged with a pure feedback in the 21-term) is given by:

$$\mathbf{e}_+ = \frac{1}{\sqrt{-ih_{21}^2\Omega^2 + \left(\Omega_+^2 - \Omega_{\parallel 1}^{\ 2}\right)^2}} \begin{pmatrix} ih_{21}\Omega \\ \Omega_+^2 - \Omega_{\parallel 1}^{\ 2} \end{pmatrix}, \tag{4.84}$$

which is now a complex vector in $\mathbb{C}^2$, representing a rotating eigenvector. It looses its linear character when $h_{21}\Omega \gg \Omega_+^2 - \Omega_1^2 + g_{11} \approx \Omega_2^2 - \Omega_1^2$. With the current nanowire ($\Omega_{1,2}/2\pi = 8270\,\mathrm{Hz}, 8340\,\mathrm{Hz}$), a value $h_{21} > 830\,\mathrm{Hz}$ is required to achieve a regime where the eigenmode acquires an elliptical character.

The measurement is then conducted analogously to other cases, starting with small feedback gains and successively increasing the gain towards negative and positive values. The limits of the feedback intensity is given by the appearance of an instability or auto-oscillation of the nanowire. We again record the temporal trajectories of the nanowire’s Brownian motion in 2D and perform a spectral analysis. Figure 4.30a presents the spectro-angular tomography for some positive gain values. The constant frequency splitting shows the proper alignment of feedback force and readout vectors. With increasing feedback gain, the second mode becomes a ring in the spectro-angular tomographic representation and while there are angles where it is not detectable at zero gain, traducing its linear character, it is now measurable for any measurement angle for gains larger than 0.3.

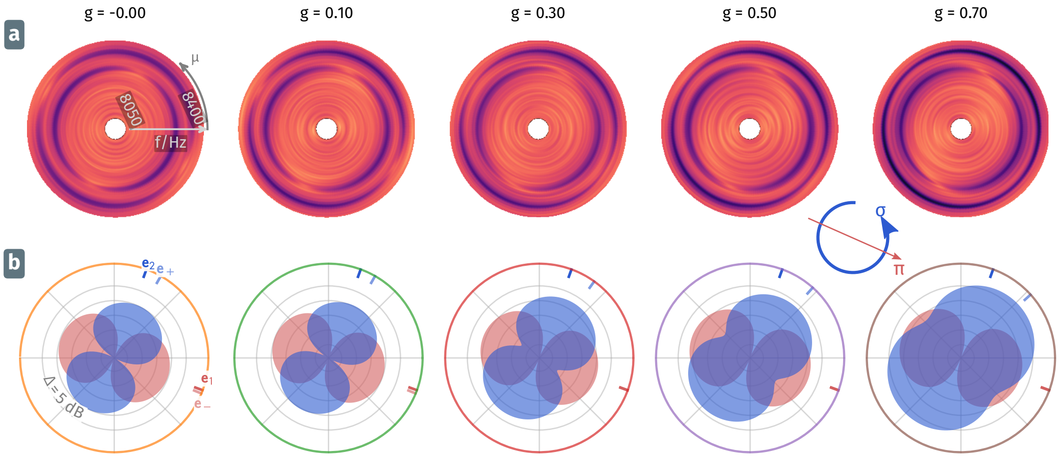

Fig. 4.30: The spectro-angular tomography of a perpendicular delayed feedback with positive gains (**a**) shows the transition of the second mode from a purely linear eigenvector to a quasi-circular structure which leads to a circular pattern in the tomographic plot for larger gains. The angular plots of the resonances' amplitudes in (**b**) shows the same trend. While the second mode (blue) has initially clear preferential orientations, the signal strength grows in the perpendicular direction for larger gains. One also observes a slight rotation of the mode similar to the case of direct perpendicular feedback, which is caused by an imperfect calibration of the feedback delay.

An angular analysis of the modes' amplitudes is given in 4.30b. Here, one observes that the second mode loses its linear character as can be seen in the strongly reduced angular contrast and preserves a significant amplitude along the angle perpendicular to its initial orientation.

In Figure 4.30b, one can also observe a small rotation of the second mode, caused by a nonzero instantaneous component g_{21} of the feedback, as well as an increase of both modes amplitudes, which is more pronounced for the second mode. The fit of the feedback force gradients g_{ij}, h_{ij} in Figure 4.31 confirms this assumption. However, the amplitude of g_{21} is not large enough to rotate the second mode significantly so that the dominating effect is caused by the delayed component that reaches about half the magnitude required for the second mode to become purely circular.

This situation illustrates one of the signatures that can be obtained using a delayed artificial force field, which adds non-diagonal terms to the damping matrix. In such a situation, the damping matrix and the restoring force matrix cannot be diagonalized in the same basis, meaning that we expect the system to break the normal mode expansion. Furthermore, we also expect the system to deviate from the fluctuation-dissipation relation, as observed in the instantaneous rotational force field, meaning that one cannot define a temperature for each mode.

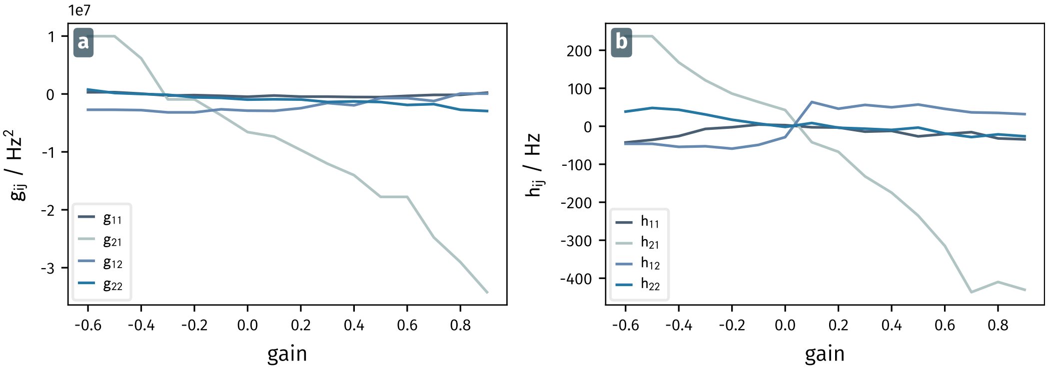

Fig. 4.31: The g_{ij}'s fitted with the full complex model of the susceptibility are drawn in (**a**). The linearly increasing amplitude of g_{21} is caused by an imperfect setting of the FPGA filters that are used to regulate the delay of the feedback. While its change is measurable, its value remains about two times smaller than the splitting of the squared frequencies $\Omega_+^2 - \Omega_1^2$, so that the rotation of the second mode does not surpass 30°. Subfigure (**b**) presents the delayed feedback components. Here, the only significantly varying term is again the h-component that decreases roughly linear with an increasing gain.

5 Conclusions and perspectives

✦

Rapid force microscopy

When this project started, the first successful experiments of nanowire force microscopy had already been realized in our group but they relied on spectro-angular analysis of the nanowire's thermal noise which was time consuming to execute and analyse. The first step in this project was therefore the integration of a dual channel lock-in measurement with eigenmode tracking done by two independent PLLs using the ZI-HF2LI. The integration of this measurement into the control software and standard measurement protocols reduced the time necessary to acquire a full map of the force field from days to several hours. It also provided critical information at rapid pace such as the resonators mode properties, from which the force field gradients can be determined, in quasi-realtime (10 measurements per second), allowing direct imaging of the 2D force field experienced by the nanowire, a feature that is crucial when it approaches a surface with rapidly varying force field gradients, or when determining orientation and alignment of the measurement window on the sample.

The second technical improvement of the experiment was the development of a custom FPGA module based on a low cost hardware, for the continuous lock-in measurement of the readout vectors. The adapted FPGA code and server module can perspectively be used to perform measurements at more than two frequencies simultaneously. The methods and programs developed for this part of the thesis are now used standardly in our experiments, which comprise beside room-temperature force field microscopy also cryogenic nanomechanics [37] and cavity opto-mechanics [36].

Thanks to the fast measurement protocols we could realize force field microscopy measurements at much smaller sample separations than before, without fearing to touch the surface due to the realtime readout of the force field structure, and perform a complete map while sweeping the bias voltage that is applied between the sample and nanowire. This permits the differentiation of the quadratic, linear and residual force field contributions. While the quadratic force is caused by the sample's topology only, the linear and

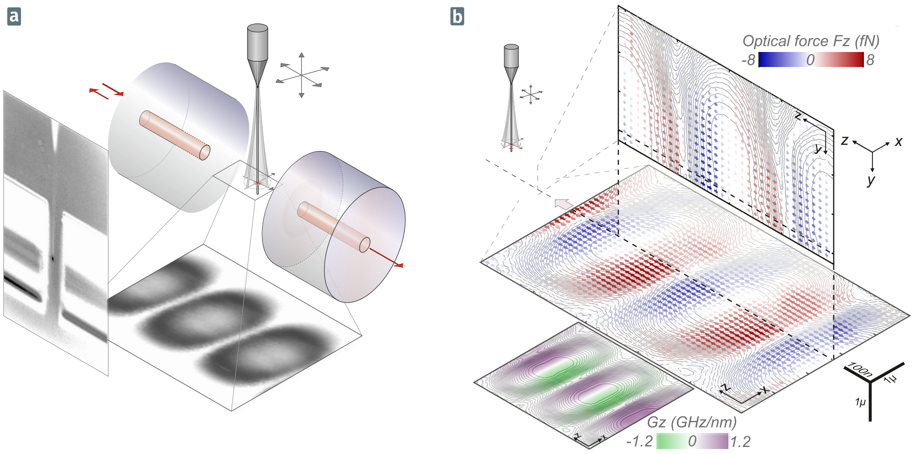

Fig. 5.1: The cavity nano-optomechanical experiment: The insertion of the nanowire in a high finesse microcavity allowed to measure and map the opto-mechanical coupling strength by scanning the nanowire in the cavity mode. Some of the protocols developed in this manuscript were implemented during the PhD of Francesco Foligano [35] to map the opto-mechanical force field experienced by the nanowire (right). The extreme coupling strength achieved allowed to measure the optomechanical force exerted by an intracavity field populated by less than a single mean photon.

residual terms contain constant surface fields that can for example be caused by electrostatic patches. Using an interpretation based on the Maxwell stress tensor formalism, we could acquire a more quantitative description of the forces acting on the nanowire's apex and their dependence on the electric field structure.

We experimentally investigated the effects from the surface fields in this model and extracted in particular the local offset potential V_0 similar to the one obtained in KPFM measurements. In maps of the force field divergence and V_0, one can observe the presence of large scale surface contaminations and surface patches scaling around 100 nm, which both contribute to the measured linear and residual force field gradients. This shows that the surface fields play an important role when working with mechanical systems at a separation of a few hundreds of nanometers, and that a good knowledge of the surface fields is needed when realizing the measurement of proximity forces with nanometric resolution. With its high sensitivity and its intrinsic 2D susceptibility, the nanowire represents a very sensitive probe for the investigation of the electrostatic properties of nanofabricated samples.

A combined measurement of electrostatic force and electrostatic force gradient experimentally validated the protocols developed for of the force gradient measurements. It relies on the direct modulation of the electrostatic force which cannot be used to lock the PLLs, as the resonant response to the force depends on its orientation with respect to the nanowire's eigenmodes and thus rapidly varies with the position of the nanowire above the sample of interest. The alternation between an optical driving force and the electrostatic modulation provides access to both the force field gradients and the force vector respectively by only increasing the measurement time by a factor of two. This type of measurement presents a novel method which has not been possible to implement before due to the large number of points that need to be sampled, requiring good stability even using the fast measurement protocols.

Perspectives The methods developed for the electrostatic force measurements can be employed equally well in other experiments such as in force microscopy with functionalized nanowires to image magnetic force fields or currents, or in cryogenic conditions [37]. The measurement protocols employed here can directly be transposed to ultralow temperature measurements, where the nanowire force sensitivity has been shown to improve by four orders of magnitude, down to $40\,\mathrm{zN}/\sqrt{\mathrm{Hz}}$, with a theoretical sensitivity to force field gradients at the level of a few $\mathrm{fN\,m^{-1}}$ in ten seconds.

In this and previous works [29, 43] we have shown that two dimensional force field microscopy is possible using the two degenerated eigenmodes of a vibrating nanowire. The extreme linearity of the system permits a resonant measurement at multiple frequencies simultaneously, as it is done in the combined force and gradient measurement for example. We have already tested measurements where we do not track the modes of the nanowire but measure the response at several frequencies [36]. The advantage is that the measurement is not affected by the eigenmode rotations induced by the force field under investigation or by sign changes of the projected force and that one would gain direct access to the modulated force vector as in the combined measurement. To do so, we estimated that a simultaneous detection of about 20 frequencies should be sufficient for most force field measurements. Such measurements could be realized building onto the FPGA module developed in this work.
While the simultaneous measurement at the fundamental and at higher order modes is widely applied in atomic force microscopy, we have not yet exploited this possibility. Also, the measurement of non-linear interactions between the sample and nanowire via the detection at higher harmonics can be an option for future experiments.

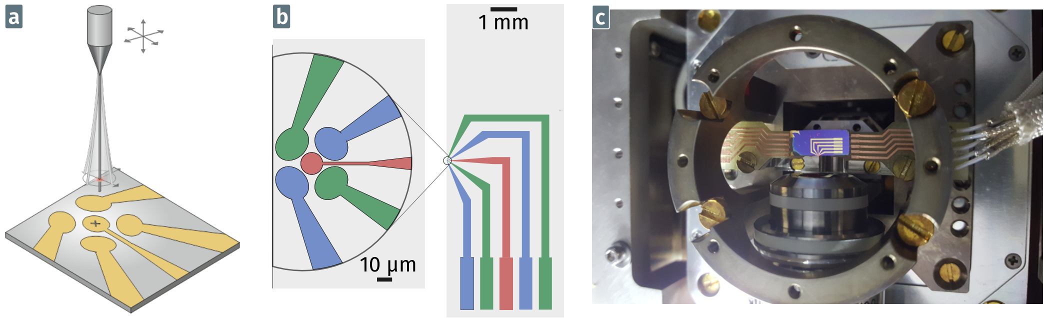

Fig. 5.2: Adding four additional control electrodes around the sample, one can control the field at the nanowire apex in 3D (**a**). The electron pairs are created by lithography on a Si chip using the geometry shown in (**b**). The round sample area can then be nano-structured or a sample can be positioned there. In (**c**), the installed sample in the microscope setup can be seen.

A next step for nanowire force field microscopy, that is already being tested experimentally, is to control the electromagnetic field at the nanowire apex along all three axes which requires additional degrees of freedom. To do so, two additional perpendicular pairs of electrodes were lithographied around the sample (with the help of *B. Fernandez*, *J.F. Motte* and *G. Julie*), as shown in Figure 5.2 that helps generate homogenous electrostatic control fields which will serve to compensate the local electric surface fields experienced by the nanowire. Controlling the electrostatic field along three directions permits a better understanding and characterization of the residual surface fields which is crucial for quantitative measurements of the Casimir force. In first tests of the electrodes we observed a dependence of the optically modulated force on the electrostatic field whose origins are not yet fully understood, but are believed to arise from a electron-hole pair creation within the nanowire, which are subsequently affected by the surrounding electric fields. The current investigation of this additional force, which is linear in the lateral electric field is likely to play a similar role as a residual electrostatic field which generates a force field linear in the bias voltage, will be another step forward in nanowire force microscopy. A mitigation of this effect would be to use a non-optical drive of the nanowire such as piezo-actuation or to turn towards metallic nanowires.

Casimir forces

The measured force does not only contain the contributions of the static electromagnetic fields but also the time-averaged contribution from fluctuating fields and in particular the vacuum fluctuations which are at the origin of the Casimir force. It is, like the quadratic contribution of the surface fields, voltage independent. We developed an approximate method to evaluate the mean offset potential V_0 that accounts for the average effect of the residual surface fields. From this evaluation, one can extract a residual force field that contains only the quadratic contributions from the residual electrostatic fields and the Casimir force. By putting this value in relation with the simulated Casimir force above nanostructures, we found that the obtained residual force is similar to the simulations in shape and amplitude. However, for a quantitative assessment of the Casimir contribution, we need to fully control the surface fields, for instance using the control electrode method described above.

Perspectives Exploring the proximity forces above nanostructures provides interesting perspectives in Casimir physics as one would for instance be able to measure the shape of the force field above chiral structures. Nanowire force microscopy can be a valuable tool since it allows to measure the Casimir interaction between single nanostructures, not relying on the measurement of ensembles of nanostructures, which is done in only few, if any, experiments. The small size of the probe also permits better characterizing the effect patches play in Casimir physics, as common experiments often use large surfaces compared to the average patch size, whereas the nanowire is of comparable size.

Experimentally speaking, the Casimir measurements will benefit from the compensation of the residual surface fields in 3D, taking a step towards quantitative results. Additionally, we saw in this work that the use of metallic nanowires can increase the Casimir contribution and the fact that the fields are concentrated between nanowire apex and sample can simplify the compensation of the surface fields.

Also, the electrostatic force above nanostructures can be large compared to the nanowire's stiffness, even though the separation is still larger than hundreds of nanometers, rendering force measurements impossible. The sample geometry for Casimir forces must therefore be selected carefully. Regarding the sample's material, one could probably test different annealing and surface treatments after the nano-structuration. This would ideally go along with a detailed study of the surface fields so that the nanowire based surface force microscopy is likely to bring useful information in such sample analyses.

Two-dimensional realtime force feedback

The last part of the thesis discussed the implementation of realtime active feedback schemes on the nanowires Brownian motion in 2D. We used the fast signal processing capacity of the customized FPGA module and adapted its functionality so that it measures the nanowire displacement along an arbitrary direction and creates a force feedback signal proportional to this displacement or to its time derivative. Here, we investigated the linear regime of the feedback scheme, but it can be changed to more complicated functions easily. In particular there exists some theoretical interest to generate a circulating force field with a non-linear radial dependence [6, 7] to investigate non-hamiltonian dynamics.
With the feedback being exerted via the electrostatic force of a single electrode, we create a uniaxial feedback which, in the case that feedback force and readout are parallel to one of the modes, causes a shift of that mode's frequency without affecting the second mode.

In the transverse case, where the force is perpendicular to the readout direction but aligned with one mode, one can vary the mode's orientation, which causes a 3 dB squeezing of the nanowire's noise in position and velocity spaces. An interesting perspective of this effect is that one can in principle apply a similar feedback scheme in ultracold systems to investigate how nanowires with a low phonon number react to further squeezing.

We also realized feedback schemes using a retarded force, by adding a temporal phase shift of 90° to the measured displacements. With such a delayed force it was possible to cold-damp the oscillator in the parallel configuration and to create a single elliptical eigenmode in the transverse case.

Perspectives Adding a second feedback force vector to the setup, the FPGA module would already allow to output two arbitrary feedback forces acting along different orientations. Then, by combining the instantaneous parallel and transverse feedback algorithms, one would have a tool to create a feedback force on the nanowire that could compensate any external local force field. Like this, it should be possible to correct for the rotation and the frequency shift caused by the external force – the nanowire would then operate at a stable point where its mechanical properties remain linear even under strong external forces. This would allow to perform measurements even closer to nanostructures where Casimir forces or surface forces are stronger. Such an approach would be essential to assert the true spatial resolution of those ultrasensitive force field sensors.

Beside presenting a potential improvement of the measurement, the reaction of the 2D oscillator to the feedback itself is an interesting research subject. Since the FPGA allows to create basically any shape of force field (at least when the desired force field is an analytic function of the nanowire's position), we could investigate the nanowire dynamics in more exotic force fields such as quadratic or double well potentials, or purely rotational but non-linear force fields (such as a vortex like patterns).

Furthermore, one should further investigate the ultimate limits of the studies realized in Chapter 4, especially when implemented on cold oscillators close to their fundamental ground state. If the existence of a squeezing in the position-speed space is preserved, its observability should be studied in greater detail, in particular if one attributes one interferometric per mechanical mode, conveying two independent readouts.

Global perspectives

Some of the above perspectives have already been pursued. We fabricated a chip that supports a sample area surrounded by four electrodes which create a homogeneous electrical field at the sample position (see Figure 5.2). By applying four control voltages one can create an arbitrary field in 2D. Adding an additional voltage bias to all control electrodes and to the sample area, the electrostatic field could be controlled in 3D. First tests have shown that this method works, and can potentially be used to perform a full electrostatic analysis of the force created by the sample field and by the residual surface fields.

During the tests we also observed that the homogeneous electrical field caused a rotation of the optical force via a combined electro-optical interaction, with causes not yet fully understood. To mitigate this effect for the measurements of Casimir forces and the effect of the surface fields, we could employ a piezoelectric drive that is not negatively affected by an interaction with the electric control field.

The current state of the nanowire force field microscope that is presented in this thesis can already be used to realize novel measurements. As such, the measurement of magnetic fields could be realized by employing functionalized nanowires with a magnetic apex.
Another functionalization with an NV center could be used to realize an experiment where the magnetic field is measured via the luminescence of the NV center [52] and the electric field is measured using the nanowire force probe. Such a nanowire can also be used to realize a mechanical readout of the NV spin state using the measurement protocols developed in this work.

Lastly, all methods and protocols presented in this thesis are also applicable under low temperatures, where the sensitivity of the nanowire is much higher than at room temperature, opening the road towards scanning force microscopy above ultracold samples. Among other applications, the possibility to isolate and manipulate single electrons in quantum electronics devices will provide an interesting perspective.

A The customized digital signal processing unit on a RedPitaya FPGA

The costumized Red Pitaya FPGA platform was introduced in Section 1.4.6, since the use as digital lock-in has been explained in detail, this appendix will just list the key components of the unit that have been realized. For the adapted feedback unit some additional information are added to what has been discussed in Chapter 4.

Due to an unclear situation regarding the licensing of the developed software and scripts at the point of the publishing of this thesis, we can not point the reader towards a public repository containing the full software with documentation at this moment.

A.1 Dual signal acquisition

For the 2 signal 2 frequency analysis we implemented:

A digital signal processing unit (DSP) with:

- 2 first order HP input filters
- 2 local oscillators
- 4 demodulators
- 2 second order LP filters
- data acquisition and transfer control
- downsampling

The server with:

- device control
- data management module
  - trigger processing
  - data compression (statistics)
  - buffering
- communication

Client tools:

- python module combining SCPI commands to set up demodulators in a single command
- integration of python module in high level UI for dynamic beta measurement

A.2 Adapted feedback

The realtime feedback/radar realization contains

A DSP with:

- 2 high pass input filters
- fast multiplication
- scaling

The server for:

- device control
- input signal correction
- rotation coefficient calculation

Client

- Direct communication via SCPI commands in Jupyter notebook

A.2.1 Objective

The digital signal processing of the FPGA is fast enough to process the measured voltage of the photodiode and to generate a feedback based on the processed signal at a rate much higher (125 MHz) than the frequency of the mechanical oscillation of a nanowire (10 kHz). Since the bare signals on the two linearly independent photodiode channels $\oplus$ and $\ominus$ are not aligned with the laboratory frame the DSP needs to apply the correct orientation matrix on the signal in order to apply a feedback based on the position of the nanowire in the lab coordinates . Based on the rotated signal a force could be applied either by using a lookup table or by applying a mathematic operation on the raw signal. A simple case of such an operation is the application of a feedback proportional to a signal read out along the vector $\mathbf{e}_{\mu_1}$ in the direction of a perpendicular vector $\mathbf{e}_{\mu_2}$. This case reflects a purely shearing force field.

A.2.2 Rotation

The two input signals are read out along two independent vectors $\boldsymbol{\beta}_{\ominus} = \|\beta_{\ominus}\|\mathbf{e}_{\ominus}$ rotated anticlockwise by an angle $\beta^{\angle}_{\ominus}$ from the x-axis and $\boldsymbol{\beta}_{\oplus} = \|\beta_{\oplus}\|\mathbf{e}_{\oplus}$ rotated anticlockwise by an angle $\beta^{\angle}_{\oplus}$. The values of $\boldsymbol{\beta}_{\ominus,\oplus}$ can be measured as described in Section 1.3.1.1. The measured projected signal on the channel is

$$\begin{aligned}\delta S_{\beta_{\ominus}} &= \delta\mathbf{r}\cdot\mathbf{e}_{\ominus}\\ &= \|\beta_{\ominus}\|\left(\cos\beta^{\angle}_{\ominus}\delta r_x + \sin\beta^{\angle}_{\ominus} r_z\right) \qquad \text{(A.1)}\end{aligned}$$

with $r_{\ominus} = \frac{\delta S_{\beta_{\ominus}}}{\|\beta_{\ominus}\|}$ and similar for channel $\oplus$ we have

$$\begin{pmatrix}\delta r_{\ominus}\\ \delta r_{\oplus}\end{pmatrix} = \begin{pmatrix}\cos\beta^{\angle}_{\ominus} & \sin\beta^{\angle}_{\ominus}\\ \cos\beta^{\angle}_{\oplus} & \sin\beta^{\angle}_{\oplus}\end{pmatrix}\begin{pmatrix}\delta r_x\\ \delta r_z\end{pmatrix} = \mathscr{R}\begin{pmatrix}\delta r_x\\ \delta r_z\end{pmatrix} \tag{A.2}$$

and inversely:

$$\begin{pmatrix}\delta r_x\\ \delta r_z\end{pmatrix} = \begin{pmatrix}\cos\beta^{\angle}_{\ominus} & \sin\beta^{\angle}_{\ominus}\\ \cos\beta^{\angle}_{\oplus} & \sin\beta^{\angle}_{\oplus}\end{pmatrix}^{-1}\begin{pmatrix}\delta r_{\ominus}\\ \delta r_{\oplus}\end{pmatrix} \tag{A.3}$$

So we can calculate the calibrated projections of the oscillation trajectory

$$\begin{aligned}\delta r_x &= \frac{\sin\beta^{\angle}_{\oplus}}{\det\mathscr{R}}\frac{\delta S_{\beta_{\ominus}}}{\|\beta_{\ominus}\|} - \frac{\sin\beta^{\angle}_{\ominus}}{\det\mathscr{R}}\frac{\delta S_{\beta_{\oplus}}}{\|\beta_{\oplus}\|} &&= c_{11}\delta S_{\ominus} + c_{21}\delta S_{\oplus} \qquad \text{(A.4)}\\ \delta r_z &= -\frac{\cos\beta^{\angle}_{\oplus}}{\det\mathscr{R}}\frac{\delta S_{\beta_{\ominus}}}{\|\beta_{\ominus}\|} + \frac{\cos\beta^{\angle}_{\ominus}}{\det\mathscr{R}}\frac{\delta S_{\beta_{\oplus}}}{\|\beta_{\oplus}\|} &&= c_{12}\delta S_{\ominus} + c_{22}\delta S_{\oplus} \qquad \text{(A.5)}\end{aligned}$$

For the projection of the trajectory on an arbitrary read out vector $\mathbf{e}_{\mu}$ we calculate

$$\begin{aligned}\delta r_{\mu} &= \cos\mu\delta r_x + \sin\mu\delta r_z \qquad \text{(A.6)}\\ &= \left(\frac{\cos\mu\sin\beta^{\angle}_{\oplus}}{\|\beta_{\ominus}\|\det\mathscr{R}} - \frac{\sin\mu\cos\beta^{\angle}_{\oplus}}{\|\beta_{\ominus}\|\det\mathscr{R}}\right)\delta S_{\beta_{\ominus}} + \left(\frac{\sin\mu\cos\beta^{\angle}_{\ominus}}{\|\beta_{\oplus}\|\det\mathscr{R}} - \frac{\cos\mu\sin\beta^{\angle}_{\ominus}}{\|\beta_{\oplus}\|\det\mathscr{R}}\right)\delta S_{\beta_{\oplus}} \qquad \text{(A.7)}\\ &= c'_1\delta S_{\beta_{\ominus}} + c'_2\delta S_{\beta_{\oplus}} \qquad \text{(A.8)}\end{aligned}$$

The last operation is the only step that needs to be executed in real time and therefore the coefficients $c'_{1,2}$ are the values that have to be provided to the FPGA while the rest are unique operations that can be performed on the software level.

Additionally, a feedback gain g_{fb} can be applied as a proportional on the value δr_μ to control the output amplitude of the generated signal.

B Fourier analysis of nanowire trajectory recorded as demodulated data

For the calculation of the spectrum, we first reconstruct the complex displacement quadratures $\delta r_{\ominus,\oplus}$, using the positional quadratures $X_{i,r}, Y_{i,r}$:

$$\delta r_{\ominus} = \sqrt{2}(X_{\ominus,r} + iY_{\ominus,r}), \delta r_{\oplus} = \sqrt{2}(X_{\oplus,r} + iY_{\oplus,r}), \tag{B.1}$$

and derive their projections in the x, z basis via Equation 4.54.

We then calculate the coefficients of the discrete Fourier transform (DFT) with

$$\delta r'_k = \sum_{n=0}^{N-1} \delta r_{t_n} e^{-i2\pi \frac{nk}{N}} \tag{B.2}$$

for each displacement $\delta r_{x,z}$. Each coefficient k corresponds to a frequency

$$f'_k = \left[-\frac{N}{2}; \frac{N}{2}\right] \cdot \Delta t \cdot N \tag{B.3}$$

Since the DFT is performed on the demodulated data, the Fourier frequencies are centered around the demodulation frequency and not around zero and we get the correct frequency values via

$$f_k = f'_k + f_{\mathrm{demod}} \tag{B.4}$$

To get physical Fourier coefficients in $\mathrm{m\,Hz^{-1}}$ we need to multiply δr_k with the sample spacing Δt:

$$\delta r_k = \delta r'_k \Delta t \tag{B.5}$$

Since we define the Fourier transformation as

$$A[\Omega] = \int_{-\infty}^{\infty} \mathrm{d}t e^{\mathrm{i}\Omega t} A(t), \quad A(t) = \int_{-\infty}^{\infty} \frac{\mathrm{d}\Omega}{2\pi} e^{-\mathrm{i}\Omega t} A[\Omega], \tag{B.6}$$

with a different sign for forward and backward transformation compared to the DFT, the phase of the calculated Fourier coefficients is wrong by π which needs to be taken into account when analysing the data.

The demodulated data is low-pass filtered, and we need to correct the calculated δr_k by the filter response $F[f_k] = F_k$:

$$\delta\tilde{r}_k = \frac{\delta r_k}{F_k} \tag{B.7}$$

Following the definition for the

- Fourier transform in [23, p. 54] , the Fourier

transform needs to be calibrated with $1/\sqrt{T}$ where T is the total acquisition time (thus the inverse of the equivalent RBW in a DFT). Thus we have

$$\delta\underline{r}_k = \frac{1}{\sqrt{T}}\delta\tilde{r}_k \tag{B.8}$$

in the units of $\mathrm{m}/\sqrt{\mathrm{Hz}}$.

C Calculation of the noise variance via spectral density integration

C.1 Position variance

The variance of the displacement noise is given by the integral from Equation 4.65, which writes:

$$\sigma^2_{\delta r_\mu} \equiv \int \frac{d\Omega}{2\pi} S_{\delta r_\mu}[\Omega]. \tag{C.1}$$

Where $S_{\delta r_\mu}[\Omega]$ is the projected thermal noise spectrum with

$$S_{\delta r_\mu}[\Omega] = \frac{S_{F_{th}}}{|\det \chi^{-1}|^2} \left(\begin{array}{c} \cos^2 \mu\big(|\chi_{11}|^2 + |\chi_{12}|^2\big) \\ + \sin^2 \mu\big(|\chi_{22}|^2 + |\chi_{21}|^2\big) \\ +2 \cos \mu \sin \mu(\Re(\chi^*_{11}\chi_{21}) + \Re(\chi^*_{12}\chi_{22})) \end{array} \right). \tag{C.2}$$

We can integrate each summand separately and write (C.1) as:

$$\Delta r^2_\mu = \Delta r^2_{cc} \cos^2 \mu + \Delta r^2_{ss} \sin^2 \mu + \Delta r^2_{cs} \cos \mu \sin \mu, \tag{C.3}$$

with the coefficients

$$\Delta r^2_\# \equiv S_F \int \frac{d\Omega}{2\pi} \frac{f_\#}{\left|\det \chi^{-1}[\Omega]\right|^2}. \tag{C.4}$$

Here $f_\#$ expresses the coefficients of the sine and cosine products in (C.2) for each corresponding subscript. Since the nominator in the integral is a complex term, we apply the residue theorem. The poles of the integrand area then given by the solution of

$$\left|\det \chi^{-1}[\Omega]\right|^2 = \left|\big(\Omega^2_+ - \Omega^2 - i\Omega\Gamma\big)\big(\Omega^2_- - \Omega^2 - i\Omega\Gamma\big)\right| \overset{!}{=} 0, \tag{C.5}$$

which is solved by the eight quantities $\pm A, \pm B, \pm A^*, \pm B^*$, where the asterisk denotes the complex conjugate. They are obtained from the expressions:

$$A \equiv i\frac{\Gamma}{2} + \sqrt{\Omega^2_- - \Gamma^2/4} \text{ and } B \equiv i\frac{\Gamma}{2} + \sqrt{\Omega^2_+ - \Gamma^2/4}. \tag{C.6}$$

We choose the half space with positive imaginary part for the application of the residue theorem, so that we need to calculate the residues at the poles $A, -A^*, B, -B^*$ (which have a positive imaginary part). Applying the residue theorem, we thus obtain:

$$\Delta r_\#^2 \equiv \frac{S_F}{2\pi} 2i\pi \sum_{A,-A^*,B,-B^*} \mathrm{Res}_i \left(\frac{f_\#}{\left|\det \chi^{-1}[\Omega]\right|^2} \right) = iS_F \sum_{P=A,-A^*,B,-B^*} \frac{f_\#[P]}{z[P]}, \tag{C.7}$$

where $z[P] = \lim_{\Omega \to P} \frac{\left|\det \chi^{-1}[\Omega]\right|^2}{\Omega - P}$. One can show the following properties for z and $f_\#$:

$$\begin{aligned} z(P) &= -z(-P^*) \\ f_\#(-P^*) &= f_\#(P)^*, \end{aligned} \tag{C.8}$$

so that the sum of the residues simplifies to:

$$\sum_{P=A,-A^*,B,-B^*} \frac{f_\#(P)}{z(P)} = 2i\Im \frac{f_\#(A)}{z(A)} + 2i\Im \frac{f_\#(B)}{z(B)} \tag{C.9}$$

and we obtain for the remaining residues:

$$\frac{f_\#(A)}{z(A)} = \frac{f_\#(A)}{2A2i\Im(A)2\Re(A)\left(\left(\Omega_+^2 - A^2\right)^2 + \Gamma^2 A^2\right)}, \tag{C.10}$$

Where we can replace $2\Im(A)$ and $|\Re(A)|^2$ by their expressions and then get:

$$\frac{f_\#(A)}{z(A)} = \frac{-i}{4\Gamma\left(\Omega_+^2 \Omega_-^2\right)} \frac{f_\#(A)A^*\left(\Omega_+^2 - Omega_-^2 + \Gamma^2 - 2i\Gamma\Re(A)\right)}{\Omega_-^2 \Re(A)\left(\left(\Omega_+^2 - \Omega_-^2\right)^2 + 2\Gamma^2\left(\Omega_+^2 + \Omega_-^2\right)\right)}. \tag{C.11}$$

In order to get the corresponding intermediate result for B, one replaces $+$ with $-$ and vice versa. Thus we obtain for $\Delta r_\#^2$:

$$\begin{aligned} \Delta r_\#^2 = & \frac{k_B T / M_{\mathrm{eff}}}{\left(\Omega_+^2 - \Omega_-^2\right)^2 + 2\Gamma^2\left(\Omega_+^2 + \Omega_-^2\right)} \\ & \times \left\{ \frac{1}{\Omega_-^2} \left(\frac{\Re(f_\#(A)A^*)}{\Re(A)} + \frac{\Gamma^2}{\Omega_+^2 - \Omega_-^2} \left(\frac{\Re(f_\#(A)A^*)}{\Re(A)} - \frac{\Im(f_\#(A)A^*)}{\Gamma/2} \right) \right) \right. \\ & \left. + \frac{1}{\Omega_+^2} \left(\frac{\Re(f_\#(B)B^*)}{\Re(B)} - \frac{\Gamma^2}{\Omega_+^2 - \Omega_-^2} \left(\frac{\Re(f_\#(B)B^*)}{\Re(B)} - \frac{\Im(f_\#(A)A^*)}{\Gamma/2} \right) \right) \right\} \end{aligned} \tag{C.12}$$

We can now insert the tree coefficients $f_{cc,ss,cs}$ from (C.2), replacing the χ_{ij} as:

$$\begin{aligned} f_{cc}[\Omega] &= (\Omega_{\|_2}^{\;2} - \Omega^2)^2 + \Omega^2\Gamma^2 + g_{21} \\ f_{ss}[\Omega] &= (\Omega_{\|_1}^{\;2} - \Omega^2)^2 + \Omega^2\Gamma^2 + g_{12} \\ f_{sc}[\Omega] &= g_{12}(\Omega_{\|_2}^{\;2} - \Omega^2) + g_{21}(\Omega_{\|_1}^{\;2} - \Omega^2) \end{aligned} \tag{C.13}$$

and obtain the **position variance** :

$$\Delta r_\mu^2 = \Delta r_{cc}^2 \cos^2 \mu + \Delta r_{ss}^2 \sin^2 \mu + \Delta r_{cs}^2 \sin \cos \mu, \tag{C.14}$$

with

$$\begin{aligned}
\Delta r_{cc} &= \Theta \frac{\left(\Omega_{\parallel 2}^{\ 4} + \Omega_+^2 \Omega_-^2 + g_{21}^2\right)\left(\Omega_+^2 + \Omega_-^2 + 2\Gamma^2\right) - 4\Omega_{\parallel 2}^{\ 2} \Omega_+^2 \Omega_-^2}{\Omega_+^2 \Omega_-^2} \\
\Delta r_{ss} &= \Theta \frac{\left(\Omega_{\parallel 1}^{\ 4} + \Omega_+^2 \Omega_-^2 + g_{12}^2\right)\left(\Omega_+^2 + \Omega_-^2 + 2\Gamma^2\right) - 4\Omega_{\parallel 1}^{\ 2} \Omega_+^2 \Omega_-^2}{\Omega_+^2 \Omega_-^2} \\
\Delta r_{cs} &= \Theta \frac{\left(g_{12} \Omega_{\parallel 2}^{\ 2} + g_{21} \Omega_{\parallel 1}^{\ 2}\right)\left(\Omega_+^2 + \Omega_-^2 + 2\Gamma^2\right) - 2\Omega_+^2 \Omega_-^2 (g_{12} + g_{21})}{\Omega_+^2 \Omega_-^2}
\end{aligned} \tag{C.15}$$

where the prefactor Θ is:

$$\Theta = \frac{k_B T / M_{\text{eff}}}{(\Omega_+^2 - \Omega_-^2)^2 + 2\Gamma(\Omega_+^2 + \Omega_-^2)}. \tag{C.16}$$

This reduces to the variances of the Langevin driven noise trajectory when no force field is present:

$$\Delta r_{cc}^2 \to \frac{k_B T}{M_{\text{eff}} \Omega_1^2}, \quad \Delta r_{ss}^2 \to \frac{k_B T}{M_{\text{eff}} \Omega_2^2}, \quad \Delta r_{cs}^2 \to 0, \tag{C.17}$$

which do not depend on the mechanical damping Γ.

C.2 Speed variances

The speed variance is defined by a similar integral as the position variance:

$$\sigma_{\delta v_\mu}^2 \equiv \int \frac{d\Omega}{2\pi} S_{\delta v_\mu}[\Omega] = \int \frac{d\Omega}{2\pi} \Omega^2 S_{\delta r_\mu}[\Omega]. \tag{C.18}$$

The evaluation of this integral is analog to the position variance and similar to Equation C.4 we obtain the coefficients of the sine/cosine terms:

$$\Delta v_\#^2 \equiv S_F \int \frac{d\Omega}{2\pi} \frac{\Omega^2 f_\#}{\left|\det \chi^{-1}[\Omega]\right|^2}, \tag{C.19}$$

with the same poles as the position variance. With the new numerator $f_\#[\Omega] \rightarrow \Omega^2 f_\#[\Omega]$, the coefficients $\Delta v_\#^2$ become:

$$\begin{aligned}\Delta v_\#^2 = & \frac{k_B T/M_{\mathrm{eff}}}{\left(\Omega_+^2 - \Omega_-^2\right)^2 + 2\Gamma^2\left(\Omega_+^2 + \Omega_-^2\right)} \\ & \times \left\{ \frac{\Re(f_\#(A)A)}{\Re(A)} + \frac{\Re(f_\#(B)B)}{\Re(B)} \right. \\ & \left. + \frac{\Gamma^2}{\Omega_+^2 - \Omega_-^2} \left(\frac{\Re(f_\#(A)A)}{\Re(A)} - \frac{\Im(f_\#(A)A)}{\Gamma/2} - \frac{\Re(f_\#(B)B)}{\Re(B)} + \frac{\Im(f_\#(B)B)}{\Gamma/2} \right) \right\}\end{aligned} \tag{C.20}$$

And after insertion of A, B and the functions $f_\#[\Omega]$, we calculate the **speed variance**:

$$\Delta v_\mu^2 = \Delta v_{cc}^2 \cos^2 \mu + \Delta v_{ss}^2 \sin^2 \mu + \Delta v_{cs}^2 \sin \cos \mu, \tag{C.21}$$

with

$$\begin{aligned}\Delta v_{cc} &= \frac{k_B T}{M_{\mathrm{eff}}} \left(1 - \frac{2 g_{21}(g_{12} - g_{21})}{(\Omega_+^2 - \Omega_+^2)^2 + 2\Gamma^2(\Omega_+^2 + \Omega_+^2)} \right) \\ \Delta v_{ss} &= \frac{k_B T}{M_{\mathrm{eff}}} \left(1 + \frac{2 g_{12}(g_{12} - g_{21})}{(\Omega_+^2 - \Omega_+^2)^2 + 2\Gamma^2(\Omega_+^2 + \Omega_+^2)} \right) \\ \Delta v_{cs} &= \frac{k_B T}{M_{\mathrm{eff}}} \frac{(g_{12} - g_{21})\left(\Omega_{\parallel 2}^{\;2} - \Omega_{\parallel 1}^{\;2}\right)}{(\Omega_+^2 - \Omega_+^2)^2 + 2\Gamma^2(\Omega_+^2 + \Omega_+^2)}\end{aligned} \tag{C.22}$$

D

Solution of the Fokker-Planck equation for the 2D Nanowire

In Chapter 4, we have used the Fokker-Planck equation to calculate the probability density function of the orthoradial velocity for a pure shearing feedback. Here, we provide the solution of the Fokker-Planck equation, based on which the calculation was done. The presented solution has been part of previous works in our group [28].

The Fokker-Planck equation [113] is defined by:

$$-B_{ik}\,\partial_{x_i}\Big(x_k\,p_{st}(\mathbf{x},t)\Big)+\frac{D_{ij}}{2}\,\partial^2_{x_ix_j}p_{st}(\mathbf{x},t)=0, \tag{D.1}$$

with the following definitions

$$\mathbf{B}=\begin{pmatrix}0 & 0 & 1 & 0\\ 0 & 0 & 0 & 1\\ -\Omega^2_{1\|} & g_{21} & -\Gamma & 0\\ g_{12} & -\Omega^2_{2\|} & 0 & -\Gamma\end{pmatrix}\quad \text{et} \quad \mathbf{D}=\frac{2\Gamma k_B T}{M}\begin{pmatrix}0 & 0 & 0 & 0\\ 0 & 0 & 0 & 0\\ 0 & 0 & 1 & 0\\ 0 & 0 & 0 & 1\end{pmatrix}. \tag{D.2}$$

The solution, which is Gaussian, to this equation is given as general form in [113]:

$$p_{st}(\mathbf{x})=\frac{1}{N}exp\Big[-\sum_{i,j}A_{ij}\,x_i\,x_j\Big],\qquad \mathbf{A}\equiv\frac{1}{2}\begin{pmatrix}2a_{r_1r_1} & a_{r_1r_2} & a_{r_1v_1} & a_{r_1v_2}\\ a_{r_1r_2} & 2a_{r_2r_2} & a_{r_2v_1} & a_{r_2v_2}\\ a_{r_1v_1} & a_{r_2v_1} & 2a_{v_1v_1} & a_{v_1v_2}\\ a_{r_1v_2} & a_{r_2v_2} & a_{v_1v_2} & 2a_{v_2v_2}\end{pmatrix}, \tag{D.3}$$

with the normalization coefficient N^{-1} obtained from integration over the entire space:

$$N=\int_{\mathbb{R}^4}\mathrm{d}\mathbf{x}\ \exp\Big[-\sum_{i,j}A_{ij}\,x_i\,x_j\Big]. \tag{D.4}$$

For the 2D nanowire oscillator, the formal expressions (see [113]) become:

$$\begin{aligned}
a_{r_1r_1} =& K\Bigg\{\Omega_{1\|}^2\Big[2\Gamma^2\big(\Omega_{1\|}^2+\Omega_{2\|}^2\big)+(g_{12}+g_{21})^2+\big(\Omega_{1\|}^2-\Omega_{2\|}^2\big)^2\Big]^2-\Gamma^2(g_{12}+g_{21})(g_{12}-g_{21})^3\\
&-\frac{1}{2}\big(g_{12}^2-g_{21}^2\big)\big(2\Gamma^2+\Omega_{1\|}^2+\Omega_{2\|}^2\big)\Big[2\Gamma^2\big(\Omega_{1\|}^2+\Omega_{2\|}^2\big)+(g_{12}+g_{21})^2+\big(\Omega_{1\|}^2-\Omega_{2\|}^2\big)^2\Big]\\
&+\frac{1}{2}(g_{12}-g_{21})^2\Bigg[4\Gamma^4\big(\Omega_{1\|}^2+\Omega_{2\|}^2\big)+4\Gamma^2\big(\Omega_{1\|}^2-\Omega_{2\|}^2\big)^2\\
&\qquad+(g_{12}+g_{21})^2\big(4\Gamma^2-\Omega_{1\|}^2+\Omega_{2\|}^2\big)-\big(\Omega_{1\|}^2-\Omega_{2\|}^2\big)^3\Bigg]\Bigg\}\\
a_{r_1r_2} =& K\Bigg\{-(g_{12}+g_{21})\Big[2\Gamma^2\big(\Omega_{1\|}^2+\Omega_{2\|}^2\big)+(g_{12}+g_{21})^2+\big(\Omega_{1\|}^2-\Omega_{2\|}^2\big)^2\Big]^2\\
&-2\Gamma^2(g_{12}-g_{21})^3\big(\Omega_{1\|}^2-\Omega_{2\|}^2\big)+(g_{12}+g_{21})(g_{12}-g_{21})^2\Big[(g_{12}+g_{21})^2+\big(\Omega_{1\|}^2-\Omega_{2\|}^2\big)^2\Big]\\
&-(g_{12}-g_{21})\big(\Omega_{1\|}^2-\Omega_{2\|}^2\big)\big(2\Gamma^2+\Omega_{1\|}^2+\Omega_{2\|}^2\big)\\
&\qquad\times\Big[2\Gamma^2\big(\Omega_{1\|}^2+\Omega_{2\|}^2\big)+(g_{12}+g_{21})^2+\big(\Omega_{1\|}^2-\Omega_{2\|}^2\big)^2\Big]\Bigg\}\\
a_{v_1v_1} =& K\Bigg\{\Big[2\Gamma^2\big(\Omega_{1\|}^2+\Omega_{2\|}^2\big)+(g_{12}+g_{21})^2+\big(\Omega_{1\|}^2-\Omega_{2\|}^2\big)^2\Big]^2\\
&-\big(g_{12}^2-g_{21}^2\big)\Big[2\Gamma^2\big(\Omega_{1\|}^2+\Omega_{2\|}^2\big)+(g_{12}+g_{21})^2+\big(\Omega_{1\|}^2-\Omega_{2\|}^2\big)^2\Big]\\
&+2\Gamma^2(g_{12}-g_{21})^2\big(2\Gamma^2-\Omega_{1\|}^2+\Omega_{2\|}^2\big)\Bigg\}\\
a_{v_1v_2} =& K\Bigg\{2(g_{12}-g_{21})\Bigg[2\Gamma^2\big(g_{12}^2-g_{21}^2\big)\\
&\qquad+\ \big(\Omega_{2\|}^2-\Omega_{1\|}^2\big)\Big[2\Gamma^2\big(\Omega_{1\|}^2+\Omega_{2\|}^2\big)+(g_{12}+g_{21})^2+\big(\Omega_{1\|}^2-\Omega_{2\|}^2\big)^2\Big]\Bigg]\Bigg\}\\
a_{r_1v_1} =& K\Bigg\{4\Gamma(g_{12}-g_{21})\Big[2\Gamma^2\big(g_{12}\Omega_{1\|}^2+g_{21}\Omega_{2\|}^2\big)+g_{21}(g_{12}+g_{21})^2\Big]\Bigg\}\\
a_{r_1v_2} =& K\Bigg\{4\Gamma(g_{12}-g_{21})\Omega_{1\|}^2\Big[2\Gamma^2\big(\Omega_{1\|}^2+\Omega_{2\|}^2\big)+(g_{12}+g_{21})^2+\big(\Omega_{1\|}^2-\Omega_{2\|}^2\big)^2\Big]\\
&\qquad-8\Gamma^2g_{21}(g_{12}-g_{21})^2\Bigg\}.
\end{aligned}$$

where $K \equiv \dfrac{M/2k_BT}{4\Gamma^4(g_{12}-g_{21})^2+\Big[2\Gamma^2\big(\Omega_{1\|}^2+\Omega_{2\|}^2\big)+(g_{12}+g_{21})^2+\big(\Omega_{1\|}^2-\Omega_{2\|}^2\big)^2\Big]^2}.$

The 4 last coefficients ($a_{r_2r_2}$, $a_{v_2v_2}$, $a_{r_2v_2}$ and $a_{r_2v_1}$) are obtained by exchanging 1 and 2 in these expressions.

In the case of a large quality factor, the coefficients matrix is block-diagonal, that is, the principal directions of the elliptical Gaussian distribution are pure speeds and pure positions and not combinations of speeds and positions. This mixing of positions and speeds is therefore only a consequence of dissipation, which justifies the focus on the pure-position and pure-speed variances Δr_β^2 and Δv_β^2. The remaining non-zero coefficients are then:

$$\left\{\begin{array}{lcl} a_{r_1r_1} & = & K\Big[\Big(\Omega_{1\|}^2+\Omega_{2\|}^2\Big)g_{21}^2+g_{12}g_{21}\Big(3\Omega_{1\|}^2-\Omega_{2\|}^2\Big)+\Big(\Omega_{1\|}^3-\Omega_{1\|}\Omega_{2\|}^2\Big)^2\Big] \\ a_{r_2r_2} & = & K\Big[\Big(\Omega_{1\|}^2+\Omega_{2\|}^2\Big)g_{12}^2+g_{12}g_{21}\Big(3\Omega_{2\|}^2-\Omega_{1\|}^2\Big)+\Big(\Omega_{2\|}^3-\Omega_{1\|}^2\Omega_{2\|}\Big)^2\Big] \\ a_{r_1r_2} & = & K\Big[-2g_{21}\Omega_{2\|}^4-2g_{12}\Omega_{1\|}^4+2(g_{12}+g_{21})\Omega_{1\|}^2\Omega_{2\|}^2-4g_{12}g_{21}(g_{12}+g_{21})\Big] \\ a_{v_1v_1} & = & K\Big[\Big(\Omega_{1\|}^2-\Omega_{2\|}^2\Big)^2+2g_{21}(g_{12}+g_{21})\Big] \\ a_{v_2v_2} & = & K\Big[\Big(\Omega_{1\|}^2-\Omega_{2\|}^2\Big)^2+2g_{12}(g_{12}+g_{21})\Big] \\ a_{v_1v_2} & = & K\Big[2(g_{12}-g_{21})\Big(\Omega_{2\|}^2-\Omega_{1\|}^2\Big)\Big] \end{array}\right. \tag{D.5}$$

with $K \equiv \frac{M/2k_BT}{(g_{12}+g_{21})^2+(\Omega_{2\|}^2-\Omega_{1\|}^2)^2}$.

For no present force field the coefficients are

$$\begin{aligned} a_{r_1r_1} =& K\left\{\Omega_{1\|}^2\left[2\Gamma^2\Big(\Omega_{1\|}^2+\Omega_{2\|}^2\Big)++\Big(\Omega_{1\|}^2-\Omega_{2\|}^2\Big)^2\right]^2\right\} \\ a_{r_1r_2} =& 0 \\ a_{v_1v_1} =& K\left\{\left[2\Gamma^2\Big(\Omega_{1\|}^2+\Omega_{2\|}^2\Big)+\Big(\Omega_{1\|}^2-\Omega_{2\|}^2\Big)^2\right]^2\right\} \\ a_{v_1v_2} =& 0 \\ a_{r_1v_1} =& 0 \\ a_{r_1v_2} =& 0 \end{aligned}$$

Acronyms

AFM	Atomic Force Microscopy
CCD	Charge-coupled Device
CNT	Carbon Nanotube
DFT	Discrete Fourier Transform
DSP	Digital Signal Processing
EM	Electromagnetic
FPGA	Field Programmable Gate Array
KPFM	Kelvin Probe Force Microscopy
NA	Numerical Aperture
NV	Nitrogen Vacancy
NW	Nanowire
PFA	Proximity Force Approximation
PLL	Phase-locked Loop
PSD	Power Spectral Density
QPD	Quadrant Photodiode
RBW	Resolution Bandwidth
SEM	Scanning Electron Microscopy
SiC	Silicon Carbide
SiN	Silicon Nitride
SNB	Signal Noise to Background Noise Ratio
SNR	Signal to Noise Ratio
SPM	Scanning Probe Microscopy
STM	Scanning Tunneling Microscopy

Glossary

k_B	Boltzmann constant
Γ_m	Mechanical damping
$\delta\mathbf{r}$	Displacement of the nanowire
$Omega_{1,2}$	Eigenfrequency of the higher (+), lower (−) frequency mode
$Omega_{+,-}$	Eigenfrequency of the higher (+), lower (−) frequency mode
$\mathbf{e}_{1,2}$	Eigenvector of the higher (+), lower (−) frequency undressed mode
$\mathbf{e}_{+,-}$	Eigenvector of the higher (+), lower (−) frequency dressed mode
$\mathbf{F}_{\mathrm{ext}}$	External force (field) (measurable)
γ	Constant force divergence coefficient
λ	Linear force divergence coefficient λV
α	Quadratic force divergence coefficient αV^2
$\mathscr{F}$	Fourier transform with $\mathscr{F} f(t) = \int_{\mathbb{R}} f(t)e^{-i\Omega t}dt$
g_{fg}	Gain of the applied feedback (Chapter 4)
g_{ij}	Real part of the mass independent force field gradients in units of Hz^2
h_{ij}	Imaginary part of the mass independent force field gradients in units of Hz^2 (chapter 4)
HF2LI	Zurich Instruments dual channel lock in amplifier with two independent PLLs
$\mathrm{HFDC}_{\oplus,\ominus}$	Calibration factor of the high and low frequency response per channel of the photodiodes
M_{eff}	Effective Mass Equation 1.12
ξ_n	Matsubara frequencies Equation 3.9
T, T_{ij}	Maxwell Stress tensor and its components
$\boldsymbol{\beta}_{\oplus,\ominus}$	Measurement vector of the sum ⊕ and difference *ominus* channel of the photodiodes
PSD	Power spectral density
X, Y	Measured signal quadratures (lock-in measurement)
Q	(Mechanical) Quality factor $Q = {}^{\Omega_m}/_{\Gamma}$
rms	Root mean square, defined by $\sqrt{\frac{1}{n}\sum_{i=1}^{n} x_i^2}$.
ξ	Rotational parameter for the transverse immediate feedback

$S_{\delta r_\mu}$	Brownian motion spectrum of the nanowire measured along the vector $\mathbf{e}_\mu$
χ	Mechanical Susceptibility Matrix of an Oscillator
F_{th}	Thermal Langevin force
$\sigma_{\delta r_\mu}$	Variance of the brownian motion along the direction $\mathbf{e}_\mu$

Bibliography

1. *AFM Block Diagram*. URL: `https://upload.wikimedia.org/wikipedia/commons/7/7c/Atomic_force_microscope_block_diagram.svg` (cit. on p. 5).
2. *AFM Probe Tips for Scanning Probe Microscopy - Silicon Mems - Team Nanotec*. URL: `https://www.team-nanotec.de/index.cfm?contentid=2` (cit. on p. 83).
3. *Ampere - BIPM*. URL: `https://www.bipm.org/en/history-si/ampere` (cit. on p. 1).
4. O. Arcizet, P.-F. Cohadon, T. Briant, M. Pinard, and A. Heidmann. "Radiation-Pressure Cooling and Optomechanical Instability of a Micromirror". *Nature* 444:7115, 2006, pp. 71–74 (cit. on p. 194).
5. Neil W. Ashcroft and N. David Mermin. *Solid State Physics*. Repr. Brooks/Cole Thomson Learning, South Melbourne, 2012. 826 pp. ISBN: 978-0-03-083993-1 (cit. on p. 82).
6. M V Berry and Pragya Shukla. "Classical Dynamics with Curl Forces, and Motion Driven by Time-Dependent Flux". *Journal of Physics A: Mathematical and Theoretical* 45:30, 3, 2012, p. 305201 (cit. on p. 223).
7. M. V. Berry and Pragya Shukla. "Hamiltonian Curl Forces". *Proceedings of the Royal Society A: Mathematical, Physical and Engineering Sciences* 471:2176, 2015, p. 20150002 (cit. on p. 223).
8. G. Binnig, C. F. Quate, and Ch. Gerber. "Atomic Force Microscope". *Physical Review Letters* 56:9, 3, 1986, pp. 930–933 (cit. on p. 5).
9. Charles P. Blakemore, Alexander D. Rider, Sandip Roy, Qidong Wang, Akio Kawasaki, and Giorgio Gratta. "Three-Dimensional Force-Field Microscopy with Optically Levitated Microspheres". *Physical Review A* 99:2, 8, 2019, p. 023816 (cit. on p. 6).
10. J. Błocki, J. Randrup, W. J. Świątecki, and C. F. Tsang. "Proximity Forces". *Annals of Physics* 105:2, 1, 1977, pp. 427–462 (cit. on p. 138).
11. Antonio Borrielli, Michele Bonaldi, Enrico Serra, Pasqualina Maria Sarro, and Bruno Morana. *Active Feedback Cooling of a SiN Membrane Resonator by Electrostatic Actuation*. 16, 2021. arXiv: `2106.08840 [physics]`. URL: `http://arxiv.org/abs/2106.08840` (cit. on p. 194).
12. F R Braakman and M Poggio. "Force Sensing with Nanowire Cantilevers". *Nanotechnology* 30:33, 16, 2019, p. 332001 (cit. on p. 7).
13. Herbert B. Callen and Theodore A. Welton. "Irreversibility and Generalized Noise". *Physical Review* 83:1, 1, 1951, pp. 34–40 (cit. on p. 15).
14. J.B. Casady and R.W. Johnson. "Status of Silicon Carbide (SiC) as a Wide-Bandgap Semiconductor for High-Temperature Applications: A Review". *Solid-State Electronics* 39:10, 1996, pp. 1409–1422 (cit. on p. 116).
15. H. B. G. Casimir and D. Polder. "The Influence of Retardation on the London-van Der Waals Forces". *Physical Review* 73:4, 15, 1948, pp. 360–372 (cit. on p. 137).
16. Hendrik Casimir. "On the Attraction between Two Perfectly Conducting Plates". *Proceedings of the Koninklijke Nederlandse Akandemie van Wetenschappen* 51, 1948, pp. 793–795 (cit. on p. 137).
17. Henry Cavendish. "XXI. Experiments to Determine the Density of the Earth". *Philosophical Transactions of the Royal Society of London* 88, 1, 1798, pp. 469–526 (cit. on pp. 1, 2).
18. J. Chaste, A. Eichler, J. Moser, G. Ceballos, R. Rurali, and A. Bachtold. "A Nanomechanical Mass Sensor with Yoctogram Resolution". *Nature Nanotechnology* 7:5, 5 2012, pp. 301–304 (cit. on p. 4).

19. F. Chen, U. Mohideen, G. L. Klimchitskaya, and V. M. Mostepanenko. "Demonstration of the Lateral Casimir Force". *Physical Review Letters* 88:10, 25, 2002, p. 101801 (cit. on p. 139).
20. A. A. Chumak, P. W. Milonni, and G. P. Berman. "Effects of Electrostatic Fields and Casimir Force on Cantilever Vibrations". *Physical Review B* 70:8, 23, 2004, p. 085407 (cit. on p. 139).
21. V Cimalla, J Pezoldt, and O Ambacher. "Group III Nitride and SiC Based MEMS and NEMS: Materials Properties, Technology and Applications". *Journal of Physics D: Applied Physics* 40:20, 21, 2007, pp. 6386–6434 (cit. on p. 33).
22. Andrew N. Cleland. *Foundations of Nanomechanics*. Advanced Texts in Physics. Springer Berlin Heidelberg, Berlin, Heidelberg, 2003. ISBN: 978-3-642-07821-7 978-3-662-05287-7 (cit. on p. 11).
23. A. A. Clerk, M. H. Devoret, S. M. Girvin, F. Marquardt, and R. J. Schoelkopf. "Introduction to Quantum Noise, Measurement and Amplification". *Reviews of Modern Physics* 82:2, 15, 2010, pp. 1155–1208. arXiv: `0810.4729` (cit. on p. 232).
24. P. F. Cohadon, A. Heidmann, and M. Pinard. "Cooling of a Mirror by Radiation Pressure". *Physical Review Letters* 83:16, 18, 1999, pp. 3174–3177 (cit. on pp. 194, 195).
25. *CTAN: Package Pgfplots*. URL: `https://www.ctan.org/pkg/pgfplots` (cit. on p. 4).
26. Diego Dalvit, Peter Milonni, David Roberts, and Felipe da Rosa, eds. *Casimir Physics*. Vol. 834. Lecture Notes in Physics. Springer Berlin Heidelberg, Berlin, Heidelberg, 2011. ISBN: 978-3-642-20287-2 978-3-642-20288-9 (cit. on pp. 138, 144, 145, 147).
27. Vitaly V. Datsyuk and Oleg R. Pavlyniuk. "Maxwell Stress on a Small Dielectric Sphere in a Dielectric". *Physical Review A* 91:2, 23, 2015, p. 023826 (cit. on pp. 73, 144).
28. Laure Mercier de Lépinay. "Habillage mécanique d'un nanofil par un champ de force : de la mesure vectorielle ultrasensible aux systèmes quantiques hybrides". 30, 2017 (cit. on pp. 7, 11, 33, 42, 52, 56, 237).
29. Laure Mercier de Lépinay, Benjamin Pigeau, Benjamin Besga, Pascal Vincent, Philippe Poncharal, and Olivier Arcizet. "A Universal and Ultrasensitive Vectorial Nanomechanical Sensor for Imaging 2D Force Fields". *Nature Nanotechnology* 12:2, 2017, pp. 156–162 (cit. on pp. 6, 7, 9, 113, 122, 221).
30. *Draw Freely | Inkscape*. URL: `https://inkscape.org/de/` (cit. on p. 4).
31. Yves F. Dufrêne, Toshio Ando, Ricardo Garcia, David Alsteens, David Martinez-Martin, Andreas Engel, Christoph Gerber, and Daniel J. Müller. "Imaging Modes of Atomic Force Microscopy for Application in Molecular and Cell Biology". *Nature Nanotechnology* 12:4, 4 2017, pp. 295–307 (cit. on p. 5).
32. I E Dzyaloshinskii, E M Lifshitz, and L P Pitaevskii. "General Theory of Van Der Waals Forces". *Soviet Physics USPEKHI*, p. 25 (cit. on pp. 137, 145).
33. Claudia Eberlein and Robert Zietal. "Casimir-Polder Interaction between a Polarizable Particle and a Plate with a Hole". *Physical Review A* 83:5, 23, 2011, p. 052514 (cit. on p. 146).
34. Thorsten Emig, Andreas Hanke, Ramin Golestanian, and Mehran Kardar. "Normal and Lateral Casimir Forces between Deformed Plates". *Physical Review A* 67:2, 28, 2003, p. 022114 (cit. on p. 139).
35. Francesco Fogliano and Universite Grenoble Alpes. "Ultrasensitive Nanowire Force Sensorsin Extreme Conditions" (cit. on pp. 6, 220).
36. Francesco Fogliano, Benjamin Besga, Antoine Reigue, Philip Heringlake, Laure Mercier de Lépinay, Cyril Vaneph, Jakob Reichel, Benjamin Pigeau, and Olivier Arcizet. "Mapping the Cavity Optomechanical Interaction with Subwavelength-Sized Ultrasensitive Nanomechanical Force Sensors". *Physical Review X* 11:2, 8, 2021, p. 021009 (cit. on pp. ii, 7, 9, 119, 219, 221).
37. Francesco Fogliano, Benjamin Besga, Antoine Reigue, Laure Mercier de Lépinay, Philip Heringlake, Clement Gouriou, Eric Eyraud, Wolfgang Wernsdorfer, Benjamin Pigeau, and Olivier Arcizet. "Ultrasensitive Nano-Optomechanical Force Sensor Operated at Dilution Temperatures". *Nature Communications* 12:1, 1 5, 2021, p. 4124 (cit. on pp. 7, 219, 221).

38. Daniel Garcia-Sanchez, King Yan Fong, Harish Bhaskaran, Steve Lamoreaux, and Hong X. Tang. "Casimir Force and *In Situ* Surface Potential Measurements on Nanomembranes". *Physical Review Letters* 109:2, 9, 2012, p. 027202 (cit. on p. 138).
39. Joseph L Garrett, David Somers, and Jeremy N Munday. "The Effect of Patch Potentials in Casimir Force Measurements Determined by Heterodyne Kelvin Probe Force Microscopy". *Journal of Physics: Condensed Matter* 27:21, 3, 2015, p. 214012 (cit. on pp. 105, 138).
40. C. Genet, A. Lambrecht, and S. Reynaud. "The Casimir Effect in the Nanoworld". *The European Physical Journal Special Topics* 160:1, 1, 2008, pp. 183–193 (cit. on p. 138).
41. Christophe Geuzaine and Jean-François Remacle. "Gmsh: A 3-D Finite Element Mesh Generator with Built-in Pre- and Post-Processing Facilities". *International Journal for Numerical Methods in Engineering* 79:11, 2009, pp. 1309–1331 (cit. on p. 146).
42. *GIMP*. GIMP. URL: `https://www.gimp.org/` (cit. on p. 4).
43. A. Gloppe, P. Verlot, E. Dupont-Ferrier, A. Siria, P. Poncharal, G. Bachelier, P. Vincent, and O. Arcizet. "Bidimensional Nano-Optomechanics and Topological Backaction in a Non-Conservative Radiation Force Field". *Nature Nanotechnology* 9:11, 11 2014, pp. 920–926 (cit. on pp. 6, 7, 189, 190, 221).
44. Arnaud Gloppe. "Nano-Optomechanics at the Waist of a Focused Laser Beam : Cartography of the Optical Force Field and Bidimensional Backaction". Theses. Université de Grenoble, 2014 (cit. on pp. 42, 43, 56, 189).
45. *GNU Emacs - GNU Project*. URL: `https://www.gnu.org/software/emacs/` (cit. on p. 4).
46. Daniel Gomez. *Dangom/Org-Thesis*. 4, 2021 (cit. on p. 4).
47. David J Griffiths. *Introduction to Electrodynamics*. Prentice Hall New Jersey, 1962 (cit. on pp. 73, 93).
48. Leo Gross, Fabian Mohn, Nikolaj Moll, Peter Liljeroth, and Gerhard Meyer. "The Chemical Structure of a Molecule Resolved by Atomic Force Microscopy". *Science* 325:5944, 28, 2009, pp. 1110–1114. pmid: 19713523 (cit. on p. 5).
49. Olivier L. Guise, Joachim W. Ahner, Moon-Chul Jung, Peter C. Goughnour, and John T. Yates. "Reproducible Electrochemical Etching of Tungsten Probe Tips". *Nano Letters* 2:3, 1, 2002, pp. 191–193 (cit. on p. 37).
50. B. W. Harris, F. Chen, and U. Mohideen. "Precision Measurement of the Casimir Force Using Gold Surfaces". *Physical Review A* 62:5, 17, 2000, p. 052109 (cit. on pp. 138, 139).
51. Gary Lynn Harris and Institution of Electrical Engineers, eds. *Properties of Silicon Carbide*. EMIS Datareviews Series 13. INSPEC, the Inst. of Electrical Engineers, London, 1995. 282 pp. ISBN: 978-0-85296-870-3 (cit. on p. 33).
52. Sungkun Hong, Michael S. Grinolds, Linh M. Pham, David Le Sage, Lan Luan, Ronald L. Walsworth, and Amir Yacoby. "Nanoscale Magnetometry with NV Centers in Diamond". *MRS Bulletin* 38:2, 2013, pp. 155–161 (cit. on p. 225).
53. B. Ilic, Y. Yang, and H. G. Craighead. "Virus Detection Using Nanoelectromechanical Devices". *Applied Physics Letters* 85:13, 27, 2004, pp. 2604–2606 (cit. on p. 3).
54. Francesco Intravaia, Stephan Koev, Il Woong Jung, A. Alec Talin, Paul S. Davids, Ricardo S. Decca, Vladimir A. Aksyuk, Diego A. R. Dalvit, and Daniel López. "Strong Casimir Force Reduction through Metallic Surface Nanostructuring". *Nature Communications* 4:1, 2013, p. 2515 (cit. on pp. 138, 139).
55. O. Kenneth, I. Klich, A. Mann, and M. Revzen. "Repulsive Casimir Forces". *Physical Review Letters* 89:3, 25, 2002, p. 033001 (cit. on p. 138).
56. S. Kerfriden, A. Nahle, S. Campbell, F. Walsh, and James Smith. "The Electrochemical Etching of Tungsten STM Tips". *Electrochimica Acta* 43:12-13, 1998, pp. 1939–1944 (cit. on p. 37).
57. Suenne Kim, Farbod Shafiei, Daniel Ratchford, and Xiaoqin Li. "Controlled AFM Manipulation of Small Nanoparticles and Assembly of Hybrid Nanostructures". *Nanotechnology* 22:11, 2011, p. 115301 (cit. on p. 5).

58. W. J. Kim, A. O. Sushkov, D. A. R. Dalvit, and S. K. Lamoreaux. "Surface Contact Potential Patches and Casimir Force Measurements". *Physical Review A* 81:2, 16, 2010, p. 022505 (cit. on p. 138).
59. Charles Kittel. *Introduction to Solid State Physics.* 8. ed. Wiley, Hoboken, NJ, 2005. 680 pp. ISBN: 978-0-471-41526-8 978-0-471-68057-4 (cit. on p. 81).
60. R Kubo. "The Fluctuation-Dissipation Theorem", p. 31 (cit. on p. 15).
61. M. Kulawik, M. Nowicki, G. Thielsch, L. Cramer, H. Rust, H. Freund, T. P. Pearl, and P. Weiss. "A Double Lamellae Dropoff Etching Procedure for Tungsten Tips Attached to Tuning Fork Atomic Force Microscopy/Scanning Tunneling Microscopy Sensors", 2003 (cit. on p. 37).
62. M. D. LaHaye, O. Buu, B. Camarota, and K. C. Schwab. "Approaching the Quantum Limit of a Nanomechanical Resonator". *Science* 304:5667, 2, 2004, pp. 74–77. pmid: `15064412` (cit. on pp. 3, 4).
63. Astrid Lambrecht and Serge Reynaud. "Casimir Force between Metallic Mirrors". *The European Physical Journal D - Atomic, Molecular and Optical Physics* 8:3, 1, 2000, pp. 309–318. arXiv: `quant-ph/9907105` (cit. on pp. 138, 147).
64. Michael Levin and Steven G. Johnson. "Is the Electrostatic Force between a Point Charge and a Neutral Metallic Object Always Attractive?" *American Journal of Physics* 79:8, 2011, pp. 843–849 (cit. on pp. 92, 93, 139, 148).
65. Michael Levin, Alexander P. McCauley, Alejandro W. Rodriguez, M. T. Homer Reid, and Steven G. Johnson. "Casimir Repulsion between Metallic Objects in Vacuum". *Physical Review Letters* 105:9, 26, 2010, p. 090403 (cit. on pp. 139, 146–148).
66. E.M. Lifshitz and M. Hamermesh. "The Theory of Molecular Attractive Forces between Solids". In: *Perspectives in Theoretical Physics.* Elsevier, 1992, pp. 329–349. ISBN: 978-0-08-036364-6 (cit. on p. 137).
67. Evgenij M. Lifšic, Lev P. Pitaevskij, Lev Davidovič Landau, and Evgenii Mikhailovič Lifshitz. *Statistical Physics. Part 2. Theory of the Condensed State.* Reprinted. Course of Theoretical Physics by E. M. Lifshitz and L. P. Pitaevskiĭ; Vol. 9[...] Elsevier, Oxford, 2006. 387 pp. ISBN: 978-0-7506-2636-1 (cit. on pp. 144, 145).
68. Henrik Lissner. *Hlissner/Doom-Emacs.* 9, 2021 (cit. on p. 4).
69. F. Lopour, R. Kalousek, D. Škoda, J. Spousta, F. Matějka, and T. Šikola. "Application of AFM in Microscopy and Fabrication of Micro/Nanostructures". *Surface and Interface Analysis* 34:1, 2002, pp. 352–355 (cit. on p. 5).
70. Stefano Mancini, David Vitali, and Paolo Tombesi. "Optomechanical Cooling of a Macroscopic Oscillator by Homodyne Feedback". *Physical Review Letters* 80:4, 26, 1998, pp. 688–691 (cit. on p. 194).
71. James Clerk Maxwell. *A Treatise on Electricity and Magnetism.* Vol. 2. Oxford: Clarendon Press, 1873 (cit. on p. 73).
72. Alexander P. McCauley, Alejandro W. Rodriguez, John D. Joannopoulos, and Steven G. Johnson. "Casimir Forces in the Time Domain: Applications". *Physical Review A* 81:1, 28, 2010, p. 012119 (cit. on p. 146).
73. Alexander P. McCauley, Alejandro W. Rodriguez, M. T. Homer Reid, and Steven G. Johnson. *Casimir Repulsion beyond the Dipole Regime.* 2, 2011. arXiv: `1105.0404 [quant-ph]`. URL: `http://arxiv.org/abs/1105.0404` (cit. on p. 149).
74. Gustav Mie. "Beiträge zur Optik trüber Medien, speziell kolloidaler Metallösungen". *Annalen der Physik* 330:3, 1908, pp. 377–445 (cit. on p. 33).
75. Kimball A. Milton, E. K. Abalo, Prachi Parashar, Nima Pourtolami, Iver Brevik, and Simen Å. Ellingsen. "Casimir-Polder Repulsion near Edges: Wedge Apex and a Screen with an Aperture". *Physical Review A* 83:6, 13, 2011, p. 062507 (cit. on p. 149).
76. Kimball A. Milton, E. K. Abalo, Prachi Parashar, Nima Pourtolami, Iver Brevik, and Simen \AA Ellingsen. "Repulsive Casimir and Casimir–Polder Forces". *Journal of Physics A: Mathematical and Theoretical* 45:37, 2012, p. 374006 (cit. on p. 139).

77. Naruhisa Miura, Hideaki Ishii, Jun-ichi Shirakashi, Akira Yamada, and Makoto Konagai. “Electron-Beam-Induced Deposition of Carbonaceous Microstructures Using Scanning Electron Microscopy”. *Applied Surface Science* 113–114, 1997, pp. 269–273 (cit. on p. 107).
78. David C. Moore, Alexander D. Rider, and Giorgio Gratta. “Search for Millicharged Particles Using Optically Levitated Microspheres”. *Physical Review Letters* 113:25, 16, 2014, p. 251801 (cit. on p. 118).
79. J. N. Munday, Federico Capasso, and V. Adrian Parsegian. “Measured Long-Range Repulsive Casimir–Lifshitz Forces”. *Nature* 457:7226, 7226 2009, pp. 170–173 (cit. on p. 138).
80. L. Neuhaus, R. Metzdorff, S. Chua, T. Jacqmin, T. Briant, A. Heidmann, P.-F. Cohadon, and S. Deleglise. “PyRPL (Python Red Pitaya Lockbox) — An Open-Source Software Package for FPGA-controlled Quantum Optics Experiments”. In: *2017 Conference on Lasers and Electro-Optics Europe & European Quantum Electronics Conference (CLEO/Europe-EQEC)*. 2017 Conference on Lasers and Electro-Optics Europe & European Quantum Electronics Conference (CLEO/Europe-EQEC). IEEE, Munich, Germany, 2017, pp. 1–1. ISBN: 978-1-5090-6736-7 (cit. on p. 61).
81. M. Nonnenmacher, M. P. O’Boyle, and H. K. Wickramasinghe. “Kelvin Probe Force Microscopy”. *Applied Physics Letters* 58:25, 24, 1991, pp. 2921–2923 (cit. on p. 114).
82. *Org Mode*. URL: `https://orgmode.org` (cit. on p. 4).
83. Ardavan F. Oskooi, David Roundy, Mihai Ibanescu, Peter Bermel, J. D. Joannopoulos, and Steven G. Johnson. “Meep: A Flexible Free-Software Package for Electromagnetic Simulations by the FDTD Method”. *Computer Physics Communications* 181:3, 1, 2010, pp. 687–702 (cit. on p. 146).
84. Edward D. Palik and Gorachand Ghosh, eds. *Handbook of Optical Constants of Solids*. Academic Press, San Diego, 1998. 5 pp. ISBN: 978-0-12-544420-0 (cit. on pp. 33, 147).
85. Blaise Pascal. *Les Provinciales, Ou Les Lettres Escrites Par Louis de Montalte à Un Provincial de Ses Amis et Aux RR. PP. Jésuites, Sur Le Sujet de La Morale et de La Politique de Ces Pères*. 1657 (cit. on p. iv).
86. S. Perisanu, V. Gouttenoire, P. Vincent, A. Ayari, M. Choueib, M. Bechelany, D. Cornu, and S. T. Purcell. “Mechanical Properties of SiC Nanowires Determined by Scanning Electron and Field Emission Microscopies”. *Physical Review B* 77:16, 30, 2008, p. 165434 (cit. on p. 33).
87. B. Pigeau, S. Rohr, L. Mercier de Lépinay, A. Gloppe, V. Jacques, and O. Arcizet. “Observation of a Phononic Mollow Triplet in a Multimode Hybrid Spin-Nanomechanical System”. *Nature Communications* 6:1, 2015, p. 8603 (cit. on p. 7).
88. M. Pinard, P. F. Cohadon, T. Briant, and A. Heidmann. “Full Mechanical Characterization of a Cold Damped Mirror”. *Physical Review A* 63:1, 11, 2000, p. 013808 (cit. on p. 194).
89. M. Pinard, Y. Hadjar, and A. Heidmann. “Effective Mass in Quantum Effects of Radiation Pressure”. *The European Physical Journal D - Atomic, Molecular, Optical and Plasma Physics* 7:1, 1, 1999, pp. 107–116 (cit. on pp. 12, 15).
90. M. Poggio, C. L. Degen, H. J. Mamin, and D. Rugar. “Feedback Cooling of a Cantilever’s Fundamental Mode below 5 mK”. *Physical Review Letters* 99:1, 2, 2007, p. 017201 (cit. on pp. 194, 196).
91. A. Pontin, M. Bonaldi, A. Borrielli, F. S. Cataliotti, F. Marino, G. A. Prodi, E. Serra, and F. Marin. “Squeezing a Thermal Mechanical Oscillator by Stabilized Parametric Effect on the Optical Spring”. *Physical Review Letters* 112:2, 15, 2014, p. 023601 (cit. on p. 207).
92. *RedPitaya GitHub Repository*. RedPitaya GitHub Repository. URL: `https://github.com/RedPitaya/RedPitaya` (cit. on pp. 61, 62).
93. Homer Reid. *HomerReid/Scuff-Em*. 21, 2021 (cit. on p. 146).
94. M. T. Homer Reid, Alejandro W. Rodriguez, Jacob White, and Steven G. Johnson. “Efficient Computation of Casimir Interactions between Arbitrary 3D Objects”. *Physical Review Letters* 103:4, 20, 2009, p. 040401 (cit. on pp. 138, 146).
95. M. T. Homer Reid, Jacob White, and Steven G. Johnson. “Fluctuating Surface Currents: An Algorithm for Efficient Prediction of Casimir Interactions among Arbitrary Materials in Arbitrary Geometries”. *Physical Review A* 88:2, 23, 2013, p. 022514 (cit. on pp. 138, 146).

96. S. Reynaud and A. Lambrecht. *Casimir Forces.* 16, 2016. arXiv: `1410.2746 [quant-ph]`. URL: `http://arxiv.org/abs/1410.2746` (cit. on p. 138).
97. Bastian Rieck. *Pseudomanifold/Latex-Mimosis.* 9, 2021 (cit. on p. 4).
98. Alejandro W. Rodriguez, Federico Capasso, and Steven G. Johnson. “The Casimir Effect in Microstructured Geometries”. *Nature Photonics* 5:4, 2011, pp. 211–221 (cit. on pp. 137, 139).
99. Alejandro W. Rodriguez, Alexander P. McCauley, John D. Joannopoulos, and Steven G. Johnson. “Casimir Forces in the Time Domain: Theory”. *Physical Review A* 80:1, 27, 2009, p. 012115 (cit. on pp. 145, 146).
100. N. Rossi, F. R. Braakman, D. Cadeddu, D. Vasyukov, G. Tütüncüoglu, A. Fontcuberta i Morral, and M. Poggio. “Vectorial Scanning Force Microscopy Using a Nanowire Sensor”. *Nature Nanotechnology* 12:2, 2017, pp. 150–155. arXiv: `1604.01073` (cit. on pp. 6, 7, 9).
101. D. Rugar and P. Grütter. “Mechanical Parametric Amplification and Thermomechanical Noise Squeezing”. *Physical Review Letters* 67:6, 5, 1991, pp. 699–702 (cit. on p. 207).
102. Hartmut F.-W. Sadrozinski and Jinyuan Wu. *Applications of Field-Programmable Gate Arrays in Scientific Research.* 0th ed. CRC Press, 19, 2016. ISBN: 978-0-429-06346-6 (cit. on p. 61).
103. Samantha Sbarra, Pierre Etienne Allain, Aristide Lemaître, and Ivan Favero. *A Multiphysics Model for High Frequency Optomechanical Sensors Optically Actuated and Detected in the Oscillating Mode.* 17, 2021. arXiv: `2103.09509 [physics]`. URL: `http://arxiv.org/abs/2103.09509` (cit. on pp. 3, 4).
104. Silvan Schmid, Luis Guillermo Villanueva, and Michael Lee Roukes. *Fundamentals of Nanomechanical Resonators.* Springer International Publishing, Cham, 2016. ISBN: 978-3-319-28689-1 978-3-319-28691-4 (cit. on p. 11).
105. Cornelia Schwarz, Benjamin Pigeau, Laure Mercier de Lépinay, Aurélien G. Kuhn, Dipankar Kalita, Nedjma Bendiab, Laëtitia Marty, Vincent Bouchiat, and Olivier Arcizet. “Deviation from the Normal Mode Expansion in a Coupled Graphene-Nanomechanical System”. *Physical Review Applied* 6:6, 29, 2016, p. 064021 (cit. on p. 194).
106. K. V. Shajesh and M. Schaden. “Repulsive Long-Range Forces between Anisotropic Atoms and Dielectrics”. *Physical Review A* 85:1, 30, 2012, p. 012523 (cit. on p. 138).
107. *Shaofan Li, Gang Wang - Introduction to Micromechanics and Nanomechanics-World Scientific (2008).Pdf.* ISBN: 978-981-281-413-5 (cit. on p. 14).
108. Christian Sommer, Alekhya Ghosh, and Claudiu Genes. “Multimode Cold-Damping Optomechanics with Delayed Feedback”. *Physical Review Research* 2:3, 25, 2020, p. 033299 (cit. on p. 194).
109. B. C. Stipe, H. J. Mamin, T. D. Stowe, T. W. Kenny, and D. Rugar. “Noncontact Friction and Force Fluctuations between Closely Spaced Bodies”. *Physical Review Letters* 87:9, 10, 2001, p. 096801 (cit. on p. 139).
110. L. Tang, M. Wang, C. Y. Ng, M. Nikolic, C. T. Chan, A. W. Rodriguez, and H. B. Chan. “Measurement of Non-Monotonic Casimir Forces between Silicon Nanostructures”. *Nature Photonics* 11:2, 2 2017, pp. 97–101 (cit. on p. 139).
111. Felix Tebbenjohanns, Martin Frimmer, Andrei Militaru, Vijay Jain, and Lukas Novotny. “Cold Damping of an Optically Levitated Nanoparticle to Microkelvin Temperatures”. *Physical Review Letters* 122:22, 3, 2019, p. 223601 (cit. on p. 194).
112. Prashanth S. Venkataram, Sean Molesky, Pengning Chao, and Alejandro W. Rodriguez. “Fundamental Limits to Attractive and Repulsive Casimir-Polder Forces”. *Physical Review A* 101:5, 21, 2020, p. 052115 (cit. on pp. 139, 146).
113. Ming Chen Wang and G. E. Uhlenbeck. “On the Theory of the Brownian Motion II”. *Reviews of Modern Physics* 17:2-3, 1, 1945, pp. 323–342 (cit. on pp. 210, 237, 238).
114. *Welcome to Python.Org*. Python.org. URL: `https://www.python.org/` (cit. on p. 4).

115. Tobias Westphal, Hans Hepach, Jeremias Pfaff, and Markus Aspelmeyer. "Measurement of Gravitational Coupling between Millimetre-Sized Masses". *Nature* 591:7849, 11, 2021, pp. 225–228 (cit. on pp. 2, 3).
116. Norbert Wiener. "Generalized Harmonic Analysis". *Norbert Wiener.*, p. 142 (cit. on p. 14).
117. K. W. Wong, X. T. Zhou, Frederick C. K. Au, H. L. Lai, C. S. Lee, and S. T. Lee. "Field-Emission Characteristics of SiC Nanowires Prepared by Chemical-Vapor Deposition". *Applied Physics Letters* 75:19, 8, 1999, pp. 2918–2920 (cit. on p. 33).
118. Tursunay Yibibulla, Yijun Jiang, Shiliang Wang, and Han Huang. "Size- and Temperature-Dependent Young's Modulus of SiC Nanowires Determined by a Laser-Doppler Vibration Measurement". *Applied Physics Letters* 118:4, 25, 2021, p. 043103 (cit. on p. 33).
119. J. Zou, Z. Marcet, A. W. Rodriguez, M. T. H. Reid, A. P. McCauley, I. I. Kravchenko, T. Lu, Y. Bao, S. G. Johnson, and H. B. Chan. "Casimir Forces on a Silicon Micromechanical Chip". *Nature Communications* 4:1, 1 14, 2013, p. 1845 (cit. on p. 139).

Acknowledgements

Only in the rarest cases a single person is responsible for the success of a scientific work, and also this PhD project relied more on the fantastic scientific environment than on myself. Hence, I want to thank and give the proper acknowledgements to all those who participated in this work. First of all I thank my more than brilliant supervisors, *Olivier Arcizet* and *Benjamin Pigeau* who know how to motivate during the difficult times of a PhD project and how to light up the sparks of curiosity whenever they risk to be extinguished by a flood of failing experiments, unexpected results, endless errorlogs etc...
Particularly I'll keep memories about the discussions with Olivier after which my mind felt like a balloon filled up to its extremum with new background knowledge and more new research ideas than one can possibly realize in a single PhD. Without the detailed feedback on the manuscript Olivier provided, this document would never be in such a readable (and long) form and I probably speak for any PhD student when saying that such precise and valuable feedback on a manuscript as those given by Olivier is worth more than gold in the time of writing. I thank both my supervisors for having a regular eye on my experiment and for the continuous discussions we had in the lab as well as during the sometimes extensive monday morning meetings. Large parts of the results in this work could only have been presented due to the tedious calculation of some π and $\sqrt{2}$ prefactors Benjamin had verified using multiple approaches. Also I have to thank Benjamin for the late but very motivating tradition of monday meeting *patisserie*.

As well from the group, I thank my predecessor *Laure Mercier de Lepinay* for her fantastic thesis (even though the french manuscript gave me a hard first french lesson when I started in Grenoble), which is a standard reference in nanowire fore microscopy. Laure's work allowed for a direct start of my project. Special credits also go out to my long time *brother in these Francesco Fogliano* for a good companionship for about three years, and quite some hours shared in lab/office and the Shakesbeer pub, as well as for some valuable advice that however did not prevent my taking of four years for the PhD. Furthermore, I thank my other team members, *Antoine Reigue* for the numerous conversations we had covering far more topics other than science, *Hugo Weltz* for continuing the experiments and making new discoveries in nanowire force microscopy based on my work which provides some kind of sense to it (even though his latest results should led us to reconsider the role of charges in the nanowire, *Clément Gouriou* and *Alex Fontana* for encouraging me and always helpful contributions to our discussions. During the last years my research has also been accompanied by several interns which helped making the time at Néel an unforgettable time for me.

Of course I thank our collaborators, in particular *Serge Reynaud* and *Romain Guérout* for the useful discussions about the Casimir force and the help with theory and simulation. Furthermore, I want to name *Jean-Philippe Poizat* who has always been close to the project and together with *Hermann Sellier* supervised the progress of the work and provided useful input during the regular CST meetings.

The experimental work could not have been realized without some helping hands at the institute. First of all I thus thank the *Nanofab Team* around *Jean-Francois Motte*, *Gwenaelle Julie* and *Bruno Fernandez* for the help with sample fabrication and characterization. I am also very happy that *Simon Le Denmat* contributed his experience about AFM and KPFM to this project and helped us to optimize sample design and to characterize them before force measurements. The manifold of improvements on the experimental setup would not have been possible without the help of the mechanical workshop and associates, namely *Richard Haettel*, *Julien Jarreau*, *Laurent Del-Rey*, *Eric Eyraud* and *Denis Maillard*.

Regarding the developments around the FPGA I am infinitely thankful to have had the help and good counselling of *Julien Minet*. Also on the IT side I thank *Julien Michel* and in particular *Patrick Belmain* who helped me a lot to set up the simulation infrastructure on the institute's cluster. A completely different kind of help I got from the administrative staff in Néel, while arriving in France is a bureaucratic nightmare, the guidance of people like *Florence Pois* and *Aurelie Laurent* made the paperwork a simple and nearly enjoyable task.

Close to lastly, I thank the quantum engineering programs *GreQuE* and the Cofund program *QuEnG*, both of which my PhD project has been part of. Firstly, this allowed us to expand the simulation cluster of the institute by a powerful machine, particularly suited to solve our Casimir problems and secondly it permitted me to be in regular exchange with students in other quantum related research fields.

Special thanks goes to my friends and flatmates which more than once succeeded to convince me to spend time in Ardeche or the mountains instead of the lab. And lastly but not less important for the success of my work, I thank my family for their support that has always been strong despite about a thousand kilometres distance.

Summaries

General summary

Over the last decades, nanotechnology became a flourishing field of discoveries in science, enabled by the constant progress made in microfabrication and characterization capabilities. Following the original developments of the atomic force microscope, the field of nanomechanical force microscopy significantly evolved, offering a new approach for imaging on the nanoscale complementary to direct optical or electronic microscopy. It now represents a standard tool for the characterization of structures with sub-nanometer resolution. In this thesis, we employ an ultrasensitive force sensor in the form of a suspended vibrating nanowire to image force fields above nanostructures in the vicinity of the vibrating extremity of the nanowire.

While an AFM probe is sensitive to forces perpendicular to the surface, the nanowire probe measures forces in the horizontal plane. Its ability to vibrate equally along both transverse directions allows to realise measurement of 2D force fields. An optical readout serves to probe the mechanical vibrations of the subwavelength-sized nanowires, which function as a force transducer.

While former experiments were based on time-consuming measurements of the nanowire's random, thermal noise trajectories in 2D, followed by a large analysis effort, the methods and protocols developed in this thesis allow the realization of force field imaging in quasi-realtime (10 measurements per second). This is achieved by recording resonantly driven trajectories in the 2D space, whose frequency shifts are tracked by a double phase lock loop and multiple lock-in demodulators, which allow determining the nanowire's eigenmode orientations. The 2D force field under investigation can then be determined by analyzing the perturbation of the nanowire's eigenmodes.

With these achievements we extended the use cases towards the measurement of proximity forces which requires good controllability and stability of the experiment due to the both the small separations between the nanowire extremity and the sample, and the large force gradients found above nanostructured surfaces.

We present measurements of the electrostatic force fields above nanostructured surfaces that are caused by electric field gradients generated by the sample's geometric structuration as well as by residual surface fields. The former cause a quadratic dependence on an externally applied voltage, while the surface fields are independent of the applied sample bias voltage. The different field contributions are analyzed using the Maxwell stress tensor formalism which allows compensating the linear contribution of the residual electrostatic field, and estimating the residual force field gradient. The latter is found in good qualitative agreement with the numerical estimation of the Casimir force we realized, both in magnitude and shape. For a quantitative comparison of the experimental results with the theoretical expectations, we subsequently propose a method to compensate the residual surface fields in all three directions, which is already being tested experimentally.

The last topic of this thesis concerns the control and analysis of the nanowire's dynamics by an artificial force field produced by a realtime feedback in 2D that allows to create any structure of force field. We realized a proof of concept, applying a control force in an arbitrary direction, whose magnitude is proportional to the vibrations of the nanowire along a chosen arbitrary direction. We explored different configurations of the application of an uniaxial parallel and a transverse feedback. Additionally, we show that a delayed feedback scheme can be used to realize cold-damping of a single nanowire mode. Furthermore, we use a single transverse feedback to squeeze the nanowire's noise if position and velocity space up to values close to the theoretical limit.

Résumé

Au cours des dernières décennies, le développement des nanotechnologies a permis des avancées conséquentes dans le domaine des sciences appliquées et fondamentales, grâce à la maîtrise croissante des techniques de micro-fabrication et des progrès réalisés dans les domaines de la caractérisation.

En particulier, les sondes de force nano-mécaniques, héritières de l'emblématique microscope à force atomique, ont réalisé des progrès importants et permettent d'explorer des surfaces via les forces qu'elles exercent sur le nano-résonateur, fournissant une microscopie complémentaire des mesures optiques ou électroniques.

Dans ce manuscrit, nous présentons les développements effectués afin de réaliser une sonde de force ultrasensible basée sur la lecture optique des vibrations d'un nanofil suspendu de carbure de silicium, dont l'extrémité vibrante est balayée au dessus de la nanostructure d'intérêt. Cette dernière produit un champ de force qui perturbe les propriétés mécaniques du nanofil, en générant des décalages en fréquence, des changements de son amortissement ainsi qu'une rotation des modes propres, dont la mesure permet de déterminer à la structure bidimensionelle du champ de force. Les nanofils mesurent essentiellement les forces parallèles à la surface, avec une sensibilité de quelques $\mathrm{aN}/\sqrt{\mathrm{Hz}}$ à température ambiante.

Alors que les expériences précédentes étaient basées sur une analyse spectro-angulaire du bruit thermique des nanofils, requérant des temps d'acquisition et d'analyse relativement longs, les protocoles développés dans cette thèse permettent d'imager les champs de force quasiment en temps réel (10 mesures par seconde) tout en préservant la sensitilité de la mesure ainsi que son caractère bidimensionnel. Les protocoles de mesure sont basés sur des trajectoire cohérentes, produites en excitant le nanofil simultanément à ses deux fréquences de vibration transverse, tandis que l'analyse des perturbations de ses propriétés mécaniques est réalisée à l'aide de deux boucles à verrouillage de phase et de détections synchrones.

Ces développements nous ont permis d'approcher plus finement des surfaces afin d'étudier les forces de proximité. Nous présentons une étude des champs de force électrostatiques au-dessus des surfaces nanostructurées créées par la topologie de surface, mais aussi des forces crées par les champs électriques résiduels. Les premiers présentant une dépendance en la tension d'échantillon, contrairement aux champs de surface. Ces différentes contributions sont analysées à l'aide du tenseur de Maxwell ce qui permet en particulier de compenser la contribution linéaire en tension générée par les champs de surface et d'identifier leur contribution intrinsèque. Cette dernière contient également les forces de Casimir générées par les fluctuations du vide électromagnétique, et les champs de force obtenus sont en bon accord, tant en amplitude qu'en profil spatial avec les simulations numériques réalisées.

Enfin, nous proposons une méthode permettant de compenser les champs de surface par un champ de contrôle extérieur, ce qui devrait permettre de rendre la mesure des forces de proximité plus quantitative.

Le dernier volet du manuscrit concerne la mesure et le contrôle de la dynamique des nanofils sous l'action d'un champ de force artificiel permettant de générer n'importe quelle structure de champ de force. Ces derniers sont produits grâce à une force ajustable en orientation, dont l'amplitude est proportionelle aux vibrations du fil mesurées dans une direction arbitraire. Nous démontrons qu'ils permettent de contrôler complètement les propriétés mécaniques du nanofil et nous explorons en particulier sa dynamique sous l'action d'un champ de force circulant. Ce dernier est en particulier capable de comprimer le bruit thermique du nanofil, en position et en vitesse, et crée une circulation de son bruit thermique.

Popular summary

This thesis presents recent developments in nanowire-based force field microscopy, a scanning probe technique aiming at a better understanding of the fundamental properties of nanostructures at short distances. It is based on the optical readout of the vibrations of a singly clamped nanowire as long as a hair is thick and about 100 times thin-

ner. By contactlessly moving the nanowire over a nanostructured sample surface, the changes of the vibration properties can be measured and used to learn about the forces acting on the nanowire. In doing so, we obtain information about the surface topology and its electrostatic properties. We apply this force microscopy to probe electrostatic surface fields, a step towards the detection of the fundamental Casimir force. In a last part, we present a technique to generate arbitrary force fields to gain control over the mechanical properties of the nanowire, opening perspectives for force field microscopy and the investigation of fundamental physics.

Résumé populaire

Ce manuscrit présente les développements réalisés dans le domaine de la microscopie de force à base de nano-résonateurs mécaniques, dans le but d'étudier les propriétés des nanostructures à courtes distances. Pour ce faire les vibrations d'un nanofil suspendu de carbure de silicium sont lues optiquement, tandis que son extrémité vibrante est approchée d'une nanostructure. Les modifications de ses propriétés mécaniques permettent de déterminer le champ de force exercé par la surface sur le nanofil. Ces mesures permettent d'étudier la topographie des nanostructures, ainsi que les champs électriques de surface. Ces derniers devront être compensés afin de détecter les forces de Casimir ressentis au-dessus de la nanostructure. Dans une dernière partie, on étudie des champs de force artificiels et on démontre que l'on peut contrôler les propriétés mécaniques du nanofil, et en partie changer ses directions de vibration sous l'action d'un champ de force circulant.